University of Trento

Department of Cellular, Computational and Integrative Biology

PhD in Biomolecular Sciences, 33rd Cycle

Folding, Misfolding and Therapeutics in Prion Diseases

Supervisor

Emiliano Biasini

Author

Giovanni Spagnolli

Academic Year 2019/2020

Folding, Misfolding and Therapeutics in Prion Diseases

Giovanni Spagnolli

Abstract

Prion diseases are rare neurodegenerative disorders affecting humans and other animals, caused by a proteinaceous infectious agent named prion. The pivotal event in these pathologies is the conversion of PrP^C, a physiologically expressed protein of poorly characterized function, into a misfolded conformer, named PrP^{Sc}, which is capable of replicating its conformationally-encoded information by inducing the conversion of its physiological counterpart. The aggregates resulting from this misfolding process accumulate in the central nervous system of affected organisms leading to neuronal death. Prion diseases are always fatal and no therapy is currently available. The lack of an effective therapeutic strategy to tackle such conditions is the result of the poor available information regarding many aspects of PrP^{Sc}, such as its structure, pathogenicity, and its replication mechanism. To complicate things further, PrP^{Sc} can appear as a set of distinct conformers, named strains, characterized by the capacity to evolve through modification and selection of their conformations, promoting resistance to treatments. In this work, we focus on two main aspects of prion biology, the elucidation of prion structure and propagation, and the development of a novel pharmacological strategy to tackle prion diseases. In both projects, we exploited the potential of integrative schemes combining computational methods and experimental data. Such approaches allowed us to build a plausible atomistic model of PrP^{Sc} and to propose a propagation mechanism describing the series of events underlying prion propagation. Moreover, the application of advanced computational schemes enabled us to identify a PrP folding intermediate displaying unique druggability properties. By exploiting the structural information of this protein conformer we identified a compound capable of acting as a pharmacological degrader for PrP by interfering with its folding pathway. Overall, this work highlights how the integration of computational and experimental methods is an extremely valuable scheme to answer complex biological questions, such as unraveling the mechanisms of protein misfolding and providing the tools to design pharmacological strategies for untreatable diseases.

Declaration

I, Giovanni Spagnolli, confirm that this is my own work and the use of all material from other sources has been properly and fully acknowledged.

Signature

Giovanni Spagnolli

The contents presented in this thesis are the result of an interdisciplinary study that involved the effort of experimental and computational scientists from different institutions. My specific contributions as well as that of the other researchers collaborating in this work are described in detail on page 155.

Contents

Results & Discussion

Methods

Chapter 1

An Overview of Amyloids & Prions

1.1 Protein Folding and Misfolding

Protein expression and function in cells are finely-tuned processes modulated by the combination of different regulatory mechanisms. These may intervene at the level of gene transcription, processing, stability, and translation of the mRNA as well as in the post-translational modifications, sorting, recycling, and degradation of the corresponding protein chain[1]. One of the fundamental conditions required to ensure the proper functioning of the cells is that the expressed proteins achieve their correct, functional three-dimensional conformation. In physiological conditions, the polypeptides are usually capable of spontaneously acquire their native form, as evidenced by the fact that a large number of proteins can be refolded *in vitro*. However, the presence of destabilizing mutations, the alteration of the cellular environment, or stochastic fluctuation during the folding process can induce the protein to misfold. When this happens, the polypeptide fails to achieve its correct three-dimensional shape and instead assumes an aberrant, aggregation-prone conformation[2]. To minimize the accumulation of misfolded species, cells are equipped with a quality control system responsible for monitoring proteins and ensuring that they properly reach their native structures. This machinery relies on two main strategies by which misfolded proteins can be refolded or degraded[3]. Molecular chaperones play a crucial role in assisting protein folding and refolding, furthermore, they are involved in the assembly of quaternary structures as well as the translocation of proteins across the membranes. They can support these processes in an ATP-dependent manner by promoting conformational rearrangements, or by stabilizing partially unfolded states to prevent their aggregation in the crowded cellular environment[4]. When the intervention of molecular chaperones is not sufficient to correct the protein misfolding, the aberrant conformer is usually sent to degradation. The most common pathway responsible for protein clearance is the ubiquitin-proteasome system (UPS). The UPS involves the recruitment of ubiquitin ligase enzymes that label the target polypeptide to be degraded by the proteasome[5]. Importantly, one of the main sites in which the protein quality control takes place is the endoplasmic reticulum (ER). Since the UPS is located in the cytosol, the majority of proteins that misfold inside the ER need to be retrotranslocated in the cytoplasm to be eliminated by the proteasome through a process that is called ER-associated protein degradation (ERAD)[6]. However, some polypeptides that enter aggregated states or displaying particular physico-chemical features (i.e. the presence of a glycosylphosphatidylinositol, GPI, anchor[7]) cannot undergo

retrotranslocation and are typically cleared from the ER through a different pathway that reroutes the target conformers directly to the lysosomes, namely the ER-to-lysosomes associated degradation (ERLAD)[8]. Due to its importance, any alteration of the protein quality control functioning may result in deleterious effects for the cell. An outcome that can be largely attributed to the formation of aggregated misfolded species.

1.1.1 The Formation of Amyloids

Partially unfolded states represent an important crossroad between protein folding and misfolding. They can be explored by a polypeptide along its folding pathway or by denaturation of its native state. These conformations typically display hydrophobic patches on their surface that may act as initiator sites for aggregation. Indeed, while a single polypeptide can spontaneously fold into a non-native aberrant conformation, the process of protein misfolding is usually driven by the formation of quaternary contacts that are established mainly through the interaction of exposed hydrophobic surfaces[10]. The resulting aggregated species can display different structural features depending on the protein type, its concentration, and the environmental conditions, giving rise to amorphous aggregates, oligomers, or amyloid fibrils (figure 1.1)[11].
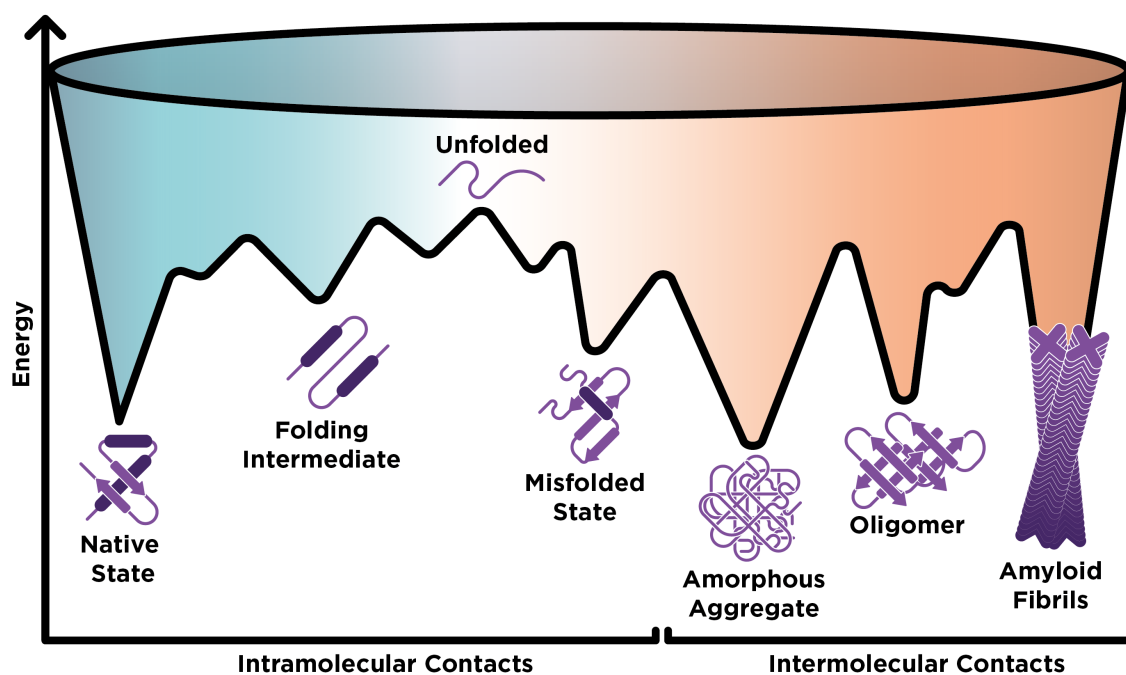
Figure 1.1: Aggregated species originating from protein misfolding. The process of protein folding (cyan) is generally driven by the formation of intramolecular contacts. Along this path, the polypeptide can visit several intermediate states before ultimately reaching the native state. Misfolded species can originate due to errors of the folding process or as a consequence of native state denaturation. These conformers are usually characterized by the presence of exposed hydrophobic patches that act as initiator sites for clumping. As this species appear, different processes, driven by the formation of intermolecular contacts (red), can lead to the formation of distinct aggregated species. A rapid hydrophobic collapse can usually lead to the appearance of amorphous aggregates, namely, quaternary assemblies lacking well-defined structural features. In other cases, depending on the physicochemical properties of the protein and the environment, oligomeric states can appear. These are dynamic and transient species, that generally evolve into high-order structures, yielding amorphous aggregates or more ordered states, such as amyloid fibrils[11].

Amorphous aggregation is a common process that is observed both *in vitro*, when expressing recombinant proteins, and in vivo resulting from physiological and pathophysiological processes. Depositions of this type of aggregates are found in different pathological conditions and can be related to cytotoxic effects[12]. However, most of the aggregated species that have been linked to disease progression and in particular to neurodegenerative disorders are arranged as amyloids[13]. Originally, these structures were classified based on histopathological features, such as the capacity to be stained by particular dyes, such as Congo red[14]. Currently, a broader definition is employed, and includes any polypeptide which can polimerize to form a cross-β structure (see section 1.1.2). The amyloid state is achieved through the assembly of monomeric precursors, usually unfolded and/or partially denatured conformers, into fibrils through a common nucleation-growth mechanism[15]. The initial phase of fibril generation involves the formation of oligomers, which are dynamic, transient, and of unknown and heterogeneous structure. Additional association of oligomers produces higher-order species, which can collapse into amorphous agregates or can lead to the formation of amyloid fibrils[16]. The latters emerge when a critical nucleus of oligomers is reached and a major structural rearrangements occurs, resulting in the formation a β-sheet-rich structure (protofibril) that elongates to form the mature amyloid fibril. The amyloid can then fragment producing new seeds capable of recruiting and converting new monomers, thus resulting in the exponential growth of the fibrillary structures (figure 1.2)[17]. Importantly, the misfolded conformation assumed by each monomer in the fibril typically does not bear any resemblance to the native structure[18].
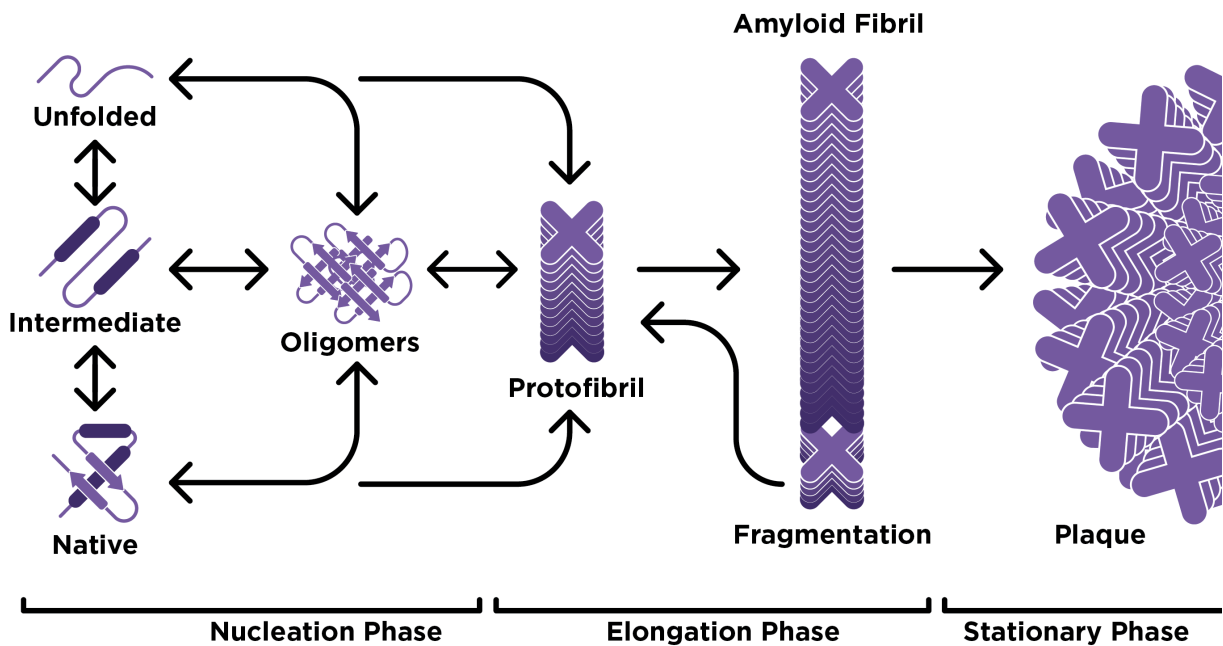
Figure 1.2: Formation of amyloid fibrils. Misfolding processes originating from different conformational states of a polypeptide can lead to the appearance of oligomers. Additional association of these species, through a process named nucleation, can lead to a major structural rearrangement of the aggregates resulting in the formation of a β-sheet-rich structure (protofibril). The protofibril can elongate by recruiting and converting soluble monomers. The mature amyloid fibril can then fragment into smaller structures, yielding new seeds for the propagation of the amyloid. Large clumps of fibrils, named plaques, are usually observed in the brain of patients affected by amyloid diseases[18].

1.1.2 The Structure of Amyloid Fibrils

A structural characteristic shared by amyloid fibrils is the cross-β fold, an architecture featuring a ladder of stacked β-strands aligned perpendicularly to the fibril axis. The resulting β-sheet displays the typical repeating length of ∼4.8 Å, corresponding to the hydrogen bond distance between paired amide and carbonyl groups in the backbone of adjacent strands[20]. These strands can be additionally stabilized by the presence of characteristic interactions, such as steric-zippers and asparagine (or glutamine) ladders. Steric zippers are tight interfaces of interdigitated hydrophobic side-chains that are established between amino acids located in laterally-interacting β-strands[21]. Instead, asparagine (or glutamine) ladders consist in a repetitive pattern of hydrogen bonds between the side-chain groups of residues located in vertically-interacting beta strands[22]. Amyloid fibrils have been shown to consist of one or more protofilaments. In the case of multiple protofilament assemblies, the resulting fibrils have morphologies ranging from twisted-rope structures to flat tapes[23]. The structure of a typical amyloid fibril composed of a single protofilament as well as the most recurrent types of stabilizing interactions are depicted in figure 1.3.
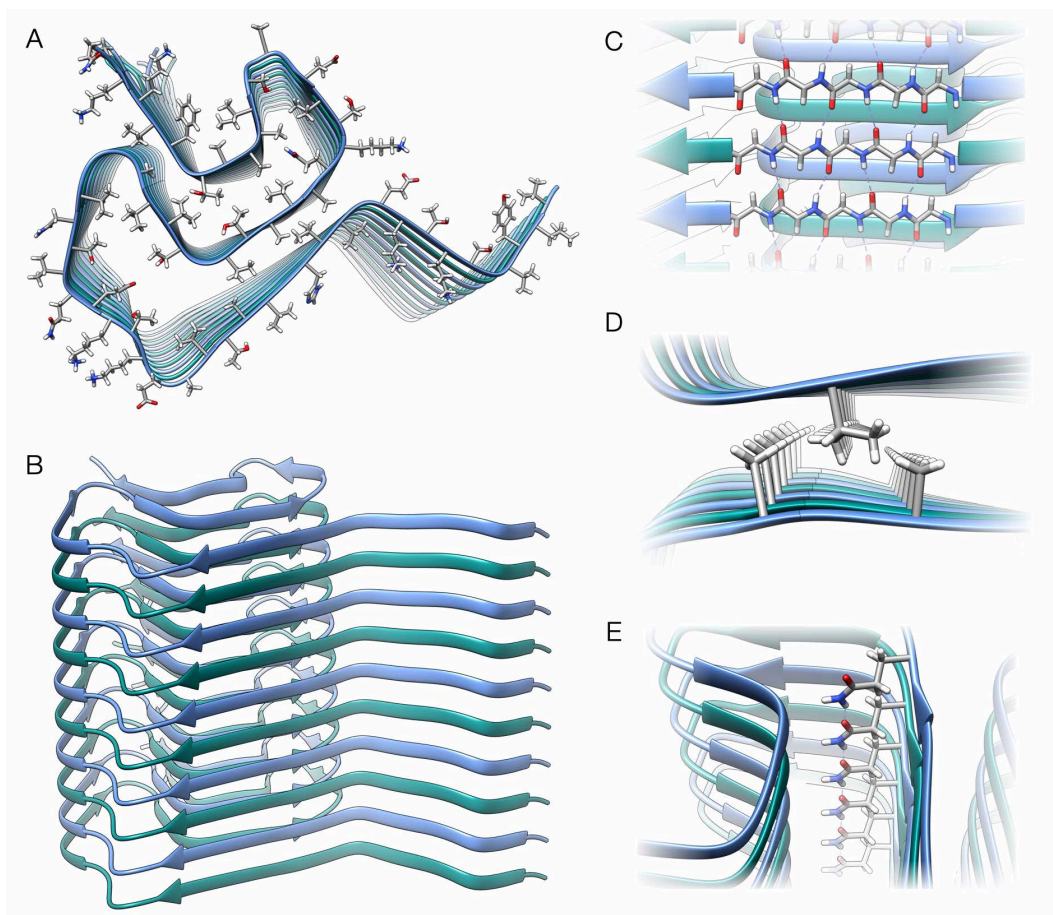
Figure 1.3: Structure of a representative amyloid fibril. Top (A) and lateral (B) view of an α-synuclein amyloid fibril (PDB 2N0A)[24]. Different monomers are depicted in alternating colors. (C) Visualization of the cross-β pattern characterized by hydrogen bonds between the backbones of vertically stacked β-strands. (D) Steric zipper interactions between hydrophobic side-chains of residues located in laterally adjacent β-strands. (E) Glutamine ladder formed by hydrogen bonding between amide and carbonyl groups located in the side-chains of vertically-interacting residues.

Most amyloids are formed by intermolecular stacking of monomers aligned in the same direction, an architecture defined as parallel in-register β-sheet (PIRIBS). Several disease-related aggregates of different polypeptides including α-synuclein (figure 1.3), the amyloid beta (Aβ) peptide, and even the prion protein can display this particular structural arrangement[18, 19]. However, the cross-β fold is not unique to the PIRIBS architecture, as it can also be found in antiparallel β-sheets[25] and in β-solenoids[26]. The latters are characterized by a helical winding of the polypeptide chain in which each repeating unit is an individual coil of the solenoid. These repeats named 'rungs' consist of ~12–30 amino acids configured as consecutive β-strands connected by turns and loops[27]. The interior of the solenoid usually contains tightly packed side-chains, forming a compact, mostly hydrophobic, core. The β-solenoid/β-helical fold is found in several soluble proteins including bacterial lyases, antifreeze proteins, and viral tailspikes[26]. One main characteristic of the non-amyloid structures featuring this architecture is that they usually contain 'capping domains' at their edges. This is to avoid that the unpaired β-strands at the helix termini provide templating surfaces that can promote further polymerization by interacting with other soluble monomers[28]. Importantly, a few functional amyloids of yeast involved in signal transduction and in the non-mendelian inheritance of particular phenotypic traits are characterized by this type of architecture. The fungal proteins HET-s (figure 1.4) and HELLF contain a C-terminal domain that in particular conditions can rearrange into a β-solenoid fold with self-propagating properties[29, 30].
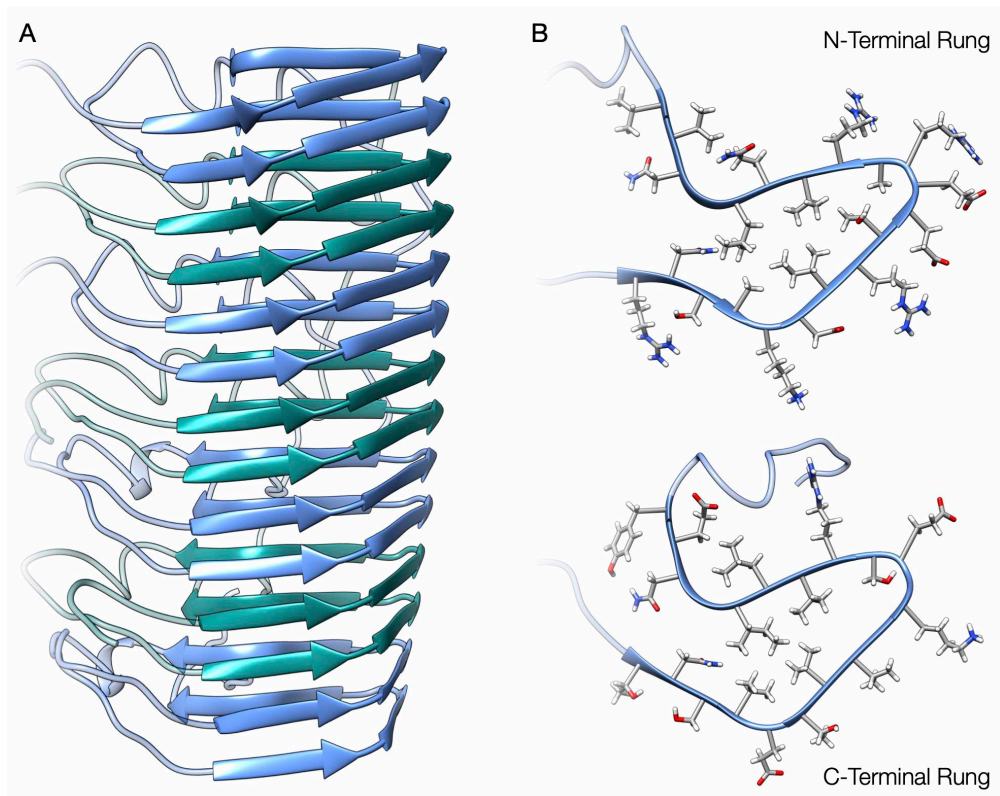
Figure 1.4: Structure of the HET-s amyloid fibril. (A) Lateral view of an HET-s amyloid composed by repetitions of its C-terminal domain arranged as a 2-rung-β-solenoid (PDB 2KJ3). Different monomers are depicted in alternating colors. (B) Top view of the N-terminal and C-terminal rungs of the fibril monomer. Each rung is composed of consecutive β-strands connected by turns and loops. The inner core of the solenoid is characterized by tightly packed hydrophobic side-chains.

The features displayed by these yeast proteins match the broad definition of prions, namely self-replicating proteinaceous particles that may act as infectious agents and/or can convey heritable changes in phenotype without relying on nucleic acids[31]. For this reason, the HET-s C-terminal domain is widely used as a simplified model to understand the molecular mechanism underlying prion replication and protein-based inheritance.

1.1.3   Amyloids and Diseases

The deposition of misfolded aggregates is the hallmark of several diseases known as proteopathies[32]. These include more than 40 different disorders and most of them are characterized by a neurodegenerative phenotype. The pathogenesis of amyloidosis remains largely uncharacterized and effective treatments are currently lacking. The only possible therapeutic approach that is currently employed to tackle these diseases is limited to the management of signs and symptoms. A growing body of research supports the concept that the development of different neurodegenerative proteopathies such as Alzheimer's and Parkinson's diseases are directly dependent on the seeded misfolding and aggregation of endogenous proteins (mainly Aβ and tau for the first and α-synuclein for the latter)[33]. In all proteopathies the spreading mechanism of protein misfolding is limited within the organism of the affected patient with the only exception of prion diseases in which the causative agent is also infectious and can be transmitted between individuals[34].

Prion diseases, also known as transmissible spongiform encephalopathies (TSEs), are a set of progressive neurodegenerative conditions caused by the propagation of a misfolded protein conformer, PrP^{Sc}, that is capable of replicating by inducing the conversion of its physiological counterpart, the cellular prion protein (PrP^C), without using nucleic acids[35]. These diseases have an estimated incidence of 1-2 people per million annually and occur in inherited, sporadic, and acquired forms[36]. Familial prion diseases originate from mutations in the *PRNP* gene, resulting in an increased misfolding propensity of the encoded prion protein. They are inherited in an autosomal dominant pattern and account for 10-15% of all cases of prion diseases[37]. Sporadic forms are likely attributable to spontaneous PrP misfolding or somatic gene mutations and constitute more than 80% of TSEs episodes[38]. Acquired prion diseases are instead transmitted through infected material, such as during medical operations or by consumption of contaminated food[39]. While the latter represent the minority of TSE cases it appears as an important concern for public health due to the risk of zoonosis, namely, the transmission of a pathogen from non-human animals to humans. A relevant case of TSE epidemic is represented by the outbreak of bovine spongiform encephalopathy (BSE). From its identification in 1986, more than 180000 cattle in the United Kingdom developed BSE, and ∼2 million have likely been infected, most of which were slaughtered for human consumption before showing signs of the disease[40]. Fortunately, enforcement of strict control measures resulted in the consistent decline of the epidemic and a substantial species barrier protected people from a widespread illness; indeed, less than 230 cases of TSE were linked to the consumption of contaminated beef products[41].

The most common TSE in humans is the Creutzfeldt-Jakob disease (CJD), a progressive dementia characterized by personality changes, visual problems, loss of brain function and mobility. The disease duration can substantially vary, however, CJD is usually lethal within five months from the onset of symptoms that occurs in late adulthood[42]. The origin of this pathology can be familial or

sporadic, and a rarer acquired variant (vCJD) also exists. This acquired form is characterized by a slower disease progression and earlier onset of symptoms (usually in young adulthood) with more prominent psychiatric problems compared to the classic CJD[43]. The diffusion of this encephalopathy was primarily attributed to eating BSE-infected beef, however, its spread may also occur via blood transfusion or contaminated surgical equipment (iatrogenic CJD)[44]. Importantly, vCJD is not the only documented case of prion infections in humans. Kuru, identified in the early 1950s, was a common form of TSE among the Fore people in Papua New Guinea. This disease was transmitted via a funerary cannibalism practice in which deceased people were cooked and eaten by the family members[45]. The Kuru epidemic was likely caused by a sporadic case of CJD that was first transmitted to the relatives of the affected individual and then spread to other villagers who ate their infected brain[46]. The epidemic declined and later disappeared after cannibalism was banned by the Australian administration[47].

Two less common forms of prion diseases are the Gerstmann-Sträussler-Scheinker syndrome (GSS), characterized by a CJD-like phenotype but with slower disease progression, and the fatal familial insomnia (FFI), which causes sleep deprivation progressively leading to mental deterioration[48]. Both are predominantly inherited, even if sporadic cases of FFI have been documented[49] and the extremely rare 'variably protease-sensitive prionopathy' has been proposed to be a sporadic form of GSS[50]. Different prion diseases not only may display distinct clinical manifestations, but they also show different neuropathologic hallmarks, such as abundant deposition of amyloid plaques in GSS, focal thalamic neuronal loss and gliosis in FFI, and distributed spongiform degeneration in CJD[51]. The standard method to diagnose prion diseases consists in biopsy, postmortem analysis of contaminated tissues, or examination of the cerebrospinal fluid. Recently, the introduction of a new test based on nasal brushings from olfactory epithelium has enabled to diagnose CJD with a sensitivity of ∼97% in a rapid and non-invasive fashion[52].

Due to the low incidence and the late onset of symptoms, prion diseases (except for epizootics episodes) are considered a minor concern for public health. However, a few important points should be raised to highlight the relevance of prion research. First of all, while the annual number of TSEs cases is low, the estimated lifetime risk of developing such pathologies is much higher, indeed, approximately 1:6000 of all-cause deaths in the United States have been attributed to prion diseases[53]. Furthermore, psychological and social effects on the relatives of affected individuals are not negligible: besides the acceptance of the inevitable death of the loved one, the families have to deal with the rapidly progressive conditions of the patients which will require home nursing or access to hospice care. Ultimately, protein misfolding is the leading cause of other, more frequent but non-infectious, neurodegenerative diseases such as Alzheimer's and Parkinson's disease[54]. Propagation of protein misfolding in these pathologies occurs with a prion-like mechanism that results in the deposition of fibrillary material in the central nervous system of the patient. Therefore, the advances provided by the comprehension of the prion propagation process would not only affect prion research, but also the entire field of neurodegeneration.

1.2 The Molecular Basis of Prion Diseases

Several decades of debate regarding the chemical nature of the causative agent of prion diseases lead to the formulation, in 1982, of the protein-only hypothesis by Stanley Prusiner, after he identified the pathogen responsible for the scrapie TSE in sheep[35]. Prusiner suggested that the agent accountable for prion diseases is constituted by a proteinaceous infectious particle, hence the name 'prion', capable of propagating in the absence of nucleic acid[35]. The misfolded protein conformer constituting the infectious material was named 'scrapie prion protein' (PrP^{Sc}), while its physiological counterpart, identified in 1986, was defined as 'cellular prion protein' (PrP^C)[55]. Importantly, the formal demonstration that a misfolded protein conformer is the solely responsible for the development of these pathologies arrived only several years later: first in 1993, when it was shown that mice lacking the *Prnp* gene, encoding for the prion protein, do not develop the disease when inoculated with PrP^{Sc}; and then, in the early 2000s, when infectious prions were successfully generated with bacterially expressed recombinant PrP[56,57]. For the sake of clarity, the term PrP will be used throughout the text when generically referring to the prion protein without specifying its particular conformation.

1.2.1 The Structure and Function of PrP^C

The prion protein is expressed as a major precursor consisting of 253 amino acids[58]. This polypeptide contains two signal sequences, one at the N-terminus, required for the protein translocation into the endoplasmic reticulum (ER), and one at the C-terminus, promoting the attachment of a glycophosphatidylinositol (GPI) group necessary for PrP anchoring to the cellular membrane[59]. The resulting native conformer, PrP^C, features a flexible N-terminal segment (residues 23-124 in human), and a structured, C-terminal domain (residues 125-231)[60]. The N-terminal moiety contains an octapeptide-repeats (OPR) sequence (residues 51-89) responsible for the binding of divalent cations[61], and a hydrophobic region (residues 112-134) that is highly conserved between animal species[62]. The latter was shown to play a role in lipid interactions[63] and to be fundamental for prion replication, indeed, PrP molecules lacking residues 112-119 cannot be converted into infectious prions[64]. The C-terminal domain of PrP^C is characterized by a well-defined globular fold that is stabilized by the presence of a disulfide bond between C179 and C214[65]. This sequence also contains two glycosylation sites at residues N181 and N197, as well as the attachment position for the GPI anchor[66]. A schematics of the PrP polypeptide is represented in figure 1.5.
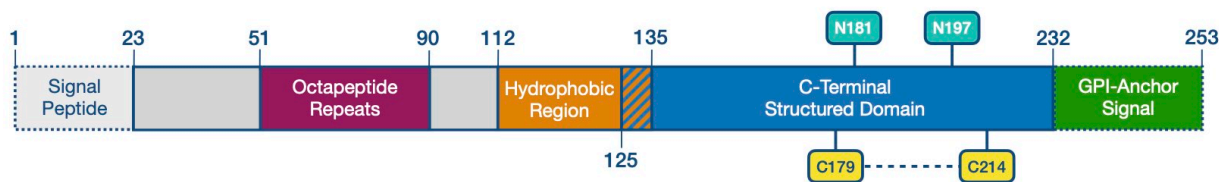
Figure 1.5: Schematics of the PrP polypeptide sequence. The picture illustrates a representation of the main features of the human prion protein. The N-terminal region includes a signal peptide (1-22, light gray), five octapeptide repeats (51-89, purple), and a conserved hydrophobic region (112-134, orange). The C-terminal region features a structured globular domain (125-231, blue) and a signal sequence for GPI linking (232-253, green). Importantly, both the N-terminal and C-terminal peptides are removed during the biogenesis. Residues involved in the formation of the disulfide bond (C179-C213) are indicated in yellow, while glycosylation sites (N181 and N197) are shown in cyan. Figure adapted from Spagnolli et al.[67] ©①

The structure of the C-terminal domain of PrP[C] has been largely characterized by employing nuclear magnetic resonance (NMR)[68] and X-ray crystallopraphy[69]. It consists of a three-helix bundle and two short antiparallel β-strands flanking helix-1. A representation of the globular domain of PrP[C] is shown in figure 1.6.
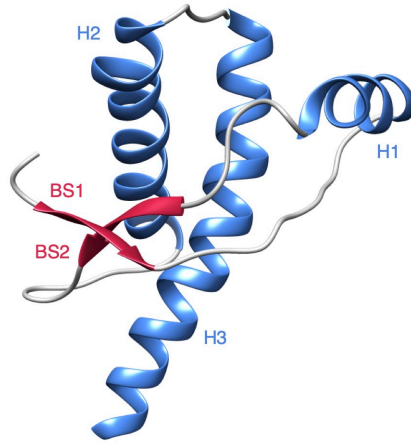
Figure 1.6: Ribbon diagram of the C-terminal domain of PrP[C]. The structure of the PrP globular domain (PDB 1QLX) is composed of two small anti-parallel β-strands (residues 128–131; and 161–164) depicted in red, and three α-helices: H1 (144-154), H2 (173-194), and H3 (200-227), depicted in blue. Figure adapted from Spagnolli et al.[67] ⓒⓘ

Investigating the physiological function of PrP[C] is crucial for understanding the mechanisms underlying TSEs pathogenesis since its alteration could play a role in the disease process. Even though PrP[C] was linked to several biological pathways its precise molecular role in cellular functioning is still poorly characterized[70]. Several studies on mice lacking the *Prnp* gene revealed that the absence of PrP expression typically results in minor phenotype alterations, such as deficits in spatial learning[71] and deregulation of the circadian rhythm[72]. The only significant exception is represented by a chronic demyelinating neuropathy that is observed in the late-adulthood of PrP null mice[73,74]. This mechanism was elucidated at the molecular level when it was shown that the N-terminal tail of PrP[C] can activate the Adhesion G Protein-Coupled Receptor G6, a protein known to be fundamental in myelin maintenance, on the surface of Schwann cells[75].

Additional studies identified PrP[C] as an important interactor with other membrane proteins, such as the neural cell adhesion molecule (NCAM)[76] and the N-methyl-D-aspartate receptors (NMDARs)[77]. Physical interaction of PrP[C] to NCAM was found to promote neuritogenesis through the activation of the FYN kinase signaling pathway[78,79], while PrP[C] association to NMDARs results in the receptors inhibitions by nitrosylation[80,81]. The latter supports a putative role of PrP[C] in the cellular stress response since hyperactivation of NMDARs induces the so-called excitotoxicity, a process resulting in death-signaling events such as reactive oxygen species generation and mitochondrial damage[82]. Importantly, PrP[C] was found to be linked with the ischemic response in vivo, a process in which excitotoxicity plays a fundamental role. In particular, it was shown that postischemic rodent brains display a marked overexpression of PrP[C], while in PrP null mice stroke enhances caspase-3 activation[83]. In summary, PrP[C] was shown to be associated with several molecular pathways, however this pleiotropism has led to confusion about the precise molecular function of the cellular prion protein. Currently, a definitive elucidation of the role of PrP[C] in the central nervous system is still lacking.

1.2.2 Sequence Variants of PrP

So far, the only established function of PrP is related to the development and progression of prion diseases, in fact, PrP^C not only acts as a substrate for prion replication, but its spontaneous misfolding typically constitute the initiating event of these pathologies. The propensity of PrP misfolding is strongly affected by mutations and polymorphisms on the *PRNP* gene, indeed, more than 20 genetic variants have been reported to be associated with the development of prion diseases (Figure 1.7)[51].
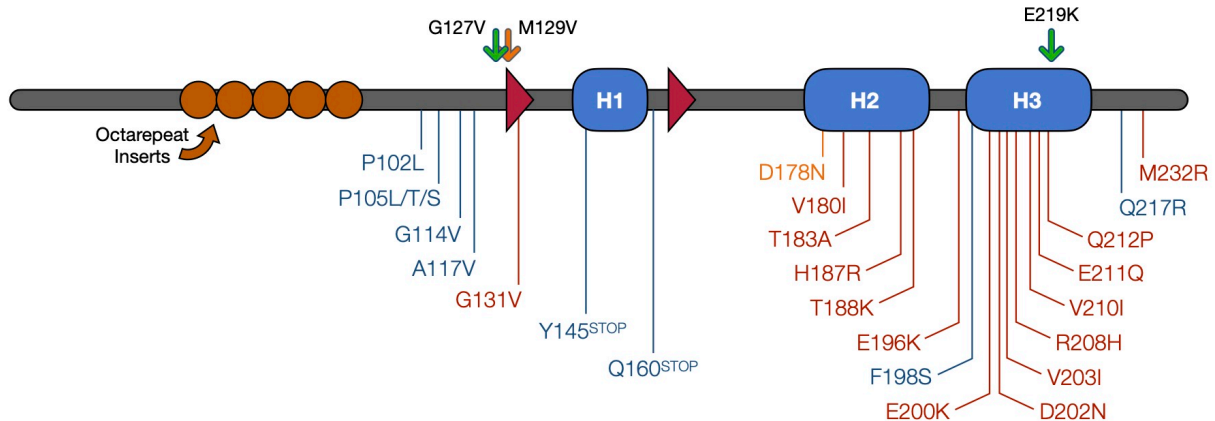
Figure 1.7: Summary of PrP variants linked to prion diseases. Schematic representation of PrP with the major disease-associated variants. Mutations linked to CJD are colored in red, while those associated with GSS in blue. D178N is depicted in orange, since the resulting phenotype can be either CJD or FFI, depending on the polymorphism at codon 129 (indicated with an orange arrow). Protective polymorphisms G127V and E219K are indicated with green arrows. The secondary structures of PrP^C are represented with blue boxes (α-helices) and red triangles (β-strands). The octapeptide-repeats region, whose expansion is also linked to the development of prion disease, is represented in brown. Sequence stretches are not in scale.

The likelihood of developing TSEs is highly dependent on the type of mutation in the *PRNP* gene. For instance, P102L, A117V, D178N, and E200K were confirmed to be completely penetrant and are responsible for more than 50% of familial cases. Others, such as V180I, V210I, and M232R have a controversial role since their associated risk of disease is significantly low[84]. Polymorphisms also play an important contribution in affecting the likelihood of developing TSEs, as well as in modifying the disease phenotype. The G127V and E219K variants were reported to confer resistance against prion diseases. In particular, G127V, identified only in the Fore people in Papua Nuova Guinea is strongly protective against Kuru[85], while E219K was reported to reduce the risk of sCJD[86]. The most relevant PrP polymorphism is the one at the level of codon 129, which can encode for methionine or valine. The presence of a single V129 allele is associated with a longer disease duration[87] and heterozygous (MV) individuals also have a lower risk to develop sCJD with respect to homozygous genotypes[88]. Furthermore, the polymorphism at codon 129 determines the phenotype expression related to the D178N mutation. In particular, the presence of valine in position 129 of the mutated gene leads to the development of CJD, while the presence of methionine results in FFI[89]. Sequence variations in the OPR-region have also been detected in patients with prion disease. These consist in a series of insertion with one to nine additional OPR and although high phenotypic variability and different histopathology is associated with these mutations, in general, the longer the OPR insertion, the earlier the disease onset[90].

1.2.3 PrP Homeostasis in Health and Disease

The biogenesis of PrP^C follows the typical pathway of GPI-anchored proteins[91]. The PrP polypeptide is directly translocated during synthesis through the Sec61 complex into the lumen of the ER[92]. In this compartment, PrP folds and undergoes a series of post-translational modifications, including the removal of the signal sequences, the addition of N-linked oligosaccharides, and GPI-anchoring. Then, PrP^C transits the Golgi apparatus, where glycans maturation occurs, to reach the late compartments of the secretory pathway. Here, in physiological conditions, a substantial fraction of PrP^C molecules are subjected to α-cleavage, a process in which a putative α-PrPase catalyzes the hydrolysis of the amide bond between residues 111-112 [93]. This cleavage releases the N-terminal flexible region of PrP^C (N1 fragment) while leaving the structured C-terminal domain (C1 fragment) attached to the membrane via its GPI anchor[94]. The N1 fragment was shown to exert antiapoptotic functions[95] and to protect against toxic effects induced by the amyloid-β peptide[96], while the C1 fragment was associated with the role of PrP^C in myelin maintenance[73]. The most important consequence of α-cleavage is the disruption of the hydrophobic region, which is critical for prion propagation. Indeed, PrP^{Sc} is not capable of converting PrP^C molecules that underwent this processing[97]. Once localized at the cellular membrane, PrP^C could be subjected to an additional post-translational modification named 'shedding', that consists in a cleavage, performed by the metalloprotease ADAM10, at the extreme C-terminus of PrP^C resulting in the release of almost the entire protein chain[98].

The PrP^C molecules that are still attached to the membrane can be reinternalized by the endosomal recycling pathway which directs the molecule in the early endosome through a clathrin-dependent[99] or a clathrin-independent route[100]. At this point PrP^C can be further processed and rerouted to the cellular membrane or sent to the late endosomes and to lysosomes for degradation (figure 1.8A)[101]. During its biogenesis, the fraction of PrP molecules failing to achieve the natively folded conformation are primarily cleared through the ERLAD[102]. This pathway, which reroutes the target polypeptide from the ER directly to the lysosome, is characteristic of proteins included in aggregates or displaying physicochemical features preventing retrotranslocation[8]. The ERLAD was shown to play an important role in the elimination of aggregation-prone PrP molecules carrying disease-causing mutations[102, 103]. In particular, the expression of PrP-T182A, a mutant characterized by an aberrant trafficking, causes a significant activation of autophagy with the consequent rerouting of misfolded PrP aggregates from the ER to the lysosomes[102]. A few studies proposed that misfolded PrP could also be eliminated by the proteasome after retrotranslocation in the cytoplasm in physiological conditions[104], however, these observations were likely biased by experimental artifacts, such as the use of strong promoters for PrP expression and/or by the use of proteasome inhibitors that inevitably results in the overload of the protein quality control[103]. Indeed, experiments on mice inoculated with infective brain homogenates showed that ubiquitination of PrP species occurs only at the terminal stage of the disease, namely, when the proteostasis network of the cell is completely compromised due to the accumulation of misfolded species[105].

The replication of PrP^{Sc} is highly dependent on the mechanisms of PrP^C trafficking, processing and degradation. PrP^C molecules carrying disease-linked mutations usually misfold in the ER and the Golgi apparatus. Conversely, during cell infection the major site of prion propagation is represented by the plasma membrane. PrP^{Sc} aggregates can be internalized following the endosomal

recycling pathway and propagate inside the cellular compartments. The accumulation of misfolded species can damage the membranes of the endocytic vesicles and lysosomes, causing the leakage of PrP^{Sc} in the cytoplasm of the cell (figure 1.8B)[106]. PrP^{Sc} can spread in tissues throughout several mechanisms, such as its exosomal secretion in the extracellular space[107], direct contacts between cells[108] and through cytoplasmic extension (tunnelling nanotubes) connecting cells as intercellular bridges[109]. The development of pathological conditions alters the processing of PrP^{C}. In the brain of patients with CJD[110] as well as in prion-affected animals[111] and cells[112], a substantial fraction of PrP molecules are cleaved around position 90 to generate the N2 and C2 fragments[113]. This process is named β-cleavage and it is almost absent in physiological conditions; it can be performed by calpains[114], lysosomal proteases[112] or by direct reaction with reactive oxygen species[115]. Importantly, while α-cleavage renders the resulting polypeptides incapable of being converted into PrP^{Sc}, β-cleavage yields a fragment (C2) that is a suitable substrate for prion propagation[116].
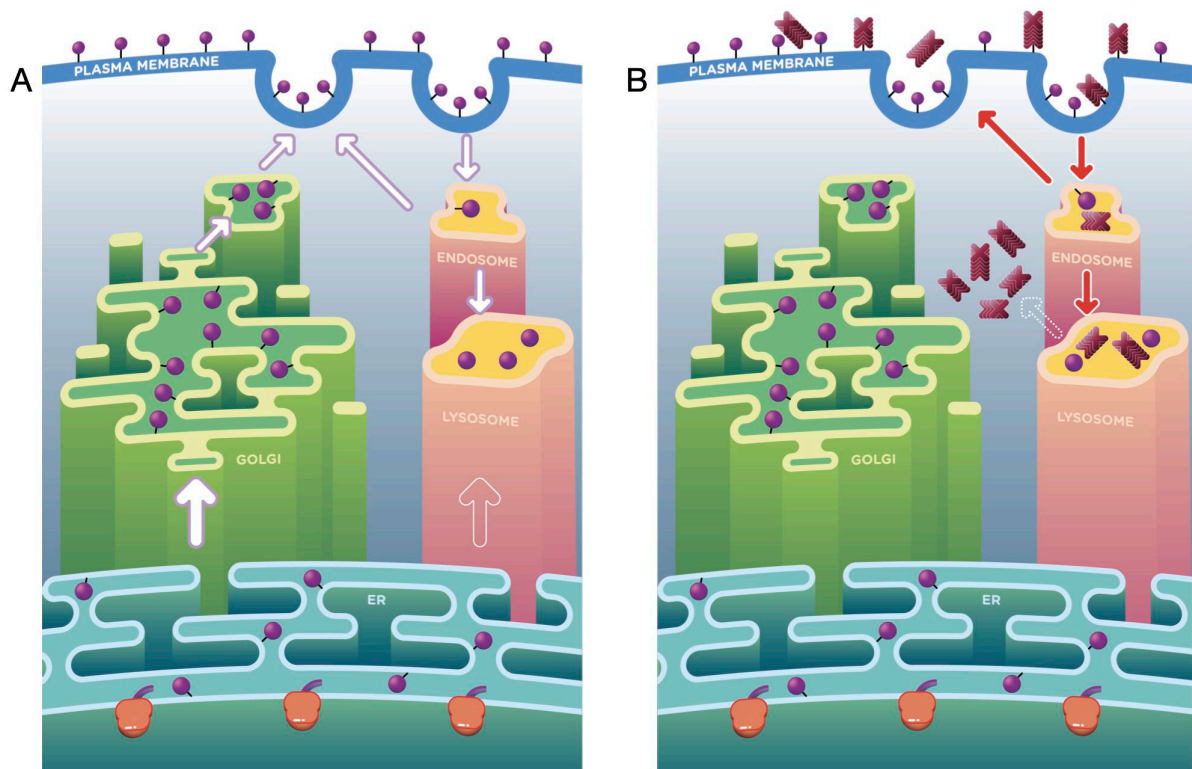
Figure 1.8: PrP and PrP^{Sc} trafficking in physiological conditions and during prion infection.
(A) PrP biogenesis follows the secretory pathway, which is typical of GPI-anchored proteins. The polypeptide is synthesized into the lumen of the ER, where it folds and immature sugars are attached. Then the protein transits the Golgi apparatus, where sugar moieties are matured, and ultimately reaches the plasma membrane. From the cell surface, PrP^{C} molecules could be internalized, by the endosomal recycling pathways, and eventually be redirected into the lysosomes for degradation. Arrows indicate PrP^{C} trafficking in physiological conditions. (B) The major site of prion replication in an infected cell is represented by the plasma membrane. PrP^{Sc} aggregates can then be internalized, following the same recycling pathway of PrP^{C} and can continue to replicate in the endosomal compartments. The accumulation of aberrantly folded species can ultimately lead to damage of these intracellular vesicles, leading to PrP^{Sc} leakage into the cytoplasm. Arrows indicate PrP^{Sc} trafficking in a prion-infected cell. Figure adapted from Spagnolli et al.[67] ©①

1.2.4 The Neurotoxicity of PrP^{Sc}

While prion propagation represents the central event in the development of prion diseases, the exact mechanisms by which PrP^{Sc} exerts its neurotoxic effects are still debated. One of the reasons that hamper the finding of a direct link between PrP^{Sc} and neurodegeneration is the complete dependence of the disease progression on the expression of PrP^{C} [117]. Indeed, not only the absence of *Prnp* preclude the development of the disease[56], but also the disease phenotype can be reverted after the onset of symptoms if the expression of PrP^{C} is discontinued. This was shown in an experiment in which PrP^{C} was ablated during the course of prion infection by employing a mouse model with homozygous floxed PrP gene and expressing the Cre recombinase under the control of the neurofilament heavy chain promoter. This strategy enabled to activate the expression of the Cre recombinase and the consequent deletion of the *Prnp* gene only in neuronal cells and after ∼10-12 weeks of age. Inoculation with prions before PrP knockout resulted in the development of the initial stages of the disease. However, after *Prnp* excision, prion disease was prevented and the spongiform lesions were reversed. Notably, prion replication in non-neuronal cells, as well as the deposition of extra-neuronal PrP^{Sc} by astrocytes continued after the interruption of PrP expression[118]. This result, which strongly indicates a decoupling between prion propagation and toxicity, is further corroborated by other observations in mice expressing a C-terminally deleted PrP polypeptide lacking the GPI-signal sequence (GPI-anchorless PrP). In these mutants, PrP^{Sc} is capable of propagating and maintaining its infectivity, however, the resulting pathological condition does not resemble prion diseases, but rather the milder cerebral amyloid angiopathy observed in other disorders such as Alzheimer's disease. This observation suggests that PrP^{Sc}, in order to elicit toxic effects, must rely on the cellular internalization mediated by the PrP GPI anchor[119].

Although the link between PrP^{Sc} and its neurotoxicity is far from being clarified, there are different effects induced by PrP^{Sc} replication and aggregation that can explicate some of the deleterious cellular alterations observed in prion diseases. The major consequence of the accumulation of aberrant misfolded species inside the cell is the overload of the protein quality control machinery[120]. This effect results in aberrant signaling related to the unfolding protein response, such as the hyperactivation of the PKR-like endoplasmic reticulum kinase (PERK) that attenuates protein translation by phosphorylating eIF2α[121]. Additionally, PrP^{Sc} propagation in the cellular compartments has been associated with the impairment of the ubiquitin-proteasome system (UPS)[122] and with an increased activation of autophagy[123]. However, it should be noted that these effects might be more an indirect effect rather than a direct consequence of PrP^{Sc} toxicity. In particular, the induction of autophagy can be a cellular response that confers neuroprotection by increasing the clearance of PrP^{Sc} aggregates[117], while the initial overload of the UPS is not dependent on the presence of PrP species which are found polyubiquitinated only in the later stages of the disease[105].

Other molecular pathways have also been linked to neurotoxicity in prion diseases, such as the hyperactivation of the NDMARs[124] that are proposed to be regulated by PrP^{C} [77], however, the key mechanisms responsible for the development of the detrimental phenotype observed in prion diseases have not been identified yet.

1.3   The Structure of PrP^{Sc}

When reviewing studies focused on the structural characterization of PrP^{Sc} is important to consider the biochemical and biological features underlying the original definition of prion, namely, a pathologically-relevant protein capable of replicating without relying on nucleic acids[35]. From a structural standpoint, PrP^{Sc} is generally conceived as a protease-resistant aggregate rich in β-sheets, in contrast to its physiological counterpart PrP^{C}, which is soluble and monomeric. However, different aggregated assemblies of PrP can display biochemical features similar to the ones of PrP^{Sc} while not being infectious[125]. This is the case of some synthetically-generated PrP amyloids or a few naturally occurring mutant PrP aggregates, that can induce the pathology in animals but are unable to transmit infectivity[126]. Some of these non-infectious PrP aggregates can propagate *in vitro* and *in vivo*, following a 'seeding' mechanism shared by many different amyloids[127]. This seeding process usually results in the replication of the original PrP amyloid conformation by conversion of the soluble monomers, however, in some rare cases it can promote the formation of alternative self-replicating conformers with completely different structural arrangement, even infectious prions[128]. This process is called 'Deformed Templating' and was firstly observed in an experiment in which Syrian hamsters were inoculated with a noninfectious PrP amyloid generated in vitro. None of the animals developed any clinical signs of prion disease but some of them accumulated abnormally folded forms of PrP. Inoculation of their brain homogenates to wild type animals in two serial passages induced a full-fledged prion disease with PrP^{Sc} deposits in the brain of the affected animals[129]. Importantly, the initial recombinant PrP amyloid displays different structural features as compared to PrP^{Sc}, such as the length of the β-sheets core, spanning residues 175-225 in the synthetic PrP amyloid[130] and ∼90-231 for the infectious prion[131].

An additional aspect to consider for properly interpreting the available data on the structure of PrP^{Sc} regards the features of the sample subjected to characterization. The use of brain-derived PrP^{Sc} represents the ideal choice since it constitutes the authentic prion. However, this material has a high level of molecular heterogeneity and it is difficult to purify due to the presence of the GPI-anchor and the N-linked glycans[132]. A valid alternative is represented by brain-derived GPI-anchorless PrP^{Sc}, obtained by transgenic mice expressing PrP lacking the GPI-signal sequence. This sample is less heterogeneous, also due to the substantial underglycosylation of the fibrils, and retains full infectivity[119]. Importantly, while brain-derived samples are suitable for different structural characterization techniques, including cryo-electron microscopy (cryo-EM), they cannot be used for ssNMR. In particular, elucidation by NMR requires the isotopic labeling of the protein, namely, the enrichment of the sample in atomic nuclei with low natural abundance (i.e. ^{13}C and/or ^{15}N), a process that cannot be employed to generate substantial amounts of protein in vivo[133]. For this reason, different experimental strategies have been developed to yield infectious material starting from prion protein expressed in bacteria. Initial attempts based on simple amyloid fibrilization failed to generate recombinant material with significant infectivity or fully recapitulating the characteristics of the infectious agent[57, 134]. Later, the group of Jiyan Ma employed a modified version of PMCA, involving the addition of cofactors in the reaction, that enabled the successful generation of a recombinant PrP^{Sc} capable of infecting wild type mice with incubation times similar to those typical of brain-derived PrP^{Sc} [135].

The last important point to be examined when dealing with the structural elucidation of prions is defining which particular form is the specific subject of the study. Prions are known to exist under different conformations, with distinct biochemical and biological characteristics (prion strains)[136]. Different strains, despite originating from the same primary structure, can induce TSEs with different clinical and histopathological features[137]. To complicate things further, particular genetic variants resulting in truncated forms of PrP have shown to be causative of prion diseases[51]. One of these infectious mutants[138], the Y145^{STOP}, was characterized by solid-state ssNMR showing that residues 112-144 form a compact core, while the rest of the structure is largely disordered[139], thus showing a significantly different 3D arrangement compared to *bona fide* PrP^{Sc}. From now on, unless otherwise noted, we will use the term prions to indicate the set of infectious conformers composed by full-length PrP^{Sc} or its protease digested form, also known as PrP$^{27-30}$, spanning residues ∼90-230.

1.3.1 Low-Resolution Approaches to Study the Structure of PrP^{Sc}

The use of different low-resolution techniques has provided important information about the structure of PrP^{Sc}. Fourier-transform infrared spectroscopy (FTIR) and circular dichroism (CD) spectroscopy were among the first methods employed to collect data regarding the PrP^{Sc} structure[140,141]. These techniques initially revealed a high β-sheet content of PrP$^{27-30}$ but the incorrect interpretation of the ∼1660 cm^{-1} band in FTIR spectra led to the conclusion that a substantial fraction of PrP^{Sc} folding retained the original α-helical conformation also present in PrP^C. More recently, improved purifications methods, as well as new FTIR spectroscopy and hydrogen/deuterium (H/D) exchange data have confirmed that the structure of PrP^{Sc} is devoid of α-helices[142]. Limited proteolysis was also used to provide insights regarding the solvent accessibility of different PrP^{Sc} regions, exploiting the fact that, under limiting conditions, proteases show a preference for targeting accessible and flexible regions of the protein such as loops and coils while sparsing β-strands. This technique, coupled with mass spectrometry, was first employed to obtain the Proteinase-K (PK) sensitivity map of GPI-anchorless PrP^{Sc} and recombinant PrP^{Sc} (figure 1.9)[143,144].
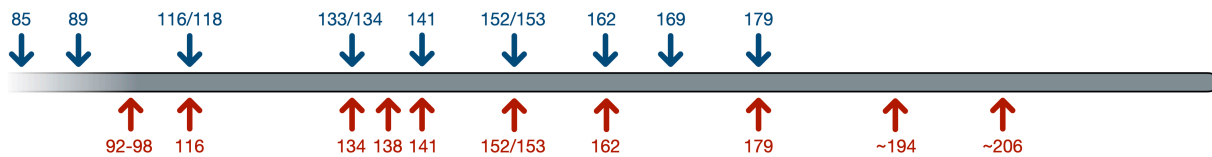
Figure 1.9: PK sensitivity maps comparison between GPI-anchorless and recombinant PrP^{Sc}. The scheme represents the locations of the PK cleavage sites identified on mouse GPI-anchorless PrP^{Sc} (blue) and recPrP^{Sc} (red). PK sites retrieved from Vázquez-Fernánzed and Sevillano et al.[143,144]

Another technique that was used to visualize mature PrP^{Sc} fibrils is atomic force microscopy (AFM). In this approach, a nano-tip attached to a cantilever was employed to scan a silica surface where PrP aggregates have previously been immobilized, giving rise to unique 3D scanning profiles for each aggregate[145]. Because of its simplicity, this technique was used to estimate the height and helical periodicity of individual amyloid fibrils derived from purified preparations prions, as well as to compare the morphology of *in vitro* generated PrP^{Sc} fibrils containing different co-factors[146].

1.3.2 Towards the High-Resolution Characterization of PrP$^{\text{Sc}}$

Even though low-resolution techniques provided important insights that greatly contributed to our current understanding of the PrP$^{\text{Sc}}$ structure, their application cannot yield the necessary level of detail to enable a full structural characterization of this misfolded protein conformer. The first observation of PrP$^{\text{Sc}}$ fibrils was achieved almost 40 years ago by employing negative stain electron microscopy, which showed fibrils of paired protofilaments around 40-60 Å[147]. However, the amount of structural information that could be gathered was greatly limited by the highly aggregated nature of the protein and by the intrinsic resolution of the technique ($\sim$20 Å). The discovery of 2D crystals of PrP$^{\text{Sc}}$ represented another possible avenue to look into the structure of prions using electron crystallography[148]. Even though the use of this technique provided very little information, by considering the packing of the crystals as well as the previously estimated size of the fiber, Govaerts et al. proposed that each stacking-unit of the prion fibril is composed of a trimer of PrP$^{\text{Sc}}$ molecules and that each PrP chain had to be coiled several times on itself[149]. Several technical advances including methods for purification and alignment of fibril preparation, as well as the use of synchrotron-based X-ray sources, enabled the study of prions using X-ray fiber diffraction. The application of this technique on mice brain-derived PrP$^{27\text{-}30}$ fibrils gave a series of meridional diffraction signals at 9.6, 6.4, and 4.8 Å, corresponding to the second, third, and fourth-order diffraction, of a four-stranded β-sheet unit with 19.2 Å height[150]. Additional analysis using small-angle X-ray scattering (SAXS) also allowed the measurement of a $\sim$110 Å diameter for two intertwined PrP$^{\text{Sc}}$ protofilaments[151]. Motivated by the success obtained in elucidating the structure of other amyloid proteins, such as HET-s, several groups tried to study PrP$^{\text{Sc}}$ using ssNMR. In one of these attempts, the technique was employed to characterize PrP amyloid fibers generated by seeding isotopically-labeled recombinant PrP with full-length PrP$^{\text{Sc}}$ purified from sheep brain. This analysis enabled to identify a general architecture of the employed amyloid, which includes a flexible stretch until residue $\sim$114, a central region (residues $\sim$115–154) composed by adjacent β-turns or by residual α-helical content, and a β-sheet-rich core from residue $\sim$155 to the end. However, the sample prepared in such a way exhibited modest infectivity, with only 3/12 inoculated mice developing symptoms[152].

Due to its aggregation propensity and structural heterogeneity, the high-resolution characterization of an infectious mammalian prion has remained elusive for almost 40 years. For this reason, different atomistic models based on low-resolution experimental data have been suggested, such as the left-handed-β-helix (LβH), which until recently was considered the reference model for the prion architecture[149], and the parallel-in-register-β-sheet (PIRIBS)[153]. In the LβH structure (figure 1.10A), the amyloid β-helical core spans from residue 89 to 175 (mouse sequence), while the two original C-terminal α-helices of PrP$^{\text{C}}$ are retained[149]. This model was mainly derived from the electron crystallography experiments and was later supported by X-ray fiber diffraction data, however, this architecture also retains a substantial fraction of the initial α-helical content (due to the initial misinterpretation of FTIR data) and it is now inconsistent with more recent structural information. The PIRIBS architecture (figure 1.10B) is instead characterized by intermolecular stacking of aligned PrP monomers and originated from a great deal of data, some of which at high-resolution. However, since they were originally acquired on poorly or non-infectious PrP amyloids, the possibility that this conformation could also be assumed by infectious material was largely debated (figure 1.10B)[153].
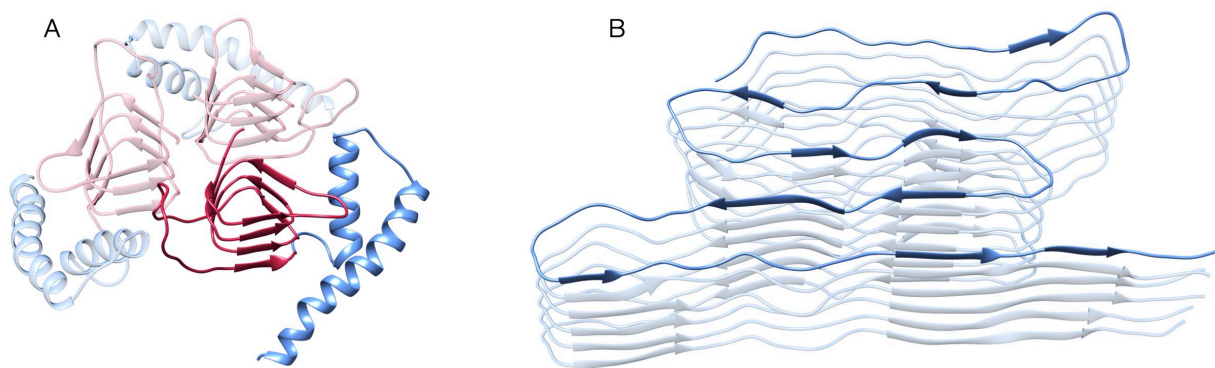
Figure 1.10: Proposed models for the structure of PrP^{Sc}. (A) Ribbon diagram of the LβH model. In this architecture, each stacking unit is composed of a trimer of PrP^{Sc} molecules. Each monomer is formed by a N-terminal region with a left-handed β-helical fold (residues 89-170, red) and a C-terminal moiety retaining the α-helices H2 and H3 of PrP^C (residues 171-230, blue). (B) Ribbon diagram of the PIRIBS model, characterized by an in-register stacking of aligned PrP monomers. In both figures, one monomer is highlighted while the others are shown in semitransparency. The images of the LβH and PIRIBS models were created using the PDB structures described in Govaerts et al.[149] and Groveman et al.[153]

The recent advances in the field of cryo-EM provided the tools to get high-resolution insights regarding the structure of PrP^{Sc}. The first attempt in this direction was represented by the application of this technique in characterizing GPI-anchorless PrP²⁷⁻³⁰ purified from mouse brain[132]. This analysis enabled to directly visualize the fibrils without possible artifacts introduced by negative staining and provided a more reliable volumetric measurement showing that each fiber is composed of two approximately 50 x 30 Å ovally-shaped protofilaments. Furthermore, single particle analysis revealed 19.2 Å and $\sim$40 Å signals upon Fourier-transform of averaged fibril segments, corresponding to 4 and 8 multiples of 4.8 Å β-strands. These features suggest the existence of a subunit with a height of 4 β-strands that stacks vertically with another subunit to form a higher-order dimeric structure (figure 1.11)[132] and are compatible with previous results obtained with X-ray fiber diffraction, suggesting the presence of a 4-rung-β-solenoid unit repeating along the fibril axis. Unfortunately, despite this experiment yielded important information regarding the structure of PrP^{Sc}, it was not possible to achieve an all-atom reconstruction of the prion structure. Indeed, the use of underglycosilated PrP^{Sc} was not sufficient to obtain a sample containing a reasonable amount of monodispersed fibrils, the *conditio sine qua non* to yield atomistic (or quasi-atomistic) resolution after single particle analysis. Of note, the infectivity of the analyzed fibrils was questioned in a recent work from the group of John Collinge[154]. This point arose after the comparison of brain-derived WT-mouse PrP^{Sc} with recombinant PrP amyloid fibrils by employing cryo-EM and AFM. They showed that the size of GPI-anchorless fibers, measured in the previous study, is comparable to the one of noninfectious PrP amyloids ($\sim$100 Å) while infectious materials would feature a larger section of $\sim$200 Å. The authors suggested that the purification protocol employed by Wille and Requena resulted in the preferential enrichment of noninfectious PrP fibrils from amyloid deposits that are present in the brain of prion-infected mice expressing GPI-anchorless PrP but not in WT rodents[154]. However, this study suffers from a lower resolution compared to the previous work, and in particular, it lacks a single particle analysis to assess the presence (or absence) of the 19.2 Å axial repeats that have never been observed in noninfectious recombinant PrP amyloids.
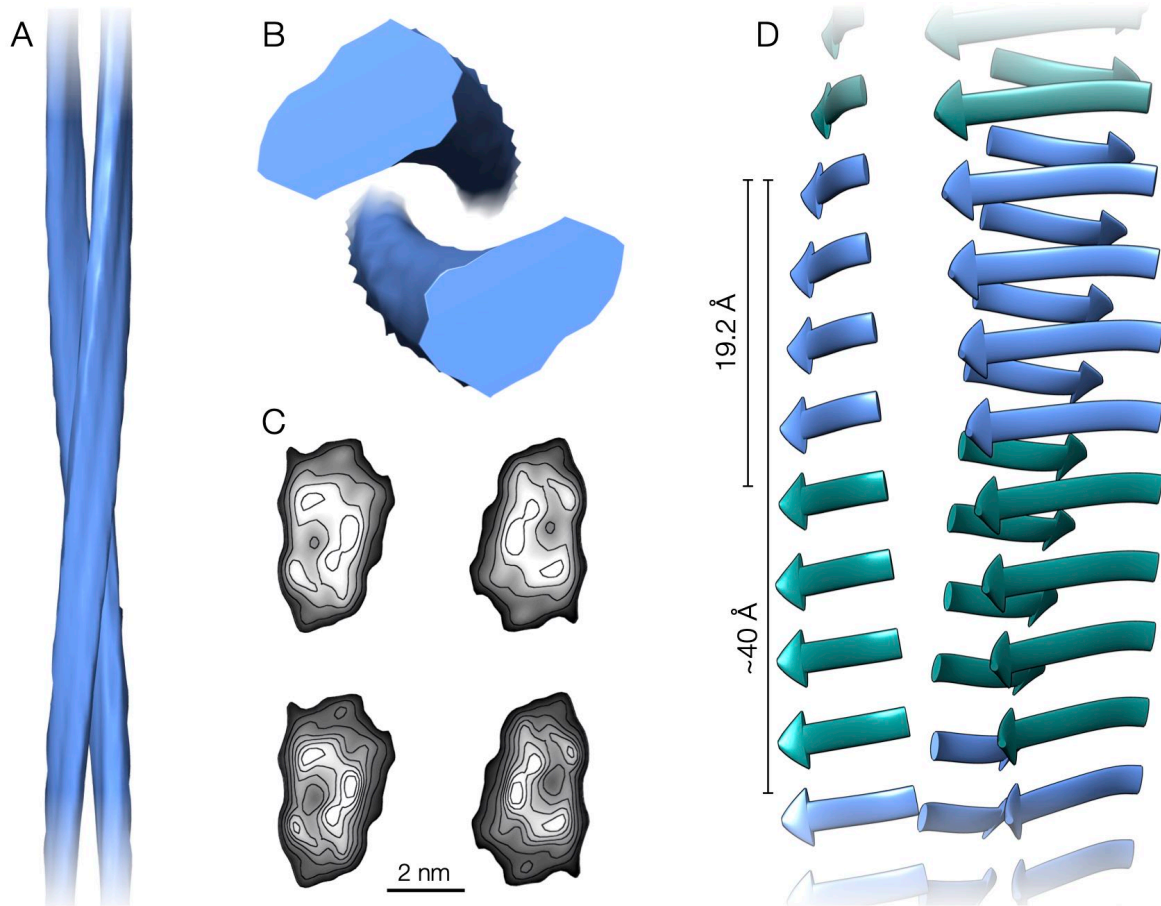
Figure 1.11: Cryo-EM reconstruction of a mouse GPI-anchorless prion fibril. (A) 3D reconstruction of an individual GPI-anchorless PrP 27–30 fibril characterized by two intertwined protofilaments. (B) Cross-section of the reconstructed fibril. (C) Contoured density maps of cross-sections. Lines are contoured at increasing levels of 0.25 σ and 0.125 σ (top and bottom respectively). (D) Representation of the stacking of a putative four-rung β-solenoid monomer in a protofilament. Each unit consists in a coiled conformation with 4 full-turns (rungs), each one composed of multiple β-strands. Different monomers are depicted in alternating colors. Characteristic distances of the four-rung β-solenoid architecture are indicated. Figure adapted from Vàzquez-Fernández et al.[132] ⓒⓘ

The use of cryo-EM has finally enabled the group of Byron Caughey to achieve the first structural characterization of an infectious mammalian prion at backbone-level of resolution[19]. In this work, the authors unquestionably demonstrated that the architecture of PrP[Sc] fibrils derived from brains of clinically-hill hamsters (infected with the 263K prion strain) consist of a single protofilament with size 130 x 35 Å in which each PrP monomer is arranged as a PIRIBS. Unexpectedly, this morphology is remarkably different from the one observed in mouse GPI-anchorless fibrils (which are characterized by two intertwined protofilaments) and it shows no evidence of 19.2 Å axial repeating units. One possible explanation for this discrepancy is that PrP[Sc] might appear as a range of completely different possible conformations, that vary between species and also within strains of the same species. Indeed, the phenomenon of structural heterogeneity is a characteristic underlying the nature of prions and reflects the variety of biochemical features observed, as well as the wide spectrum of phenotypic manifestations characterizing prion diseases.

1.4 Therapeutic Strategies for Prion Diseases

Decades of research aimed at identifying a possible therapy for prion diseases have so far failed to provide an approach capable of increasing the chance of survival of affected patients. This unsuccess can mainly be attributable to the little knowledge available on several aspects of PrP^{Sc}, such as its structure, its replication mechanism, and the molecular pathways involved in its neurotoxic effects. Different strategies have been proposed acting at different levels of prion pathogenesis, including the direct targeting of the disease-related conformer, the blockade of PrP^{Sc} propagation mechanism and the inhibition of molecular pathways involved in neurotoxicity[155].

1.4.1 Targeting PrP^{Sc}

A standard approach that is employed when dealing with an infectious disease is to directly act on its causative agent, possibly by promoting its clearance or by inhibiting its replicative cycle. Likewise, several strategies aimed at treating prion diseases focused on targeting PrP^{Sc}. One of these approaches consisted in the generation of PrP-specific antibodies, capable of interacting with the infectious protein conformer, by immunizing mice lacking the *prnp* gene with PrP^{Sc}. Unfortunately, this scheme has often resulted in the generation of antibodies also recognizing the physiological PrP conformer[156]. In fact, very few PrP^{Sc}-specific antibodies exist, and many of these were shown to also react with non-infectious aggregates of the prion protein[157]. The use of antibodies specific for PrP^{Sc} or interacting with both the relevant PrP conformers resulted in a poor therapeutic effect or in conferring disease protection only in the case of peripheral prion infection[158,159].

An alternative strategy to confer protection against prion disease progression was aimed at stabilizing PrP^{Sc} fibrils. While this rationale seems counterintuitive, it relies on the knowledge that the prion particles with the highest converting activity are not represented by the large aggregated clumps, but rather by small oligomers formed by 14-28 PrP molecules[160]. Furthermore, the kinetics of amyloid growth is primarily dominated by secondary nucleation events resulting from the breakage of the large fibers[161]. A set of anionic compounds, named luminescent conjugated polythiophenes (LCPs) were proposed to hyperstabilize PrP^{Sc} by laterally binding to its β-sheets stacks through electrostatic interactions. This mechanism of action is supported by the structural characterization of the LCP-LIN5001 in complex with the HET-s amyloid (PDB: 2MUS). The presymptomatic treatment of prion-infected mice with LCPs resulted in an increased survival time of the animals, furthermore, one of these compounds was shown to prolong the disease duration even in the case of postsymptomatic administration. Despite the encouraging results, it should be noted that the effect in slowing the disease progression after post-symptomatic administration is quite moderate, resulting in an increase of survival time of ~22%[162].

A high-throughput screening campaign was performed to identify small molecules capable of reducing the levels of PrP^{Sc} in prion-infected cells. This strategy led to the identification of a series of aminothiazoles molecules that also underwent optimization by structure-activity-relationship studies (figure 1.12A)[163]. These compounds showed a remarkable effect in prolonging the disease incubation times in prion-infected mice, however, none of them was effective in extending the survival period in a mouse model expressing a chimeric PrP transgene (supporting the replication of human PrP^{Sc}) infected with Creutzfeldt-Jakob disease prions (figure 1.13A)[164].

1.4.2 Targeting Cellular Pathways

Although the exact mechanism by which PrP$^{\text{Sc}}$ exerts its neurotoxicity has not been characterized yet, several cellular pathways have been linked to the detrimental effects observed in prion diseases. Among these, the unfolding protein response was associated with synaptic failure and neuronal death due to the hyperactivation of the PERK kinase that causes the attenuation of protein translation[121]. A specific inhibitor of PERK was shown to exert neuroprotective effects on prion-infected mice by restoring the synthesis of synaptic proteins and reducing neuronal loss. While this study shows a delayed onset of prion disease symptoms, it lacks an appropriate analysis regarding the effects of the compound on the survival times and no further studies were performed to assess its efficacy in treating prion diseases (figure 1.13B)[165].

Other strategies that were proposed to tackle prion diseases by targeting cellular pathways include the stimulation of autophagy[166] or the upregulation of molecular chaperones such as Hsp70[167]. However, none of these approaches has yet proven to be a valid therapeutic option.

1.4.3 Targeting PrP$^{\text{C}}$

One of the main limitations of PrP$^{\text{Sc}}$-targeting strategies is represented by the heterogeneity of this infectious agent. Indeed, different anti-prion compounds, including aminothiazoles, have been shown to act in a strain-specific fashion, a property that severely limits their therapeutic potentials[164, 168]. A possible strategy to overcome these limitations could be to target PrP$^{\text{C}}$ in order to abrogate its conversion into its pathological form. Sulfated glycans, such as pentosan polysulfate (PPS) can bind the N-terminal region of PrP$^{\text{C}}$ and hamper its conversion into PrP$^{\text{Sc}}$ possibly by competing with the binding of natural cofactors supporting prion propagation[169] and/or by promoting PrP$^{\text{C}}$ endocytosis[170]. PPS was shown to be capable of inhibiting prion replication in cell culture[171] and to prolong incubation periods in rodent models[172]. Unfortunately, patients treated with PPS did not show any significant amelioration of the disease phenotype[173]. Other polyanionic molecules, including phosphorothioate oligonucleotides, with the same mechanism of action of PPS were studied, however, despite the encouraging results obtained in animal models they have not been further developed for human testing[155, 174].

A repositioning approach of drugs capable of crossing the blood–brain barrier enabled the identification of a few compounds with antiprion activity. Among these, the antimalarial agent quinacrine (figure 1.12B) and the antipsychotic drug chlorpromazine showed inhibition of PrP$^{\text{Sc}}$ formation in prion-infected cells in the high nanomolar and low micromolar concentration range, respectively[175, 176]. Initially, the effects of these drugs were attributed to their direct interaction with PrP$^{\text{C}}$. However, their dissociation constants measured in vitro were much higher than the active concentrations of these compounds in cells[177]. This discrepancy suggested a different mechanism of action that was actually clarified for chlorpromazine, which exerts its effects by altering the PrP$^{\text{C}}$ localization (figure 1.13C)[178]. Importantly, the activity and safety of quinacrine were assessed in animal models and in clinical trials on patients with CJD but no beneficial effects were observed[179]. The lack of clinical efficacy of quinacrine against CJD was mainly attributed to metabolic instability, scarce accumulation of the drug into the brain and the formation of drug-resistant prion strains[180]. An alternative strategy that has been pursued to inhibit prion conversion is to enhance the stability

of the physiological conformer of PrP (figure 1.13D). This approach is based on the assumption that increasing the activation energy required for the unfolding of PrP^C can reduce its misfolding propensity[177]. The most effective compounds acting as pharmacological chaperones of PrP^C are represented by cyclic tetrapyrroles[181]. In particular, the cationic tetrapyrrole Fe^{3+}-TMPyP (figure 1.12C) was shown to bind the C-terminal globular domain of PrP^C with a low-micromolar affinity and resulted active in the same concentration range in inhibiting prion replication[182]. Unluckily, the therapeutic potential of porphyrins like the iron-tetrapyrrole is limited by their poor pharmacokinetic properties, such as possible non-specific interactions with plasma proteins, and negligible capacity to cross the blood–brain barrier[183]. A recent multi-disciplinary study identified a new small-molecule chaperone (MC, figure 1.12D) showing high affinity for PrP^C and efficacy in cell-based assays. Preliminary data collected on mice and macaques suggested a possible therapeutic potential of this molecule[184]. However, the reported increase in survival time of treated-mice lies within the range of lifespan variability of mouse models for prion diseases. Furthermore, the number of macaques employed for the study was too small to allow statistical analysis[185].
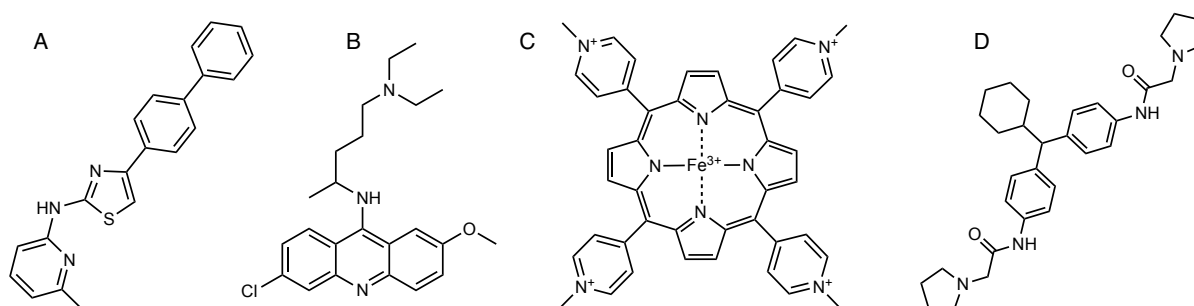

Figure 1.12: Molecular structures of antiprion compounds (A) The aminothiazole derivative IND24. (B) Quinacrine. (C) Fe^{3+}-TMPyP. (D) Molecular chaperone MC.

1.4.4 Reducing the Levels of PrP

The development of TSEs is completely dependent on the expression of PrP^C that acts both as a substrate for prion replication and as a mediator for PrP^{Sc} toxicity. Notably, in physiological conditions, the presence of PrP^C is not essential for the correct functioning of the cells. For these reasons, the depletion of the cellular levels of PrP would inevitably confer a strong protective effect against the progression of prion diseases without resulting in detrimental side effects. Following this rationale, one of the most promising strategies to treat prion diseases was developed, namely, the use of antisense oligonucleotides (ASOs) to decrease the expression of PrP. ASOs are oligomers of single-stranded nucleic acids designed to bind the target mRNA by exploiting the sequence complementarity. The interaction of the ASOs with mRNA induces the suppression of the latter through different possible mechanisms, such as direct steric blockage or by promoting the target degradation (figure 1.13E). A recent study enabled the identification of two effective ASOs, named ASO-1 and ASO-2, capable of delaying the mortality of prion-affected mice by >60% and >75% after prophylactic administration. Furthermore, ASO-1 showed a significant effect also in the case of administration after the establishment of the prion neuropathology in mice, but prior to the onset of clinical symptoms. In this case, the oligonucleotides treatment was capable of delaying the onset of clinical signs

by 33% and to increase the survival time by 55% as compared to control mice[186]. Encouraged by the promising results, Ionis Pharmaceuticals™, a company developing antisense medicine, started to work on an ASO-based therapy against prion diseases that is currently under assessment in pre-clinical trials[187].

The main limitation of this approach is represented by the route of administration of the ASOs. Indeed, oligonucleotides cannot cross the blood-brain barrier, and they require to be delivered through intrathecal injection in the cerebrospinal fluid[188]. However, despite the invasive therapeutic procedure, the benefits outweigh the risks since, at the moment, a valid alternative to ameliorate prion diseases phenotype does not exist. The last point that remains to be clarified is whether an improved design of the ASOs would enable to completely block the disease progression or their effect will only be limited in prolonging the survival of the patients.
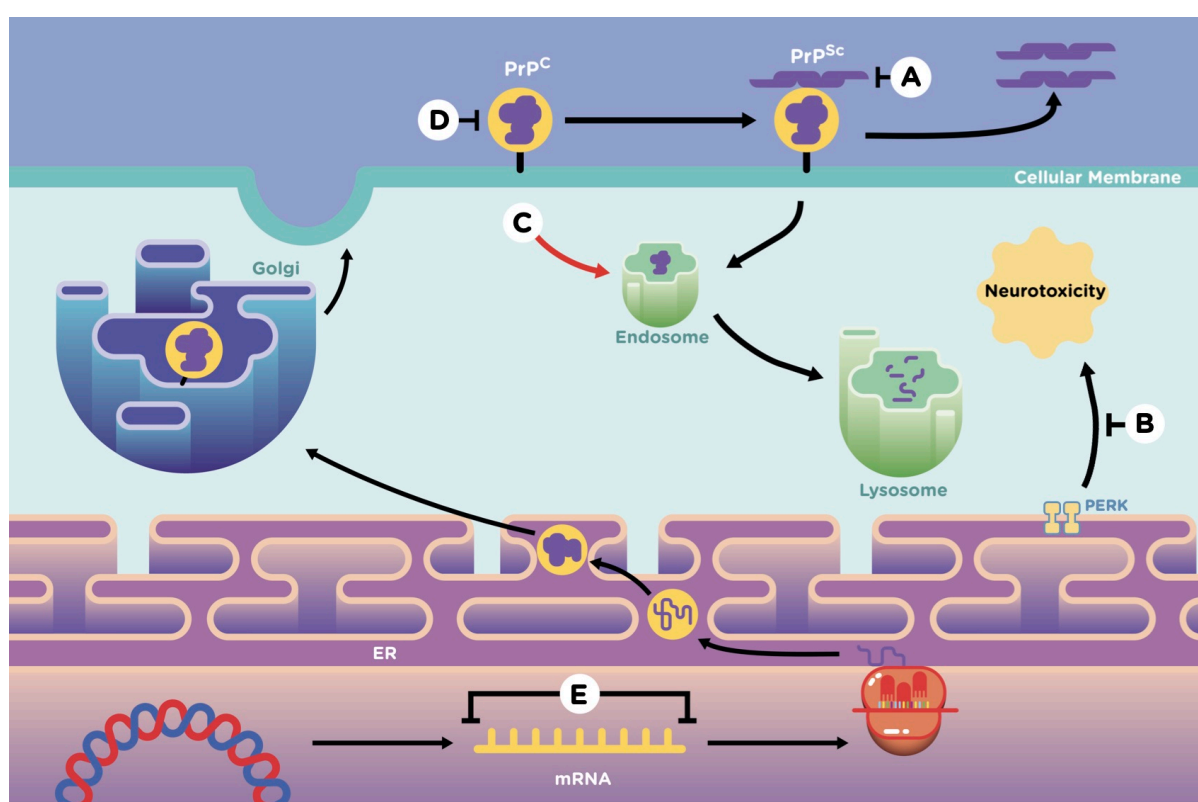
Figure 1.13: Therapeutic approaches for prion diseases. The picture illustrates different strategies that have been tested as possible therapies for prion diseases. (A) Targeting of PrP^{Sc} by antibodies or small molecules. (B) Inhibiting cellular pathways of neurotoxicity (i.e. decrease PERK activation). (C) Favoring PrP^{C} internalization to decrease its levels on the plasma membrane. (D) Stabilizing the structure of PrP^{C} to increase the energetic barrier for its conversion into PrP^{Sc}. (E) Silencing the expression of the PrP gene (i.e. ASO therapy). Figure adapted from Astolfi et al.[189]. ©①

Chapter 2

Characterizing Folding & Misfolding

2.1 Laying the Foundation to Tackle Prion Propagation

How does a prion propagate? Answering this question remains one of the most outstanding challenges in biology. The high-resolution reconstruction of prion replication would illuminate the striking molecular mechanism underlying the phenomenon of protein-based inheritance. Furthermore, the all-atom characterization of this process would pave the way for the use of rational drug design approaches to target prion propagation. The complete elucidation of this replicative mechanism would require to define how a prion can convey its conformationally-encoded information to its soluble substrate. However, without the atomistic information regarding the structure of PrP$^{\text{Sc}}$ this task is virtually impossible. The possibility of achieving this goal has recently been opened up by the application of high-resolution structural characterization techniques which enabled to obtain information regarding possible arrangements displayed by infectious mammalian prions. These include initial low-resolution cryo-EM studies performed on mouse GPI-anchorless PrP$^{\text{Sc}}$, as well as the more recent quasi-atomistic elucidation of hamster PrP$^{\text{Sc}}$.

Despite its importance, the all-atom characterization of PrP$^{\text{Sc}}$ can only provide the basics for the comprehension of the complex phenomenon of prion replication. The molecular mechanism of PrP$^{\text{Sc}}$ propagation is indeed characterized by several structural rearrangements underlying the highly dynamic process of PrP conformational conversion. Unfortunately, the atomistic description of this process is not approachable experimentally because of the lack of high-resolution, time-resolved biophysical techniques to study misfolding[190]. Standard computational methods, like molecular dynamics (MD) simulations, would represent valid approaches but are currently limited by the enormous calculation load required to simulate such molecular pathways[191]. More advanced schemes, that will be discussed in this chapter, are required to tackle complex molecular rearrangements and their application could fill the gap left by the absence of suitable experimental techniques.

Another key aspect at the basis of prion biology is related to the dynamics of the PrP polypeptide and the mechanism by which it achieves its native conformation. The characterization of this process would enable the identification of possible crossroads between PrP folding and misfolding, opening up the possibility of assessing the effect of disease-causing mutations at the level of the folding pathway. Furthermore, the elucidation of these conformational transitions at atomistic-level of detail can provide new perspectives for developing therapeutic strategies. Standard rational drug

discovery methods employ the structural information of the target to design compounds capable of modulating its activity. However, the application of this approach to stabilize the physiological PrP conformation has so far failed to identify successful compounds for treating prion diseases, and for this reason PrP^C has been classified as undruggable[177]. The reconstruction of the pathways underlying PrP folding and misfolding could provide new structural targets that could be employed for the rational design of novel compounds aimed at inhibiting prion propagation.

2.2 Experimental Approaches to Study Folding & Misfolding

Fundamental insights regarding the mechanisms of protein regulation could theoretically be provided by the full reconstruction at atomistic resolution of the conformational transitions underlying folding pathways. However, experimental techniques capable of reaching a sufficient temporal resolution to study the highly dynamic process of protein folding are affected by a limit in spatial resolution. Indeed, biophysical techniques aimed at studying protein folding can provide detailed kinetic information, such as the identification of intermediate states and the related rates of transitions, but can only yield limited structural insights regarding the underlying pathways. For example, methods such as fluorescence or CD spectroscopy coupled to stopped-flow apparatuses enable to study conformational rearrangements in the sub-millisecond timescales but only providing coarse-grained insights into the underlying structural changes (i.e. the secondary structure content or the chemical environment of fluorescent side-chains)[192]. Time-resolved experiments employing Förster resonance energy transfer (FRET) could, in principle, allow to obtain an accurate measurement of the distance between pairs of labeled residues[193]. Unfortunately, most positions on a protein chain cannot tolerate residue substitution or conjugation with a detection-dye, therefore, the resulting high-resolution characterization can only be achieved for a particular set of amino acids in the protein.

Additional viable options to characterize protein folding are represented by H/D exchange methods[194]. These schemes are based on the principle that solvent-excluded polypeptide regions involved in the formation of intramolecular hydrogen bonds usually undergo proton/deuteron exchange with a rate order of magnitude slower compared to solvent-exposed stretches. For this reason, by refolding a denatured deuterated polypeptide in a H_2O buffer, it is possible to label exchangeable hydrogens of the protein (which are then detected by using mass spectrometry or NMR), based on the solvent accessibility of different parts of the molecule during the folding process. While it was shown that this type of study can provide relevant structural and kinetic information regarding protein folding, its application is typically limited to polypeptides with folding times $\gg 10$ ms, since the analysis of shorter timescale hampers the use of pulse-labeling schemes[195]. Furthermore, the highest level of resolution which can be provided by this technique is coarse-grained information regarding the order in which residues become protected from the exchange reaction. Although such insights are fundamental to increase our understanding regarding the mechanisms by which proteins fold, they are insufficient for particular types of applications, for instance in structure-based drug design.

If obtaining time-resolved structural information for protein folding seems a complex task, collecting the same type of information for protein misfolding becomes even more challenging. In particular, the aggregation events characterizing this process impair the use of standard stopped-flow apparatuses or microfluidic systems, since as the precipitating species form they immediately leave the

solution, hampering a reliable measurement by employing UV-visible detection systems. For this reason, most of the kinetic experiments aimed at studying amyloid formation usually rely on the use of fluorescent probes, such as Thioflavin T[196], which change the fluorescence emission upon binding on this type of aggregates. However, the typical timescales which are monitored in this type of assay are in the range of minutes to hours, and the only type of structural information that can be gathered is whether the conformational conversion results in the formation of a cross-β pattern.

A possible strategy to overcome the limitations affecting the currently available biophysical techniques is to integrate the experimental data with high-resolution information provided by computational techniques, such as MD simulations.

2.3 Computational Approaches to Study Folding & Misfolding

The use of MD simulations can provide a valid alternative to obtain atomistic insights regarding the conformational changes of a particular protein with the desired level of temporal resolution. However, the applicability of this technique to study complex structural rearrangements is severely limited by the problem of sampling rare events[191]. Important conformational transitions occurring in processes such as the folding of biologically-relevant proteins are characterized by the presence of intermediate states separated by high energy barriers. Since the rate of crossing a transition state is exponentially suppressed by the height of the energy barrier, the conformational changes between metastable states only seldomly occur. For this reason, an extensive load of computational resources is needed to simulate long enough to collect a statistically significant number of transitions for accurately describing the process under study. As a consequence, even by relying on a special-purpose supercomputer, the largest proteins whose folding was completely elucidated with standard MD simulations are composed of less than 100 residues with folding times ranging from ∼0.6 to 65 µs[197]. Notably, the folding time of the PrP polypeptide was estimated to be ∼2 ms, a timescale that is not possible to achieve by using MD[198].

Due to the inapplicability of standard MD simulations to complex molecular transitions, the use of enhanced sampling methods becomes necessary. These techniques enable to accelerate the exploration of the protein conformational space by using different schemes that can be grouped into two main categories: collective variable (CV)-based and CV-free methods[199].

In CV-based approaches, the calculation is typically accelerated by adding a bias potential, defined on a set of chosen reaction coordinates (the CVs), to the Hamiltonian of the system. This class of enhanced sampling techniques includes different approaches, and widely used schemes are represented by umbrella sampling and metadynamics (MetaD). In the former, a series of system configurations are generated at given values of a predefined reaction coordinate, then restrained MD simulations are used to sample the configurational space around these regions (or windows). If a consistent overlap is present between the histograms obtained in different sampling windows, the weighted histogram analysis method can be used to post-process the results and recover the potential of mean forces (namely, the free energy profile along the chosen coordinate)[200]. In metaD instead, the exploration of the conformational space is achieved by iteratively 'filling' the potential energy surface by adding a history-dependent bias composed of Gaussian functions. This bias enables the system to escape from kinetic traps allowing it to visit unexplored parts of the energy landscape. The free energy

along the selected CVs can then be retrieved from the sum of the deposited Gaussian potentials[201]. The accuracy of the results in CV-based methods is strictly dependent on the choice of the proper reaction coordinates since the use of an incorrect CV can lead to a wrong prediction of the transition mechanism and the related free energy profile. It is well known that the proper reaction coordinates are not easily identified for many systems. In such cases, an alternative approach is represented by CV-free methods. Replica exchange MD (REMD) is one of the most popular enhanced sampling techniques that works without relying on any predefined reaction coordinates. In this approach, multiple simulations are run in parallel at different temperatures which are periodically swapped between the replicas. This allows conformations sampled at high temperatures to be available for simulations at low temperatures and vice versa. The exchange is accepted or rejected based on a Metropolis acceptance criterion that guarantees the detailed balance[202]. This method can enhance the sampling of metastable states that are separated from the initial structure by large kinetic barriers, however, due to the stochastic nature of the exchanges, REMD is not the ideal choice when it is important to reconstruct the mechanism of a particular transition.

Despite the significant acceleration of the conformational space exploration that is enabled by the use of enhanced sampling techniques, their applicability to study protein folding is generally restricted to fast-folding proteins. The successful employment of these methods to study folding occurring in timescales larger than 1 ms was shown to be possible only by relying on extensive cloud-computing resources such as the Folding@Home platform. However, even in this case, the larger timescales that have been so far achieved are in the range of $\sim$10 ms for proteins shorter than 100 residues[203].

Recently, the group of Shakhnovich developed a novel algorithm, named DBFOLD, specifically designed to compute folding pathways of complex proteins on reasonably small cluster computers. This method works first by using a combination of Monte Carlo simulations and umbrella sampling to enhance the exploration of the conformational space. Then the folding landscape is delineated by the identification of coarse-grained intermediates characterized by the presence of native-like substructures. Finally, high-temperature unfolding simulations are employed to extrapolate unfolding rates at physiological temperatures. These values combined with intermediate free energies inferred from Monte Carlo simulations allow to compute folding rates from detailed balance. So far, DBFOLD has been benchmarked only on a single polypeptide whose folding pathway was fully characterized by standard MD and experimental techniques, for this reason, more extensive studies are required to evaluate the accuracy of its predictions. However, DBFOLD was shown to be capable of reconstructing the folding mechanism of other 5 proteins with size up to 244 residues and with estimated folding times up to seconds. Although in this case a direct comparison with standard MD simulations and experiments was not possible (due to the lack of these data), these results highlight the applicability of this method in dealing with the reconstruction of folding pathways[204].

Despite the advances in the simulation of protein folding, the application of MD to study misfolding still remains extremely challenging. In particular, the formation of amyloid protofibrils has so far been achieved only by using coarse-grained methods (schemes in which each amino acid of the protein is represented by one or several beads with united atoms)[205, 206]. These approaches enable to reach timescales that cannot be achieved with all-atom MD simulations, mainly due to the reduction of the degrees of freedom of the system. However, the level of approximation introduced by using coarse-grained potentials and the model-dependency of these approaches can undermine the reliability of

the predictions[207]. The application of all-atom MD simulations and enhanced sampling techniques has so far been limited to study equilibrium properties of amyloid protofibrils[208] or to investigate early aggregation events between soluble monomers[209]. Indeed, the successful reconstruction of an amyloid propagation mechanism at atomistic level of resolution has yet to be achieved.

The last part of this chapter is devoted to describe the Bias Functional (BF) approach[210] and the self-consistent path sampling (SCPS) scheme[211]. These methods enable to compute atomistic molecular transitions (including folding pathways) of polypeptides with sizes up to hundreds of residues without relying on massive computational resources.

2.3.1 The Bias Functional Approach

The BF is a method for predicting the all-atom folding mechanisms of biologically-relevant proteins. This approach is based on identifying the most realistic reaction pathways in an ensemble of trajectories which are generated by integrating the equations of motion using a biased scheme. The application of the BF consists in three steps: first, a number of denatured conditions are generated by performing thermal unfolding using standard MD, then a set of trajectories connecting each unfolded conformation to the native state is produced by using ratchet-and-pawl MD (rMD). Finally, for each set of pathways starting from the same initial condition, the trajectory with the highest probability to realize in absence of bias is identified by applying a variational scheme (figure 2.1).
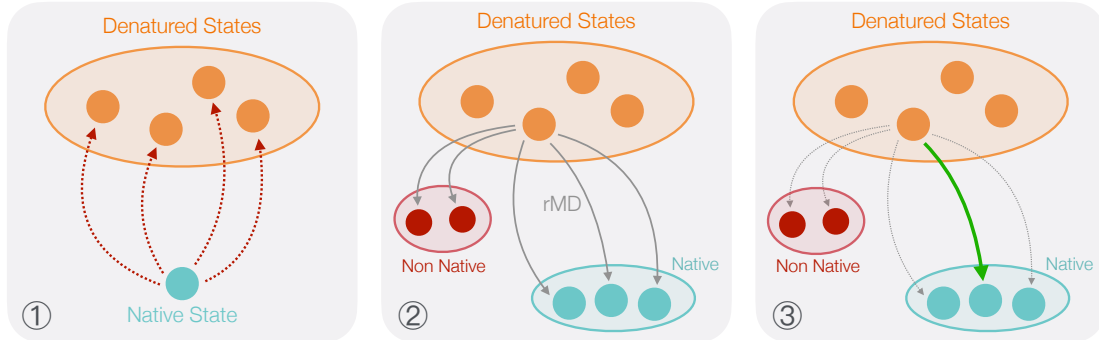

Figure 2.1: Schematics of the BF approach. (1) High-temperature MD simulations are used to obtain denatured conditions starting from the experimental structure; (2) rMD is employed to generate a set of trial trajectories connecting the denatured to the native state (defined within a threshold of structural similarity with respect to the experimental structure); (3) The trajectory with the highest probability to realize in absence of bias is selected for each set among those that successfully reached the native state.

The generation of folding pathways in the bias functional approach relies on the use of rMD. In this type of biased dynamics the sampling of the transition is accelerated by introducing an external force that prevents the backtracking towards previously visited states. To define the progress of the reaction a CV, named $z(X)$, is introduced:

$$z(X) = \sum_{i<j}^{N} [C_{ij}(X) - C_{ij}(X_{\text{Ref}})]^2 \tag{2.1}$$

where $C_{ij}(X)$ is the contact map of the instantaneous protein conformation and $C_{ij}(X_{\text{Ref}})$ is the contact map in the reference state (usually the native conformation). The entries of the contact map

are a continuous function of the atomic configuration, defined as:

$$C_{ij}(X) = \frac{1 - (|\mathbf{x}_i - \mathbf{x}_j|/r_0)^6}{1 - (|\mathbf{x}_i - \mathbf{x}_j|/r_0)^{10}} \tag{2.2}$$

in which r_0 is a reference distance defining atomic contacts (usually set to 7.5 Å) and $\mathbf{x}$ indicate the coordinates of the ith or jth atom. The biasing force acting on each atom is computed as:

$$\mathbf{F}_i^{\mathrm{rMD}}(X, z_m) = -k_R \nabla_i z(X)[z(X) - z_m] \cdot \theta[z(X) - z_m(t)] \tag{2.3}$$

where $\theta(x)$ is the Heaviside step-function, k_R the ratchet constant determining the strength of the biasing force, and $z_m(t)$ the minimum value attained by $z(X)$ up to time t. In this scheme, the system evolves with standard MD as long as the chain spontaneously evolve towards the target state ($\theta(x) = 0$ if $z(X) \leq z_m$) and the external force is only applied when the system attempts to explore previously visited states defined along $z(X)$, by definition, $\theta(x) = 1$ if $z(X) > z_m$.

For each set of trajectories starting from the same denatured condition, the pathway with the highest probability to realize in the absence of biasing force is selected. This scheme is applied by first selecting a target threshold, usually defined in terms of root mean squared deviation of atomic positions (RMSD) with respect to the reference. Then, the trajectories reaching below the target value are scored by their BF (T), computed as:

$$T = \sum_i^N \frac{1}{m_i \gamma_i} \int_0^t d\tau |\mathbf{F}_i^{\mathrm{rMD}}(X, \tau)|^2 \tag{2.4}$$

where t is the time at which the trajectory reached the target state, m_i and γ_i are the mass and friction coefficient of the ith atom, and $\mathbf{F}_i^{\mathrm{rMD}}$ is the ratchet force acting on it. The folding pathway minimizing the BF for each set of trajectories starting from the same denatured condition is referred to as the least biased (LB) trajectory. The LB trajectory represents the pathway with the highest probability to realize in absence of biasing force among those generated from the same initial state[210].

The BF approach was benchmarked first by reproducing the folding mechanisms of two short polypeptides whose folding pathways were characterized by standard MD simulations[210]. Then this scheme was validated against experimental data regarding the folding of two biologically-relevant proteins. In particular, the sampling of structures from intermediate states enabled to predict CD spectra showing quantitative agreement with biophysical data obtained from time-resolved CD[212]. The use of the BF method opens up the possibility of simulating folding pathways of large macro-molecules on small cluster computers in extremely short times. As an example, two weeks of calculation on a single GPU-workstation are sufficient to predict the folding pathway of a $\sim$150 residues protein. However, when employing this method, it is important to consider two important drawbacks that restrict the applicability of the BF scheme. The first one is that the introduction of the biasing force breaks the microscopic reversibility of the dynamics, hampering an accurate computation of the free energy profile using trajectories obtained with the BF. For this reason, this method does not represent a valid choice when it is important to retrieve the rates of the conformational changes.

The second is that the sampling of the states along the folding pathway is completely dependent on the selection of the CV. While a good reaction coordinate is available for protein folding[213], the same does not apply to other complex transitions such as misfolding. To overcome the second limitation it is possible to rely on the recently developed self-consistent path sampling (SCPS) algorithm. A scheme in which the reaction coordinate is not heuristically postulated, but is instead calculated self-consistently through an iterative process[211].

2.3.2 The Self Consistent Path Sampling Algorithm

SCPS is an enhanced sampling algorithm that can be used to generate transition pathways of biologically-relevant proteins. Similar to BF, this method is powered by rMD-type simulations, however, instead of completely relying on the initial choice of the CV, in this approach the reaction coordinate is iteratively refined through a self-consistent scheme, rigorously obtained from theoretical arguments[211]. The application of SCPS begins with the generation of transition pathways using the same ratchet dynamics and reaction coordinate, $z(X)$, employed in the BF scheme. The trajectories successfully reaching the native state are then employed to obtain the mean-path:

$$\langle C_{ij}(t) \rangle = \frac{1}{N_T} \sum_{n=1}^{N_T} C_{ij}^n[X(t)] \tag{2.5}$$

where $C_{ij}^n[X(t)]$ is an element of the contact map computed at time t for the n_{th} trajectory, and N_T is the total number of reactive trajectories generated from that initial condition. Usually, the mean path is downsampled for computational convenience to a low number of contact maps, N_C, equally spaced in $z(X)$ distance, namely $\langle C_i \rangle_{k=1...N_C}$. The mean path is then used to compute two new reaction coordinates, defined as:

$$s_\lambda(X) = 1 - \frac{\frac{1}{N_C} \sum_k^{N_C} k e^{-\lambda \|C(X) - \langle C \rangle_k\|^2}}{\sum_k^{N_C} e^{-\lambda \|C(X) - \langle C \rangle_k\|^2}} \tag{2.6}$$

$$w_\lambda(X) = \frac{1}{\lambda} \ln \sum_k^{N_C} k e^{-\lambda \|C(X) - \langle C \rangle_k\|^2} \tag{2.7}$$

in which $\|...\|$ is the norm defined in equation 2.1, $\langle C \rangle_k$ is the k_{th} contact map along the mean path, N_C is the total number of contact maps and λ is a parameter that to ensure computational efficiency is usually set equal to the average distance between consecutive contact maps. In the large λ limit, $s_\lambda(X)$ represents the progress of the reaction with respect to the mean path. By definition $s_\lambda(X)$ is 0 in the native state and 1 in the denatured state. while the second coordinate $w_\lambda(X)$ measures the shortest distance of a given configuration X from the mean path.

These new CVs are used in a modified version of the rMD algorithm to generate a new set of folding trajectories. Here, two biasing forces analog to the one defined in equation 2.3 are introduced, but acting on $s_\lambda(X)$ and $w_\lambda(X)$ instead of $z(X)$. The trajectories obtained in this way that successfully reach the target state are then used to compute a new mean path and this procedure is repeated until convergence, namely when a new iteration produces identical results to the previous one, according to some convergence criterion (figure 2.2)[211,214].
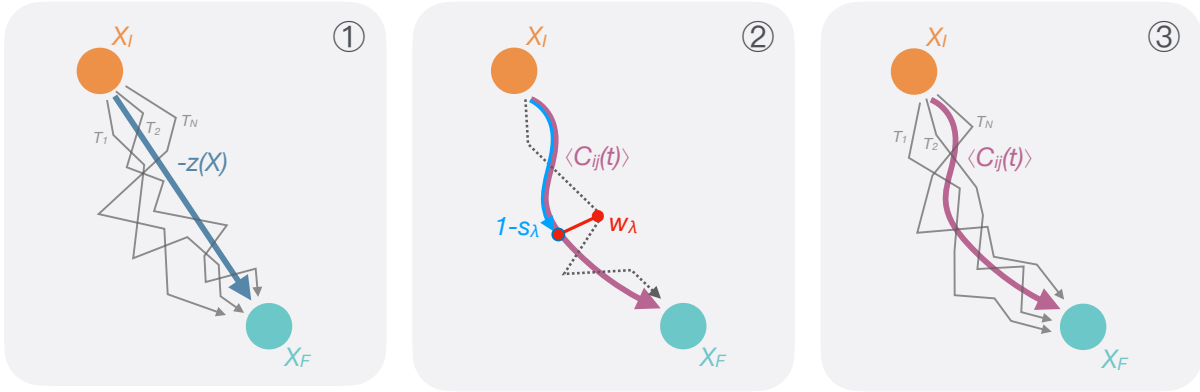
Figure 2.2: Schematic representation of the SCPS method. In this figure X_I represents the initial conformation, X_F the target state, and $T_{1...N}$ the trajectories connecting X_I to X_F. In step (1) an ensemble of trajectories starting from X_I and reaching X_F is generated by using rMD, biasing along $z(X)$. Since $z(X)$ decreases as long as the proximity of X to X_F increases, the progression along the path is here defined as $-z(X)$. In step (2) the trajectories successfully reaching the target state are used to compute the mean path $\langle C_{ij}(t) \rangle$, represented in purple. This is then used to define two new coordinates: s_λ, depicted in blue, which value is 1 in the unfolded state and 0 in the target state, therefore $(1 - s_\lambda)$ is used here to define the progress along the mean path; and w_λ, depicted in red, represents the distance to the mean path. In step (3), a modified version of rMD is employed to generate a new set of trajectories by introducing two biasing forces, acting along s_λ, and w_λ. The trajectories successfully reaching the target state are then used to compute a new mean path, step (2), to perform a new iteration. Figure adapted from Terruzzi et al.[214] ©①

We have recently validated the SCPS algorithm against five proteins whose folding was fully characterized by means of plain MD simulation. The folding pathways of all these polypeptides were found to be indistinguishable from those obtained with the same force field using plain MD simulations. However, the application of the SCPS scheme did not lead to a significant improvement over rMD, because the folding events generated by rMD are already in good agreement with MD (a detailed report of this benchmark can be found in the supplementary information)[214]. This finding is consistent with the notion that the CV used in rMD simulations correlates with the fraction of native contacts, which is considered a good reaction coordinate for the folding of small globular proteins[213]. On the other hand, it is expected that SCPS can significantly lead to an improvement of the predictions, with respect to standard rMD, where the initial guess of the reaction coordinate is poorer, as in the case of amyloid propagation.

Aims of the Thesis

Despite almost 40 years have passed since the discovery of the first mammalian prion, several aspects related to the biology of these infectious misfolded species still remain poorly characterized. In particular, the lack of knowledge regarding the structural determinants of prion propagation and the molecular underpinnings of PrP^{Sc} neurotoxicity has strongly limited the development of successful therapeutic strategies for prion diseases. To fill this gap, in this thesis we applied integrative schemes, based on the combination of computational methods with experiments, to lay the foundation for understanding the phenomenon of prion propagation and to design an innovative pharmacological approach for prion diseases. In particular:

- In chapter 3, we focused on the structure of PrP^{Sc} and the related propagation mechanism. We aimed at testing the hypothesis that innovative methods of computational biophysics could be employed to elucidate some of the aspects of prion structure and propagation. Our work led to the formulation of a plausible PrP^{Sc} model which was then employed as a basis to reconstruct the series of events underlying prion propagation.

- In chapter 4 we capitalized on the concept that the suppression of PrP expression is a viable strategy against prion diseases. We evaluated the possibility of negatively regulating the levels of PrP by blocking its folding pathway. We aimed at testing this hypothesis by developing a novel paradigm for drug discovery designed to identify compounds capable of binding to a PrP folding intermediate, thus interfering with the correct attainment of the native state. This analysis led to the discovery of the first pharmacological degrader against PrP.

Chapter 3

The Study of Prion Structure and Propagation

3.1 The Construction of a Plausible PrP^{Sc} Model

One of the main subjects of investigation in prion biology is the mechanism by which a misfolded protein can convey its structurally-encoded information to replicate without relying on nucleic acid. The understanding of this process could clarify several aspects underlying the development of prion diseases. However, to provide a description of such phenomenon at a molecular level it is required to possess atomistic insights regarding the structure of the target conformer. At the time when we started this study, no high-resolution information regarding PrP^{Sc} was available, and the previously proposed models were, at least partially, inconsistent with the most recent data regarding the mammalian prion structure. For this reason, we decided to build a new structural model of PrP^{Sc} by comprehensively including a large number of low-resolution constraints derived from different experiments performed on the Rocky Mountain Laboratories (RML) mouse prion strain. In particular, we focused on building a structure compatible with the cryo-EM data collected on GPI-anchorless PrP^{Sc} and X-ray fiber diffraction study, suggesting that the architecture of this misfolded conformer is compatible with a 4-rung-β-solenoid (4RβS). In this section we describe the process of model building, challenging and its refinement by the exploitation of newly available information. The resulting structures provided us with the basis for the investigation of the mechanism of prion replication.

3.1.1 Building the 4-Rung-β-Solenoid Model of PrP^{Sc}

To satisfy the available experimental evidence regarding the mammalian prion structure, we built a new atomistic model of mouse PrP^{Sc} based on the 4-rung-β-solenoid (4RβS) architecture. The construction of the model considered an array of experimental data, including: (I) cryo-EM and X-ray fiber-diffraction studies, which showed that the fold of PrP^{Sc} is compatible with a 4RβS architecture with L- or triangular-shaped cross-section[132, 150]; (II) CD and FTIR data, suggesting that the prion structure contains approximately 40–50% β-sheet and 50–60% coil/turns[131]; (III) Mass Spectrometry (MS) analysis indicating the presence of an intact disulfide bond between cysteines 178 and 213

(mouse sequence)[65], as well as (IV) the PK-sensitive residues map (figure 1.9)[143], which reflect amino acids likely excluded from the resistant core of the protein; and (V) the possibility for asparagines 180 and 196 to accommodate bulky glycans[66]. All these constraints were employed to design a 2D threading scheme including mouse PrP residues 89–230, by using a generic scaffold typical of L-shaped right-handed β-solenoid proteins. This process also considered the structural propensities of different amino acids: stretches of glycines and prolines were positioned in loops due to their destabilizing effects on β-strands; charged sidechains were excluded from the inner core of the protein or counterbalanced by salt bridges (figure 3.1)[215].
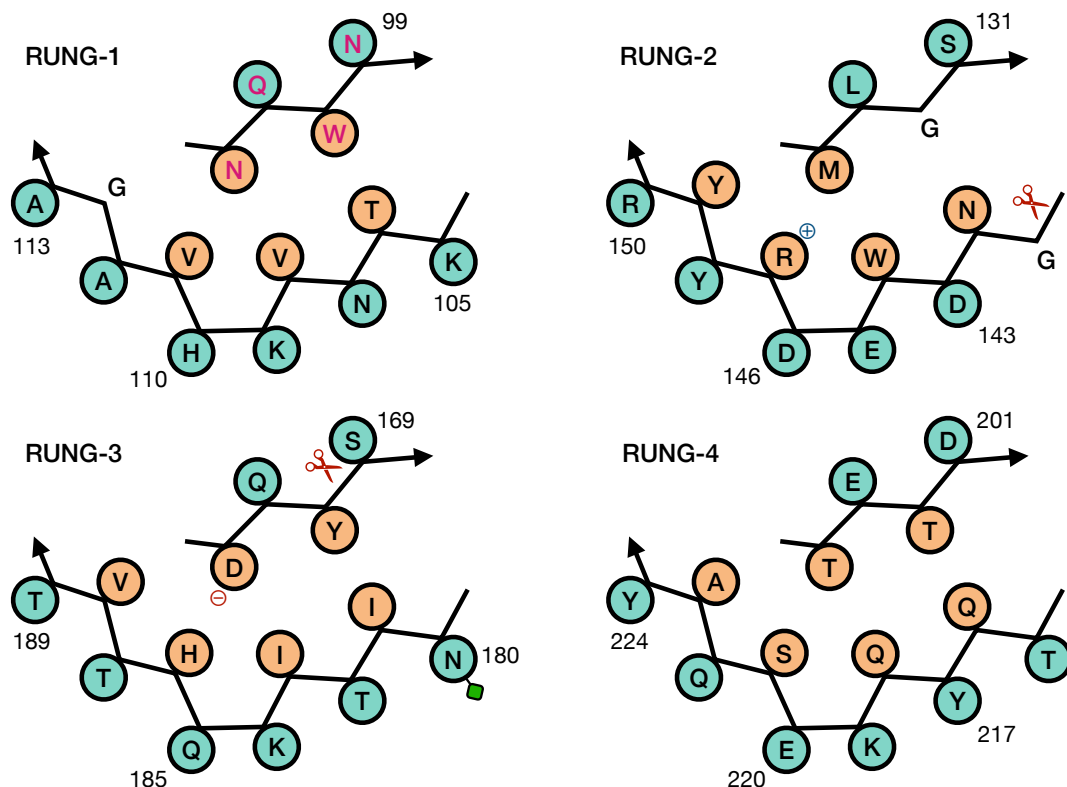

Figure 3.1: 2D threading scheme of the β-solenoid core of mouse PrP^Sc. Schematics of the mouse PrP sequence threaded into the general architecture of right-handed β-solenoid proteins with L-shaped cross-section. Side-chains pointing towards the solvent are colored in cyan while side-chains facing the interior of the structure are depicted in orange. The ⊕ and ⊖ symbols label R147 and D166, respectively, which are involved in the formation of a buried salt bridge. Red scissors indicate PK-cleavage sites and the green box the attachment position for glycans (N196 is predicted to reside in a loop, therefore it is not displayed in this scheme)[215].

The 3D model was then obtained by threading this 2D scheme into the core of a prototypical β-solenoid protein featuring a right-handed twist and L-shaped cross-section (*D. dadantii* Pectate Lyase; PDB 1AIR). Loops connecting consecutive β-strands were built *de novo* using a template-free method. The resulting structure (figure 3.2) features an inner core mainly composed of hydrophobic or mildly polar side-chains (T94, T106, L108, V111, Y127, M128, W144, Y149, V165, Y168, I181, I183, V188, F197, T198, and T200), few polar side-chains involved in hydrogen bonding (N142-HB-Y168, H168-HB-T198, Q216-HB-T200, and Q218-HB-S221), and a salt bridge (R147-SB-D166). Conversely, most of the highly-polar residues (N and Q) including the glycosylation sites (N180 and

N196) and charged side-chains (E, D, K, and R) are solvent-exposed. The structure also encompasses identified PK cleavage sites localized in loops/turns, or at the edge of the β-strands, and the intact disulfide bond between C178 and C213[215].
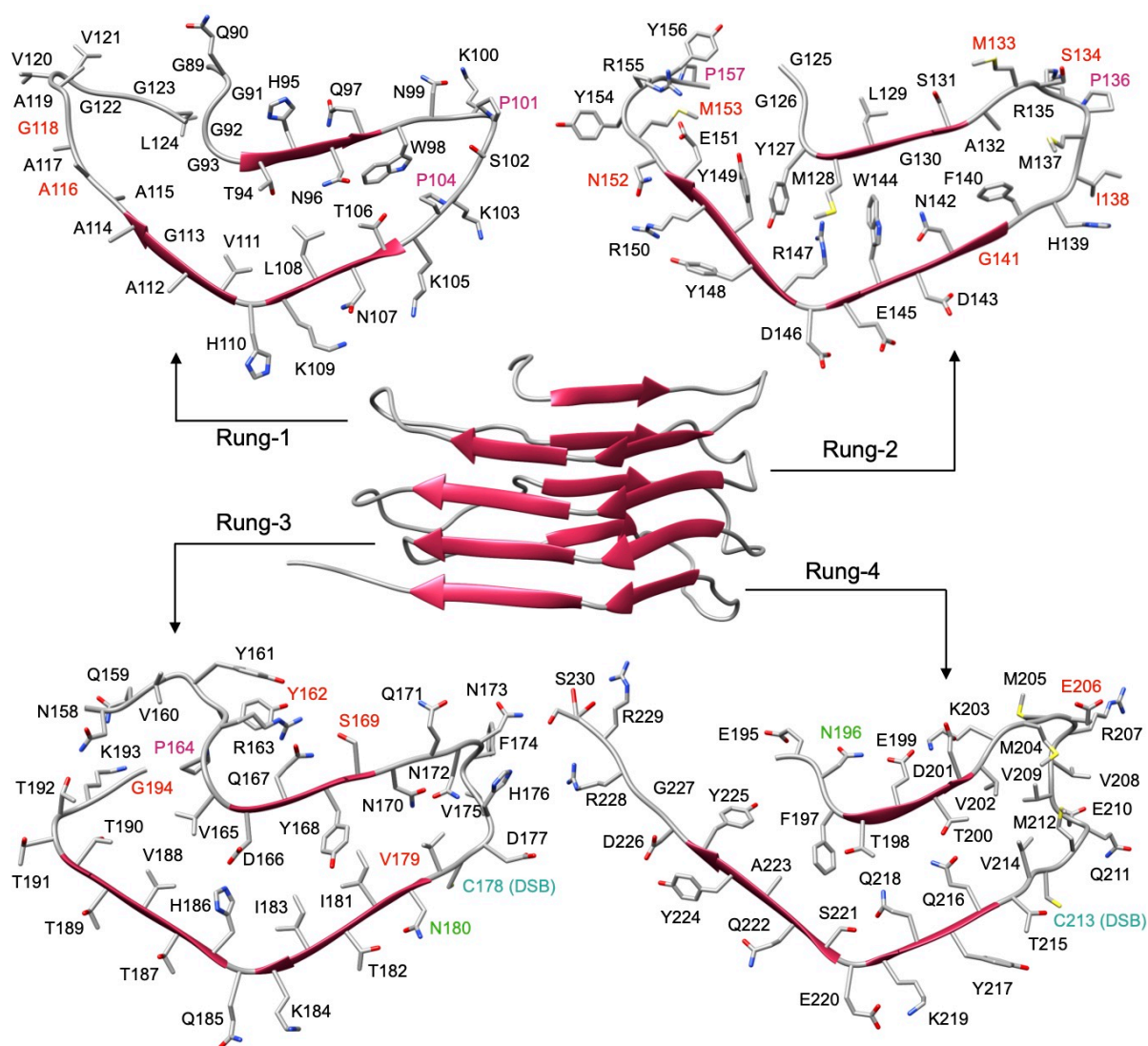

Figure 3.2: View of the 4RβS model of PrP^Sc. The structure of PrP^Sc modeled as a 4RβS (β-strands represented as red arrows) is depicted in the center of the figure. Residues are displayed in each individual rung with different colors. PK cleavage sites identified by mass spectrometry are colored in red. Glycosylation sites are labeled in green. Prolines are colored in purple. Cysteines involved in the formation of a disulfide bond are indicated in cyan. Figure from Spagnolli et al.[215] ⓒ⊕

To test the physical consistency of the 4RβS model, we challenged its stability by all-atom MD simulations in explicit solvent. First, three independent, 20 ns simulations were performed by restraining hydrogen bond distances between atoms involved in β-sheets (supplementary figure 1). This process allowed the relaxation of protein loops and side chains of the core. Next, the imposed restraints were released, and three plain-MD trajectories of 100 ns each were simulated. As a reference, we repeated the same protocol on a dimer of the prion-forming domain of the fungal prion HET-s and to the previously proposed LβH model of PrP^Sc. Structural stability was assessed by measuring the RMSD relative to the initial frame and the secondary structures content (figure 3.3)[215].
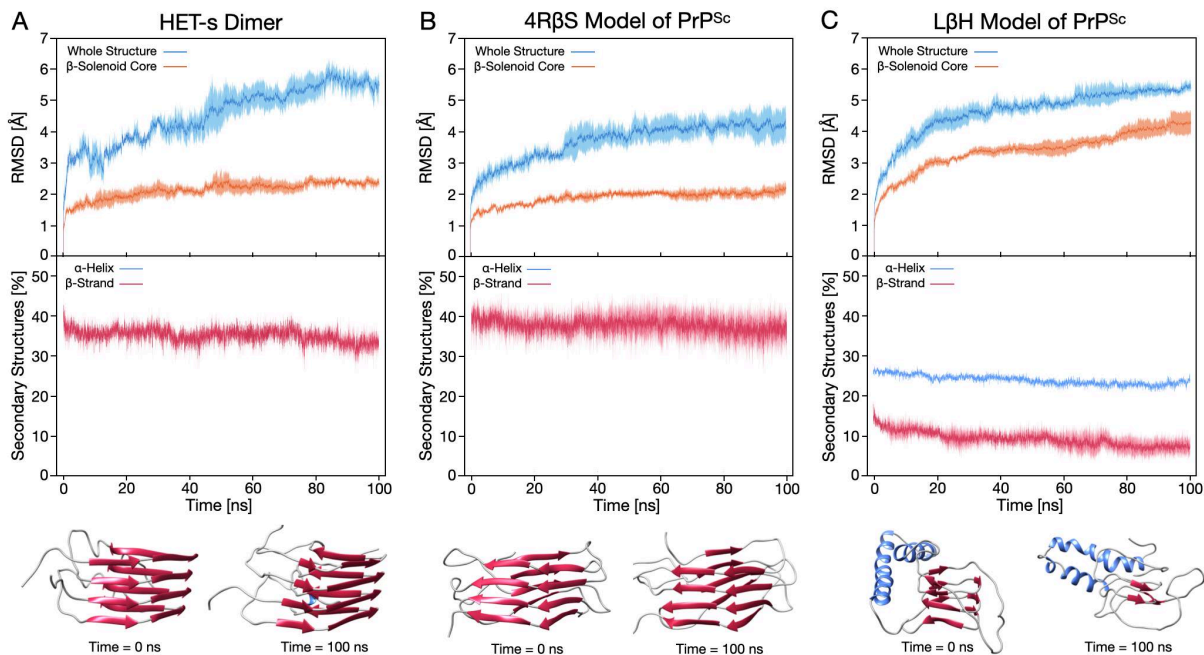
Figure 3.3: MD simulations of a HET-s Dimer, 4RβS and LβH PrP^{Sc}. Upper graphs report the RMSD from the initial conformation for the whole structure (blue lines) or excluding the loops and the helical regions (β-solenoid core, orange lines) of the different proteins. Filled curves indicate the standard error of the mean. Results show comparable stability between the HET-s dimer (A) and the 4RβS model (B), with a final RMSD of the hydrophobic core (calculated as the average of the three trajectories over the last 5 ns, ± standard deviation) of 2.4 ± 0.2 Å for the HET-s dimer and 2.1 ± 0.3 Å for the 4RβS. In contrast, the structural deviation of the LβH (C) hydrophobic core is approximately two-fold higher, reaching a value of 4.3 ± 0.6 Å. Lower graphs indicate the α-helical (blue lines) or β-sheet (red lines) content of each protein. The HET-s dimer showed a variation from an initial 41.8 ± 2.3% to a final 33.2 ± 2.8%. Similarly, the 4RβS model deviates from an initial 41.3 ± 2.3% to a final 36.6 ± 5.4%. Instead, the LβH model deviates from a starting 18.3 ± 1.4% to a 7.5 ± 3.1%. These results are illustrated by the structures shown below the graphs, which represent the initial (left) and final (right) frames of the MD trajectories. Figure from Spagnolli et al.[215] 🅭🅯

We obtained values in the same range of fluctuation for our 4RβS model and the dimer of HET-s, conversely, we found a significant instability of β-helical domain of the LβH which was evident after few tens of ns. To reproduce the behavior of a PrP^{Sc} protofibril, we built a tetrameric 4RβS model by stacking monomers in a head-to-tail fashion (superimposition of this model with cryo-EM maps of GPI-anchorless mouse PrP^{Sc} is shown in supplementary figure 2). This assembly showed comparable stability to the monomer. Moreover, the characteristic structural features related to the employed experimental constraints were maintained during the course of the simulations; i.e. the ~20 Å and ~40 distances between the same residues on two contiguous or alternate monomers, and the β-strands probability relative to the PK-cleavage sites (figure 3.4)[215].

Finally, by introducing prototypical sugar moieties (GlcNAc$_2$Man$_3$Fuc) at positions N180 and N196 of each monomer, we observed the absence of steric clashes, confirming that the 4RβS model also accommodates the presence of glycans (supplementary figure 3). Taken together, these findings indicate that the 4RβS architecture is a solid arrangement for PrP^{Sc}. Conversely, the LβH model, which at that time represented the most accepted architecture for PrP^{Sc}, revealed a high instability when challenged with MD simulations[215].
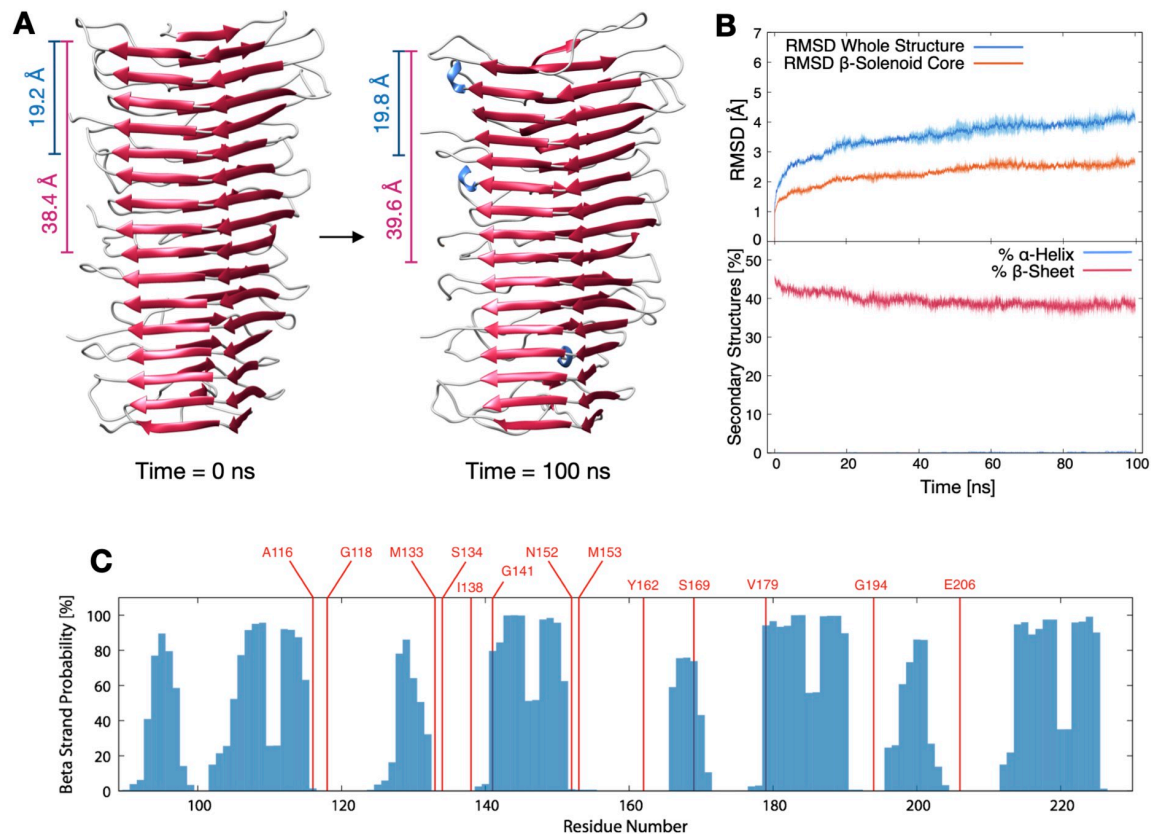
Figure 3.4: MD simulation and PK restriction map of a 4RβS tetramer. (A) 3D representation of a 4RβS tetramer at the beginning (left) and the end (right) of MD simulations. Blue bars indicate the distance between two residues in the same position on two consecutive monomers, which corresponds to 19.2 ± 0.4 Å (t = 0 ns) and 19.8 ± 2.2 Å (t = 100 ns). Purple bars indicate the distance between a residue in one monomer and the same residue on the second forthcoming monomer, which corresponds to 38.4 ± 0.5 Å (t = 0 ns) and 39.6 ± 1.8 Å (t = 100 ns). A similar pattern of signals reflecting monomeric and dimeric repeats has previously been observed by cryo-EM studies on HET-s[216]. Both values are in almost perfect agreement with the two main signals obtained by Fourier transform single particle analysis in the cryo-EM experiment on mouse GPI-anchorless PrP[Sc] (19.1 Å and the 40 Å signals). (B) The upper graph shows the RMSD of the tetramer from the initial state for the entire structure (blue lines) or the β-solenoid core (orange lines). Structural deviation over the 100 ns of simulation corresponds to 2.6 ± 0.2 Å. The lower graph reports the percentage of secondary structures, initial β-strand content is 46.2 ± 1.2%, while the final 38.6 ± 1.7%. Filled curves indicate the standard error of the mean. These results show comparable stability between monomeric and tetrameric 4RβS structures. (C) Map of the experimentally observed PK cleavage sites (colored in red) overlapped with the probability of each residue to be in a β-strand conformation, calculated over the last 5 ns of the MD trajectories. Figure from Spagnolli et al.[215] ⓒ⊕

45

3.1.2 Refining the PrP^{Sc} Model Explaining Deformed Templating

Deformed templating is the process by which self-replicating protein conformations with a given architecture can seed the formation of an alternative self-replicating state arranged in a different conformation. In particular, non-infectious PrP amyloid can promote the formation of infectious PrP[Sc] through deformed templating[128]. This process can take place both *in vitro* and *in vivo* and involves a forced conversion in which there is a mismatch between the original template and the final structural arrangement. This type of propagation is characterized by the emergence of intermediate conformers exhibiting biochemical features that are between those of the initial PrP amyloid and the final prion. Importantly, an accurate atomistic model of PrP[Sc] should display an arrangement compatible with deformed templating. In other words, the prion structure must be such that with reasonable deforming it can be reached from a non-infectious PrP amyloid as a starting point[217]. The structure of a PrP amyloid generated *in vitro* was recently deciphered by using cryo-EM (figure 3.5), one year after the release of the 4RβS model[218]. This information offered a unique opportunity to challenge our PrP[Sc] model and to provide a possible explanation for deformed templating.
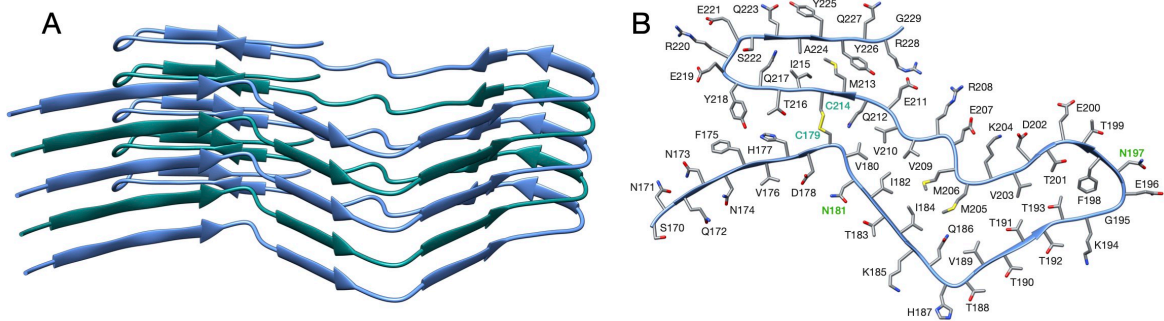
Figure 3.5: Structure of a non infectious human PrP amyloid showing a PIRIBS architecture. Lateral (A) and top (B) view of a non-infectious PrP amyloid fibril (PDB 6LNI)[218]. In (A), different monomers are depicted in alternating colors. In (B), cysteines involved in the formation of a disulfide bond are depicted in cyan, while PrP glycosylation sites are represented in green. Figure adapted from Spagnolli et al.[217] 🅭🅯

To propose a model consistent with deformed templating we first focused on the atypical misfolded PrP species emerging after the first passage in animals inoculated with recombinant PrP amyloids. This conformer displays a PK cleavage pattern similar to that of the initial material but differs in terms of glycosylations. In particular, PrP amyloids obtained *in vitro* are devoid of glycosylations, conversely, the atypical propagative species is characterized by the presence of the N-linked glycans as well as the C-terminal GPI-anchor. Therefore, we built a glycosylated version of the recombinant PrP amyloid by introducing a GlcNAcMan$_3$Gal$_2$FucNeuNAc$_2$ glycan at positions N181 and N197 to each monomer of the fibril. This type of glycosylation is representative in size and complexity of the most abundant glycans found in PrP[C] and PrP[Sc] [220].

Based on prior considerations we expected that a stack of more than two monomers of such modified conformer would be disfavored due to steric clashes between the bulky glycans[66]; however, we were able to build a pentamer of diglycosylated units (supplementary figure 4A) that revealed to be highly stable when subjected to MD (figure 3.6). This analysis showed that the PIRIBS architecture is fully consistent with a high degree of glycosylations since throughout the entire length of the simulations the protein-RMSD remained below 2 Å and the percentage of β-strands greater than 60%.
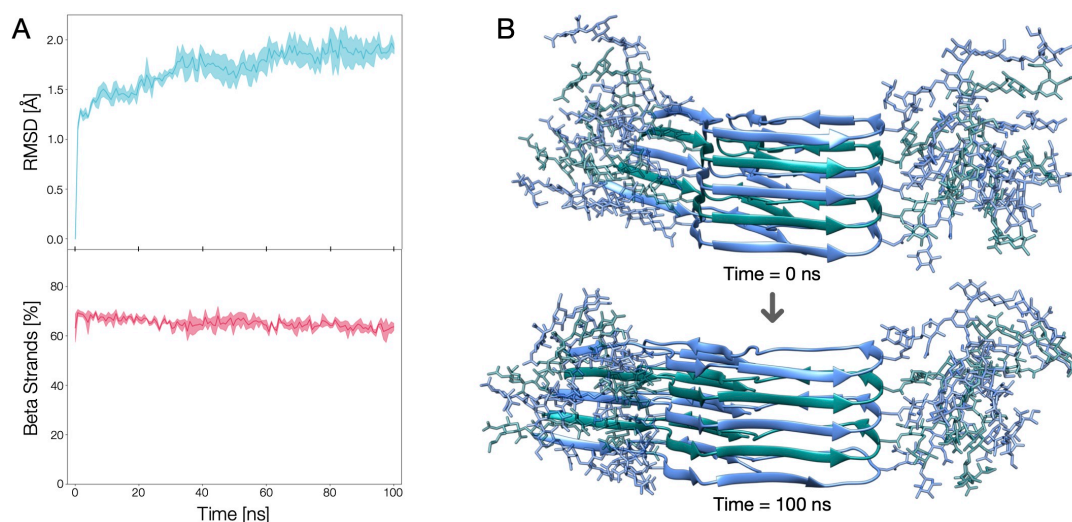
Figure 3.6: MD simulations of the fully glycosylated PrP amyloid. (A) The graphs show the RMSD with respect to the initial conformation (above) and the percentage of β-strands (below) as a function of the simulation time. The line and the filled curve indicate the mean and the standard error, respectively, computed on 3 performed simulations of 100 ns each. The low RMSD and constant β-strand content reveal a high stability of the protein conformation (comparable with the one of a non-glycosylated structure, supplementary figure 5A). The compatibility of the PIRIBS architecture with a full-glycosylation was also confirmed in a recent *in silico* work by the group of Byron Caughey[219]. (B) Representative snapshot extracted at the beginning and at the end of the MD simulations. Different monomers are displayed in alternating colors, glycan residues are explicitly represented. Figure adapted from Spagnolli et al.[217] ©①

Having defined the putative structure of the atypical propagative PK-resistant PrP conformer, we proceeded to model the core of the deformed templating process. We noticed that the cross-section of the recombinant PrP amyloid features a triangular core spanning residues ∼181-208 (human numbering). Such a surface is relatively compatible with the cross-section of the previously proposed architecture of PrP^Sc. Therefore, we built a modified version of the 4RβS model by using this region of the amyloid as a template for the four rungs. Due to the poor structural information available regarding the human prion, we designed the deformed-templating-compatible (DTC) 4RβS threading by considering the previously employed mouse-derived experimental constraints (figure 3.7)[217].
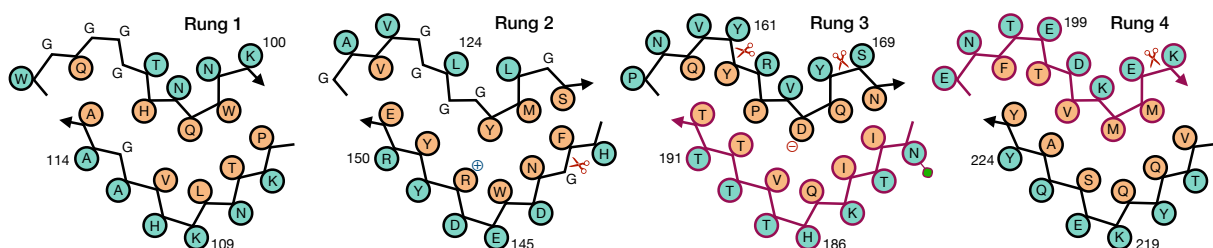
Figure 3.7: Threading scheme of the deformed-templating-compatible mouse PrP^Sc model. 2D scheme of the mouse PrP sequence threaded into four repetitions of the amyloid triangular core composed of residues 180-207 (mouse numbering). Side-chains pointing towards the solvent are colored in cyan while side-chains facing the interior of the structure are depicted in orange. The ⊕ and ⊖ symbols label R147 and D166, respectively, which are involved in the formation of a buried salt bridge. Red scissors indicate PK-cleavage sites and the green box the attachment position for glycans. The conserved region between the recombinant PrP amyloid and the putative PrP^Sc structure is depicted in purple. Importantly, the triangular core defined by residues 181–208 (human) and 180– 207 (mouse) share 100% sequence identity.

Starting from this scheme we constructed the DTC-4RβS model by threading the PrP sequence into four repetitions of the triangular core obtained from the PrP amyloid (PDB 6LNI). The residues 169–179 and 209–231 at the termini of the triangular core were rearranged according to the architecture proposed in figure 3.7. Loops were built *de novo* using a template-free method.

The resulting model (Figure 3.8), resembles our previously proposed one in many features: residues forming the inner core (T106-A114 , Y127-L129 , N142-Y149, and T215-Y224) are structurally conserved in the two putative PrP^{Sc} conformation (namely, residues pointing inward, or outward the hydrophobic regions are the same in both models); furthermore, important interactions are also shared between the two conformations, such as the buried salt-bridge between R147 and D166. Despite these common characteristics, the two models also display notable differences, such as the overall shape of the β-solenoid, the orientation of particular residues composing the resistant core (T94-N99 , Q167-Y168, and Q185-H186), and the stretch composed of residues 198–201 that is excluded by the central part of the triangular core, with residues 203–206, occupying that region[217].
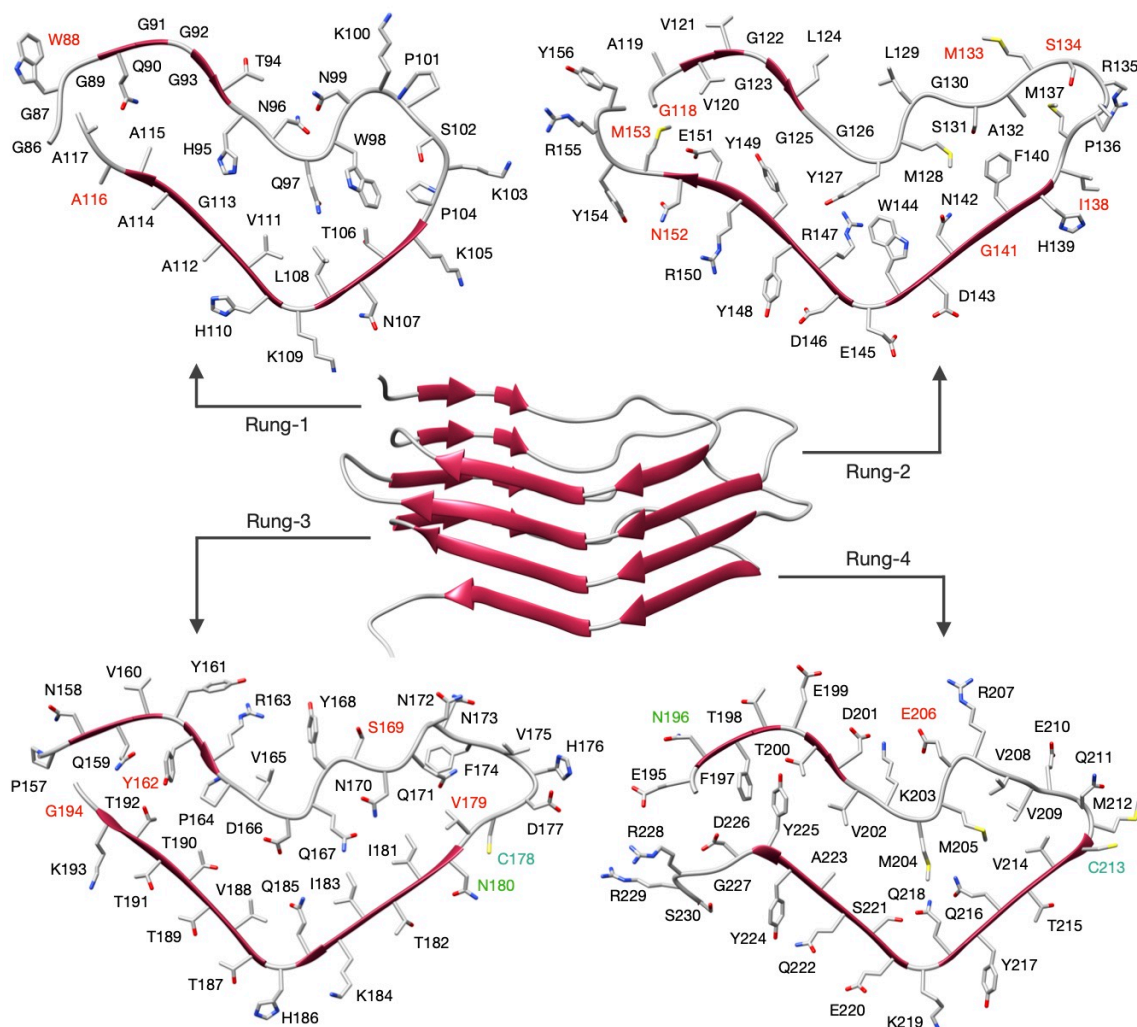
Figure 3.8: 4RβS model of mouse PrP^{Sc} compatible with deformed templating (DTC-4RβS). The structure of the DTC PrP^{Sc} modeled as a 4RβS is shown in the figure center. Residues are depicted as sticks and displayed in each individual rung with labels in different colors. PK cleavage sites identified by mass spectrometry are labeled in red. Glycosylation sites are labeled in green and cystine in cyan. Residue numbering is relative to the mouse sequence. Figure from Spagnolli et al.[217] ©⊕

We next subjected a fully-glycosylated tetrameric model of the DTC-4RβS to MD simulations. The stability of this structure was assessed by computing the RMSD and the β-strands content along the trajectories. The average RMSD at the end of the simulation resulted to lower than 4 Å, while the average percentage of β-strands remains above 40% for the entire length of the simulations. These results show that the stability of this structure is comparable to the one observed in our previously proposed tetrameric model (figure 3.9).

Figure 3.9: MD simulations of a fully glycosylated DTC-4RβS tetramer of PrP^Sc. (A) Representative frames extracted at the beginning (t = 0 ns) and at the end (t = 100 ns) of the MD simulations. Different monomers are depicted in alternating colors and glycans are explicitly represented as sticks. The graph in (B) shows the RMSD, while in (C) it is shown the percentage of β-strands as a function of the simulation tim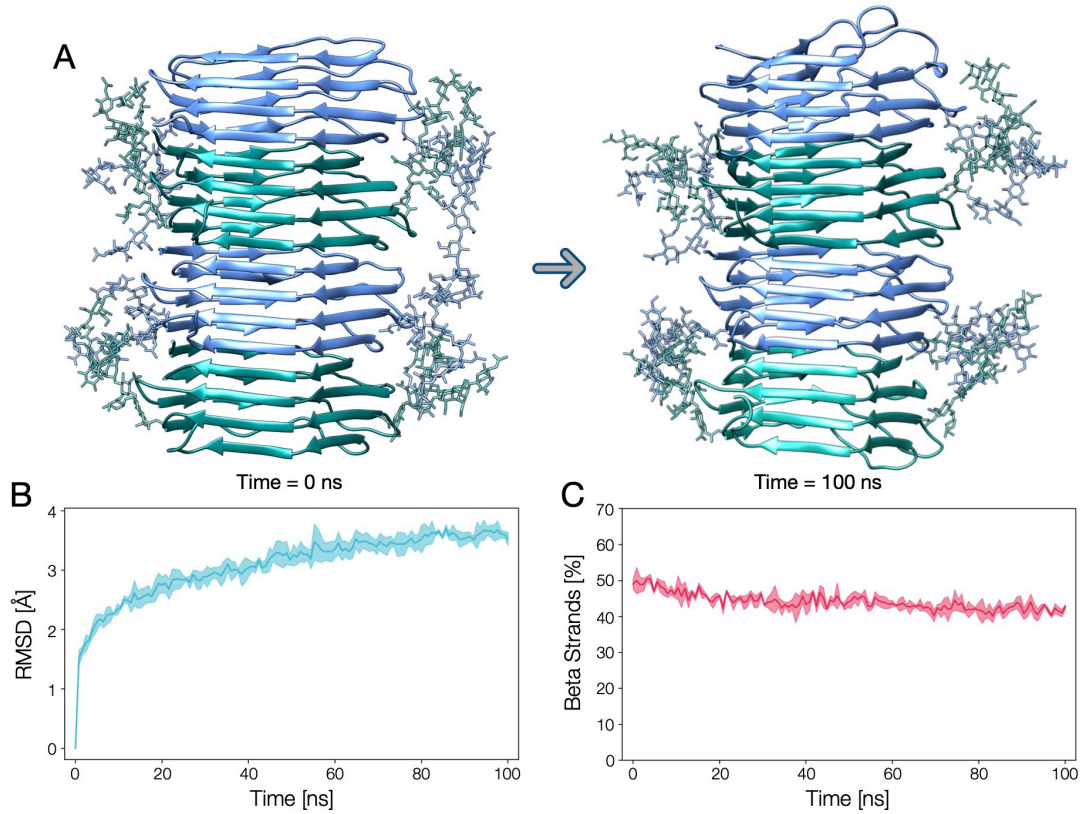e. The line and the filled curve indicate the mean and the standard error, respectively, computed on 3 performed simulations of 100 ns each. The observed structural stability is comparable to the unglycosylated DTC-4RβS (supplementary figure 5B).

Finally, we elaborated a model of the transition between the PIRIBS atypical propagative PrP amyloid to *bona fide* PrP^Sc arranged as a 4RβS. In the proposed mechanism, the triangular core of the PIRIBS architecture, defined by residues 180-207 (mouse numbering), plays the crucial role of templating the formation of the β-solenoid rungs. The deformed templating begins with the structural rearrangement of the C-terminus of the PrP amyloid monomer at the fibril end. In this conformational change, residues 182–192 of the triangular core engage hydrogen bonds with residues 215–225, resulting in the formation of two new β-strands. This structure now displays a C-terminal surface that is indistinguishable from the C-terminal rung (rung 4) of the 4RβS, as residues 196–230 are now forming a complete fourth-rung. This active end has now the templating properties of a prion, thus can induce the conversion of PrP^C into a 4RβS PrP^Sc (figure 3.10)[217].
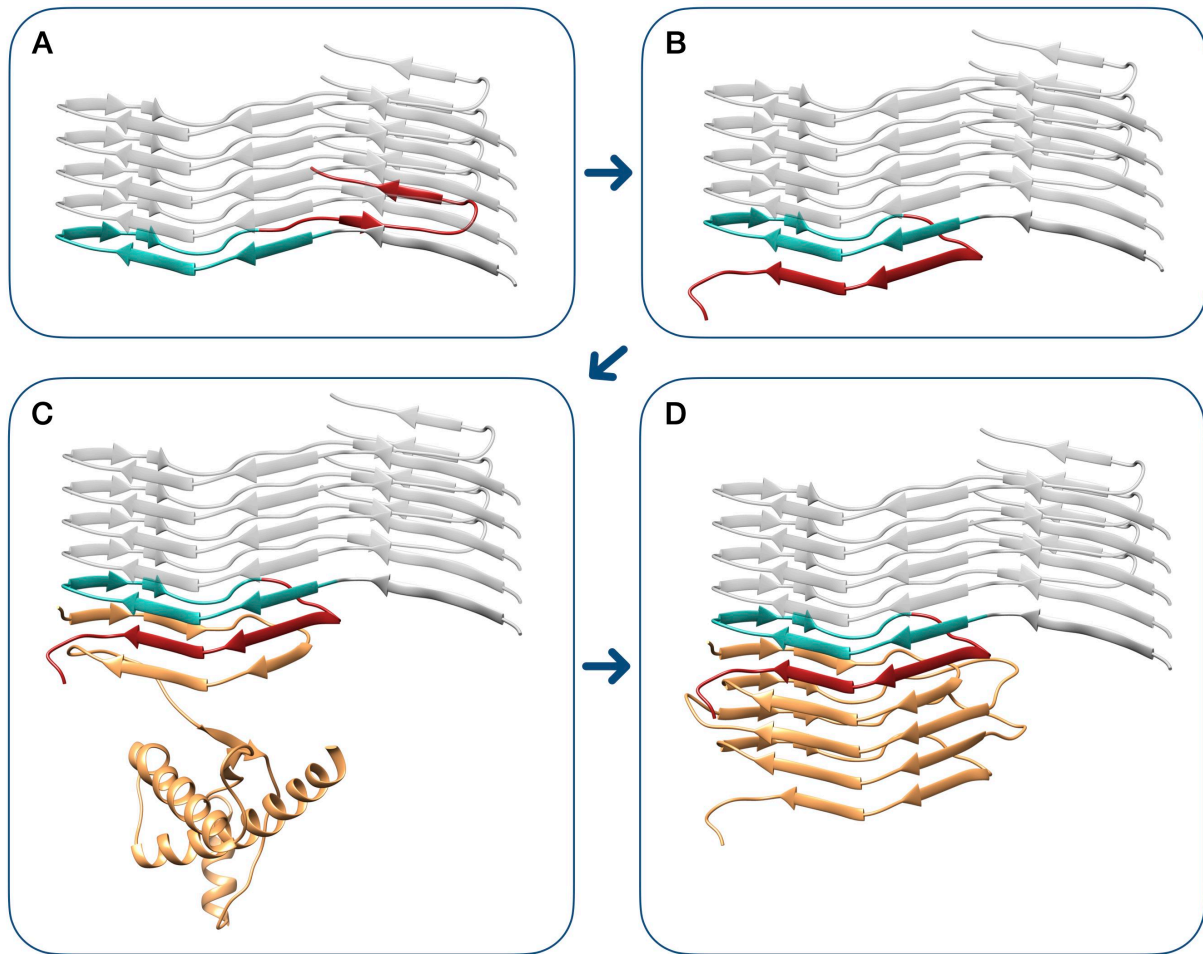
Figure 3.10: Transition from the PIRIBS atypical propagative PrP to 4RβS PrP^Sc. The deformed templating event begins with the conformational transition of the terminal PIRIBS monomer (A), in which the C-terminal stretch (residues 208–230), depicted in red, rearranges to engage intramolecular contacts with the central triangular core (residues 180–207), represented in cyan. This event generates an active-end, compatible with the propagation of the 4RβS architecture (B). The C-terminal terminal surface is now capable of templating the conversion of the unstructured region of PrP^C (depicted in orange), leading to the formation of the first rung of the β-solenoid, composed by residues 89–115 (C). The completion of the conversion into 4RβS PrP^Sc can then occur through the conformational propagation of the sequential rungs (D). Glycans are not shown for simplicity. It should be highlighted that this is not the result of MD simulations, but a schematic representation to propose a putative mechanism underlying deformed-templating conversion. Figure from Spagnolli et al.[217] ©①

This study highlights how new experimental data can be employed to propose refined versions of a plausible PrP^Sc model. Indeed, to design the archetypal 4RβS arrangement we relied on the knowledge about structurally-characterized β-solenoid proteins. While this information enabled the selection of a scaffold compatible with the cross-section of prion protofibrils, the conformation of the template rung was unlikely to reflect the real arrangement of PrP^Sc. The observation that a stack made of triangular cores of a non-infectious PrP amyloid would result in a shape compatible with the cryo-EM volume inspired us to use that particular arrangement as a more realistic template for the PrP^Sc rungs. The resulting model features a sufficient structural similarity with the PrP amyloid to explain deformed templating while maintaining the solenoid architecture suggested by cryo-EM and X-ray fiber diffraction data obtained on mouse RML prions[217].

3.2 The Molecular Mechanism of Prion Propagation

The characterization of the mechanism by which PrP^{Sc} propagates its conformationally-encoded information would provide fundamental insights underlying the molecular basis of prion diseases. However, the lack of atomistic information regarding the structure of PrP^{Sc} has so far hampered the elucidation of this process. The reconstruction of a plausible mammalian prion model provided us with an important tool to investigate the mechanism of prion replication at an atomistic level of resolution. To deal with this challenge, we employed a coarse-grained statistical approach to define the dominant reaction pathway underlying the conversion of PrP^{C} into PrP^{Sc}. This information was then used to sample a realistic prion propagation pathway by using rMD. Importantly, the application of this scheme relied on the main assumption that a model based on low-resolution experimental constraints can fully recapitulate the molecular behavior of the real PrP^{Sc}. For this reason, to obtain a validation of the obtained propagation mechanism, we employed the SCPS algorithm to reconstruct the replication of the prototypical HET-s fungal prion, whose atomistic structure has been defined. In particular, we simulated the series of events underlying the conformational rearrangements occurring during the inclusion of a soluble HET-s monomer into a growing fibril. To date, these represented the first attempts to characterize the mechanism of protein-based inheritance with full-atomistic resolution.

3.2.1 Reconstructing the Propagation Mechanism of PrP^{Sc}

The 4RβS model allowed us to develop an original scheme to perform for the first time a simulation of the conformational transition from PrP^{C} to PrP^{Sc}. In order to bridge the gap between the computationally-accessible and the biologically-relevant time scales, we employed rMD to sample relevant states along the pathway of misfolding. However, this scheme provides a sampling of the transition path ensemble only if the biasing force is applied along a reliable reaction coordinate[221]. Therefore, the first step towards developing our rMD simulation was to build a statistical model to identify the reaction coordinate of the process. In order to describe the reaction kinetics, we developed a simple stochastic model in which the key rate-limiting processes are assumed to be the irreversible formation and docking of the four rungs of the 4RβS. We indicated R_0 as the C-terminal rung of the pre-formed 4RβS PrP^{Sc}, and with R_1 R_2 R_3 R_4 the consecutive rungs of the converting monomer. The instantaneous state of the system can be represented as a 4-dimensional vector of binary entries S = [n_0, n_1, n_2, n_3], where n_k = 1 in the presence of docking between rung R_k and rung R_{k+1}, and n_k = 0 otherwise. We emphasize that this model excludes the presence of standalone rungs, which would correspond to an entropically-unfavorable single extended conformation, not stabilized by hydrogen bonds of nearby β-strands. On the other hand, misfolded rungs can be stabilized either upon docking to a pre-existing misfolded region (template mechanism) or through a process in which two rungs simultaneously form and dock. We modeled the transition of an initial state S_R = [0, 0, 0, 0] (in which the PrP^{C} monomer is in the native state and none of the rungs are formed) to the fully misfolded state S_P = [1, 1, 1, 1] (in which the PrP monomer is completely converted into PrP^{Sc}). The resulting network is represented in figure 3.11A which contains all the possible combinations of docking events leading S_R to S_P through a sequence of irreversible transitions. The model can be simplified considering that the rate k_2 is expected to be negligible as compared to k_0. Indeed, while

the event associated with k_0 only requires the structuring of a disordered PrP region, the events associated with k_2 require the loss of native content (breakage of hydrogen bonds in the helical regions) together with the simultaneous formation of two rungs (two-fold entropic cost). Thus, it is possible to disregard all the reaction pathways in which the first step of the reaction is a transition occurring at a rate k_2 and consider only events starting from $[1, 0, 0, 0]$. The network of the resulting simplified model is depicted in 3.11B. Furthermore, we can set $k_3/k_1 \gg 1$ and $k_3/k_2 \gg 1$, since the docking of two pre-formed rungs occurs at a rate much faster than all processes involving misfolding. The reaction kinetics in this stochastic model was simulated through a kinetic Monte Carlo algorithm (arbitrarily setting $k_3/k_1 = 10^6$) and the resulting reaction mechanisms were studied as a function of the k_2/k_1 ratio. Namely, we enumerated all the reaction pathways (indicated in the table below) and computed the corresponding probabilities (figure 3.11C)[215].

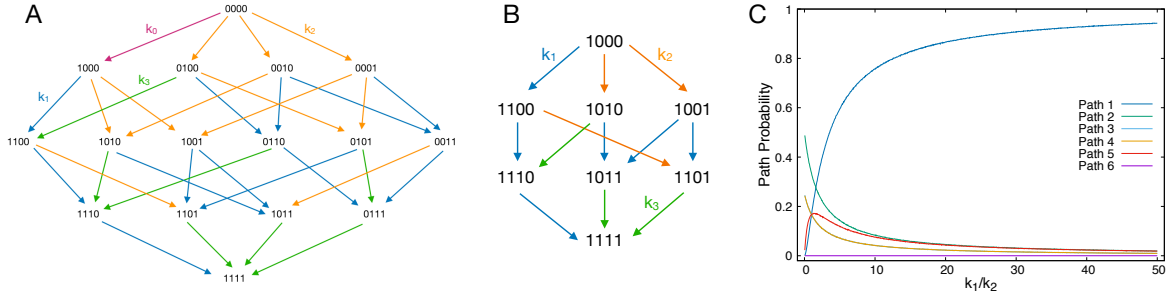|	Step 1	Step 2	Step 3	Step 4
Pathway 1	1, 0, 0, 0	1, 1, 0, 0	1, 1, 1, 0	1, 1, 1, 1
Pathway 2	1, 0, 0, 0	1, 0, 1, 0	1, 1, 1, 0	1, 1, 1, 1
Pathway 3	1, 0, 0, 0	1, 0, 0, 1	1, 0, 1, 1	1, 1, 1, 1
Pathway 4	1, 0, 0, 0	1, 0, 0, 1	1, 1, 0, 1	1, 1, 1, 1
Pathway 5	1, 0, 0, 0	1, 1, 0, 0	1, 1, 0, 1	1, 1, 1, 1
Pathway 6	1, 0, 0, 0	1, 0, 1, 0	1, 0, 1, 1	1, 1, 1, 1

Figure 3.11: Statistical model for prion propagation mechanism. (A) Schematic representation of the network of transitions leading to the incorporation of PrP^C into PrP^{Sc}. The purple arrow describes the formation of a single rung by templating the unstructured region of PrP^C (89–115) on PrP^{Sc} (rate k_0). The blue arrows describe the formation of a single rung by means of a templating process which involves breaking the native contacts and docking onto a pre-formed rung (rate k_1). The orange arrows indicate the spontaneous formation and docking of two *de novo* rungs (rate k_2). Finally, the green arrows indicate the docking of preformed rungs belonging to two adjacent misfolded regions of the same chain (rate k_3). (B) Simplified version of the network assuming as a priming reaction step the formation of the first rung. (C) Probability of the 6 reaction pathways computed using a kinetic Monte Carlo algorithm as a function of the k_1/k_2 rate ratio. Figure adapted from Spagnolli et al.[215] ⓒ①

We find that Pathway 1 (which consists in the consecutive formation of all rungs by templating on previously misfolded structures) dominates over all others as soon as $k_1/k_2 \geq 4$. Using Kramers' theory and assuming comparable pre-factors, we find that the templating mechanism is the most prominent reaction pathway when the activation energies for single and double rung formations obey the relationship:

$$\ln \frac{k_1}{k_2} = \Delta G_2^{\ddagger} - \Delta G_1^{\ddagger} \gg 1.5\ k_B T \tag{3.1}$$

We expect this condition to be always satisfied. Indeed, processes 1 and 2 are characterized by the formation of the same number of hydrogen bonds, leading approximately to the same enthalpic gain. However, the process described by rate k_2 requires the breaking of the double amount of native contacts, together with a two-fold entropic loss (compared to the single rung formation) when forming two *de novo* rungs. We can therefore conclude that the propagation reaction proceeds through a subsequent formation of individual rugs, using as template pre-existing 4RβS free end[215]. We emphasize that our approach is likely to underestimate the dominance of the sequential misfolding mechanism. Indeed, it does not account for the direct cooperativity of hydrogen bonds and the long-range electrostatics favoring β-strand formation in presence of pre-formed β-sheets, as directly supported by previous computational and experimental evidence[222, 223].

We then exploited the coarse-grained information about the reaction mechanism to set up an all-atom rMD simulation of the PrP^C conversion into PrP^{Sc}, using the 4RβS model as a target structure. The initial state for the conversion simulation was generated by assuming that PrP^C engages the first contacts with PrP^{Sc} through its residues belonging to the unstructured stretch 89-104. The rationale behind this scheme derives from multiple previous reports indicating that PrP^C sequence 89-104 is a primary site for PrP^{Sc} interactions[224]. The resulting rMD simulations yielded a transition pathway in which the C-terminal rung of the solenoid acts as a primary conversion surface for PrP^C unstructured N-terminus (residues 89–124). This first event initiates a cascade of conformational transitions in which each newly formed rung acts as a template for the formation of the following one, ultimately leading to the complete conversion of PrP^C into PrP^{Sc} (figure 3.12)[215]. This analysis provides a detailed description of the active role of protofilament ends in the templated propagation of prions, and it is compatible with previous observations suggesting the presence of a structured intermediate conformer of PrP^C in its transition to PrP^{Sc} [225].
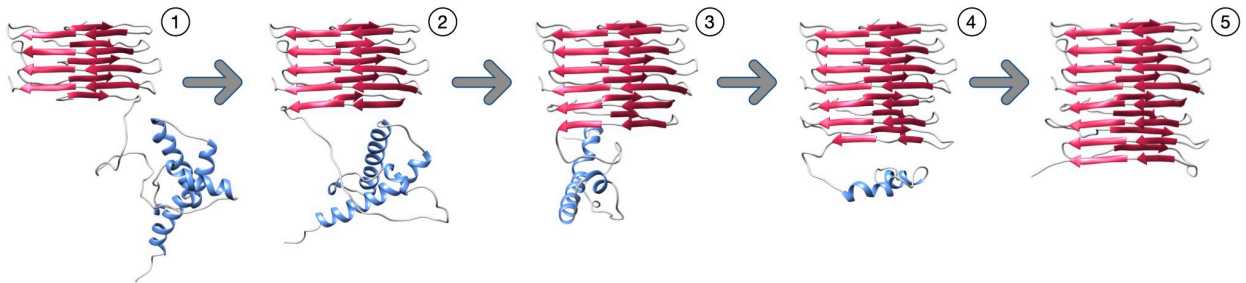
Figure 3.12: Conformations sampled from the rMD simulation of PrP^C to PrP^{Sc} conversion. Pictures of the evolving complex represent frames extracted from the entire conversion simulation at precise rMD steps, corresponding to the refolding of PrP^C as follow: (1) residues 89-104; (2) residues 89–115; (3) residues 89–151; (4) residues 89–190; (5) residues 89–230. The process highlights the progressive unfolding and refolding of PrP^C onto the 4RβS template, which initially involves the unstructured region, followed by the loss of α-helices and a progressive formation of β-sheets. Figure adapted from Spagnolli et al.[215] ⓒ①

3.2.2 Self-Consistent Simulations of a Prototypical Prion Propagation

While our study on the conformational conversion of PrP^C into PrP^{Sc} represented a pioneering attempt to study prion propagation, the obtained reconstruction only provided a qualitative description of the process underlying this misfolding event. In particular, the application of the simulation scheme was possible by relying on three assumptions, namely: (I) the initial contact point between PrP^C and the templating surface of PrP^{Sc}; (II) the validity of a model based on low-resolution constraints for the 4RβS architecture; and (III) that a simple statistical model could provide a reasonable CV to instruct the reaction progression[215]. To overcome the limitations of this work we employed the SCPS algorithm to reconstruct the replication mechanism of the HET-s prion, whose two-rung-β-solenoid (2RβS) structure was elucidated by ssNMR. Since in SCPS the reaction coordinate is refined through a self-consistent process, the results of the simulations at convergence should not be affected by the initial choice of the CV. Furthermore, the soluble monomer of the HET-s prion forming domain is completely unstructured, therefore it is likely that a polymerization event can occur at both termini of the fibril.

To perform the SCPS simulations, we used as a product state a trimeric structure of the HET-s prion forming domain in the amyloid conformation (PDB 2KJ3, figure 3.13). While the conformations for the reactant state were generated by performing high-temperature MD simulations on the HET-s trimer introducing position restraints on heavy atoms on two out of the three monomers. We obtained a total of 10 initial unstructured conditions (supplementary figure 6): 5 in which the unstructured monomer resides at the N-terminus (by introducing the restraints on the two C-terminal monomers), and 5 initial conditions in which the unstructured monomer resides at the C-terminus (by introducing the restraints on the two N-terminal monomers). For each initial condition in the reactant state, we applied the SCPS protocol and retained only the trajectories which successfully reached the product state[214].
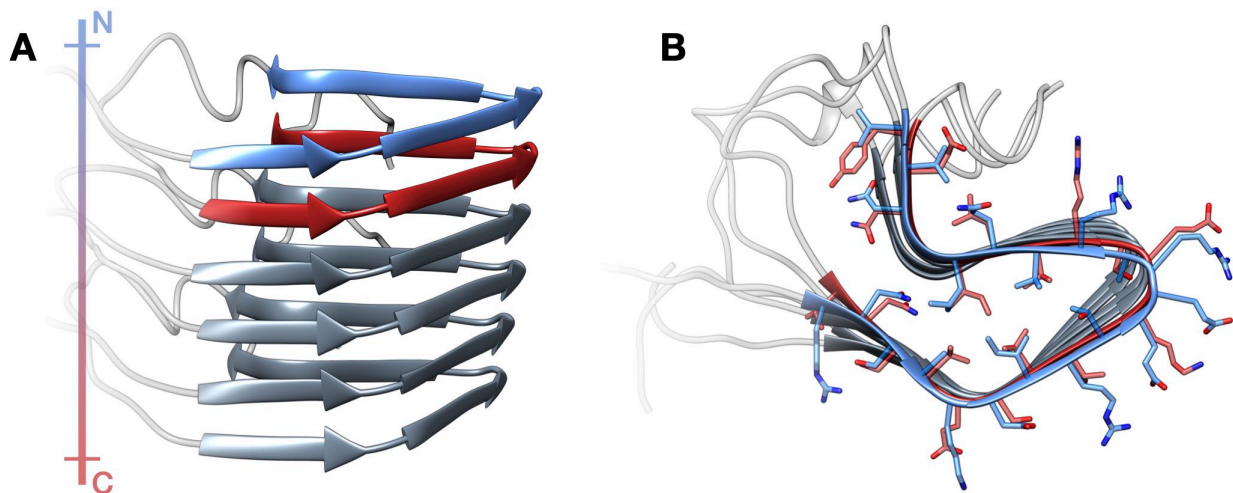
Figure 3.13: Structure of the HET-s prion forming domain in the amyloid state. Lateral (A) and top (B) view of a HET-s amyloid trimer retrieved from PDB 2KJ3. Each monomer of the fibril displays a 2-Rung-β-Solenoid conformation. The N-terminal rung (NT-Rung, residues 225–245) is depicted in blue, while the C-terminal rung (CT-Rung, residues 261–281) is depicted in red. The colored bar at the left represents the polarity (N to C, blue to red) of the fibril. Figure adapted from Terruzzi et al.[214] ⓒⓘ

The results obtained are reported in figure 3.14, where we represent the conformations explored by the trajectories projected on the plane defined by the RMSD to the reference state of each rung of the converting monomer. Namely, the transition path energy landscapes display the quantity $G(RMSD_{CT-Rung}, RMSD_{NT-Rung}) = -\ln[P(RMSD_{CT-Rung}, RMSD_{NT-Rung})]$, where $P(RMSD_{CT-Rung}, RMSD_{NT-Rung})$ is the probability of observing specific RMSD pairs, calculated from a frequency histogram of the SCPS trajectories[214].
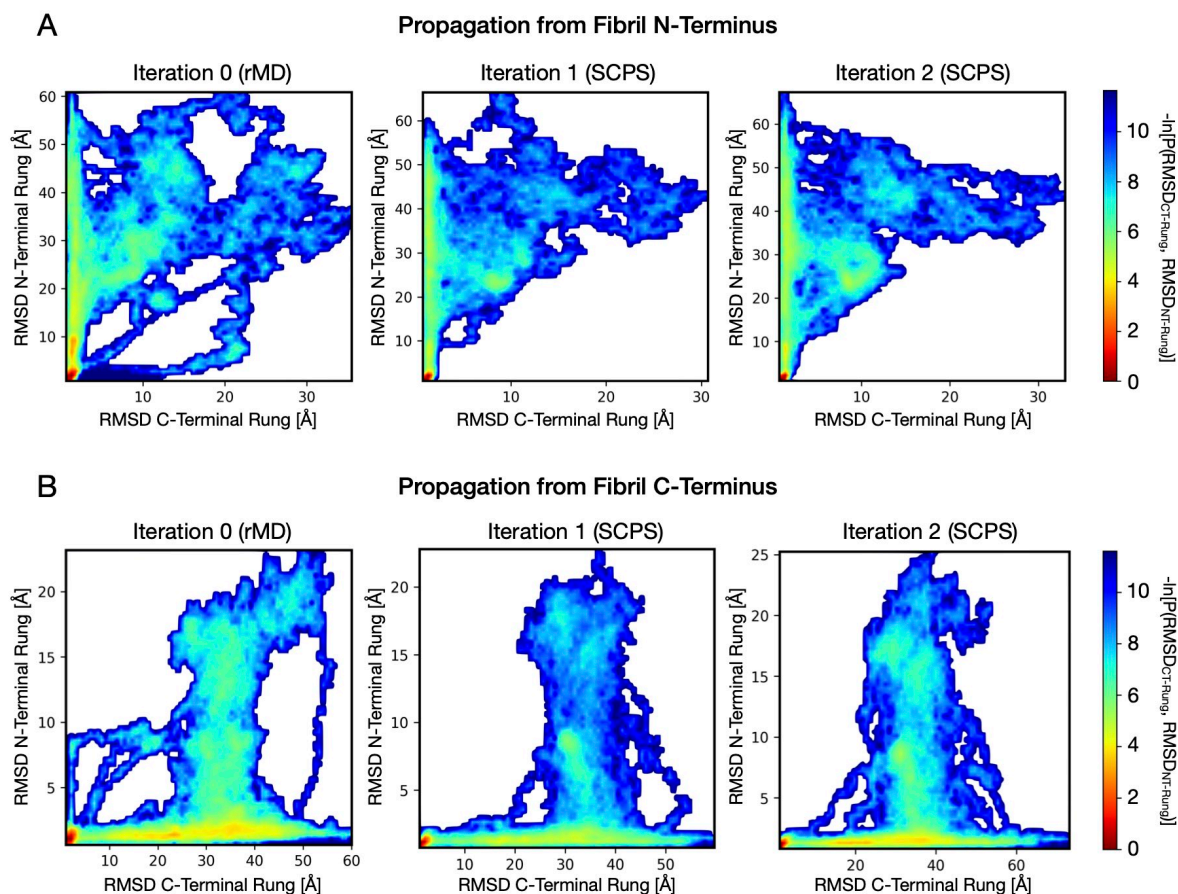
Figure 3.14: Reaction pathways in HET-s rungs formation. The heatmaps represent the negative logarithm of the probability density calculated from the reactive pathways at subsequent SCPS iterations, as a function of the RMSD from the target structure of the N- and T-terminal rungs. (A) Graphs relative to trajectories propagating from the fibril N-terminus. (B) Graphs relative to the trajectories propagating from the fibril C-terminus. In both cases, a dominant pathway, consisting in the consecutive formation of rungs starting at the fibril end, begins to appear in the rMD-generated trajectories. However, the rMD scheme also yields pathways with cooperative or inverted rung formation. These alternative events disappear after a single SCPS iteration. Of note, a second iteration does not produce a consistent change in the heatmaps of both (A) and (B), indicating the convergence of the algorithm. Figure from Terruzzi et al.[214] ©①

To further characterize the reaction process underlying the templated conversion of the HET-s prion, we performed additional analysis on the SCPS pathways of the last iteration. In figure 3.15, we show the median value of the reaction progress variable Q at which each residue assumes the β-strand conformation (the value of Q is 0 in the reactant state and 1 in the product state and corresponds to the fraction of reference contacts). The sequence of secondary structures formation can be interpreted as the order with each residue of the monomer dock to the fibril. In the case of initial anchoring occurring at the N-terminus of the HET-s fibril, the C-terminus of the incoming monomer acquires a

β-sheet conformation by progressively establishing intermolecular hydrogen bonds with the exposed edge residues. Once completed, the newly formed rung templates the formation of intramolecular hydrogen bonds with the remaining residues of the polypeptide. Insertion of monomers at the C-terminal edge of the HET-s fibril proceeds in a specular fashion. These observations indicate that the two exposed edges of the HET-s amyloid provide the initial scaffold for the templated conversion of incoming monomers, which become new edges after completion of the reaction[214].
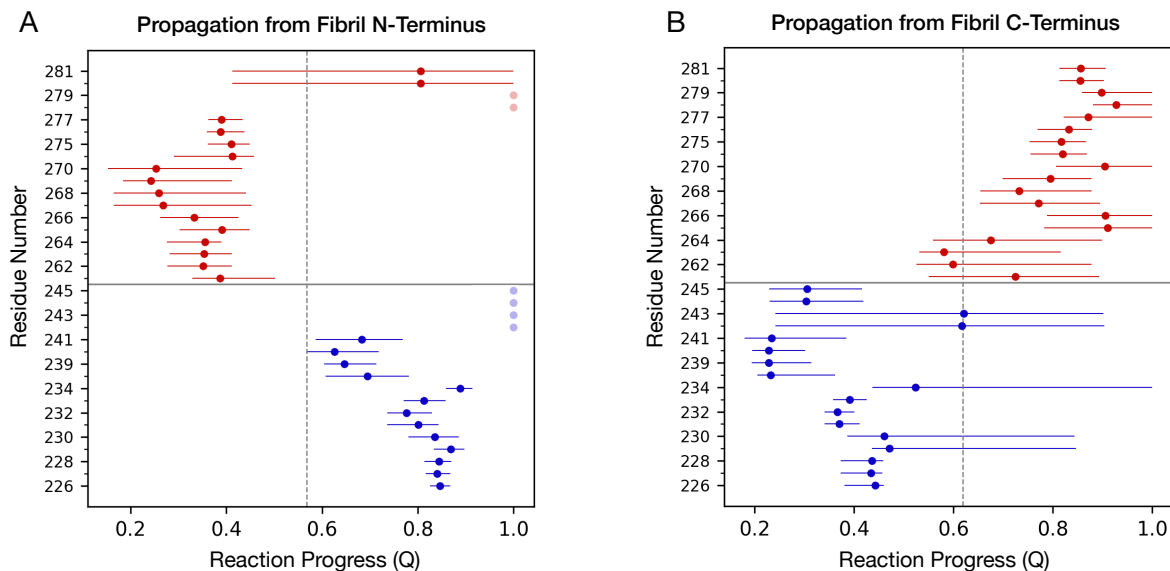

Figure 3.15: Order of β-strand formation along the HET-s propagation pathway. The graphs report the median value of the reaction progress variable Q at which each residue of the rungs assumes the β-strand conformation. Blue dots correspond to residues in the N-terminal rung while red dots correspond to residues in the C-terminal rung. Dots shown in transparency indicate residues not achieving a stable β-strand conformation. Horizontal bars span between the first and the third quartile of the distribution. The vertical dashed line delineates the average reaction progress at which half of the rungs-residues are incorporated into β-strand conformation. In the propagation starting from the fibril N-terminus (A) the residues of the C-terminal rung of the converting monomer are incorporated first (mean Q = 0.44), followed by the residues in the N-terminal rung (mean Q = 0.69). The opposite sequence of events is observed when propagation starts from the fibril C-terminus (B): the residues of the N-terminal rung of the converting monomer are incorporated first (mean Q = 0.42), followed by the residues in the C-terminal rung (mean Q = 0.81). Figure from Terruzzi et al.[214] ⓒⓘ

To obtain an unbiased projection of the reaction paths without selecting *a priori* the collective variables for its representation, we performed a principal component analysis (PCA) on the Cα contact maps of the sampled transition pathways (figures 3.16A and 3.16D). The PCA energy landscape representation showed that in both N-terminal and C-terminal propagation pathways the reaction initially occurs almost exclusively along the principal component 2 (PC2), and only subsequently toward the principal component 1 (PC1). Further analysis of the contribution of each contact distance to the two principal components was performed by grouping the contacts in three sets: (I) contacts between residues belonging to the same rung (intra-rung); (II) contacts between residues of different rungs (inter-rung); (III) contacts between residues of the converting monomer and the structured fibril (monomer-fibril) (figures 3.16B and 3.16D). This analysis revealed that the main contact contributors for PC1 belong to the inter-rung set, while contributors of PC2 belong mainly to the monomer-fibril set. Overall, these findings corroborate a rung-by-rung propagation model for

HET-s. Interestingly a highly populated region appears at the elbow of the landscape graph, in both the N-terminal and C-terminal fibril growths. Such a region reflects long-living misfolding intermediates occurring during the HET-s templated conversion, characterized by the presence of only one rung of the converting monomer attached to the elongating fibril (figures 3.16C and 3.16F)[214].
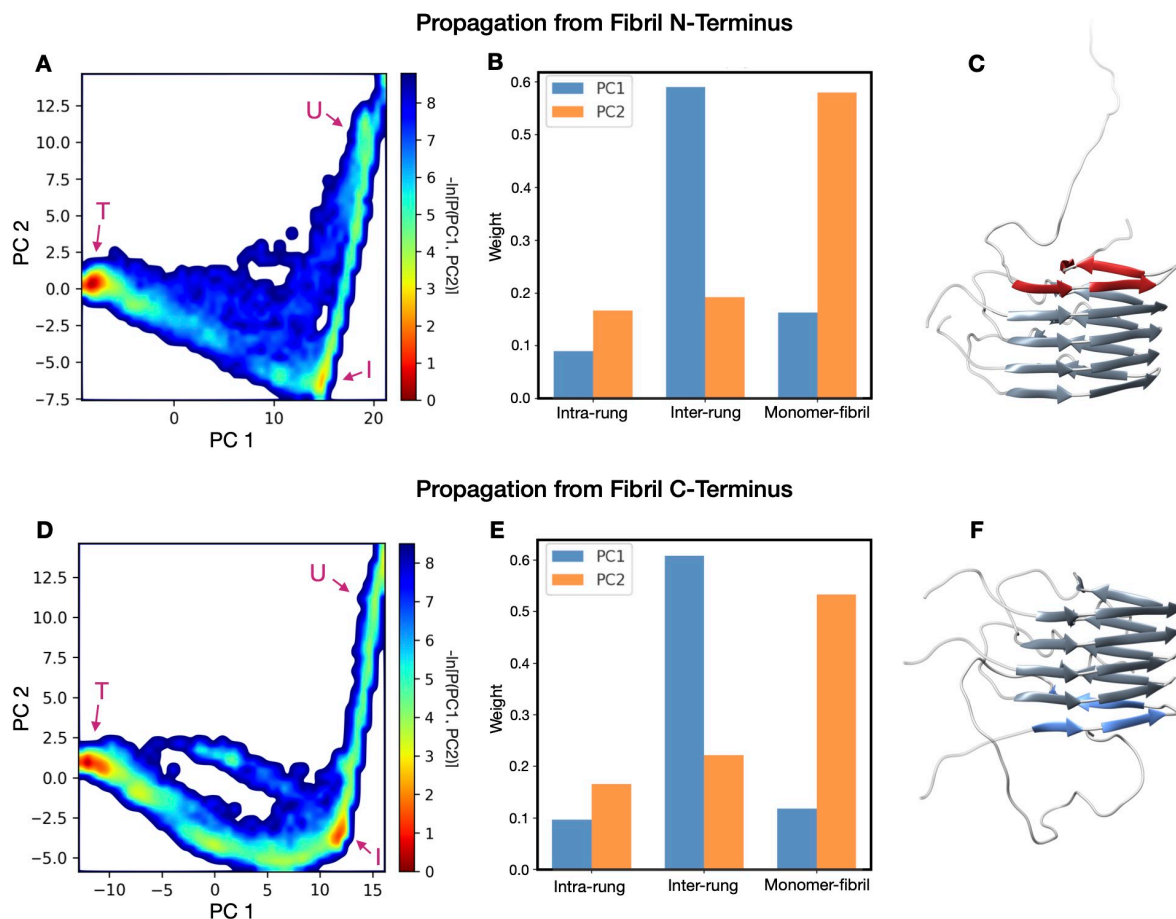
Figure 3.16: Principal component analysis of the HET-s propagation trajectories. Graphs (A) and (D) represent the transition energy landscape in the principal component plane of the trajectories propagating from the fibril N- and C-terminus respectively. The letters "U", "I" and "T" indicate the unstructured, intermediate, and the final (target) state, respectively. The residue contacts were classified in three categories: contacts between Cα in the same rung (intra-rung), contacts between Cα belonging to different rungs (inter-rung) and contacts between Cα of the converting monomer and Cα of the structured fibril (monomer-fibril). The contribution of these sets of the two principal components is shown in bar plots (B) for the N-terminal propagation and (E) for the C-terminal propagation. Images (C) and (F) show representative protein conformations sampled from the intermediate state, for the N- terminal and C-terminal propagations, respectively. Figure from Terruzzi et al.[214] ©①

Collectively, our simulations indicate that HET-s prion conversion occurs through a series of templating events occurring at the N-terminal and C-terminal ends of the fibrils. In these sites, incoming HET-s monomers are initially incorporated by establishing intermolecular hydrogen bonds with the exposed β-strands, leading to the formation of a first rung, which then forms new intramolecular hydrogen bonds with the remaining parts of the polypeptide, giving rise to a new 2RβS fibril subunit (figure 3.17). These findings corroborate the results of our previous simulation, in which we showed that the conversion of PrP^C into the 4RβS PrP^{Sc} proceeds by the sequential formation of

rungs. Importantly, the results of our SCPS simulation of the entire sequence of events underlying the incorporation of HET-s monomers into a growing fibril were obtained without completely relying on a specific choice of the CV, namely in the absence of strong ad-hoc assumptions concerning the reaction mechanism.
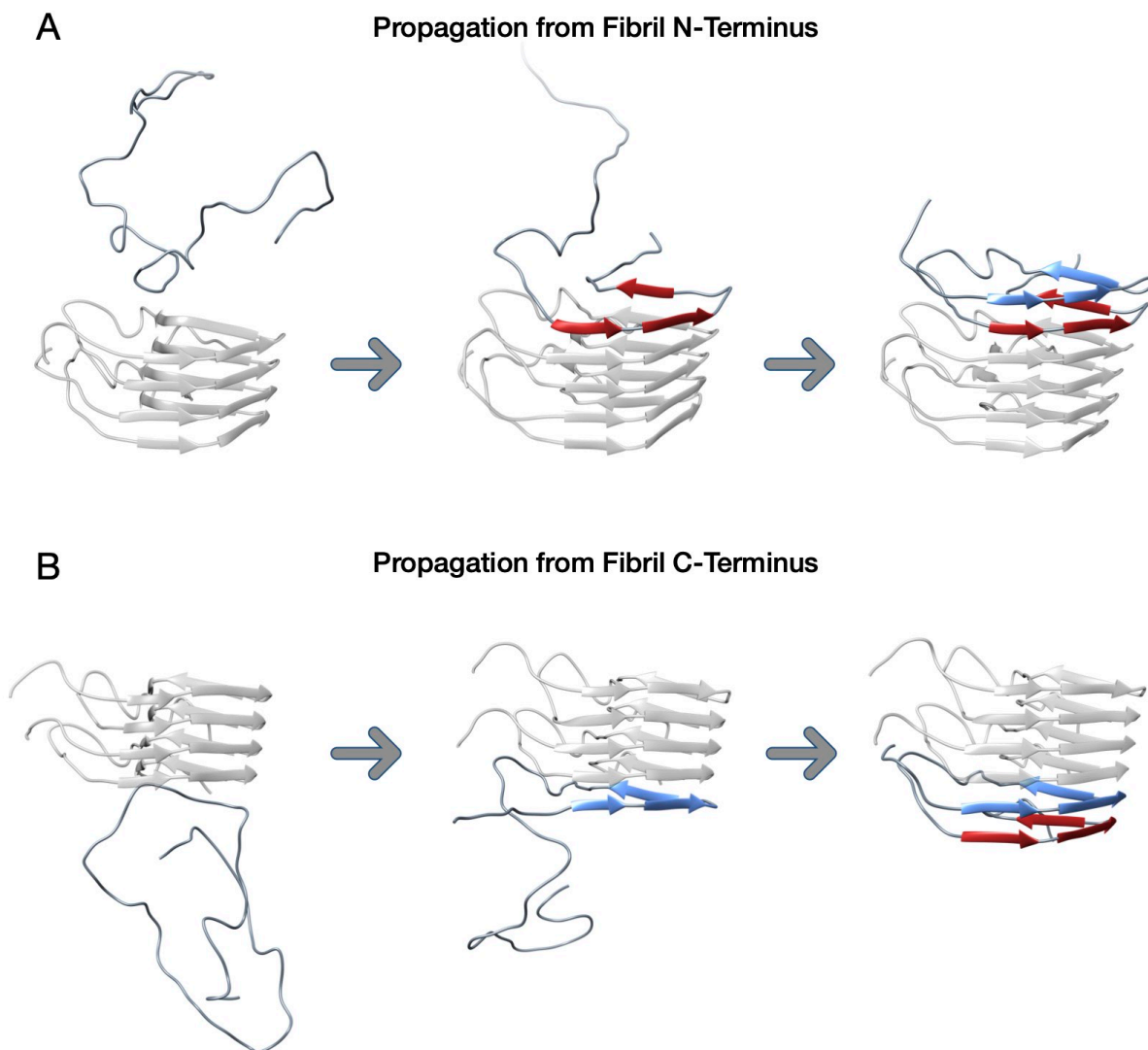
Figure 3.17: Representative scheme for HET-s prion propagation. (A) Propagation scheme starting from the N-terminal end of the fibril. In this process, the C-terminal rung of the converting monomer (depicted in red) is formed by templating onto the structured N-terminal rung of the fibril (shown in transparent grey). Subsequently, the N-terminal part of the converting monomer forms the second rung (depicted in blue). (B) Propagation scheme starting from the C-terminal end of the fibril. In this process, the N-terminal rung of the converting monomer (depicted in blue) is formed by templating onto the structured C-terminal rung of the fibril (shown in transparent grey). Subsequently, the C-terminal part of the converting monomer forms the second rung (depicted in red). Figure adapted from Terruzzi et al.[214] ©①

3.3 Conclusions & Future Perspectives

3.3.1 The Structure of PrP$^{\text{Sc}}$

In this work, we used computational tools to build a plausible atomistic model of PrP$^{\text{Sc}}$ by integrating several experimental constraints derived from the mouse RML prion. These included cryo-EM and X-ray fiber-diffraction analysis which indicate that the general architecture of this strain is compatible with a 4RβS, and limited proteolysis studies providing insights regarding the solvent accessibility of different PrP$^{\text{Sc}}$ regions. The resulting model showed physical stability comparable to the one of the structurally-characterized HET-s prion. Conversely, the previous reference model for PrP$^{\text{Sc}}$ architecture, the LβH[149], collapsed after a few tens on nanoseconds when challenged with MD simulations. Initially, we relied on the structure of a prototypical β-solenoid protein to provide the scaffold for our modelling scheme. While this approach enabled the construction of a model compatible with the fibril cross-sections observed by cryo-EM, the arrangement of the employed template likely reflected only a general approximation of a real PrP$^{\text{Sc}}$ rung. Later, the availability of a high-resolution structure of a non-infectious PrP amyloid (figure 3.5)[218] allowed us to refine the 4RβS model in such a way that it can explain the phenomenon of deformed templating. In the newly proposed structure, one rung of the solenoid is shared with the triangular core of the non-infectious PrP amyloid and provides the basis for a putative conversion of this species into an infectious prion. Importantly, while modelling deformed templating we showed that the PIRIBS architecture, which was previously considered incompatible with a high degree of glycosylation[66], can actually accommodate bulky glycans on both the target asparagines in each monomer.

In a recent study posted on the bioRxiv server, the group of Byron Caughey showed by cryo-EM that the 263K hamster prion features a PIRIBS architecture[19]. This work represents the first success in characterizing the structure of an infectious prion at a quasi-atomistic level of resolution and revealed that each fibril of this strain is composed of a single protofilament with size 130 x 35 Å. Importantly, this conformation is completely different from the 4RβS model, which is instead based on cryo-EM data obtained from mouse RML PrP$^{\text{Sc}}$ indicating the presence of two intertwined protofilaments with cross-sections of ∼50 x 30 Å. While it has been debated that the lower resolution of the cryo-EM reconstruction obtained from mouse GPI-anchorless PrP$^{\text{Sc}}$ could have led to misinterpreting a single protofilament as two symmetrical volumes, it is also possible to attribute the observed discrepancy to a substantial difference in the structure of these prion strains. Indeed, the different structural arrangements of prions might actually reflect the distinct biochemical and pathological features displayed by different strains. However, only further studies will enable to characterize the range of structural changes underlying the heterogeneity of PrP$^{\text{Sc}}$ and to determine whether both PIRIBS and β-solenoids architectures can constitute possible arrangements of infectious mammalian prions.

3.3.2 Unraveling the Mechanism of Prion Replication

The reconstruction of a plausible atomistic model of PrP^{Sc} based on the 4RβS architecture allowed us to propose the first scheme describing how the information encoded in the conformation of a protein could be propagated in a directional fashion. This was achieved by building a stochastical model to identify a reasonable reaction coordinate which was then employed to sample the conformational transitions underlying prion conversion, using rMD simulations. Despite its innovative character, the approximations introduced to allow such an approach could strongly have impacted the reliability of the predictions and likely led to an underestimation of the pathways variability. To validate the proposed replication mechanism, we employed the SCPS method to simulate the conformational changes underlying the inclusion of an unstructured HET-monomer into a growing fibril. This study provided an assumption-free reconstruction describing the replication of a structurally characterized fungal prion featuring a 2RβS architecture. The observed propagation mechanism, characterized by the sequential formation of rungs, revealed to be highly similar to the one we previously proposed for PrP^{Sc}. These results suggest that different amyloid conformers characterized by a β-solenoid architecture may share a conserved mechanism of propagation, regardless of their primary sequence. In this work we showed the validity of refined computational tools, such as the SCPS method, to provide important insight into the atomistic details of amyloid propagation. Indeed, it should be highlighted that the application of the SCPS method for studying misfolding is not only limited to the specific case of prions, but it can be extended to investigate the propagation mechanism of other amyloidogenic proteins also involved in the development of severe diseases, such as α-synuclein, tau, and Aβ.

From a broader perspective, the advent of these enhanced sampling techniques opens up the possibility to characterize previously unexplored targets for rational drug discovery. In particular, amyloid fibrils, due to their significant structural stability and heterogeneity, are well known to be highly resistant to pharmacological treatments. For this reason, designing a therapeutic strategy acting on these aggregated species does not seem a viable option to successfully treat misfolding diseases. Conversely, transient intermediate states appearing along the misfolding pathway could represent valuable targets to inhibit the process of amyloid propagation. In the next chapter we describe an attempt in this direction aimed at designing a possible therapeutic strategy against prion diseases, but acting on protein folding instead of misfolding.

Chapter 4

Identification of Pharmacological Degraders for PrP

4.1 Pharmacological Targeting of a PrP Folding Intermediate

Suppressing the expression of PrP represents one of the most promising therapeutic strategies against prion diseases. Preclinical testing of ASOs clearly supports the validity of this approach against TSE[186] and antisense therapy has already been shown to be applicable to other degenerative conditions of the central nervous system, in particular in Huntington's disease[226]. However, while the currently available anti-PrP ASOs can significantly extend the survival in prion-infected mice, they are still ineffective in completely block the disease progression. For this reason, such an approach would strongly benefit from the application of a synergistic strategy, such as the combination ASOs with another drug capable of reducing PrP loads but acting on another level of protein regulation. Pharmacological degraders, such as proteolysis targeting chimeras (PROTACs), could represent promising candidates to achieve such a goal. This strategy employs bi-functional molecules composed of two covalently linked chemical moieties, one interacting with the target protein and the second recruiting the E3 ubiquitin ligase, which then labels the polypeptide to be sent to degradation by the proteasome[227]. While two PROTAC compounds targeting hormone-receptor proteins have recently reached the clinical phase, the application of this technology is unlikely to succeed in suppressing the levels of PrP. Indeed, these molecules target native states of proteins, thus suffering from the same limitations of classical pharmacological approaches when dealing with undruggable targets.

Here, we designed and applied a novel drug discovery paradigm, named pharmacological protein inactivation by folding intermediate targeting (PPI-FIT), on PrP. The rationale underlying this scheme exploits the design of compounds against a long-lived folding intermediate of a given protein, in order to stabilize such conformer and block its transition to the native state. In the cellular environment, a stabilized folding intermediate could be detected by the quality control machinery as an improperly folded polypeptide and targeted for degradation[67].

4.1.1 Identification of a PrP Folding Intermediate

To reconstruct the folding pathway of PrP at an atomistic level of resolution we employed the previously described BF approach (section 2.3.1). We initially generated nine denatured PrP conformations by thermal unfolding, starting from the native structure of the C-terminal domain of PrP^C. Each unfolded conformation was used as an initial condition to produce a set of 20 rMD trajectories (making a total of 180, whose lower-bound approximation of the transition path energy is represented in figure 4.1A). From each set of folding trajectories, the most statistically significant pathway was selected according to the BF. This enabled the identification of nine least biased trajectories that were then employed for in-depth structural analysis. In particular, conformations residing within the energy wells of interest in the bidimensional distribution were extracted from each least biased trajectory (figure 4.1B). This analysis revealed the presence of an on-pathway folding intermediate structurally close to the native state, that is explored by all the least biased trajectories[67]. This observation is in agreement with several previous reports indicating that the folding pathway of PrP is characterized by the presence of at least one folding intermediate[198, 228].
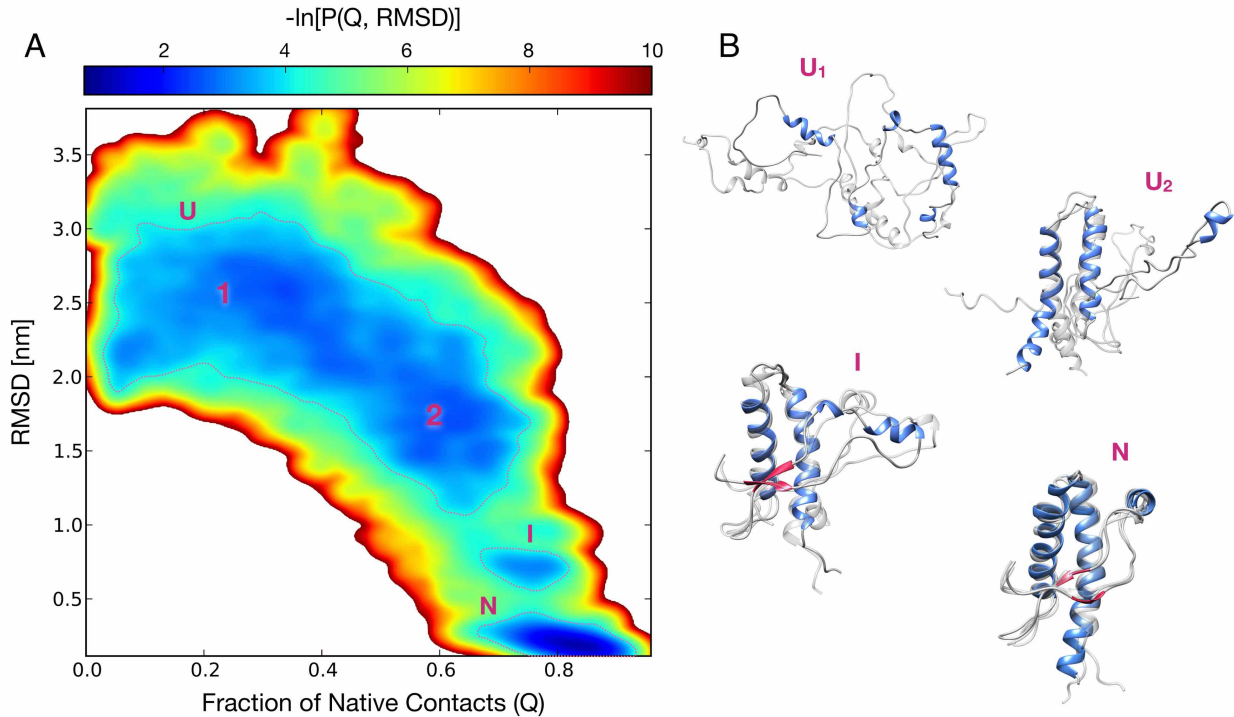
Figure 4.1: Atomistic reconstruction of the PrP folding pathway. (A) Lower-bound approximation of the transition path energy related to the folding of PrP, obtained from 180 rMD trajectories. This quantity is plotted as the negative logarithm of the probability distribution expressed as a function of the collective variables Q (fraction of native contacts) and RMSD. The dashed magenta lines define the metastable regions of interest ($G \leq 3.7\ k_BT$). (B) Representative structures of unfolded (U_1 and U_2), folding intermediate (I) and native state (N). Each conformation represents the cluster centers of one of the corresponding populated regions (structures depicted in transparency are sampled from the same region, showing conformations variability): the first two (corresponding to the unfolded states U_1 and U_2) are characterized by RMSD > 1.8 nm and a Q < 0.5 (U1), and 1.2 < RMSD < 1.8 nm and a 0.5 < Q < 0.75 (U2); a third one (corresponding to the folding intermediate state I) with 0.55 < RMSD < 0.90 nm and a 0.65 < Q < 0.85; a fourth one (corresponding to the native state N) with RMSD < 0.40 nm and Q > 0.80. Figure adapted from Spagnolli et al.[67] ©①

The conformations belonging to the intermediate state were then clustered by using the k-mean approach. Here we employed the Frobenius norm of the contact maps as a clustering distance, while the number of clusters was selected by relying on the elbow method. A summary of the clustering results is reported in figure 4.2A-B[67].
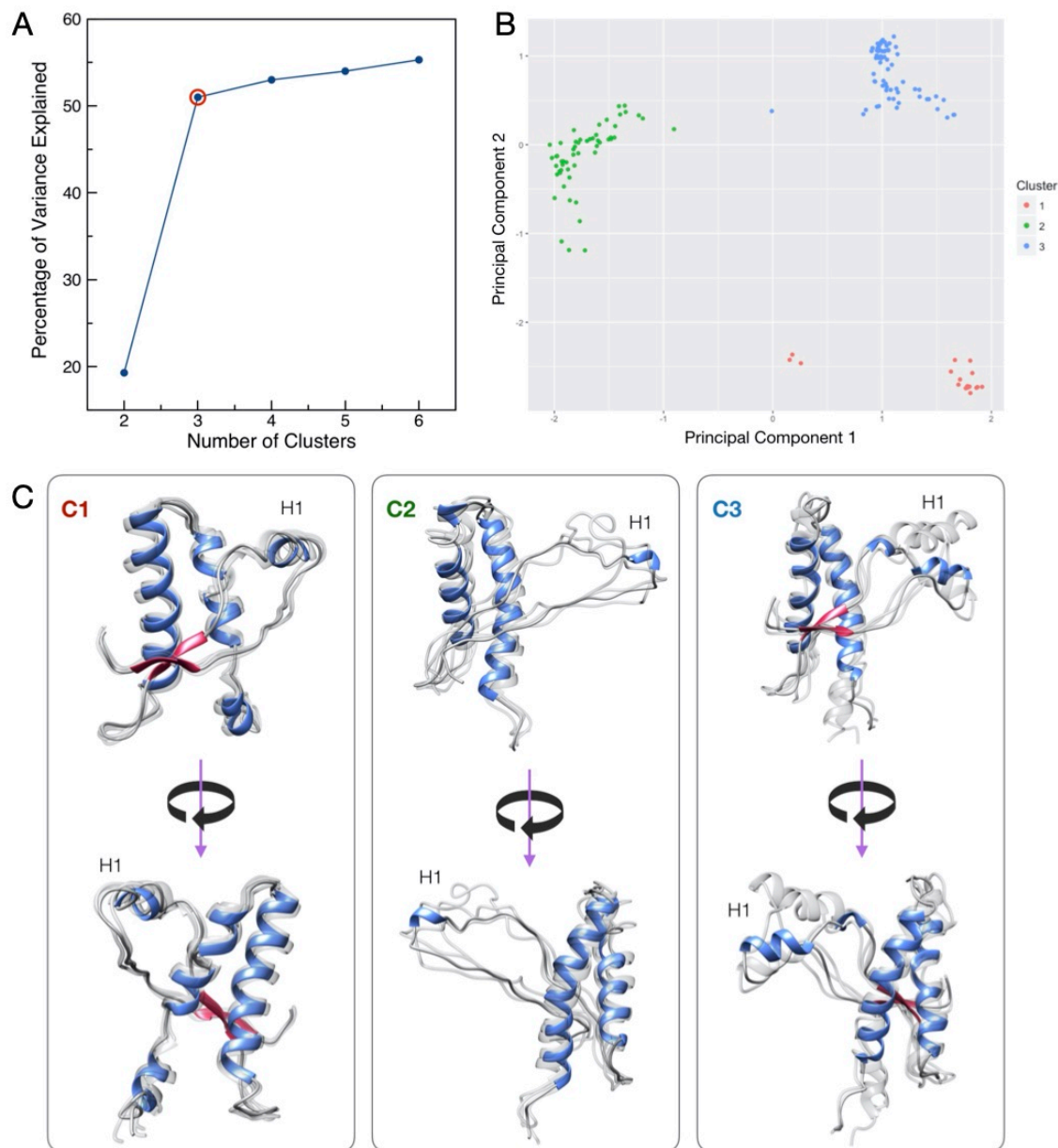
Figure 4.2: Clustering of conformations extracted from the PrP folding intermediate. (A) Elbow plot showing the percentage of explained variance as a function of the number of clusters. The ideal number of clusters suggested by the elbow criterion is the one at which the marginal gain in explained variation obtained from the addition of a cluster drops ($k = 3$, red circle). (B) Clustering results are represented in the principal component space. (C) Structures corresponding to the three cluster centers. Conformations obtained from C1 (explored by 2/9 least biased trajectories) are characterized by an unstructured H2-H3 contact region, while structures from C2 and C3 feature a displaced H1 that in the native state is docked onto H2-H3. The main distinction between C2 and C3 is that H1 is more structured in the conformations belonging to the latter. Importantly, C3 is represented by 7/9 least biased trajectories while C2 only by 1/9. Figure from Spagnolli et al.[67] ©①

The three identified clusters (figure 4.2) were characterized by a lack of native contacts in the H2-H3 region (C1), or by a displaced helix-1 missing its final docking with helix-3 (C2 and C3). Importantly, C3 was the most represented cluster among the least biased trajectories (7/9), therefore, we selected its centroid as the representative conformation of the PrP folding intermediate[67].

4.1.2 Identification of Virtual Hits for the PrP Folding Intermediate

To identify small ligands specific for the PrP folding intermediate we first scouted the surface of this conformer for unique druggable sites that are absent in the native state. This step was performed by using SiteMap[229] and DoGSiteScorer[230] software. Specific structural properties such as volume, depth, enclosure/exposure, and balance as well as different druggability scores were computed focusing on regions exclusively exposed in the intermediate state. The results revealed the presence of a possible ligand-binding site, placed between helix-1 and the loop connecting helix-2 with helix-3 defined by 14 residues: E152, N153, R156, Y157, P158, H187, E196, N197, F198, D202, V203, M205, M206, V209 (structural features and druggability scores of this pocket are reported in supplementary table 1). To refine the structure of the putative binding site we performed 50 ns of MD simulations with position restraints on backbone atoms and clustered the sampled conformations based on the RMSD of the side-chains defining the previously identified pocket. In particular, a hierarchical approach was used to obtain 10 clusters whose centroids were subjected to a re-evaluation of the binding site (druggability scores are reported in supplementary table 2). This analysis enabled us to identify a pocket conformation with highly favorable druggability descriptors (figure 4.3) that was subsequently used as a target for a virtual screening campaign[67].
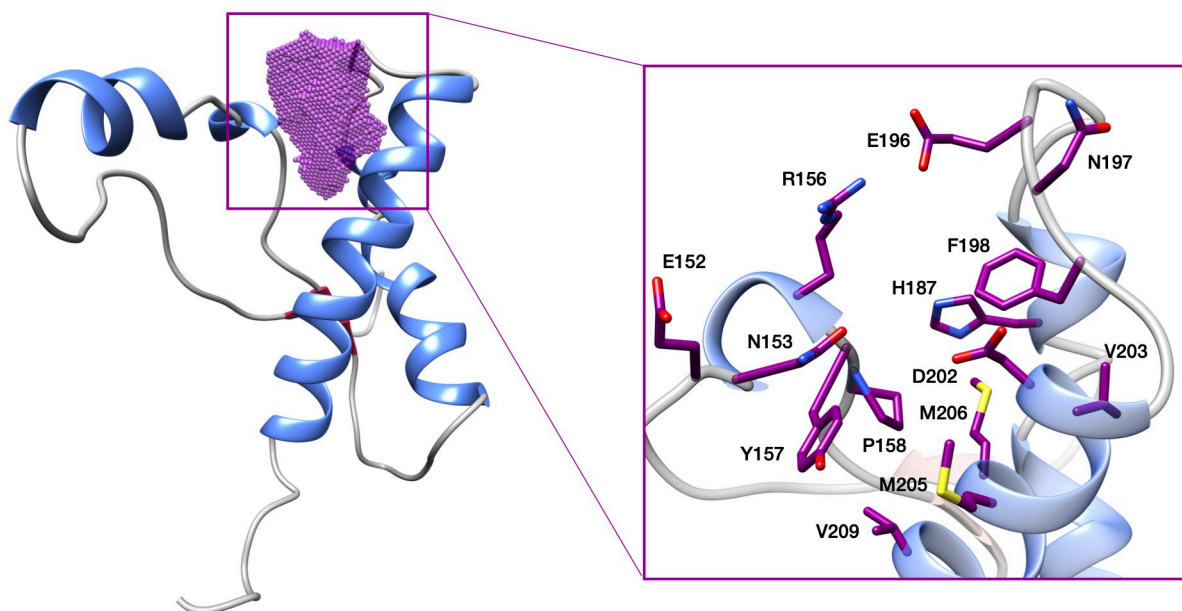
Figure 4.3: Druggable site on the PrP folding intermediate. Ribbon diagram of the PrP intermediate highlighting the ligand-binding pocket (purple dots) as identified by DogSiteScorer tools. The purple volume indicates the unique druggable site identified in the PrP-folding intermediate. The box shows individual side-chains defining the site. Notably, several of these chains, such as Y157, P158, M205, M206, and V209 are poorly or not solvent-exposed in the native state. Figure adapted from Spagnolli et al.[67] ⊚⊕

Virtual screening was carried out by using the FlexX algorithm of LeadIT, which performs fragment-based molecular docking[231]. A library of ∼3.2 x 10^5 commercially available compounds was screened and the obtained poses ranked according to the estimated affinity (re-scored using SeeSAR[232]) and 3D assessment of the ligand-binding interaction. Additional predicted physicochemical, and ADMET (absorption, distribution, metabolism, excretion, and toxicity) properties were considered for ligand filtering. Finally, cheminformatics methods for similarity and clustering analysis were applied to support a diversity-based selection. This screening process yielded 30 promising virtual hits that were purchased for biological validation (supplementary figure 7)[67].

4.1.3 Cell-Based Validation of Virtual Hits

Based on the role of the ERLAD in the quality control of retrotranslocation-defective species, a compound binding to a PrP folding intermediate may produce a relatively stable, immature conformer that could be recognized by the ER quality control machinery and sent to degradation through redirection to the lysosomal compartments[8]. Following this rationale, the 30 putative ligands were tested in cells for their capacity of reducing the amount of PrP at a post-translational level. HEK293 cells stably expressing mouse PrP were treated for 48 h at different concentrations in the 1-30 μM range. The expression and post-translational alterations of PrP were detected by western blotting. We identified four compounds (SM875, SM930, SM940, and SM950) capable of decreasing the levels of PrP ($\geq$ 30%) without lowering a control protein (NEGR-1) which follows the same biosynthetic pathway of PrP (supplementary figure 8). Based on its potency, SM875 was selected for further analysis (the docking pose of SM875 bound to the PrP folding intermediate is shown in figure 4.4)[67].
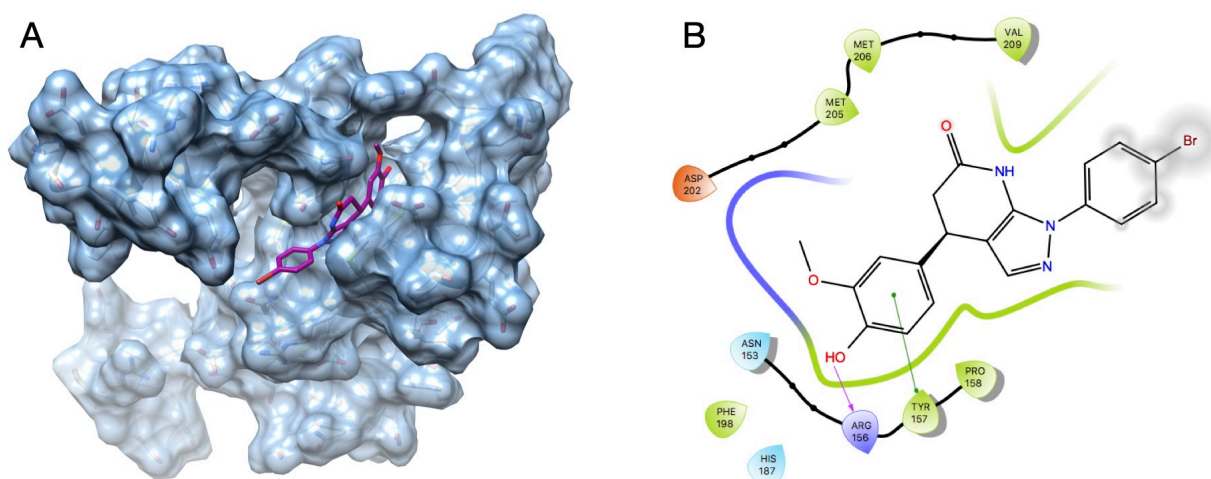
Figure 4.4: Docking pose of SM875 on the folding intermediate of PrP. (A) Structure of the predicted complex between the PrP folding intermediate (blue molecular surface) and SM875 (magenta sticks). (B) Two-dimensional ligand interaction scheme. Residues closer than 4.5 Å to the ligand are explicitly shown. Different colors reflect distinct chemical properties of the side-chains and of the pocket surface: hydrophobic (green), polar (cyan), positively charged (blue), and negatively charged (red). Grey-shaded areas indicate solvent-exposed atoms. The guaiacol moiety of SM875 is predicted to be involved in the formation of two important interactions: a hydrogen bond between its hydroxyl group and the backbone carbonyl of R156, as well as a π-stacking between its aromatic ring and the phenol group of Y157. SeeSAR predicted affinity: 0.4 μM $< K_i <$ 40 μM. Figure adapted from Spagnolli et al.[67] ⓒⓘ

The PrP-lowering activity of SM875 was validated using a larger concentration window $(0.01 - 50$ μM) in stably transfected HEK293 cells (figure 4.5). This enabled us to compute the 50% inhibitory concentration, which was found to be in the low micromolar range $(IC_{50} = 7.9 \pm 1.2$ μM). Next, to rule out possible artifacts due to the exogenous transfection of PrP, the effect of SM875 was tested in other cell lines endogenously expressing PrP (L929 mouse fibroblasts, N2a neuroblastoma, and ZR-75 human cancer cells). Compound SM875 was capable of reducing PrP levels in a dose-dependent fashion also in these lines, in the same concentration range (1–30 μM) observed in HEK293 (supplementary figure 9)[67].
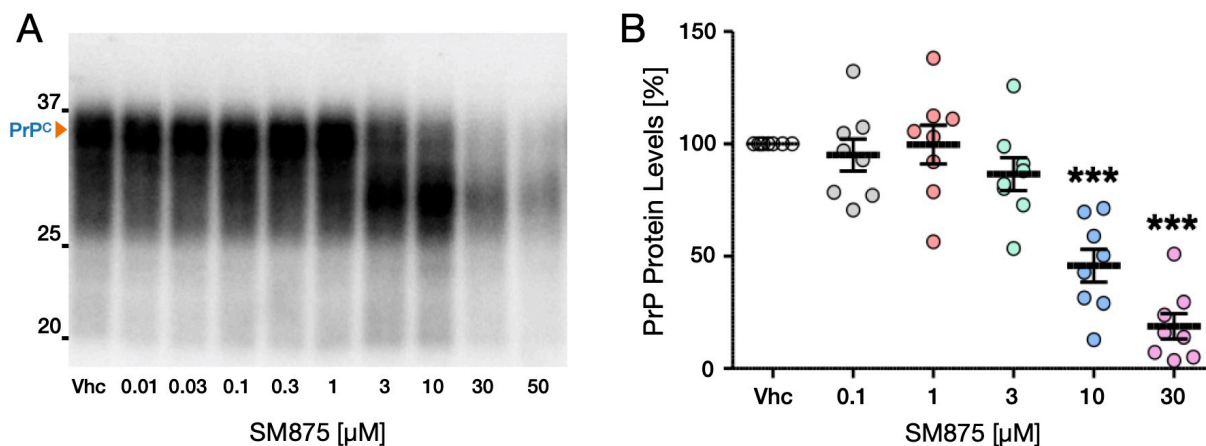
Figure 4.5: Dose-response PrP lowering activity of SM875 in HEK293 cells. HEK293 cells expressing mouse PrP were exposed to different concentrations of SM875 or vehicle (0.1% DMSO, volume equivalent) for 48 h, lysed in detergent buffer diluted in Laemmli sample buffer and analyzed by western blotting using the anti-PrP D18 antibody. (A) Western blot showing the PrP lowering activity of SM875 as a function of its concentration. (B) Densitometric quantification of eight independent biological replicates. Each signal was normalized on the corresponding total protein lane and expressed as the percentage of the level in vehicle-treated (DMSO) controls (***$p < 0.005$, by one-way ANOVA test). Courtesy of Tania Massignan. Figure adapted from Spagnolli et al.[67] ©①

4.1.4 Biological Characterization of SM875

To assess the compatibility of SM875 mode of action with the proposed PPI-FIT mechanism we first measured the levels of PrP mRNA expression at different compound concentrations by using real-time PCR. We found that treatment with SM875 did not decrease PrP mRNA in different cell lines, confirming the original hypothesis that a molecule targeting a folding intermediate should lower protein expression only at a post-translational level (figure 4.6A). Then, we decided to exclude the possibility that the molecule suppresses the levels of PrP by targeting its native state. First, we employed dynamic mass redistribution (DMR), a label-free technique that uses light to measure ligand-induced changes in the mass of a receptor covalently linked to the sensor. In contrast to the positive control (Fe^{3+}-TMPyP), SM875 (0.1–100 μM) showed no detectable affinity to human full-length (23–231) and mouse C-terminal (111–230) recombinant PrP (figure 4.6B). In order to further validate this conclusion in a cell system, we employed RK13 cells expressing mouse PrP in a doxycycline-inducible fashion[233]. In the first set of experiments, we switched on the expression of PrP with doxycycline, in the presence of SM875 or vehicle control (DMSO). Cells were then lysed and

analyzed by western blotting at different time points. In contrast to the typical size of full-length, diglycosylated PrP ($\sim$35 kDa) obtained in the control samples, SM875 induced the accumulation of a low molecular weight band ($\sim$20 kDa), previously described to correspond to a N-terminally cleaved PrP molecule formed by a lysosomal-dependent event[234]. Next, we directly tested the effect of the molecule on pre-synthesized, mature PrP. We induced the expression of PrP for 24 h, then removed the inducer, waited 4 h, treated the cells, and analyzed PrP levels at different times (5, 19, and 24 h). In this case, we found no difference between control and treated samples (figure 4.6C)[67].
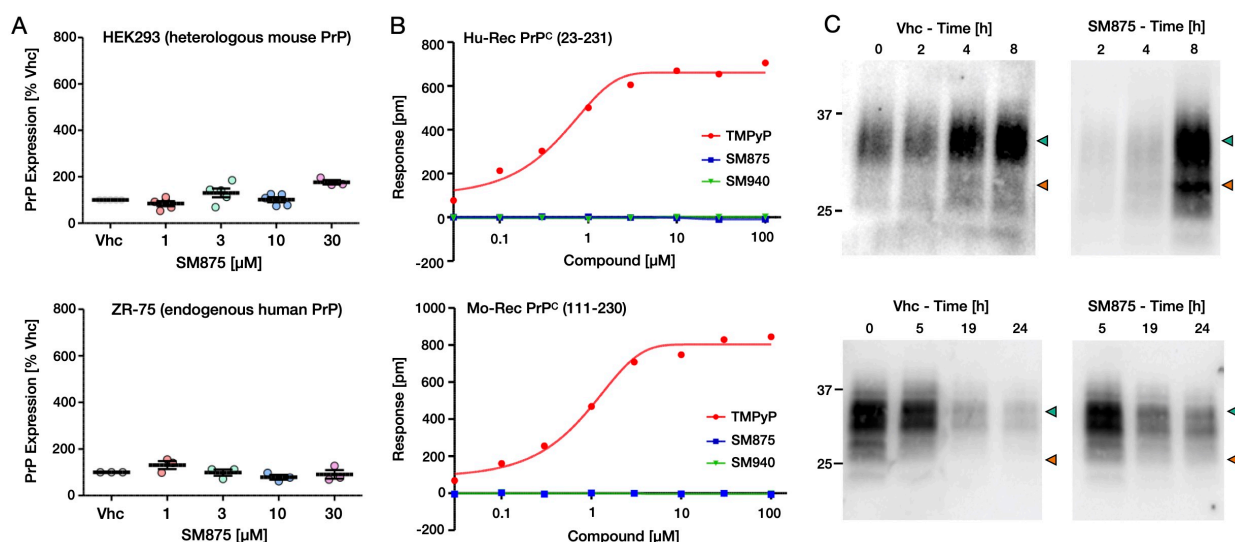
Figure 4.6: SM875 acts exclusively on the nascent PrP polypeptide. (A) The graphs show the levels of PrP mRNA upon treatment with SM875 in HEK293 and ZR-75 cells, as evaluated by RT-PCR. Relative quantification was normalized to mouse or human HPRT. Statistical analysis refer to the comparison with vehicle controls (*p < 0.05 by one-way ANOVA test). Courtesy of Michela Libergoli. (B) The SM875 binding affinity to PrP^C was assessed by using DMR. Different concentrations of SM875, SM940 or Fe^{3+}-TMPyP were added to label-free microplate well surfaces on which either human recombinant PrP (23–230) or mouse recombinant PrP (111–230) had previously been immobilized. All signals were fitted, when possible, to a sigmoidal function using a 4PL non-linear regression model. SM875 and SM940 showed no detectable binding for native PrP^C. Courtesy of Silvia Biggi. (C) In the upper panel; PrP expression was induced over 8 h, in the presence of SM875 (10 µM), or vehicle control, samples were collected at different time points and PrP signals were visualized by western blotting. In control cells, the level of full-length PrP (cyan arrowheads) increases in a time-dependent fashion. Conversely, a lower molecular weight band (orange arrowheads) is detected in SM875-treated cells. In the lower panel; PrP expression was induced for 24 h. Doxycycline was then removed, and after 4 h without inducer, the cells were exposed to SM875 or vehicle and then lysed and analyzed at different time points. In these conditions, normal PrP patterns appear in both compound-treated and Vhc-treated cells. Courtesy of Tania Massignan. Figure adapted from Spagnolli et al.[67] (cc)(i)

Collectively, these data show that SM875 acts only on nascent PrP molecules, and exerts no effects on the pre-synthesized PrP^C. This mechanism of action is compatible with our *in silico* predictions and the rationale underlying PPI-FIT. Additional experimental characterization allowed us to identify the autophagy–lysosomal pathway as a specific route for PrP degradation promoted by SM875 (supplementary figure 10)[67].

4.1.5 Biochemical Characterization of PrP-SM875 Interaction

To study the intrinsic flexibility of the C-terminal domain of PrP^C, we performed 21 μs of standard MD simulations at 310 K (37°C) starting from its native state (PDB 1QLX). Surprisingly, we were able to sample an ensemble of conformations highly similar to the previously identified folding intermediate (figure 4.7). This native-to-intermediate transition occurred only once and the life-time of the metastable conformer was relatively short (∼400 ns), compared to the entire length of the trajectories[67].
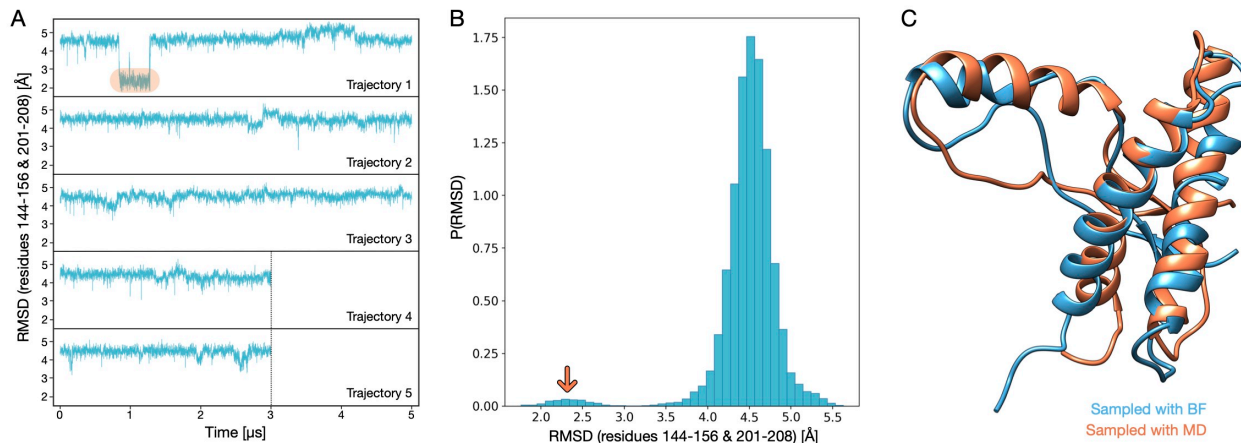

Figure 4.7: Plain MD simulations of PrP^C. (A) The C-terminal domain of PrP^C (residues 125-228, PDB 1QLX) was subjected to 21 μs of cumulative (3 x 5 μs + 2 x 3 μs) MD simulations at 310 K. The Cα-RMSD of the contact region between helix 1 and helix 3 (residues 144-156 and 201-208) was computed with respect to the structure of the PrP folding intermediate identified with BF. The transition from the native to this metastable state was observed in one trajectory (highlighted in orange). (B) Probability distribution of the RMSD computed on residues 144-156 and 201-208. The arrow indicates the population of PrP conformations resembling the folding intermediate. (C) Superimposition of the PrP-folding intermediate identified by the BF approach (blue) and its more similar conformation reached from the native state by plain-MD (orange), Cα-RMSD computed on residues 144-156 & 201-208 = 1.76 Å. Figure adapted from Spagnolli et al.[67] ⓒ①

Despite the relatively short lifetime of the intermediate state observed by standard MD simulations, its sampling indicated that this conformer can be explored due to stochastic fluctuations from the native structure. This observation inspired us to design an experimental scheme to characterize the interaction of SM875 with the PrP folding intermediate by exploiting a partial thermal denaturation. In particular, we attempted to co-crystallize the temperature-induced, semi-denatured PrP in complex with the compound. Recombinant mouse PrP (800 μM) was heated to 45°C prior to the addition of SM875 (2 mM) or control DMSO, and then slowly cooled to 20°C. We observed a significant precipitation (∼40%, measured with UV-absorbance) of the protein as soon as SM875 was added to the solution. Conversely, no detectable precipitation occurred in the control sample. In the subsequent crystallization process the remaining soluble PrP molecules yielded "thin needles"-like crystals, appearing after 2–4 days. Such crystals were obtained irrespectively of whether the protein was incubated with SM875 or DMSO. Crystals were diffracting weakly and anisotropically to 3.7 Å in the best directions, allowing the determination of orthorhombic crystal system and unit cell dimensions (a = 36.1 Å, b = 51.8 Å, c = 55.9 Å), which are highly similar to those reported for apo

human PrP in PDB 3HAK (a = 32.5 Å, b = 49.1 Å, c = 56.9 Å). These data suggest that only the native PrP molecules that do not bind to SM875 remain in solution, allowing crystallization, while those interacting with the compound rapidly aggregate, hampering crystallization.

To further characterize the PrP-induced precipitation by SM875, we performed a detergent insolubility assay to detect aggregates of mouse recombinant PrP (111–230) in the presence or absence of SM875 at different temperatures. The concentrations of the protein (0.5 μM) and compound (10 μM) were substantially lower in this assay with respect to those employed for crystallization. We found that SM875 and SM940 induced the aggregation of recombinant PrP in a temperature-dependent fashion (Figure 4.8). Conversely, no precipitation was detected in SM935 (a compound with no PrP suppressing activity) and vehicle-treated samples. These data suggest that SM875 targets a thermally induced PrP population, promoting its precipitation. This effect could reflect the presence of exposed hydrophobic patches on the folding intermediate, acting as aggregation surfaces when the lifetime of this conformer is increased by stabilization with a ligand[67].
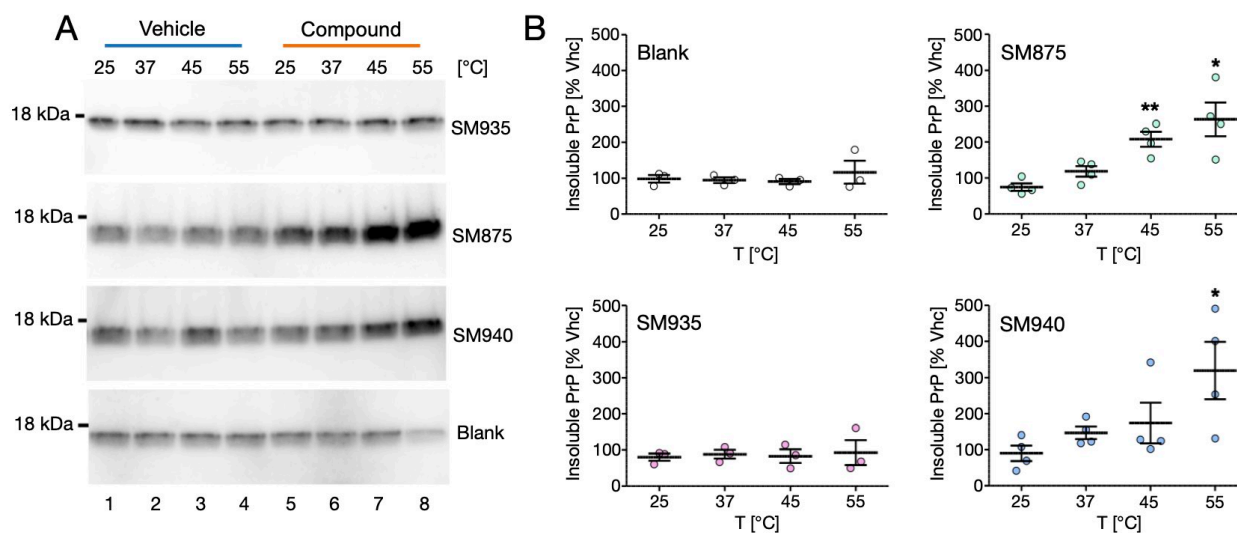
Figure 4.8: Temperature-dependent SM875-induced aggregation of PrP. (A) A solution of recombinant mouse PrP (111–230) in detergent buffer (PrP concentration = 0.5 μM) was placed at different temperatures and incubated for 1 h with either vehicle (lanes 1–4) or with the test items (lanes 5–8), namely: assay buffer (blank), SM875, SM940, or SM935 (10 μM). After incubation, samples were subjected to ultracentrifugation, and the resulting detergent-insoluble pellet was analyzed by western blotting. (B) Graphs show the densitometric quantification of recombinant PrP bands from independent replicates. Each signal was normalized and expressed as the percentage of the corresponding Vhc-treated sample (*p < 0.05, **p < 0.01, by one-way ANOVA test). Courtesy of Paolo Brunelli. Figure adapted from Spagnolli et al.[67] ©①

Finally, to gain structural insights regarding the aggregated PrP species induced by SM875 we performed field emission scanning electron microscopy (FESEM). This analysis revealed the presence of amorphous structures appearing as a collection of dots showing different sizes and shapes (∼10 nm diameter) as well as much larger clumps. Sonication did not affect the morphology of these aggregates that only resulted in the breakage of the larger structures (figure 4.9). Despite being at low resolution, these results suggest that binding to SM875 induces the formation of aggregated PrP species that are off-pathway of the folding process[67].
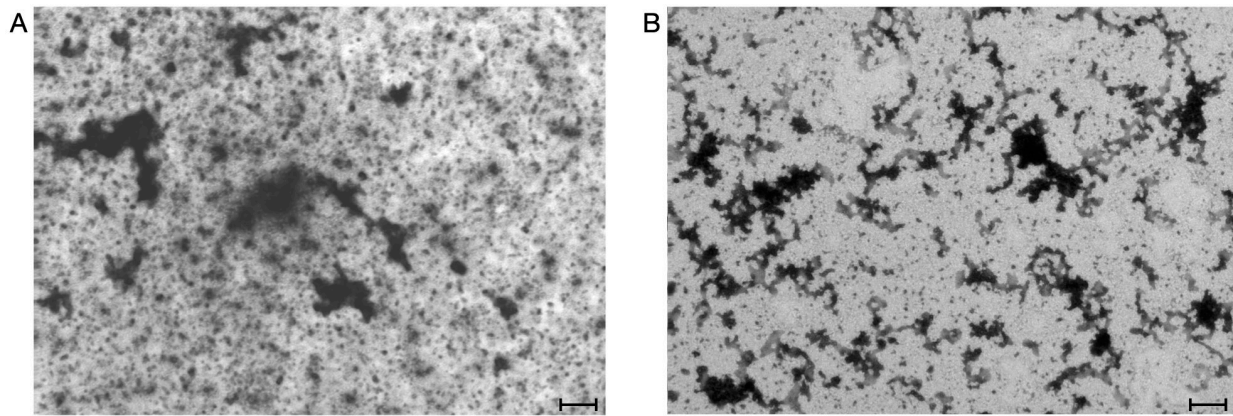
Figure 4.9: FESEM characterization of the PrP aggregates induced by SM875. Electron micrographs show aggregates of human recombinant PrP (23-231) induced upon adding compound SM875 and subjecting to mild thermal unfolding (55°C). (A) SM875 induced the formation of dots-like clumps of stained material of different sizes and shapes ($\sim$10 nm diameter) as well as much larger amorphous aggregates. (B) Sonication did not affect the morphology of these species, leading only to the breakage of the larger structures. Scale bars: 400 nm. Analysis performed in collaboration with the Prion-Lab of Jesús R. Requena. Figure adapted from Spagnolli et al.[67] ©①

4.1.6 Therapeutic Potential of SM875

One of the most solid concepts in prion research is that the suppression of PrP levels impairs prion propagation. Therefore, we tested the ability of SM875 to inhibit the replication of the Rocky Mountain Laboratories (RML) prion strain in persistently infected L929 mouse fibroblasts[235]. We found that SM875 inhibits prion replication and decreases PrP^{Sc} loads similarly to the anti-prion molecule Fe^{3+}-TMPyP (figure 4.10).
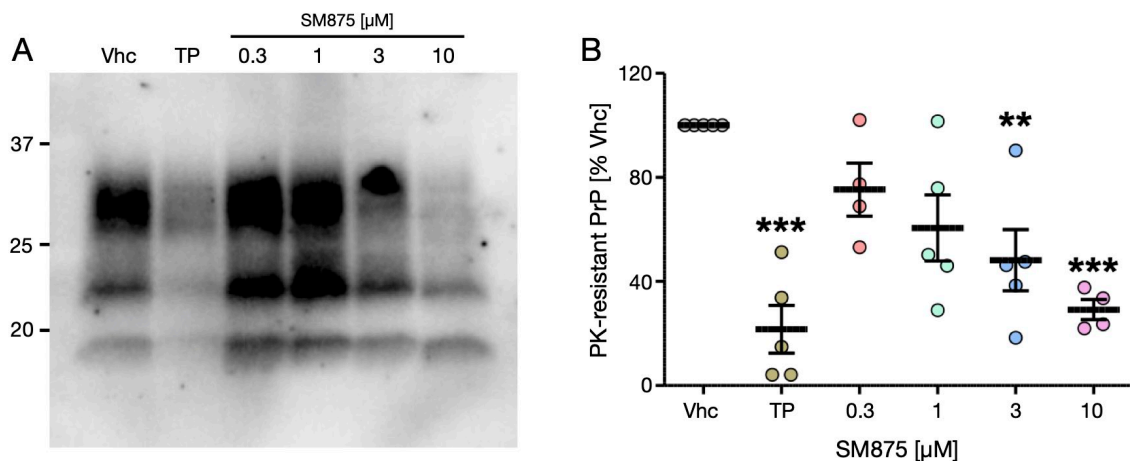
Figure 4.10: Inhibition of prion replication by SM875 in L929 mouse fibroblasts. (A) Permanently infected L929 fibroblast were exposed to SM875, the anti-prion compound Fe^{3+}-TMPyP (TP, 10 μM) or vehicle (0.1% DMSO) for 48 h. PrP^{Sc} loads were estimated by treating cell lysates with PK and analyzing the resistant material by western blotting. SM875 inhibits prion replication in a dose-dependent fashion, with an effect comparable to that of tetrapyrrole. (B) Densitometric quantification of all PK-resistant PrP bands from independent replicates. Signals were normalized on the corresponding PK-untreated lane and expressed as the percentage of vehicle (Vhc)-treated controls (**$p < 0.01$, *** $p < 0.005$, by one-way ANOVA test). Courtesy of Tania Massignan. Figure from Spagnolli et al.[67] ©①

4.2 Chemical Optimization of SM875

Despite the promising anti-prion effects exerted by SM875 in cell-based assays, this compound is still suboptimal to be considered a valid therapeutic agent for prion diseases. In particular, we measured the IC_{50} of SM875 in the low micromolar range, a remarkable potency for a hit compound, but not ideal for a molecule entering pre-clinical trials. Furthermore, we detected toxic effects in cells treated with SM875. While we observed that, as opposed to the efficacy, the SM875 induced toxicity is cell-dependent (supplementary figure 11), the therapeutic window of this molecule can be substantially improved. For this reason, we decided to perform a structure-activity-relationship (SAR) study on SM875. This type of analysis enables to correlate the chemical structure of a compound to its biological activity, thus helping to develop new analogs characterized by a higher potency and less cytotoxicity. To this end, we designed and performed a novel synthetic sequence for SM875 and fully characterized its enantiomeric forms. Then, we synthesized a set of 29 analogs which were preliminarily tested in a cell-based screening. This work represents the initial phase of the process of SM875 chemical optimization, aimed at developing a compound with the ideal features to be moved to the pre-clinical stage.

4.2.1 Synthesis and Structural Characterization of SM875

The target product SM875 was obtained according to a two-steps synthetic strategy (figure 4.11), starting from the commercially available reagents: 4-(bromophenyl)-hydrazine-HCl (which was pre-treated with a saturated $NaHCO_3$ aqueous solution to neutralize the hydrochloride salt), ethyl-2-cyano-3-ethoxyacrylate, 4-hydroxy-3-methoxybenzaldehyde and 2,2-dimethyl-1,3-dioxane-4,6-dione[67].
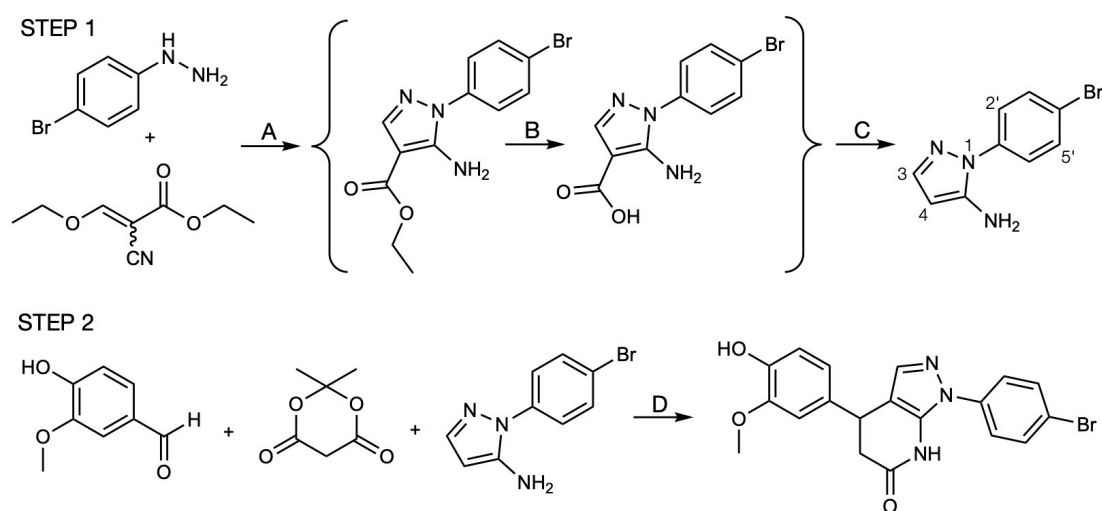
Figure 4.11: Organic synthesis of SM875. Reagents and conditions: (A) Reaction of 4-(bromophenyl)-hydrazine with ethyl-2-cyano-3-ethoxyacrylate, 2 h reflux in ethanol. (B) Basic hydrolysis of the ethyl carboxilate group; 1:1 (methanol)/(aqueous 2M NaOH), reflux 1 h. (C) Decarboxylation performed on the dried reaction mixture at 180 °C for 10 min. Yield of 1-(4-bromophenyl)-1H-pyrazol-5-amine; 61%. Arbitrary numbering is used for [^{1}H]-NMR assignment: [δ 7.58 (d, J 8.7 Hz, 2H: H-3' and H-5'), δ 7.47(d, J 8.7 Hz, 2H: H-2' and H-6'), δ 7.41(s, 1H: H-3), δ 5.62 (s, 1H: H-4)]. ESI-MS(+): m/z 239.9. Compounds between brackets have not been isolated and characterized. (D) Three-component reaction involving 4-hydroxy-3-methoxybenzaldehyde, 2,2-dimethyl-1,3-dioxane-4,6-dione and the previously synthesized precursor, ethanol reflux 2.5 h. Yield of SM875: 25% after HPLC purification. Figure adapted from Spagnolli et al.[67] ⓒⓘ

The initial step consists in the preparation of the precursor molecule 1-(4-bromophenyl)-1H-pyrazol-5-amine by performing three sequential reactions (figure 4.11-A,B,C)[236]. First, a magnetically stirred solution of 4-(bromophenyl)-hydrazine, and ethyl-2-cyano-3-ethoxyacrylate (1:1 molar ratio) was refluxed for 2 h in ethanol. Then, the mixture was concentrated *in vacuo*, suspended in 1:1 (methanol)/(2 M NaOH aqueous solution) and refluxed for 1 h. The mixture was neutralized with 1 M HCl aqueous solution and concentrated *in vacuo*. The residue was heated at 180 °C for 10 min, suspended in ethanol after cooling and stored overnight at 4 °C. The supernatant was filtered and concentrated to obtain a residue which was stirred in the presence of a NaHCO$_3$ solution. The 1-(4-bromophenyl)-1H-pyrazol-5-amine was finally obtained by extraction with ethyl acetate, followed by the treatment with anhydrous Na$_2$SO$_4$. The successful synthesis of this precursor was verified by ^{1}H-NMR and ESI-MS analysis. In the last reaction step, 4-hydroxy-3-methoxybenzaldehyde, 2,2-dimethyl-1,3-dioxane-4,6-dione and 1-(4-bromo-phenyl)-1H-pyrazol-5-amine (5:6:6) in ethanol were subjected to reflux for 2.5 h (figure 4.11-D). The reaction mixture was then cooled to room temperature and dried *in vacuo*. The raw material was purified by silica preparative thin layer chromatography (PLC) and the collected band was used for NMR, MS and FTIR analysis to verify the correct structure of SM875 (figure 4.12). NMR signals assignment was confirmed by heteronuclear multiple bond correlation (HMBC, Table 4.1). Subsequently, we performed preparative high-performance liquid chromatography (HPLC) to obtain the target product for biological testing[67].
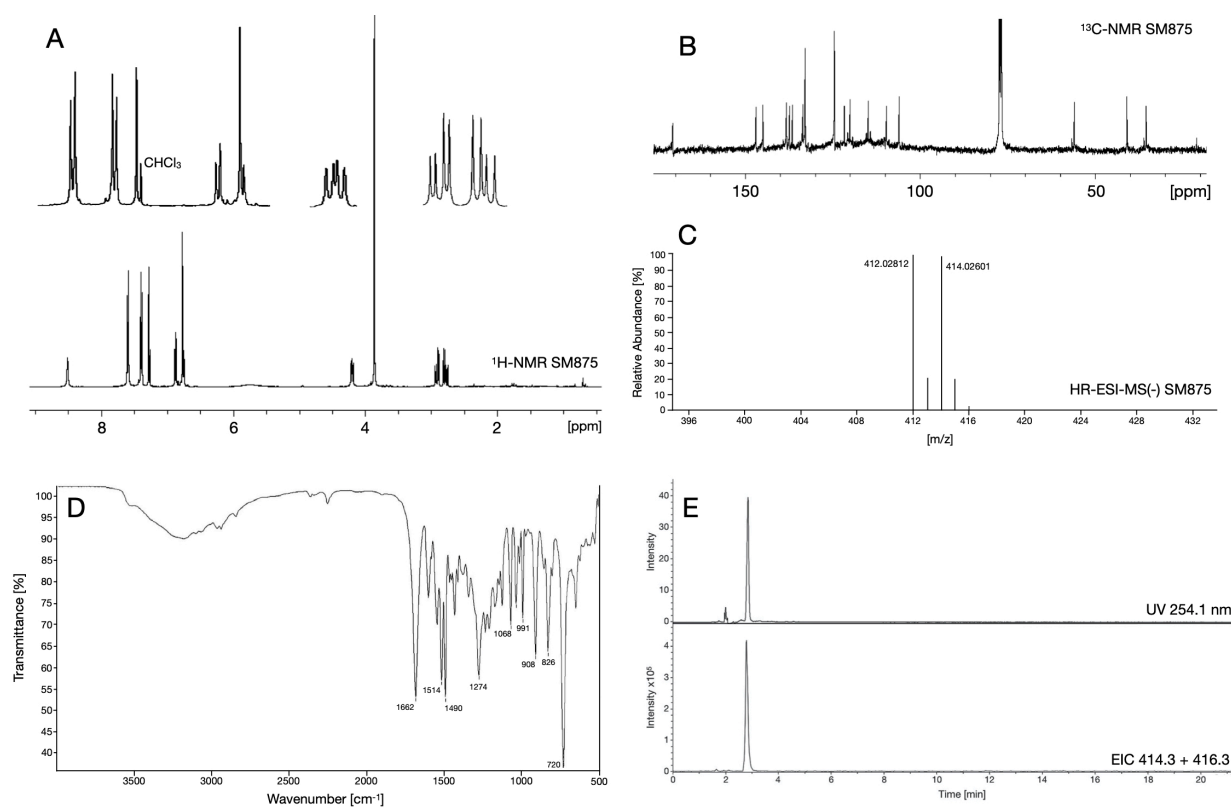
Figure 4.12: Structural characterization of SM875. (A) ^{1}H-NMR spectrum of SM875 (400 MHz, CDCl$_3$). (B) ^{13}C-NMR spectrum of SM875 (100 MHz, CDCl$_3$). (C) High resolution ESI-MS in negative ion mode, measurement of SM875 by direct infusion. (D) FTIR spectrum of SM875. (E) Upper panel: UV HPLC-chromatogram at λ = 254 nm. Lower panel: MS chromatogram by extracted-ion current of the [M+H]$^+$ peaks at m/z 414 and 416 (1:1) corresponding to the expected major isotopomers. Figure adapted from Spagnolli et al.[67] ⓒ①
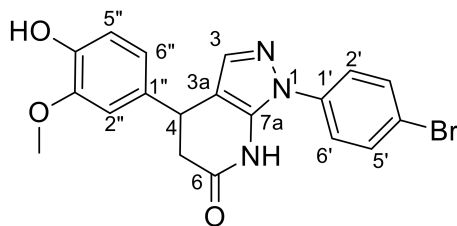
Position	δ_H [ppm] (J [Hz])	δ_C [ppm]	HMBC H $\to$ C
3	7.29 s	138.2	H2 $\to$ C3a
3a	-	105.9	-
4	4.21 dd (9.9, 6.4)	35.5	H4 $\to$ C3a, C5, C6, C7a, C1", C2"
5	2.93 dd (16.2, 6.4) 2.80 dd (16.2, 9.9)	40.9	H5 $\to$ C3a, C4, C6, C1"
6	-	170.7	-
7	8.52 s (NH)	-	H7 $\to$ C7a
7a	-	136.5	-
1'	-	137.3	-
2', 6'	7.39 d (8.6)	124.5	H2'/6' $\to$ C1', C3'/5'
3', 5'	7.62 d (8.6)	312.9	H3'/5' $\to$ C4'
4'	-	121.6	-
1"	-	133.5	-
2"	6.77 s	109.6	H2" $\to$ C4, C4"
3"	-	146.9	-
4"	-	145.0	-
5"	6.88 d (8.8)	114.7	H5" $\to$ C2", C4"
6"	6.76 m	120.0	H6" $\to$ C3"
OCH$_3$	3.87 s	55.9	OCH3 $\to$ C3"
OH	5.72 vbr s	-	-

Table 4.1: NMR data of SM875: ^{1}H, ^{13}C and HMBC. Resonances are assigned according to the carbon numbering (arbitrary) reported on the first column and shown on the chemical structure. In the second column the ^{1}H-NMR resonances (δ and J) are reported, in the third column the ^{13}C chemical shifts, and in the fourth column the most relevant long-range heteronuclear correlations (obtained by 2D-HMBC). Table adapted from Spagnolli et al.[67] ⓒⓘ

The main drawback of the developed synthetic strategy is that it yields SM875 as a racemate. The biological effect exerted by a small molecule can strongly depend on its stereochemistry, indeed two enantiomers of the same compound can feature completely different activity and toxicity. For this reason, we decided to purify the two individual SM875 species and test them on cell-based assays. To separate the two enantiomers we employed a Chiralpak HPLC analytical column, eluting a pure sample of SM875 with a solution of hexane, isopropanol, and dichloromethane (17:8:2). After separation, a small aliquot of each compound was re-injected individually, to assess the enantiomeric ratio. This analysis revealed the absence of significant cross-contamination peaks ($e_r > 97\%$ for both enantiomers, figure 4.13A). We then employed CD spectroscopy to verify the opposite configuration of the separated species. As expected, we obtained two mirror-image curves, reflecting the oppositive behavior of the compounds in absorbing the left- and right-handed circularly polarized light (figure 4.13B). To assign the absolute configuration of the purified enantiomers we compared preliminary, computationally predicted CD spectra by time-dependent density functional theory (TD-DFT) to those obtained experimentally (figure 4.13C).

This enabled us to identify the first and the second HPLC-eluted samples as the S and R enantiomers, respectively. To support this conclusion, we performed polarimetry analysis of the separated species, obtaining a value of $[\alpha]_{577} = 54 \pm 4$ deg mL g^{-1} dm^{-1} for the S form and $[\alpha]_{577} = -52 \pm 8$ deg mL g^{-1} dm^{-1} for the R form. The latter was compared to the theoretical value of -70 deg mL g^{-1} dm^{-1} predicted by DFT calculation, which corroborates the CD-based assignment.
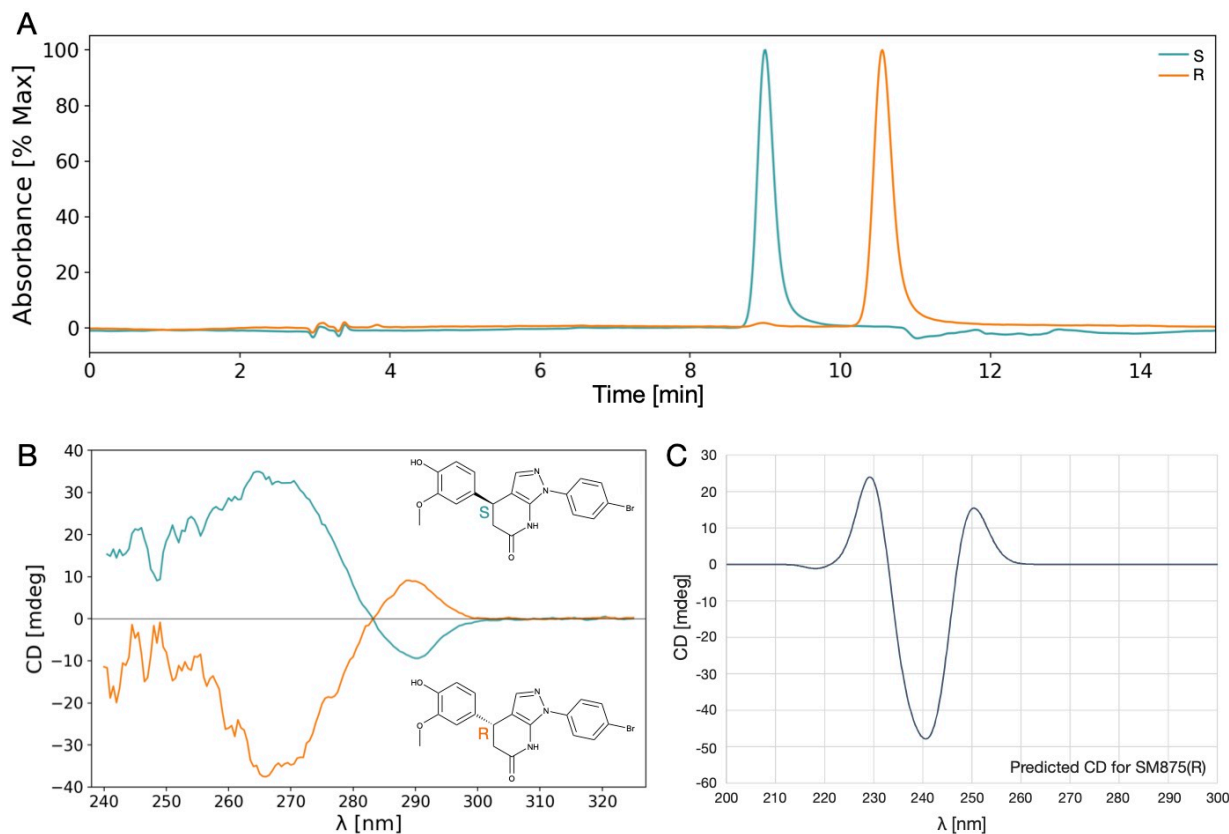
Figure 4.13: Separation of the SM875 enantiomers and assignment of absolute configuration. (A) Overlay of the chromatograms of each purified enantiomer reinjected after separation. (B) CD spectra overlay of the separated samples. To assign the absolute configurations, these graphs were compared to the DFT-predicted CD spectra of the R-enantiomer. The calculated spectrum for the R configuration is shown in (C, courtesy of Petri Tähtinen). This curve features a remarkable blue-shift compared to the experimental one, however, it is typical that in theoretically calculated spectra the maxima and minima are at smaller wavelengths in comparison to experimental observations. Besides this discrepancy, this result supports that the second eluted peak displays an R configuration. SM875 enantiomers are depicted in panel (B).

Finally, we tested the activity and toxicity of the SM875 enantiomers in HEK293 cells. We employed western blotting to detect the suppression of PrP levels and MTT-assay to evaluate the cell viability (figure 4.14). The results indicated that the (R)-SM875 is the solely responsible for both the activity and toxicity, while the S isomer is completely inactive. Interestingly, our computational predictions identified the R form as the most potent, with an estimated affinity of 0.4 µM $< K_i <$ 40 µM, while the S was predicted to be active at higher concentrations (2.2 µM $< K_i <$ 224 µM).

This study provides important information for further structural studies aimed at identifying the ligand-target interactions. However, in a preliminary SAR study the separation of the two enantiomers might not be worth the additional purification step since applying this process on tens of compounds becomes significantly time-consuming.
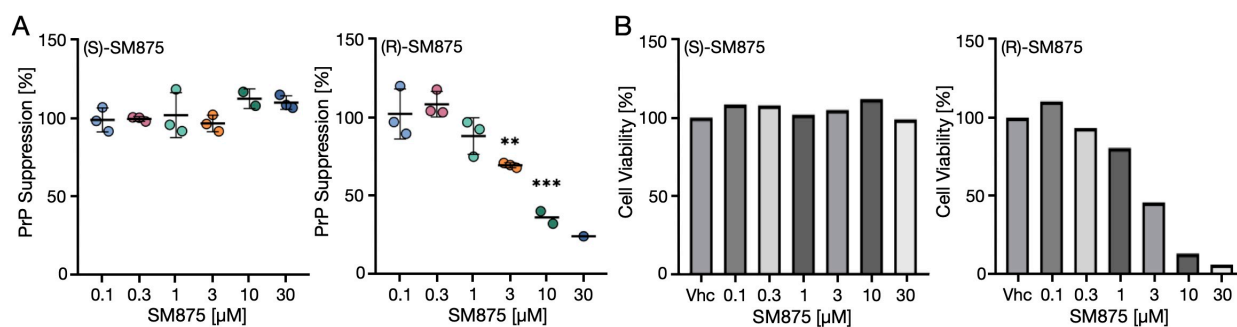
Figure 4.14: Cell-based testing of (S) and (R) SM875. (A) Western blotting was performed to detect the levels of PrP after treatment with different concentrations of the S (left panel) or R (right panel) SM875 (HEK293 cells). The image shows the densitometric quantification of independent biological replicates. Each signal was normalized on the total protein lane and expressed as the percentage of the level in vehicle-treated (DMSO) controls. The (R)-SM875 shows an IC_{50} of ~ 5 µM, while no PrP suppression is observed after treatment with (S)-SM875. (B) Cell viability measured with MTT-assay. The R enantiomer shows toxic effects in the range of its active concentrations, while cell viability was not affected by (S)-SM875 treatment (**$p < 0.01$, ***$p < 0.005$, by one-way ANOVA test). Courtesy of Valerio Bonaldo.

4.2.2 Synthesis and Cell-Based Testing of SM875 Analogues

The ultimate goal of this work is to obtain an analog of SM875 with promising features for pre-clinical testing. To this end, we began a SAR study to investigate how specific chemical modifications can alter the activity and toxicity of the compound. In this initial round of diversification we decided not to rely on the predicted complex between the ligand and the PrP intermediate to select the target analogs. Indeed, such an approach would require a highly-reliable characterization of the intermediate state bound to SM875 with experimental techniques. Furthermore, in the preliminary screening, identifying inactive molecules is almost as important as finding more potent compounds, since this allows to spot specific positions and functional groups responsible for the biological activity. Therefore, we selected the target compounds based on synthetic accessibility, relying on a set of commercially available substituted phenyl-hydrazines and aryl-aldehydes. The previously developed synthesis scheme was used to obtain analogs 1-24 (figure 4.15).

A1: R1 = H; R2 = H; R3 = O-CH3; R4 = OH; R5 = H
A2: R1 = p-F; R2 = H; R3 = O-CH3; R4 = OH; R5 = H
A3: R1 = p-Cl; R2 = H; R3 = O-CH3; R4 = OH; R5 = H
A4: R1 = p-I; R2 = H; R3 = O-CH3; R4 = OH; R5 = H
A5: R1 = p-CH3; R2 = H; R3 = O-CH3; R4 = OH; R5 = H
A6: R1 = p-CF3; R2 = H; R3 = O-CH3; R4 = OH; R5 = H
A7: R1 = m-Br; R2 = H; R3 = O-CH3; R4 = OH; R5 = H
A8: R1 = o-Br; R2 = H; R3 = O-CH3; R4 = OH; R5 = H

A9: R1 = o-F; R2 = H; R3 = O-CH3; R4 = OH; R5 = H
A10: R1 = p-F; R2 = o-F; R3 = O-CH3; R4 = OH; R5 = H
A11: R1 = p-Br; R2 = H; R3 = H; R4 = H; R5 = H
A12: R1 = p-Br; R2 = H; R3 = H; R4 = OH; R5 = H
A13: R1 = p-Br; R2 = H; R3 = H; R4 = O-Ph; R5 = H
A14: R1 = p-Br; R2 = H; R3 = OH; R4 = O-CH3; R5 = H
A15: R1 = p-Br; R2 = H; R3 = O-Et; R4 = O-CH3; R5 = H
A16: R1 = p-Br; R2 = H; R3-R4 = 1,4-dioxane; R5 = H

A17: R1 = p-Br; R2 = H; R3 = O-CH3; R4 = benzyloxy; R5 = H
A18: R1 = p-Br; R2 = H; R3 = O-CH3; R4 = O-CH3; R5 = O-CH3
A19: R1 = m-Br; R2 = H; R3 = OH; R4 = O-CH3; R5 = H
A20: R1 = o-F; R2 = H; R3 = OH; R4 = O-CH3; R5 = H
A21: R1 = p-F; R2 = o-F; R3 = OH; R4 = O-CH3; R5 = H
A22: R1 = p-F; R2 = m-Cl; R3 = OH; R4 = O-CH3; R5 = H
A23: R1 = p-I; R2 = H; R3 = OH; R4 = O-CH3; R5 = H
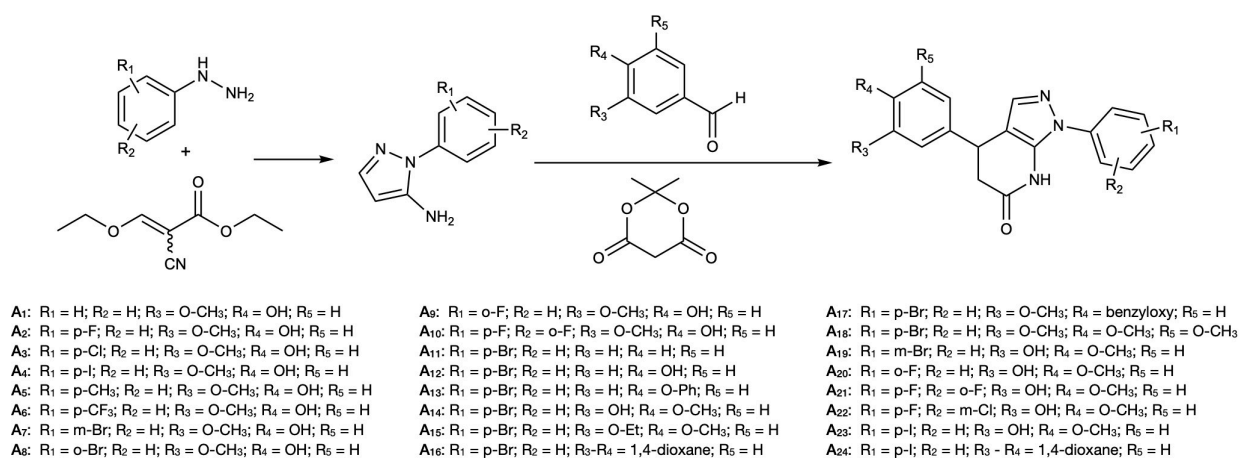A24: R1 = p-I; R2 = H; R3 - R4 = 1,4-dioxane; R5 = H

Figure 4.15: Synthesis of SM875 analogues. Reaction conditions identical to those reported in figure 4.11. This scheme was employed to synthesize 24 analogs of SM875, starting from commercially available substituted phenyl-hydrazines (groups R_1 and R_2) and substituted aryl-aldehydes (groups R_3, R_4, R_5).

75

We then modified SM875 and two of its analogs to obtain methyl-derivatives. This was achieved by reacting each of these compounds with iodomethane in a solution of K_2CO_3 (figure 4.16).
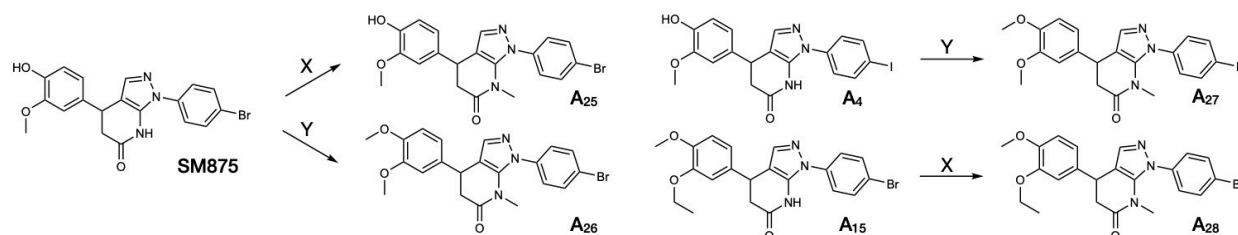

Figure 4.16: Synthesis of methyl-derivatives. Four methyl-derivatives were synthesized: two starting from SM875, one starting from A_{15} and one starting from A_4. Reaction conditions: (X) = CH_3I, K_2CO_3, 24h. (Y) = CH_3I, K_2CO_3, 48h. Method from Selvaraju et al.[237]

The last analog of this series was obtained by synthesizing the modified precursor 1-(4-bromophenyl)-3-methyl-1H-pyrazol-5-amine that was used instead of the 1-(4-bromophenyl)-1H-pyrazol-5-amine to perform the three-component reaction, as described in figure 4.17.
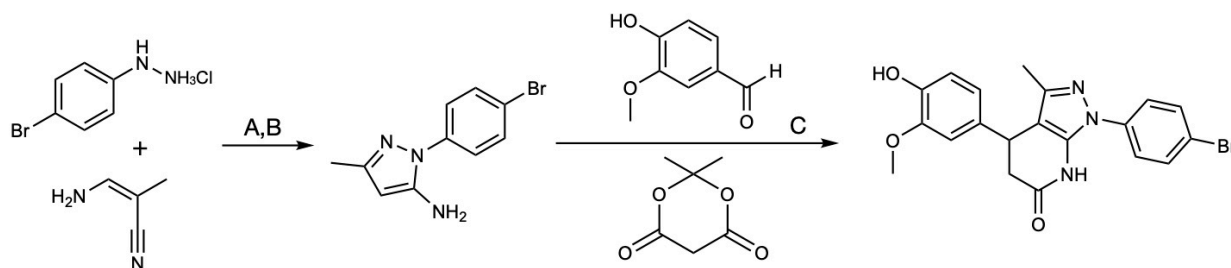
Figure 4.17: Synthesis of A_{29}. Reagents and conditions: (A) HCl 2M aqueous solution, 100°C in a microwave reactor for 1 h. (B) Neutralization with NaOH solution and extraction in dichloromethane. (C) 2.5 h reflux or alternatively 110°C in a microwave reactor for 1 h in ethanol.

An important characteristic of the synthesized set of SM875 analogs is that it comprises molecules carrying modifications in almost any possible position of the original compound. To assess the effect of these variations, we measured the activity of each analog in suppressing PrP levels on HEK293 cells (a summary of the obtained analogs and the outcome of the cellular testing is displayed in figure 4.18A). We observed that the introduction of modifications in SM875 can alter the activity in both directions. This observation allowed us to identify which groups cannot be altered to retain the compound activity. In particular, the absence of a substituent in position *para*-R_1, and the methylation of the lactam nitrogen are detrimental for the compound potency. Conversely, modifications at positions R_3 and R_4 are more tolerated. Importantly, in most of the cases, we observed a strong coupling between activity and toxicity (figure 4.18B). However, it should be noted that the cellular model employed in this screening is the most sensitive among the ones we tested, in terms of cell viability, to the SM875 treatment (supplementary figure 11). For this reason, we started to screen the analogs that in this assay showed similar or higher activity with respect to SM875 in a different cellular model. Preliminary results in ZR-75 cells showed that A_4 might represent a good candidate for further optimization since in this cell line it displays an IC_{50} in the high nanomolar range and an $LD_{50} > 50$ µM (Figure 4.18C).
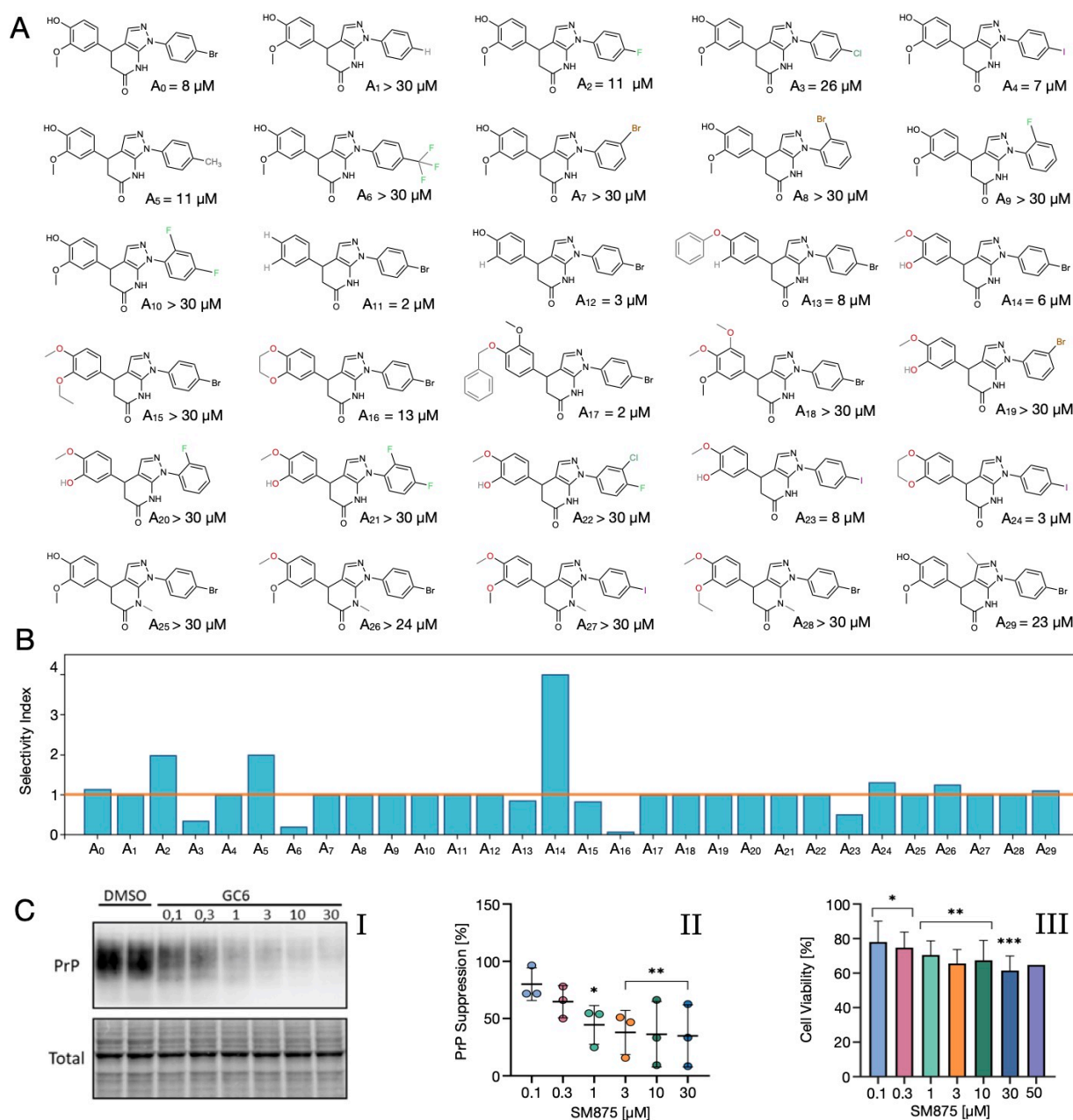
Figure 4.18: Cell-based screening of SM875 analogues. The molecular structures of the synthesized compounds as well as the related IC_{50} (estimated on cell-based assays) are reported in panel (A). The selectivity index of each compound, computed as the ratio of LD_{50} to IC_{50}, is reported in (B). The orange line denotes a selectivity index of 1. Preliminary results of activity and toxicity of the A_4 analog in ZR-75 cells are shown in (C, courtesy of Valerio Bonaldo). Panel (I) shows the western blotting of a single replicate to measure the cellular PrP loads at different concentrations of the compound A_4. The densitometric quantification of three independent replicates is shown in (II). The results of cell viability assays are reported in (III). *p < 0.05, **p < 0.01, *** p < 0.005, by one-way ANOVA test.

The main drawback of phenotype-based screening is that it does not provide direct information regarding the ligand-target complex. Indeed, in this assay, both activity and toxicity are affected by different factors that might be unrelated to the interactions with the target, such as the membrane permeability and the compound stability in the cellular environment. Despite the limitations of this approach, this study lays the foundation for further chemical optimization of SM875.

4.3 Conclusions & Future Perspective

4.3.1 PPI-FIT for Targeting Prion Diseases

We relied on advanced computational techniques to test a novel approach for selectively decreasing the level of target proteins, which we named PPI- FIT. In this method, druggable pockets appearing in intermediate states explored along the folding pathway of a protein are used as targets for virtual screening to identify small ligands for such regions. The underlying rationale is that stabilizing a folding intermediate of a protein could promote its degradation by the cellular quality control machinery. The application of this technology to PrP led to the discovery of four different chemical scaffolds capable of selectively suppressing the levels of PrP. Extensive experimental characterization of one of these compounds, SM875, provided strong support for the notion that targeting folding intermediates could represent a strategy to suppress protein levels. The demonstration that protein loads could be pharmacologically modulated by targeting a folding intermediate would ultimately require to structurally characterize the interactions between the identified ligands and the predicted metastable conformer. Unfortunately, available high-resolution techniques (i.e. NMR or X-ray crystallography) can only be applied to stable molecular species, while folding intermediates are highly dynamic and transient by definition. Despite the intrinsic approximations of all *in silico* techniques, our approach allowed us to overcome the spatiotemporal resolution limits, enabling to define the structure of a PrP folding intermediate at an atomistic level of resolution. Importantly, such conformation was also explored by standard MD simulations starting from native PrP^C, thus excluding possible artifacts resulting from the approximations introduced by the BF approach. The structural information regarding a druggable site exclusively present on the folding intermediate was exploited in a virtual screening campaign aimed at identifying small organic compounds for such pocket. Then, in light of the previously mentioned experimental limits, we performed an extensive in vitro and cell-based validation for the PPI-FIT approach. First, we identified four molecules, all capable of selectively lowering the levels of PrP. Next, we found that the most potent of the positive hits, SM875, reduces PrP loads in different cell lines, without decreasing the levels of PrP mRNA. Our data also indicate that SM875 can only act on nascent PrP molecules and does not bind native PrP. Finally, by trying to co-crystallize the complex between SM875 and the PrP-folding intermediate, we found that this compound induces the precipitation of PrP, likely by interacting with partially unfolded conformers appearing when the sample is subjected to temperatures higher than 25°C. Collectively, although we have not formally demonstrated the interaction of SM875 with its computationally-predicted druggable site, our experimental data strongly support the notion that this compound exerts its activity by targeting a folding intermediate of PrP (figure 4.19).

Prion diseases represented an ideal ground for testing the PPI-FIT approach, since compelling evidence indicates that suppressing the expression of PrP completely inhibits prion replication and toxicity. A compound like SM875 capable of promoting the degradation of PrP could be a suitable candidate to tackle prion diseases. Our data show that in prion-infected cells, the PrP-lowering activity of SM875 produces a strong inhibition of prion replication, comparable to that of the potent anti-prion compound Fe^{3+}-TMPyP. Supported by these encouraging results we decided to pursue a SAR study on SM875 with the aim of developing a candidate suitable for preclinical testing[67].
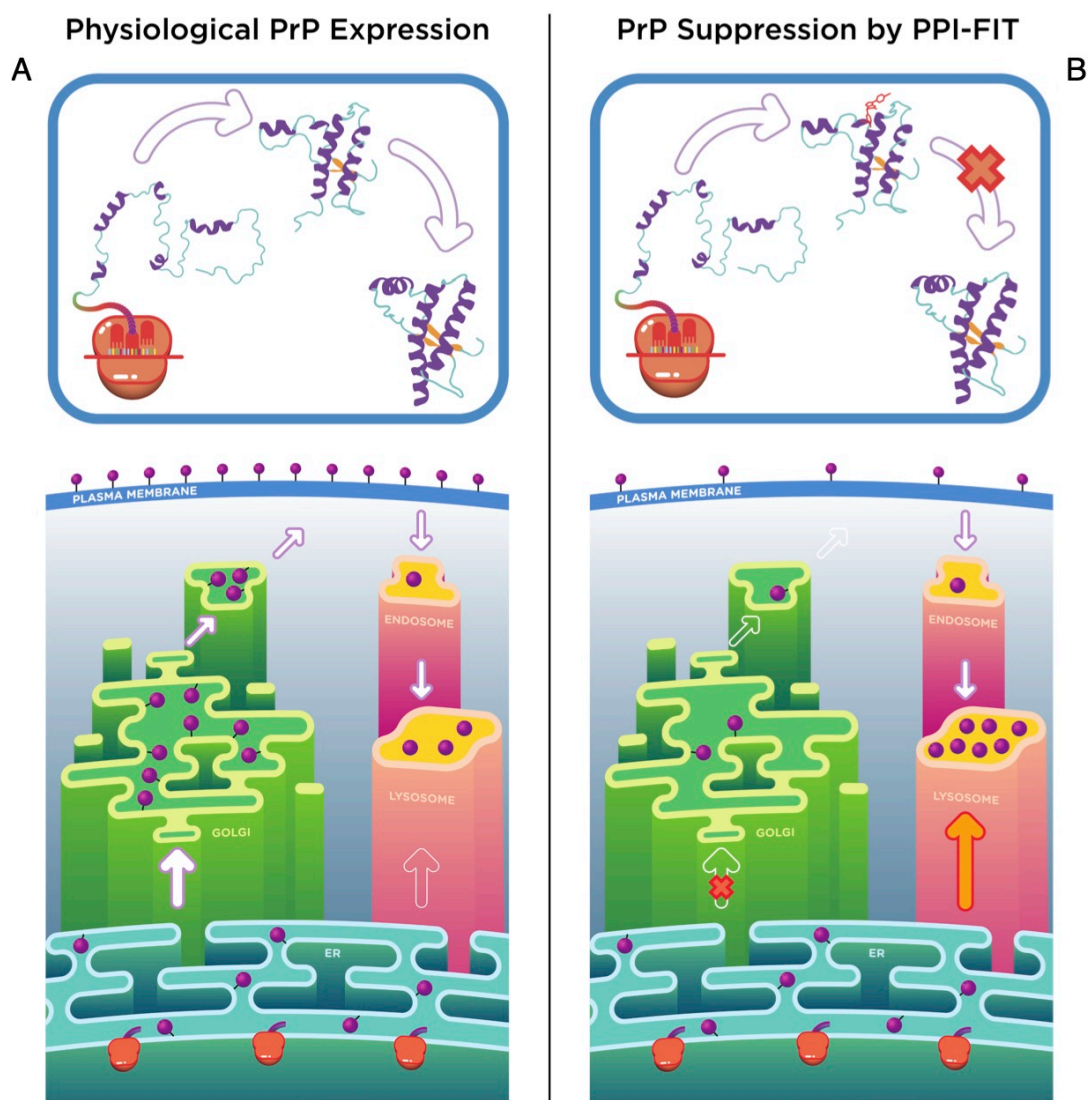
Figure 4.19: Model of PrP suppression by PPI-FIT. The schematics highlight PrP folding in the presence (A) or absence (B) of a small molecule targeting the PrP intermediate. (A) PrP polypeptide is synthesized into the lumen of the ER, once properly folded it traffics to the Golgi apparatus, and then delivered to the cell surface. From the plasma membrane, PrP molecules could enter into the endosomal recycling pathways, and eventually be degraded by the lysosomes. (B) In the PPI-FIT method, a small molecule interferes with the PrP folding pathway, generating unproperly folded species. These conformers are recognized by the protein quality control and re-routed to the lysosomes, leading to a decrease of PrP^C at the cellular surface. Figure adapted from Spagnolli et al.[67] ©①

To this end, we first performed a full structural characterization of this compound and its enantiomers, and then we synthesized 29 analogs which were tested on cell-based assays in HEK293. This first round of SAR study provided us important information regarding which positions of the chemical scaffold of SM875 can be modified without compromising its activity. Furthermore, preliminary experiments on a different cell line identified one of the synthesized analogs as a promising molecule, showing potency in the high-nanomolar range of concentrations. Ultimately, additional experiments such as the scrapie-cell assay and the evaluation of physicochemical properties of the compounds will be required to identify the ideal candidates for preclinical testing.

4.3.2 PPI-FIT Beyond Prion Diseases

The PPI-FIT approach relies on the cellular quality control to promote the degradation of the target protein. Such an effect is predicted to be achieved by targeting the folding pathway of a polypeptide and it would not be obtained by possible binding events occurring with the same intermediate generated by stochastic fluctuations from the native state. We anticipate at least two important limitations that are specific for the applicability of the PPI-FIT method to other proteins. First, the requirement of a high-resolution structure of the target, which is the *conditio sine qua non* to employ the BF or the SCPS algorithms. Second, the method does not yield reliable predictions when applied to proteins that fold by requiring chaperones. Furthermore, while this approach may in principle overcome some of the problems affecting classical pharmacology, other aspects of traditional drug discovery should be considered when designing a PPI-FIT degrader. In particular, in this method the polypeptide is always targeted inside the cell, thus, any compound developed to act in the PPI-FIT fashion should display ideal physicochemical features to cross the lipid bilayers and reaching the proper intracellular compartment (i.e. the ER in the case of PrP)[67].

Despite these limitations, the PPI-FIT approach could be theoretically applied to any other protein. Indeed, in a recent no-profit, collaborative research between our laboratory and Sibylla Biotech S.R.L. we applied the PPI-FIT method to carry out a drug-repurposing campaign aimed at identifying drugs capable of inhibiting the replication of SARS-CoV-2. To this end, we targeted the host-encoded protein angiotensin-converting enzyme 2 (ACE2), which is the cellular receptor of the virus, with the aim of reducing its levels on the cellular surface and impairing viral entry on the cells. This study enabled the identification of four compounds capable of lowering ACE2 expression in different cell lines and two of these molecules showed antiviral activity against live SARS-CoV-2[238]. These results support the applicability of the PPI-FIT technology in targeting other polypeptides, suggesting that this approach could expand the range of druggable protein conformations by targeting alternative structures explored along the folding pathway. In fact, the targeting of solvent-exposed, druggable sites hidden in the native state may result in additional advantages. For instance, a major problem in pharmacology is represented by proteins sharing a high structural similarity of their native states, a factor that significantly lowers the chances of identifying selective drugs. However, proteins with similar native topology do not necessarily share the folding mechanism[239], and even in the case of identical folding pathways, two polypeptides may differ for the lifetimes of their folding intermediates[240]. Therefore, the PPI- FIT method could target structurally and/or kinetically distinct intermediates states, allowing the identification of selective ligands even in the case of proteins sharing a high structural similarity.

4.3.3 The Role of Folding Intermediates in Protein Regulation

The observation that the levels of a target polypeptide could be modulated by affecting the stability of a non-native conformer explored along its folding pathway suggests that a similar regulation mechanism could be physiologically exploited by the cells to tune the levels of different proteins. Such a mechanism could potentially confer an additional layer for the temporal and spatial regulation of proteostasis, allowing cells to respond to stimuli more rapidly as compared to slower regulation mechanisms (i.e. transcriptional and translational regulation). This hypothesis is possibly supported by phosphoproteomic studies which reveal that a significant fraction of target sites for phosphorylation ($\sim$15%) are solvent excluded in the native state of proteins[241]. This observation indicates that those buried residues could be post-translationally modified only when the chain explores non-native conformers. While in a significant number of proteins these conformations are likely visited as a consequence of structural rearrangement of the native state, it is also possible that these states can be explored during the process of protein folding.

In conclusion, the data collected in this work support the view that the loads of target polypeptides could be regulated at the level of their folding pathways, suggesting a previously overlooked role for folding intermediates in the regulation of protein expression[67].

Chapter 5

Computational Methods

5.1 Construction and MD Simulations of PrP^{Sc} Atomistic Models

Building the first 4RβS model

To build a 4RβS model of PrP^{Sc} compatible with mouse PrP 89–230 sequence, we chose a β-solenoid template satisfying the following requirements: (I) an approximate number of β-strands residues per rung higher than 12 (needed to fit the secondary structure content of ∼40% β-sheets). (II) The possibility of introducing extended loops between consecutive β-strands, to exclude PK sites, prolines and glycine stretches from the solenoid core; (III) L-shaped or triangular cross-section, an architecture compatible with the cryo-EM maps of GPI-anchorless mouse PrP^{Sc}; (IV) Possibility of accommodating bulky side-chains in the hydrophobic core (the modeled region contains 1 Trp, 3 Phe, and 11 Tyr). These requirements are satisfied by the right-handed, β-solenoid architecture. In contrast, left-handed solenoids usually feature smaller rungs[26], impairing the accommodation of bulky residues in the core and the correct number of residues in β-strand conformation. The threading scheme displayed in figure 3.1 was designed on a general architecture shared by several L-shaped β-solenoid proteins (i.e *D. dadaanti* pectate lyase, *D. carota* methylesterase and the tailspike protein of Phage P22). In the threading process, PK sites, glycine tracts, and prolines were positioned in the loops or if not possible, at the edges of β-strands. Charged side-chains were excluded from the inner core of the solenoid or counterbalanced with residues having an opposite charge. We also took into account the positioning and solvent exposure of N180 and N196 (to accommodate glycans) and the presence of an intact disulfide bond between C178 and C213. The monomeric structure of the 4RβS model of PrP^{Sc} was constructed as follows: (I) 4 Rungs of *D. dadantii* Pectate Lyase (PDB 1AIR; two repetitions of residues 168–235) were used as a template for the β-solenoid core; (II) The original loops of the protein were removed; (III) The PrP sequence was threaded in the obtained scaffold, following the designed threading scheme, by replacing the original residues using UCSF Chimera[242]; (IV) Loops were built *de novo* using MODELLER[243]. Each loop was selected from a set of 20 proposed conformations. Structures with atomic clashes were discarded, and the best performing model was chosen in terms of DOPE score; (V) Side-chain rotamers were selected from the Dunbrack's library. In particular, for charged and highly polar side-chains in the hydrophobic core, we selected geometries capable of forming hydrogen bonds or salt bridges with nearby residues; (VI) The model was energy-minimized *in vacuum* with the steepest descent algorithm in Gromacs

4.6.5[244]. The system was treated using Amber99SB-ILDN force field[245]. We introduced the following distance-restraints potential during energy minimization between backbone H and O atoms involved in hydrogen bond formation:

$$V_{dr}(r_{ij}) = \begin{cases} 0 & \text{for } r_{ij} < r_0 \\ \frac{1}{2}k_{dr}(r_{ij} - r_0)^2 & \text{for } r_0 \leq r_{ij} < r_1 \\ \frac{1}{2}k_{dr}(r_1 - r_0)(2r_{ij} - r_1 - r_0) & \text{for } r_{ij} > r_1 \end{cases} \tag{5.1}$$

Where r_{ij} is the distance between the atoms involved in the formation of hydrogen bonds; r_0 is the original distance in the model $(2 < r_0 < 2.5)$Å and r_1 is an upper limit set to 4 Å, while k_{dr} is set to $2 \cdot 10^3$ kJ(mol·nm^2)$^{-1}$. This strategy was applied to impair the backbone deviation of the residues involved in the β-solenoid core formation when optimizing the energy of side-chains and loops. (VII) Additional backbone and side-chains refinement was performed using Coot[246]; (VIII) Absence of steric clashes was verified using Chimera, setting the VDW-overlap threshold as 0.6 Å, subtracting 0.4 Å to account H-bonding pairs and ignoring contacts of pairs less than 4 bonds apart. The tetramer structure was assembled by stacking 'head-to-tail' four 4RβS monomers using Chimera, retaining the proposed threading. The strands 198-TETD and 215-TQYQKESQAYY were stacked on the top of 94-THNQ and 105-KTNLKHVAGAA of the forthcoming monomer, respectively. Energy minimization was then carried out using the same protocol employed for the monomer[215].

Modelling the Glycosylated Atypical Propagative PK-resistant PrP

The structure of non-infectious recombinant PrP amyloid was retrieved from PDB 6LNI. Protein topology was generated in Gromacs 2018 using Amber99SB-ILDN forcefield. The residues N181 and N197 of each PrP monomer were glycosylated by using doGlycans[247], a python-based tool for modelling carbohydrate structures of glycoproteins provided the sugar-moieties sequence and the protein structure as input (carbohydrates treated with Glycam06 force field[248]). The glycans employed are composed by four N-acetylglucosamines, 3 mannoses, 2 galactoses, 1 fucose, and 2 sialic acids (GlcNAc$_4$Man$_3$Gal$_2$FucNeuNAc$_2$). The glycosylated fibril was visually inspected and torsional angles of the carbohydrates were adjusted to avoid overlap between the chains. The resulting structure was solvated in water (TIP3P) and brought to a NaCl concentration of 150 mM. The system was energy minimized using the steepest descent algorithm, following four consecutive steps. The first two were performed with position restraints on protein atoms with force tolerance equal to 1000 kJ/(mol·nm) and then 500 kJ/(mol·nm), while the 3rd and the 4th steps were carried out without restraints, using the previously employed tolerance values. The absence of steric clashes was verified using the Clashes/Contact Tool in UCSF Chimera[217].

Building the DTC-4RβS Model of Mouse PrP$^{\text{Sc}}$

The triangular core consisting of residues 181–208 (human numbering), retrieved from the structure in PDB 6LNI, was used as a template for each rung of the DTC-4RβS model. The threading scheme was obtained by considering the same experimental constraints previously employed to build the first 4RβS model (figure 3.7). The 3D structure was obtained first by building a 4-runged scaffold composed of four repetitions of the aforementioned triangular core, then the amino acids were

swapped to match the threading scheme, using UCSF Chimera. Side-chains conformations were retrieved from the Dunbrack's rotamer library. Loops were constructed using MODELLER. The topology of the protein was generated in Gromacs using Amber99SB-ILDN forcefield. The structure was solvated in water (TIP3P) and NaCl ions (150 mM). The system was energy minimized using the steepest descent algorithm with position restraints on no-H backbone atoms involved β-strands formation. A subsequent step of energy minimization was performed by removing the position restraints from all-atoms (a force tolerance of 200 kJ·mol^{-1}·nm^{-1} was set for energy minimizations). Then, low probability rotamers and Ramachandran outliers were corrected by employing Coot. UCSF Chimera was used to confirm the absence of steric clashes. The tetramer was assembled by stacking four monomers in a head-to-tail fashion followed by the previously employed energy minimization and refinement protocol. The glycosylated DTC-4RβS structure was build by following the same protocol employed to construct the glycosylated recombinant PrP amyloid[217].

MD Simulations of PrP^{Sc} models, non-infectious PrP amyloid and HET-s prion

The following protocol was applied for the whole set of MD simulations to evaluate the structural stability of the 4RβS, DTC-4RβS, LβH models, as well as the HET-s and the recombinant PrP amyloid structures. Protein topologies were generated using Amber99SB-ILDN force field. Each structure was accommodated in a dodecahedral box with a minimum wall distance from the protein equal to 12 Å. The box was filled with TIP3P water molecules. The charge of the system was neutralized with the addition of Na$^+$ or Cl$^-$ ions. Additional NaCl was added for the simulations of the DTC-4RβS model and the recombinant PrP amyloid structures to achieve the physiological concentration of 150 mM. The system was energy minimized in explicit solvent using the steepest descent algorithm, adding the restraining potential defined in equation 5.1. Three independent equilibrations (500 ps) were then launched starting from each minimized structure. The Nose-Hoover thermostat was employed for the simulations of the 4RβS, LβH, and HET-s structures while the V-rescale thermostat[249] was used to simulate the DTC-4RβS model and the recombinant PrP amyloid (in both cases the reference temperature was set to 300 K). The Parrinello-Rahman barostat[250] was employed to keep pressure constant (1 Bar) in all the simulations. For each equilibrated system, a 20 ns MD simulation with restraining potential (equation 5.1) was launched. Finally, restraints were released and each trajectory was extended up to 100 ns of standard MD. Simulations were performed using a leap-frog integrator with a step equal to 2 fs. Bonds constraints were handled using the LINCS algorithm. The cut-off for short-range Van der Waals and Coulomb interactions was set to 12 Å. Long-range electrostatics was treated using Particle Mesh Ewald. RMSD was computed in Gromacs, while the prediction of secondary structures was carried out with VMD 1.9.2[251] by employing the STRIDE method. Graphs were produced using Gnuplot and Matplotlib. Images were created using UCSF Chimera[215, 217].

5.2 Enhanced Sampling Simulations of Prion Propagation

Generation of the PrP$^{\text{Sc}}$ Propagation Model Based on the 4RβS Architecture

The coarse-grained information about the reaction mechanism described in section 3.2.1 was exploited to set up an all-atom rMD simulation to model prion propagation, using the 4RβS as a target structure. The initial 3D structure of mouse PrP$^{\text{C}}$ (residues 105–230) was obtained by linking coordinates retrieved from PDB 1XYX (residues 121–231) to the adapted N-terminal sequence (105–120) of human PrP$^{\text{C}}$ (PDB 5YJ5) which was mutated to the mouse sequence. The initial state for the propagation simulations was obtained by modifying the central dimer extracted at the end of 20 ns of restrained molecular dynamics simulation on the 4RβS tetramer. The initial contact point between PrP$^{\text{Sc}}$ and PrP$^{\text{C}}$ was generated by leaving residues 89–104 of the C-terminal monomer anchored to the β-solenoid, which was then replaced by moPrP$^{\text{C}}$ retaining the original disulfide bond. Protein topology was generated by Amber99SB-ILDN force field. The complex was energy minimized using the steepest descent algorithm first *in vacuum* and then in explicit solvent. The system was equilibrated for 200 ps in the NVT ensemble (350 K) using the Nose-Hoover thermostat, and then in the NPT ensemble (350 K, 1 Bar) for additional 200 ps by employing the Nose-Hoover thermostat and the Parrinello-Rahman barostat. The model was then subjected to a modified protocol of rMD simulations, adapting the method to a sequential biasing. Target structures included an entire 4RβS solenoid and additional rungs at the growing C-terminus: Step 1, residues 89–115; Step 2, residues 89–151; Step 3, residues 89–190; Step 4, residues 89–230. The rMD simulations were performed according to the method described in section 2.3.1 using a k_R of 10^{-2} kJ/mol and an r_0 equal to 7.5 Å. We excluded from the contact map calculations pairs of atoms farther than 12.3 Å in the target state. Each rMD simulation was terminated when the RMSD of the protein relative to the final state was lower than 0.8 Å. rMD simulations were performed in explicit solvent using Gromacs 4.6.5 and Plumed 2.0.2[252]. Integration of motion was carried out using the leap-frog algorithm with a step equal to 2 fs. The temperature was maintained at 350 K (approximately the PrP melting temperature) and pressure at 1 Bar using Nose-Hoover thermostat and the Parrinello-Rahman barostat. Cut-off for short-range Coulomb and Van der Waals interactions was set to 10 Å, while long range electrostatics was treated using Particle Mesh Ewald[215].

SCPS Simulations of HET-s Prion Replication

SCPS simulations of HET-s replication were carried out using the Charmm36m force field and the modified Charmm TIP3P water model[253]. Initial conditions were generated by thermal unfolding, in particular, the trimeric amyloid structure of HET-s (PDB 2KJ3) was positioned in a cubic box with a side length greater than 120 Å that was filled with TIP3P water molecules. The system was neutralized with 3 Cl$^-$ ions and energy minimized with the steepest descent method. Then, 200 ps of NVT equilibration using the V-rescale thermostat at 800 K were performed by introducing position restraints with a force constant of 10^3 kJ·mol^{-1}nm^{-2} on heavy atoms. Finally, 5 simulations of 2 ns each were carried out at 800 K by releasing the restraints on the N-terminal monomer; other 5 simulations were performed by releasing the restraints on the C-terminal monomer. The obtained initial states consisted of a HET-s dimer in the amyloid form and an unstructured monomer. These structures were re-solvated in a smaller cubic box with an approximate side of 100 Å; then 3 Cl$^-$ ions

were added to counterbalance the protein charge and the system was brought to a final 150 mM NaCl concentration. After energy minimization, 500 ps of equilibration in the NVT ensemble (T = 310 K) followed by 500 ps in the NPT ensemble (T = 310 K, P = 1 Bar) were carried out for each condition with position restraints on the heavy atoms. The V-rescale thermostat and the Parrinello-Rahman barostat were employed for both equilibrations and SCPS runs. First, 20 rMD simulations for each initial condition were performed, consisting of $3 \cdot 10^6$ steps employing the leap-frog integrator with 2 fs time-step. Frames were recorded every 500 steps. The value of k_R was set to $5 \cdot 10^{-5}$ kJ mol^{-1} and r_0 to 7.5 Å. The cutoff radius for neglecting distant contact pairs was set to 12 Å. A trajectory was considered to have reached the target state when one of its frames showed an RMSD with respect to the target below 3 Å, and the root-mean-squared error, computed on the subsequent frames that are above the threshold, stays within 0.3 Å. For each initial condition, the trajectories successfully reaching the reference state were used to compute the mean path (equation 2.5 of section 2.3.2) which was downsampled to 10 equally spaced contact maps. From each initial condition, 20 SCPS simulations were carried out with bias constants $k_s = 1.5 \cdot 10^{-5}$ kJ/mol and $k_w = 3 \cdot 10^{-5}$ kJ/mol. A total of 2 iterations were performed. We adopted as convergence criterion the evolution of the reaction pathways in the plane showing the RMSD to the reference state of the two terminal rungs (figure 3.14). The analysis regarding the order of rung formation was first performed by computing the RMSD to the target state of the rungs of the converting monomer. The all-atom RMSD of the two rungs (N-terminal: R225 to V245, C-terminal: T261 to Y281) was evaluated for all the trajectories successfully reaching the target state. The calculation of the RMSD was performed with alignment on the two monomers in the amyloid state (the converting monomer was not included in the alignment). For each iteration, two different probability densities were generated using frequency histograms: the first was obtained using all the productive trajectories in which the HET-s propagation starts at the fibril N-terminus. The second was obtained by employing all the productive paths in which the HET-s propagation starts at the fibril C-terminus. We want to emphasize that the negative logarithm of these distributions is not directly related to a free energy landscape, because SCPS trajectories are intrinsically out of equilibrium. We then computed the median point in the reaction progress at which each amino acid of the converting monomer assumes a β-strand conformation. A residue was considered to form a β-strand the first time that such structure was retained for more than 5 frames consecutively. The time of formation was then converted to the corresponding value of Q (fraction of formed contacts with respect to the reference structure). Secondary structures prediction was carried out using the STRIDE algorithm. Finally, PCA analysis was performed by using the Cα contact maps. For the N-terminal propagation simulations, the contact maps were computed by employing all the residues of the converting monomer and the residues belonging to the N-terminal rung of the N-terminal monomer already included in the fibril in the initial state. For the C-terminal propagation simulations, residues of the converting monomer and the C-terminal rung of the C-terminal monomer already included in the fibril were used for contact map calculation. Biased simulations (rMD and SCPS) were performed in Gromacs 2018, where we implemented the collective variables $z(X)$, $s_\lambda(t)$ and $w_\lambda(t)$. Data analysis was performed using the following libraries in python: NumPy, SciPy, and MDAnalysis. Python scripts were accelerated with the Numba compiler. Graphs were obtained by using Matplotlib in python. Images of protein conformations were generated in UCSF Chimera[214].

5.3 MD Simulations of PrP

Folding Simulations of the PrP Polypeptide

The structure of the globular C-terminal domain of human PrP^C (PDB 1QLX) was placed in a dodecahedral box with 40 Å minimum distance from the walls. The box was filled with TIP3P water molecules and neutralized with three Na$^+$ ions. The system was subjected to energy minimization by employing the steepest descent algorithm. NVT equilibration was carried out for 500 ps at 800 K using the V-rescale thermostat with position restraints on heavy atoms. Restraints were then released and nine independent standard MD simulations (3 ns each) were performed in the NVT ensemble at 800 K, yielding nine denatured conformations. Each denatured conformation was repositioned in a dodecahedral box with 15 Å minimum distance from the walls, energy minimized and then equilibrated first in the NVT ensemble (using the Nosé-Hoover thermostat at 350 K) and then in the NPT ensemble (using the Nosé-Hoover thermostat at 350 K, and the Parrinello–Rahman barostat at 1 bar). For each initial condition, 20 pathways were generated by using the rMD algorithm in the NPT ensemble (350 K, 1 bar). Each trajectory consisted in $1.5 \cdot 10^6$ rMD steps generated with a leap-frog integrator (time-step 2 fs). Frames were saved every 500 steps. The ratchet constant k_r was set to $5 \cdot 10^{-4}$ kJ/mol. Cutoff for Van-der-Waals and Coulomb interactions was set to 16 Å, while Particle Mesh Ewald was employed for long-range electrostatics. For each set of trajectories, the BF scheme was applied (see section 2.3.1) with additional filtering on the secondary structure content. In particular, trajectories reaching a final conformation with <85% of average secondary structure content compared to the target native state were excluded from the ranking. RMSD was computed using Gromacs while the fraction of native contacts (Q) was computed using VMD 1.9.2. The lower-bound approximation of the energy landscape G(Q, RMSD) was generated by plotting the negative logarithm of the 2D probability distribution of the collective variables Q and RMSD, obtained from the 180 rMD trajectories (115 x 115 bins). Protein conformations belonging to the LB trajectories and spanning over the energetic wells of interest (G $\leq$ 3.7 $k_B T$) were sampled. Conformations belonging to the intermediate state were clustered by using the k-mean approach in R-Studio[254] employing the following metrics for defining a distance between two structures:

$$D(X_A, X_B) = \sqrt{\sum_{i<j}^{N} \left[C_{ij}(X_A) - C_{ij}(X_B) \right]^2} \qquad (5.2)$$

Where $D(X_A, X_B)$ is the distance metrics between the contact maps $C_{ij}(X_A)$ and $C_{ij}(X_B)$ of the two protein conformations A and B (see equation 2.2). The appropriate number of clusters ($k = 3$) was selected using the elbow method. The representative structure of each cluster was selected by computing the average contact map of the conformations within that cluster and then extracting the structure minimizing the distance $D(X_A, X_B)$ between itself and the average contact map. Data were represented using the Matplotlib library in python, the 2D [Q, RMSD] energy plot was smoothed with a Gaussian kernel. Images of the protein conformations were created using UCSF Chimera. Protein topology was generated using Amber99SB-ILDN force field in TIP3P water and folding simulations were performed in Gromacs 4.6.5 patched with Plumed 2.0.2 [67].

Standard MD simulations of PrP^C

The native structure of the C-terminal domain of human PrP (PDB 1QLX) was used as initial conformation for extended MD simulations. System topology was generated using Charmm36m. The structure was centered in a dodecahedral box with 11 Å minimum distance from the walls. The box was filled with TIP3P water molecules, neutralized with the proper number of counterions, and brought to a final 150 mM NaCl concentration. The system was energy minimized using the steepest descent algorithm. NVT equilibration was then performed for 1 ns at 310 K using the V-rescale thermostat followed by 1 ns of NPT equilibration with the V-rescale thermostat and the Parrinello–Rahman Barostat at 310 K and 1 Bar (NVT and NPT equilibrations were carried out with positional restraints on heavy atoms). The equilibrations were repeated 5 times to generate five initial conditions. For each initial condition, a single MD trajectory was launched (NPT, 310 K, 1 Bar), yielding a cumulative simulation time of 21 μs (3 trajectories of 5 μs each, and 2 trajectories of 3 μs each). The leap-frog integrator (dt = 2 fs) was used to perform these simulations. Van-der-Waals and Coulomb cutoffs were set to 12 Å, with a force-switch Van-der-Waals modifier with a radius of 10 Å, while Particle Mesh Ewald was employed for long-range electrostatics. The Cα RMSD of the amino acids residing in the contact region between helix-1 and helix-3 (144–156 and 201–208) was computed with respect to the structure of the PrP folding intermediate previously sampled using the BF approach[67].

5.4 Computer-Aided Drug Discovery Analysis

Consensus Approach for Druggable Ligand-Binding Site Identification

A consensus approach based on SiteMap (Schrödinger) and DoGSiteScorer (BioSolveIT) software was applied to detect and evaluate druggable sites. Specific structural properties, such as volume, depth, enclosure/exposure, balance, and different druggability scores were computed for each identified site. Exposure, enclosure and depth provide a physical description of the pocket. For the exposure property, the promising sites have been shown to display a low score, with an average value for tight-binding sites around 0.49. Conversely, higher scores are preferred for the enclosure descriptor, with the average enclosure score for a tight-binding site being 0.78. The balance property of SiteMap expresses the ratio between the relative hydrophobic and hydrophilic character of a pocket. This fraction has proven to be a highly discriminating property in distinguishing between druggable and undruggable pockets, with a mean value for a tight-binding site equal to 1.6. Besides the global pocket descriptors, the applied tools provide automated methods for quantitative estimation of druggability. SiteMap predicts a general score of the site (SiteScore) and druggability score (DScore) through a linear combination of three descriptors: the size of the binding pocket, its enclosure, and a hydrophilicity penalty. The two scores differ in the coefficients, which are based on different training sets. Score values of ≥ 0.8 and ≥ 0.98 for SiteScore and DScore, respectively, are generally reported for drug binding sites. DoGSiteScorer also generates two scores, i.e., SimpleScore (computed by considering the pocket volume, enclosure and lipophilic character) and a druggability score (DrugScore), computed by the software using a support vector machine, which range from zero to one. The druggability cutoff for both scores is set to 0.5, indicating that sites with score

above this value are considered druggable. Due to the innovative character of the target (namely, a folding intermediate conformer), we used thresholds for druggability definition less stringed than those typically employed in standard virtual screening approaches. Selected values: volume ≥ 300 Å^3 ; depth ≥ 10 Å; balance ≥ 1.0; exposure ≥ 0.5; enclosure ≥ 0.70; SiteScore ≥ 0.8; DScore $\geq$ 0.90; DrugScore ≥ 0.5; SimpleScore ≥ 0.5.[67]

Identification of a Druggable Site in the Folding Intermediate of PrP

The previously described consensus approach identified a suitable ligand-binding site in the PrP folding intermediate, positioned between helix-1 and the loop that connects the helix-2 and helix-3. MD simulations were carried out to refine the structure of the binding pocket. To this end, the folding intermediate was prepared with the Schrödinger's Protein Preparation Wizard. The N- and C- terminal residues were capped with acetyl and N-methyl-amide groups, respectively. Then, protein side-chains were energy minimized using the OPLS3 force field. The obtained structure was solvated by TIP3P water molecules in a cubic box with a minimum distance from walls equal to 12.5 Å, neutralized by the addition of three Na^+ ions, and equilibrated for 100 ps of MD simulation at 300 K using the Langevin thermostat. In this simulation, position restraints on the Cα atoms were introduced (force constant 4.2 kJ/mol), in order to exclusively explore the flexibility of the side-chains. The cutoff for short-range interactions was set to 9 Å, and a reversible reference system propagator algorithm (RESPA) was used as integrator with a time-step of 2 fs, and long-range electrostatics were computed every 6 fs. MD simulations were performed using the OPLS3 force field in Desmond 5.0 software (Schrödinger Release 2017-4) and run for 50 ns, recording a total number of 1001 frames equispaced in time. The trajectory was clustered using the "Desmond trajectory clustering" tool in Maestro based on the RMSD of residues defining the pocket (152, 153, 156, 157, 158, 187, 196, 197, 198, 202, 203, 205, 206, and 209). Hierarchical clustering was employed to obtain 10 clusters of the explored site. The centroid of each cluster was then selected as a representative structure and subjected to in silico ligand-binding site prediction and druggability assessment by using the previously described consensus methods involving DogSiteScorer and SiteMap analysis[67].

Preparation of the Library of Virtual Compounds

The Asinex Gold & Platinum Library was retrieved from the Asinex webpage (~ 3.2 x 10^5 commercially available compounds). The initial round of ligand preparation was carried out in LigPrep (Schrödinger Release 2017-4). Subsequently, the compounds were imported in SeeSAR (BioSolveIT GmbH), which assigns the correct geometry, protonation states and the tautomeric forms of the compounds. This process yielded a library of ~ 4.3 x 10^5 docking clients[67].

Identification of Virtual Hits Through Docking-Based Screening.

The virtual screening workflow was performed as follows: (I) the molecular structure of the protein was prepared for docking by using the 'Prepare Receptor' tool of LeadIT (BioSolveIT GmbH). The binding site was defined on the residues of the previously identified druggable pocket (figure 4.3). The protonation states and the tautomeric forms of the residues side-chains were automatically assessed in LeadIT. Subsequently, molecular docking was performed on the ~ 4.3 x 10^5 docking clients by using the FlexX algorithm. Ten poses for each ligand were produced and SeeSAR was

employed to estimate the binding free energy and affinity (k_i HYDE) of each pose. For each ligand, the pose with the lowest k_i was extracted. Only compounds with a predicted k_i range below 5 μM were subjected to the following analysis. The rescored poses were filtered based on physicochemical and ADME properties by employing the Optibrium models of SeeSAR. In particular, the following thresholds were considered: $2 \leq \text{LogP} \leq 5$, where the LogP is the predicted partition coefficient of octanol/water; $1.7 \leq \text{LogD} \leq 5$, where logD is the distribution coefficient predicted for ionizable compounds; TPSA $\leq$ 90; where TPSA is the topological polar surface area; compounds with TPSA $\leq$ 90 have a higher chance to cross the blood-brain barrier; LogS-7.4 $\geq$ 1, where LogS7.4 is the intrinsic aqueous solubility at pH of 7.4. Selected compounds should also display a predicted positive classification for human intestinal absorption (at least 30% absorbed) and negative PgP category (P-glycoprotein transport); $300 \leq \text{MW} \leq 500$ Dalton; number of rotable bonds $\leq$ 3; number of hydrogen bond donors $\leq$ 3; number of stereocenters $\leq$ 1. This approach yielded a list of 275 virtual hits, which were first submitted to a diversity-based selection. For each compound, a binary fingerprint was derived by means of the canvasFPgen utility provided by Schrödinger. Using the created fingerprint, the 10 most different compounds (i.e. ASN03578729, SM937, SM940, SM944, SM875, SM926, BAS00340795, SM947, SM951, SM931) were extrapolated by using the canvasLibOpt Schrodinger utility. Visual inspection was carried out to select promising ligands based on the predicted binding mode and interactions with the identified druggable site. In total, 30 molecules were selected, 8 from diversity-based selection and 22 after visual inspection. Importantly, despite 10 diverse compounds were originally chosen, BAS00340795 was not in stock, and ASN03578729 was replaced by its close analog SM941, characterized by a higher predicted affinity[67]. The predicted physicochemical properties of the 4 compounds capable of suppressing the levels of PrP are reported in supplementary table 3.

CD spectra prediction

The geometries of 8 different conformations (R)-SM875 were optimized and for each of them the CD spectrum and optical rotations were computed using Gaussian[255].

Chapter 6

Experimental Methods

6.1 Cell-Based and Biochemical Assays

Cell Cultures and Treatments

Cell lines have been cultured in Dulbecco's Minimal Essential Medium (Gibco, #11960-044), 10% heat-inactivated fetal bovine serum (Δ56-FBS), 50 U/mL penicillin, and 50 μg/mL streptomycin (Pen/Strep, Corning #20-002-Cl), non-essential amino acids (Gibco, #11140-035) and L-Glutamine (Gibco, #25030-024), unless specified differently. HEK293 and N2a cells were obtained from ATCC (ATCC CRL-1573 and CCL-131, respectively). Inducible RK13 cells and L929 mouse fibroblasts cells were provided by Didier Villette (INRA, Toulouse, France)[233] and Ina Vorberg (DZNE, Bonn, Germany)[235], respectively. Cancer cell lines were provided by Valentina Bonetto (Mario Negri Institute, Milan, Italy). All the cell lines employed in this study were authenticated by the provider and have been regularly tested for possible mycoplasma contamination every two months. Cells were passaged in T25 flasks or 100 mm Petri dishes in media containing 200 μg/mL of Hygromycin or 500 μg/mL of G418 and split every 3–4 days. Compounds used in the experiments were resuspended at 30 or 50 mM in DMSO, and diluted to make a 1000x stock solution, which was then used for serial dilutions. A 1 μL aliquot of each compound dilution point was then added to cells plated in 1 mL of media with no selection antibiotics. For pulse experiments, inducible RK13 cells were seeded at a confluence of 50%. After 24 h cells were treated with doxycycline (0.01 mg/mL) or vehicle (0.1% DMSO). At the end of each time-point (2, 4, 8 and 24 h) cells were washed with PBS and then lysed in lysis buffer. For chase experiments, RK13 cells were seeded on 24-well plates at a confluence of 30%. After 24 h cells were treated with doxycycline (0.01 mg/mL) for 24 h. The medium containing doxycycline was then removed and cells kept in fresh medium for 4 h before adding SM875 (10 μM). After 5, 19, and 24 h of incubation cells wells were washed with PBS and lysed[67].

Western Blot and Antibodies

Samples were lysed in lysis buffer (Roche, #11697498001), diluted in Laemmli sample buffer (Bio-Rad) containing 100 mM DTT (Sigma Aldrich), boiled 8 min at 95 °C and loaded on SDS-PAGE, using 12% acrylamide pre-cast gels (Bio-Rad) and then transferred to polyvinylidene fluoride (PVDF) membranes (Thermo Fisher Scientific). Membranes were blocked for 20 min in 5% (w/v) non-fat dry milk in Tris-buffered saline containing 0.01% Tween-20 (TBS-T). Blots were probed with anti-PrP

antibodies D18 or 6D11 (1:5000) in BSA 3% in TBS-T overnight at 4 °C, or with specific antibodies for the target proteins, all in 5% (w/v) non-fat dry milk. After incubation with primary antibodies, membranes were washed three times with TBS-T (10 min each), then probed with a 1:8000 dilution of horseradish conjugated goat anti-human (Jackson Immunoresearch) or anti-mouse (Santa Cruz) IgG for 1 h at RT. After two washes with TBS-T and one with Milli-Q water, signals were revealed using the ECL Prime western blotting Detection Kit (GE Healthcare) and visualized with a ChemiDoc XRS Touch Imaging System (Bio-Rad)[67].

Quantitative Real Time PCR

Cells were harvested after treatment and the RNA was extracted using TRIzol (Invitrogen) or RNeasy Plus mini kit (Qiagen). An 800-ng aliquot per sample was reverse transcribed using High-Capacity cDNA Reverse Transcription kit (Applied Biosystems). Quantitative RT-PCR was performed in a CFX96 thermocycler (Bio-Rad) using PowerUp SYBR Green Master mix (Invitrogen) for 40 cycles of amplification. Specific primers were used to amplify PrP. Relative quantification was normalized to mouse or human hypoxanthine–guanine phosphoribosyl transferase as a housekeeping control[67].

Cell Viability

Cells were seeded at ∼60% confluence and compounds or control were added after 48 h at different concentrations, medium was replaced the second day, and then removed after a total of 48 h of treatment. Cells were incubated with 5 mg/mL of 3-(4,5- dimethylthiazol-2-yl)-2,5-diphenyltetrazolium bromide (Sigma Aldrich) in PBS for 15 min at 37 °C. After removal of MTT, cells were resuspended in 500 μL DMSO, and cell viability values obtained by a plate spectrophotometer measuring absorbance at 570 nm[67].

Production of Recombinant PrP

Recombinant human PrP 23-231 and mouse PrP 111-230 were expressed by competent *E. coli* Rosetta (DE3) bacteria harboring pOPIN-E expression vector. Bacteria were grown in a 250 mL flask containing 50 mL of LB broth overnight. The culture was then transferred to two 2 L flasks containing each 500 mL of minimal medium supplemented with 3 g/L glucose, 1 g/L NH$_4$Cl, 1 M MgSO$_4$, 0.1 M CaCl$_2$, 10 mg/mL thiamine, and 10 mg/mL biotin. When the culture reached an OD600 of ∼0.9–1.2 AU, expression was induced by adding Isopropyl β-D-1-thiogalactopyranoside under the same temperature and agitation conditions (overnight). Bacteria were then pelleted, lysed, inclusion bodies collected by centrifugation, and solubilized in 20 mM Tris-HCl, 0.5 M NaCl, 6 M Gnd/HCl, pH = 8. Purification of the protein was performed with a histidine affinity column (HisTrap FF crude 5 mL, GE Healthcare Amersham). The employed plasmid for recombinant human PrP 23-231 does not express a fused His-tag, but the protein displays an intrinsic affinity for the column due to the octapeptide repeat region. PrP 111-230 contains a His-tag at the C-terminus (which was removed after purification with 3C protease). After elution with buffer containing 20 mM Tris-HCl, 0.5 M NaCl, 500 mM imidazole and 2 M guanidine-HCl, pH = 8, the purity of protein batches was evaluated by BlueSafe (NZYTech) staining after electrophoresis in SDS-PAGE gels. The protein was folded to the PrP native conformation by dialysis against 20 mM sodium acetate buffer,

pH = 5. Aggregated material was removed by centrifugation. Correct folding was confirmed by CD and protein concentration was measured by absorbance reading at 280 nm. The protein was concentrated using Amicon centrifugal devices and stored at -80 °C. To remove the His-tag from PrP 111-230 we incubated the sample overnight at 4°C with a GST-tagged 3C protease (PrP:3C = 25:1) in 50 mM TRIS pH 7.2 and 0.1 mM TCEP. A first step of purification was performed on a PD-10 column (Sigma Aldrich) using a Ni-NTA resin. Then, the collected sample was eluted on a PD-10 column with a GSH resin as solid phase (to remove the 3C protease). The purity of the protein was assessed by SDS-PAGE on pre-casted stain-free gels (Biorad), and the concentration measured by reading UV absorbance at 280 nm. Protein was concentrated (up to 800 µM) using the Amicon Ultra 0.5 mL centrifugal devices in 20 mM sodium acetate buffer, pH = 5. Aliquots were flash frozen in liquid nitrogen and then stored at -80 °C[67].

Dynamic Mass Redistribution

The DMR analysis was carried out using the EnSight Multimode Plate Reader (Perkin Elmer). Immobilization of full-length (residues 23–230) or mouse N-terminally truncated (111–230) recombinant PrP (15 µL/well of a 2.5 µM PrP solution in 10 mM sodium acetate buffer, pH 5) on label-free microplates (EnSpire-LFB high sensitivity microplates, Perkin Elmer) was obtained by amine-coupling chemistry. The interaction between Fe^{3+}-TMPyP, SM875 and SM940 diluted to different concentrations (0.03–100 µM, eight 1:3 serial dilutions) in assay buffer (10 mM $NaHPO_3$, pH 7.5, 2.4 mM KCl, 138 mM NaCl, 0.05% Tween-20) and PrP, was monitored after a 30 min incubation at RT. All the steps were executed by employing a Zephyr compact liquid handler (Perkin Elmer). Data were acquired and processed using the Kaleido software (Perkin Elmer), the signals were normalized on the intra-well empty surface, and then by subtracting the levels of the control wells[67].

Crystallization

Recombinant mouse PrP (residues 111–230, 800 µM) was heated to 45 °C and slowly cooled to 20 °C using a thermal cycler, either in the presence or absence of SM875 (2 mM). We observed significant precipitation in the presence of SM875. Pellet was removed by centrifugation and a 40% reduction in PrP concentration was estimated by UV absorbance at 280 nm. Showers of very thin needles appeared in 2–4 days in the following conditions: 0.2 M $(NH_4)_2SO_4$, 10 mM $CdCl_2$, 9–14% LMW PEG smear, 9–14% MMW PEG smear, pH 6–8; irrespectively of whether the protein was incubated with SM875 or not. Data collection was performed at the Elettra synchrotron, XRD1 beamline (Trieste, Italy). Crystals were weakly and anisotropically diffracting to 3.7 Å in the best directions. Multiple diffraction patterns were present, as single needles were impossible to isolate. Orthorhombic crystal system and unit cell dimensions could be identified (a = 36.1 Å, b = 51.8 Å, c = 55.9 Å), which are extremely similar to those reported for apo human PrP in PDB 3HAK (a = 32.5 Å, b = 49.1 Å, c = 56.9 Å)[67].

Temperature-Dependent Detergent Insolubility Assay

Recombinant PrP (111-230) was diluted to a final concentration of 0.5 µM in precipitation buffer (10 mM NaAc, 2% TX100, pH 7), split into eight identical aliquots, and incubated for 1 h at different temperatures (25, 37, 45, and 55 °C), in the presence or absence of each tested compound, or vehicle

control (0.1% DMSO, volume equivalent). Each sample was then carefully loaded onto a double layer of sucrose (60% and 80%) prepared in precipitation buffer and deposited at the bottom of ultracentrifuge tubes. Samples were then subjected to ultracentrifugation at 100000 x g for 1 h at 4 °C. The obtained protein pellets were diluted in 2x Laemmli sample buffer and then analyzed by western blotting[67].

Scanning Electron Microscopy

SM875 was added to an 0.55 mL aliquot of recombinant PrP in 20 mM PBS, pH = 6 (final concentrations for both PrP and SM875 = 250 μM) and the solution was incubated for 1 h at 55 °C. The supernatant was removed and the precipitate was collected by resuspension, transferred to a vial and vortexed. A 10 μL aliquot was deposited on a glow-discharged gold-carbon grid. The grid was washed twice with distilled water and stained for 1 min with a filtered, freshly prepared solution of 2% uranyl acetate. Micrographs were acquired using a ZEISS UltraPlus field emission scanning electron microscope (FESEM) with a grid stage set at 20 kV. The experiment was then repeated on precipitates subjected to short-tip sonication (5 s, three times)[67].

Detection of Prions in L929 Fibroblast

L929 fibroblasts were grown in culturing medium and passaged 5–7 times after infection with a 0.5% homogenate of RML prion strain. Cells were seeded (day 1) at ∼60% confluence, with different concentrations of each molecule, or vehicle control (0.1% DMSO, volume equivalent). Medium containing fresh compounds or vehicle was replaced the following day, and cells were split (1:2) on day 3. Cells were collected on day 4 in PBS and centrifuged for 3 min at 3500 rpm. The pellets were rapidly stored at -80 °C. To evaluate prion loads, cell pellets were resuspended in 20 μL of lysis buffer (Tris 10 mM, pH 7.4, 0.5% NP-40, 0.5% TX-100, 150 mM NaCl) and incubated for 10 min at 37 °C with 2000 U/mL of DNase I (New England BioLabs). Half of the resulting sample was incubated with 10 μg/mL of PK (Sigma Aldrich) for 1 h at 37 °C, while the other half was incubated in the same conditions without PK. Both samples were then mixed 1:2 with 4x Laemmli sample buffer (Bio- Rad) containing DTT, boiled for 8 min at 95 °C and ran by SDS-PAGE. The quantification of PK-resistant PrP species was carried out by densitometric analysis of western blots, each signal was normalized on the corresponding PK-untreated lane[67].

Statistics and Reproducibility

All the data were collected and analyzed blindly by two different operators. Statistical analysis of cell-based and biochemical characterization was performed with the Prism software version 7.0 (GraphPad), including all the data points obtained, with the exception of experiments in which negative and/or positive controls did not give the expected outcome, which were discarded. The Kolmogorov–Smirnov normality test was applied (when possible, n ≥ 5). Results were expressed as the mean ± standard errors, unless specified. All the data were analyzed with the one-way analysis of variance test, including an assessment of the normality of data, and corrected by the Dunnet post-hoc test[67].

6.2 Synthesis and Characterization of SM875 and Analogues

Instrumentation

Thin-layer chromatography (TLC) was carried out on Merck Kieselgel 60 PF254 with visualization by UV light. Microwave-assisted reactions were carried out using a mono-mode CEM Discover reactor. Preparative thin-layer chromatography (PLC) on 20 x 20 cm Merck Kieselgel 60 F254 0.5 mm plates. High-performance liquid chromatography (HPLC) purification was performed by a Merck Hitachi L-6200 apparatus, equipped with a diode array detector Jasco UVIDEC 100 V and a LiChrospher reversed-phase RP18 column, in isocratic conditions with eluent acetonitrile/water (different ratios were employed for distinct compounds), flow 5 mL·min^{-1}, detection at 254 nm. Separation of SM875 enantiomers was performed by employing the same apparatus but in analytical conditions (flow: 1 mL·min^{-1}), using a Chiralpak column (Daicel Corporation) with amylose functionalized silica gel as stationary phase; elution conditions: hexane, isopropanol and dichloromethane (17:8:2, isocratic). NMR spectra were collected on a Bruker-Avance 400 spectrometer by using a 5 mm BBI probe ^{1}H at 400 MHz and ^{13}C at 100 MHz in CDCl$_3$ relative to the solvent residual signals δ_H 7.25 and δ_C 77.00 ppm, J values in Hz. Structural assignments were confirmed by heteronuclear multiple bond correlation experiments. High-resolution ESI-MS measurement of the final products were obtained by direct infusion using an Orbitrap Fusion Tribrid mass spectrometer. LC-ESI-MS spectrum of SM875 was acquired using a C-18 Kinetex 5 μm column, eluting with acetonitrile/water 70:30, flow 1 mL·min^{-1} using a Bruker Esquire-LC mass spectrometer equipped with an electrospray ion source. IR spectrum of SM875 was recorded by using a FT-IR Tensor 27 Bruker spectrometer equipped with ATR device at 1 cm^{-1} resolution. A thin solid layer was obtained by the evaporation of the CHCl$_3$ solution in the sample. The instrument was purged with a constant dry nitrogen flow. Spectra processing was made using the Opus software[67]. CD spectra were acquired using a Jasco J-710 spectropolarimeter while polarimetric data were collected using a Jasco DIP-181. Both measurements were performed in pure ethanol.

Synthesis of SM875 and Analogs

The target product SM875 was obtained according the synthetic scheme reported in figure 4.11. The sequence involves the preparation of the precursor 1-(4-bromophenyl)-1H-pyrazol-5-amine, which was used in a following three-component reaction with 4-hydroxy-3-methoxybenzaldehyde and Meldrum acid (2,2-dimethyl-1,3-dioxane-4,6-dione) according to a method modified and adapted from Zeng et al[256]. The 1-(4-bromophenyl)-1H-pyrazol-5-amine was synthesized starting from 4-(bromophenyl)-hydrazine that was obtained from the commercial hydrochloride by treatment with a saturated NaHCO$_3$ aqueous solution (50 mL), followed by extraction with dichloromethane (50 mL x3), treatment with anhydrous Na$_2$SO$_4$ and evaporation. To a magnetically stirred solution of 4-(bromophenyl)-hydrazine (100 mg, 0.53 mM, in 5 mL ethanol 5), ethyl-2-cyano-3-ethoxyacrylate (89.6 mg, 0.53 mM) was added and refluxed for 2 h. The reaction mixture was concentrated *in vacuo*, the residue was suspended in 1:1 (methanol/2 M NaOH aqueous solution) and refluxed for 1 h. After cooling, the mixture was neutralized with 1 M HCl aqueous solution (5 mL) and concentrated *in vacuo* using a water bath at 40 °C. The raw product was heated at 180 °C for 10 min, suspended in ethanol after cooling and stored overnight at 4 °C. The supernatant was recovered and concentrated to

give a residue which was stirred in the presence of a NaHCO$_3$ solution (10 mL). Extraction with ethyl acetate (10 mL x3), followed by the treatment with anhydrous Na$_2$SO$_4$ of the combined organic phases and concentration *in vacuo* gave the product (79 mg, 61%), which was employed in the following three-component reaction. The successful synthesis of 1-(4-bromo-phenyl)-1H-pyrazol-5-amine was verified by ^{1}H-NMR and ESI-MS. In the last reaction step, 1-(4-bromo-phenyl)-1H-pyrazol-5-amine (79 mg, 0.33 mM), 4-hydroxy-3-methoxybenzaldehyde (41 mg, 0.27 mM) and 2,2-dimethyl-1,3-dioxane-4,6-dione (46 mg, 0.32 mM) were refluxed in ethanol (5 mL) under stirring for 2.5 h. The reaction mixture was then cooled to room temperature and dried *in vacuo*. The raw product was purified by PLC eluting with n-hexane/ethyl acetate (1:1). The band collected at retention factor 0.4 was first used for structural characterization and then injected into preparative HPLC (RP18 column, acetonitrile/water 1:1, UV detection at 254 nm, flow 5 mL min^{-1}, retention time 4.5 min) to give the target product (for use on cell cultures) as a white powder after evaporation of the eluent: 34 mg, 25%. We obtained the same yield by repeating the three-component reaction by replacing the conventional heating with microwave irradiation at 110 °C for 1 h[67]. The same synthesis strategy was employed to obtain analogs 1-24, using the following commercially available reagents (Sigma Aldrich & Alfa Aesar): phenylhydrazine hydrochloride, 4-(fluorophenyl)-hydrazine hydrochloride, 4-(chlorophenyl)-hydrazine hydrochloride, 4-(iodophenyl)-hydrazine, p-tolylhydrazine hydrochloride, 4-(trifluoromethyl)-phenylhydrazine, 3-(bromophenyl)-hydrazine hydrochloride, 2-(bromophenyl)-hydrazine hydrochloride, 2-(fluorophenyl)-hydrazine hydrochloride, 2,4-(difluorophenyl)-hydrazine hydrochloride, 3-chloro-4-fluorophenylhydrazine, benzaldehyde, 4-hydroxybenzaldehyde, 4-phenoxybenzaldehyde, 3-hydroxy-4-methoxybenzaldehyde, 4-ethoxy-3-methoxy-benzaldehyde, 1,4-benzodioxan-6-carboxaldehyde, 3-methoxy-4-Benziloxybenzaldehyde, and 2,3,4-trimethoxybenzaldehyde. Derivatives A$_{25}$-A$_{28}$ were obtained by methylation of SM875 and analogs A$_4$ and A$_{15}$. In this process, ∼5 mg of starting compound was added to a solution of acetone/iodomethane 1:1. Subsequently, 50 mg of K$_2$CO$_3$ were added to the mixture and let react for 24 h, to obtain the single methylation on the lactam nitrogen, or for 48 h to obtain additional methylation on hydroxyl groups (where present). The soluble product was then obtained by filtering out the precipitated salt and concentrated *in vacuo*. Analogue 29 was obtained by employing the modified precursor 1-(4-bromophenyl)-3-methyl-1H-pyrazol-5-amine instead of the 1-(4-bromophenyl)-1H-pyrazol-5-amine. This alternative precursor was obtained by reacting 4-(bromophenyl)-hydrazine hydrochloride and 3-aminoacrylonitrile in 0.6 mL 2M HCl aqueous solution at 100 °C by microwave irradiation for 1 h. The reaction mixture was neutralized with aqueous NaOH solution (0.25 M, ∼6 mL) and after 15 min stirring it was extracted in dichloromethane. The combined organic phases were treated with anhydrous Na$_2$SO$_4$ and concentrated *in vacuo*. The successful synthesis of 1-(4-bromo-phenyl)-3-methyl-1H-pyrazol-5-amine was verified by ^{1}H-NMR [δ 7.55 (d, J 2.8 Hz, 2H), δ 7.44 (d, J 7.8 Hz, 2H), δ 7.4 (s, 1H: H-3), δ 5.44 (s, 1H), 2.2 (s, 3H)]. This compound was then employed as a reagent for the three-component reactions, as previously described, to yield A$_{29}$. All the synthesized analogues were purified using HPLC before cell-based testing. Structural data of each compound can be found in the supplementary information.

Supplementary Information

SCPS Validation in Explicit Solvent

To validate the accuracy of the SCPS approach we report a benchmark performed on 5 polypeptides whose folding pathways have been fully characterized by standard MD simulations[197]: Trp-Cage (PDB 2JOF); Villin headpiece (PDB 2F4K); WW domain (PDB 2F21); NTL9 (PDB 2HBA); and the thermostable variant of the Engrailed homeodomain (PDB 2P6J). This set includes members of α-helical, β-sheet, and mixed α/β protein structural classes. The initial denatured states were retrieved from the ultra-long MD trajectories previously performed by the group of D.E. Shaw[197], by sampling states with fraction of native contacts (Q) lower than 0.1 that are separated by at least one folding-unfolding event. Topologies were generated using Charmm22* force field with TIPS3P water model. Lys, Arg, Asp, and Glu residues as well as the N-termini and C-termini were treated in their charged states. His residues were neutral in all proteins with the exception of the Villin headpiece, where the single His was protonated. Each denatured conformation was solvated in a cubic box and neutralized with the appropriate number of Na^+ and Cl^- ions. Each system was then energy minimized using the steepest descent algorithm then equilibrated in a 500 ps NVT simulation carried out by restraining the protein heavy atoms using a harmonic potential with constant 1000 kJ·mol^{-1}nm^{-2}.

For each initial state, 20 rMD simulations were performed, consisting in $1.5 \cdot 10^6$ steps employing the leap-frog integrator with 2 fs time-step. Cutoff for Van der Waal and Coulomb interaction was set to 9 Å. The long-range Coulomb interactions were treated with Smooth Particle-Mesh Ewald (SPME). We used the Nose-Hoover thermostat with a time constant of 1 ps. A trajectory was considered successfully folded when of its frames showed an RMSD with respect to the native state below 3 Å, and the root-mean-squared error, computed on the subsequent frames that are above the threshold, stays within 0.3 Å. The folding trajectories were used to compute the mean path in the space of the contact maps. Each mean path was downsampled to 10 contact maps, equally spaced in the $z(X)$ distance. The mean paths were used to build the CVs used in the subsequent SCPS iteration. We performed a total of three SCPS iterations for each protein. The values of k_R or k_s and k_w for each condition are reported in supplementary table 4.

Folding events generated by rMD and SCPS were compared with the reactive portion of the standard MD trajectories (folding and reversed unfolding), defined as the interval of frames starting from Q < 0.1 to Q > 0.9. To assess the agreement of rMD and SCPS trajectories with standard MD data, we adopted the following path similarity definition[210]:

$$s(k, k') = \frac{2}{N(N-1)} \sum_{i<j} \delta[M_{ij}(k) - M_{ij}(k')]$$

in which k and k' refer to two distinct trajectories and $M_{ij}(k)$ is an element of a matrix M describing the relative order of contacts formation for a trajectory, defined as:

$$M_{ij}(k) = \begin{cases} 1 & \text{if } t_i(k) < t_j(k) \\ 0 & \text{if } t_i(k) > t_j(k) \\ 1/2 & \text{if } t_i(k) = t_j(k) \end{cases}$$

with i and j running over all native contacts between Cα atoms and $t_i(k)$, $t_j(k)$ the times at which they are formed. A contact between two residues was considered as formed after at least 5 consecutive frames in which the distance between the two Cα atoms was ≤ 7.5 Å. This definition of similarity implies that $s(k, k') = 1$ if all the native contacts in the two trajectories are formed in the same order, while it is 0 if they form in a completely different order. Then, a distribution of self-similarity, denoted as A, was computed using for all possible pairs of reactive trajectories sampled with standard MD. Such a distribution reflects the intrinsic degree of heterogeneity of the folding pathways computed by standard MD. Distributions of cross-similarity, R_i, were then computed at each iteration step between pairs in which the k trajectory belongs to the standard MD set and the k' from the biased folding transitions. A random reference distribution R_r was produced to compare the similarity of rMD and SCPS to plain MD with the similarity between standard MD and a random sequence of native contact formation. To this end, an ensemble of 10^5 random cross-similarity distributions were generated for each protein. Each random cross-similarity distribution was computed between the order of contact formation matrices coming from the Anton trajectories and an equal number of random matrices M generated with series of contacts formation times randomly extracted with equal probability. The generated distributions are shown in figure SCPS-1. The level of agreement between each cross-similarity R_i distribution and the self-similarity distribution, A, was computed by means of the Kullback-Leibler divergence, D_{KL}, defined as:

$$D_{KL} = (A\|R_i) = \int_0^1 a(x) \log_2 \frac{a(x)}{r_i(x)} dx$$

At each SCPS iteration, we computed the D_{KL} between the cross-similarity distribution comparing SCPS and MD trajectories (R_i) and the self-similarity distribution of the MD folding paths (A). As a reference, we also computed the D_{KL} between the random distribution R_r calculated comparing random sequences of native contact formation with MD trajectories and the self-similarity distribution A. The results, reported in figure SCPS-2, show that SCPS produces folding mechanisms that are statistically indistinguishable from those sampled by plain MD, with no significant loss of information. In 4 out of 5 of the simulated proteins, the D_{KL} distance between R_i and A is consistently lower than the distance between the random cross-similarity R_r and A. The only exception is Trp-cage, for which both R_i and R_r are indistinguishable from A. Such an exception can be explained by the trivial topology of the Trp-Cage implying a heterogeneous folding mechanism, in which many different sequences of native contact formation can be realized with comparable probability.
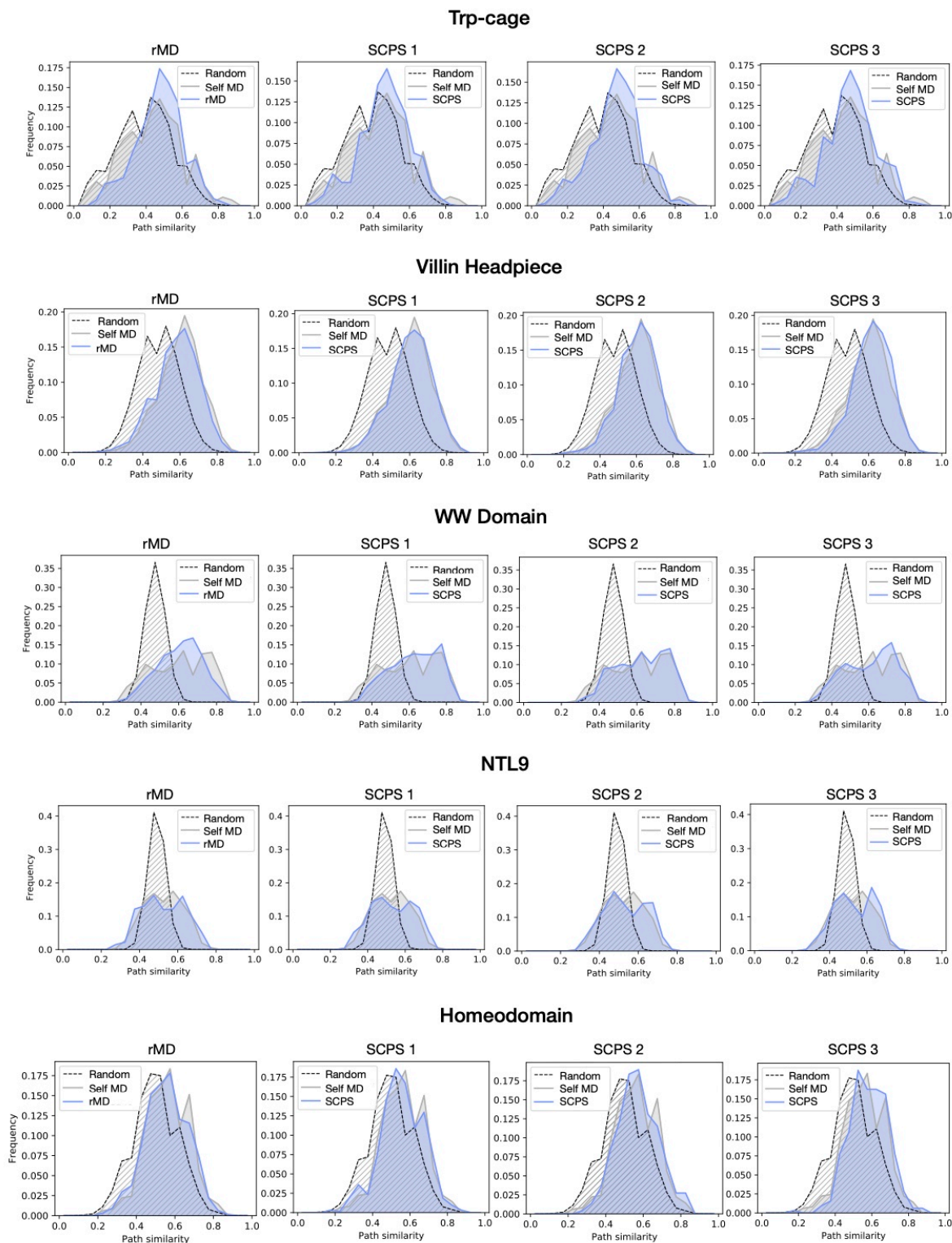
SCPS-1: Path similarity distributions. Three path similarity distributions are shown in each graph: (I) the distribution computed by comparing the order of native contact formation between biased folding trajectories (rMD or SCPS) with standard MD folding trajectories (cross-similarity R_i, blue; i indicates the iteration number); (II) the distribution obtained by comparing the order of native contact formation in the folding plain-MD trajectories within themselves (self-similarity, A, grey); (III) the path similarity computed by comparing the plain-MD trajectories with random sequences of native contact formation (random, R_r, dashed line). Figure from Terruzzi et al.[214] ⓒ ⓘ
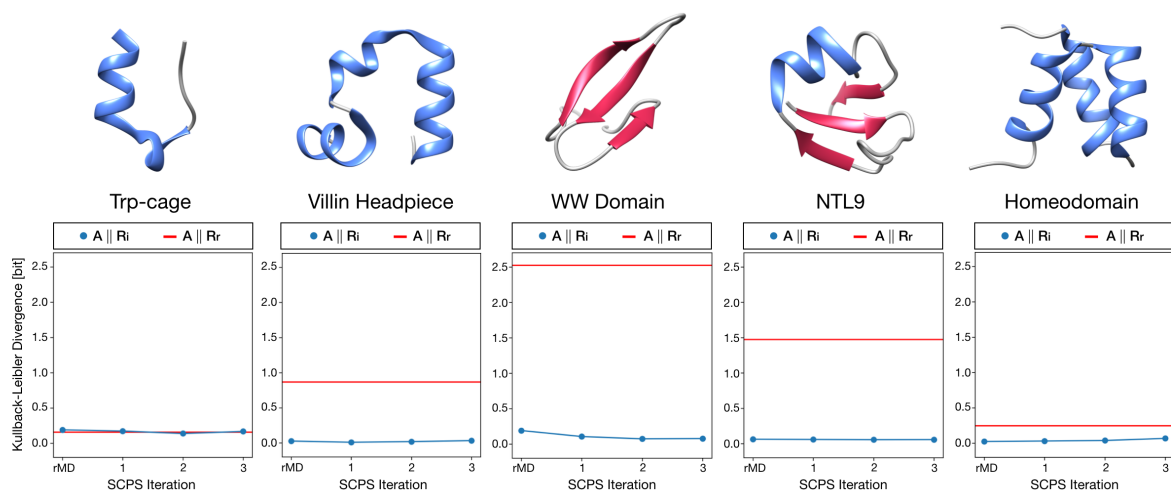
SCPS-2: Comparison between plain MD and biased (rMD and SCPS) trajectories. Each graph shows the D_{KL} between the cross-similarity distribution (R_i) of each iteration i and the self-similarity distribution (A) (blue dots). The average D_{KL} divergence between the random cross-similarity distributions (R_r) and the self-similarity distribution is depicted as a red line. These data show that both rMD and SCPS produce results that are identical to the one generated with plain MD and are different (with the exception of Trp-cage) from the randomly generated events. Figure from Terruzzi et al.[214] ⓒ①

We observed that the use of the SCPS approach did not lead to a significant improvement over rMD, as the folding events generated by rMD are already in very good agreement with standard MD. This finding is consistent with the notion that the CV we used in rMD simulations, namely $z(X)$, correlates well with the fraction of native contacts, which is considered a good reaction coordinate for the folding of small globular proteins[213,257]. On the other hand, we observed that SCPS provides different results, as compared to rMD, when the initial guess of RC is poorer such as in the case of prions propagation[214].
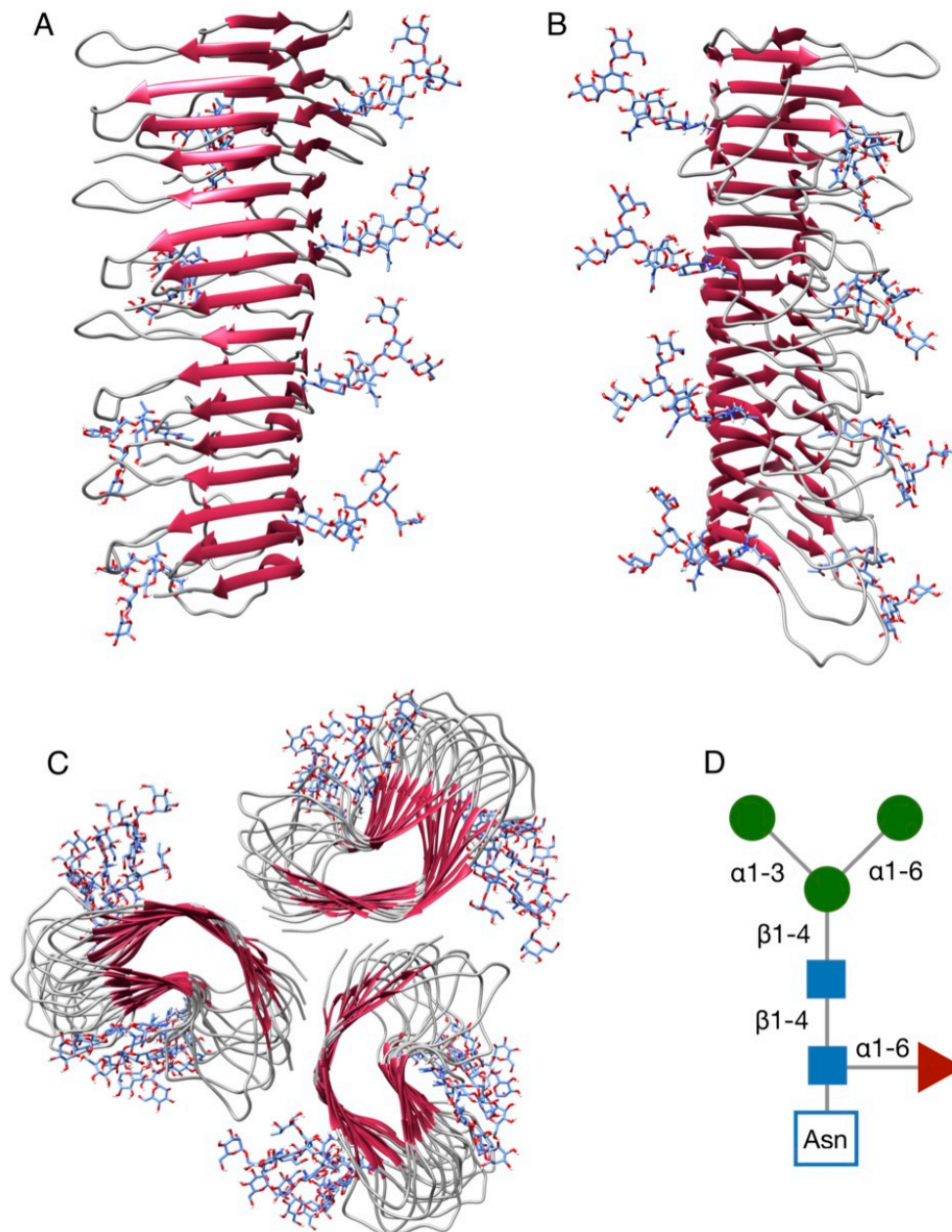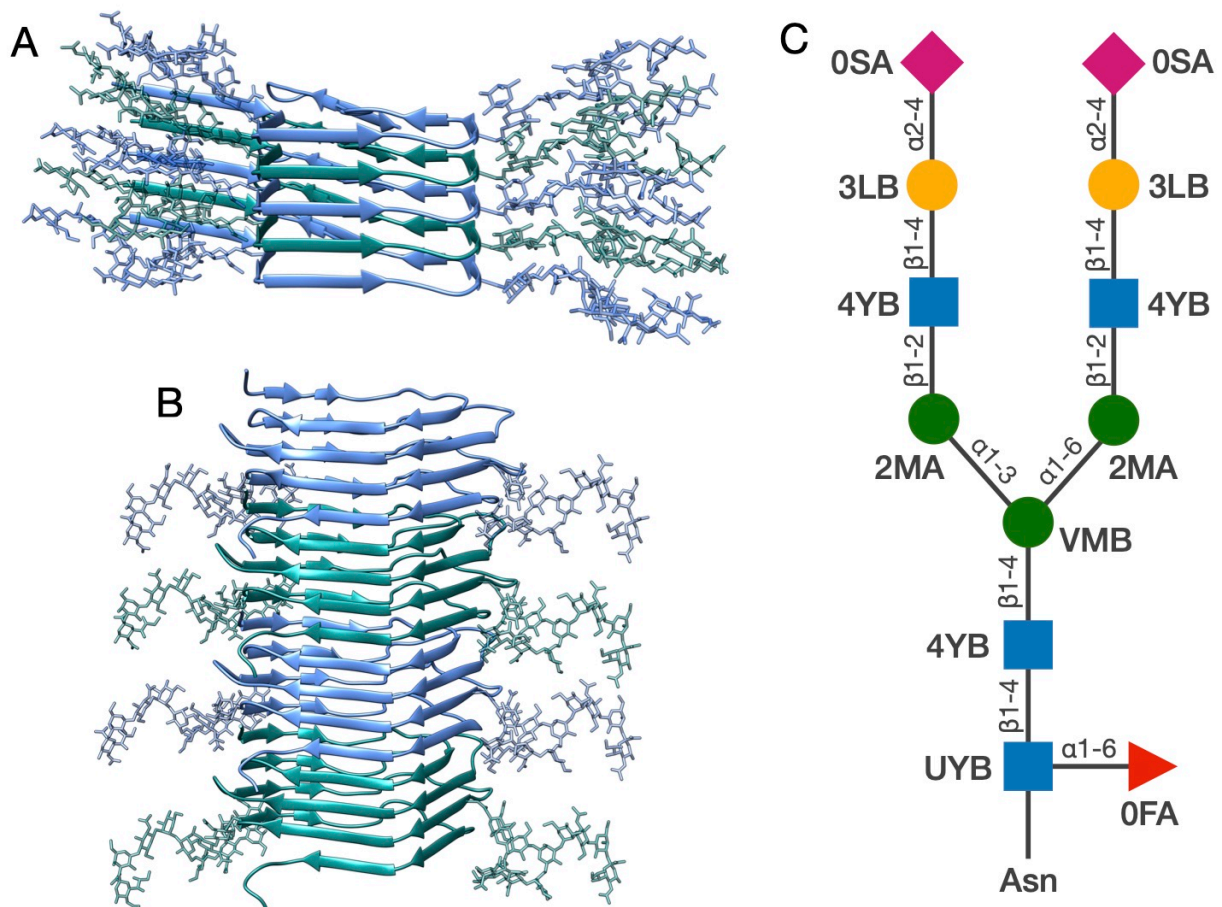
Supplementary Figures
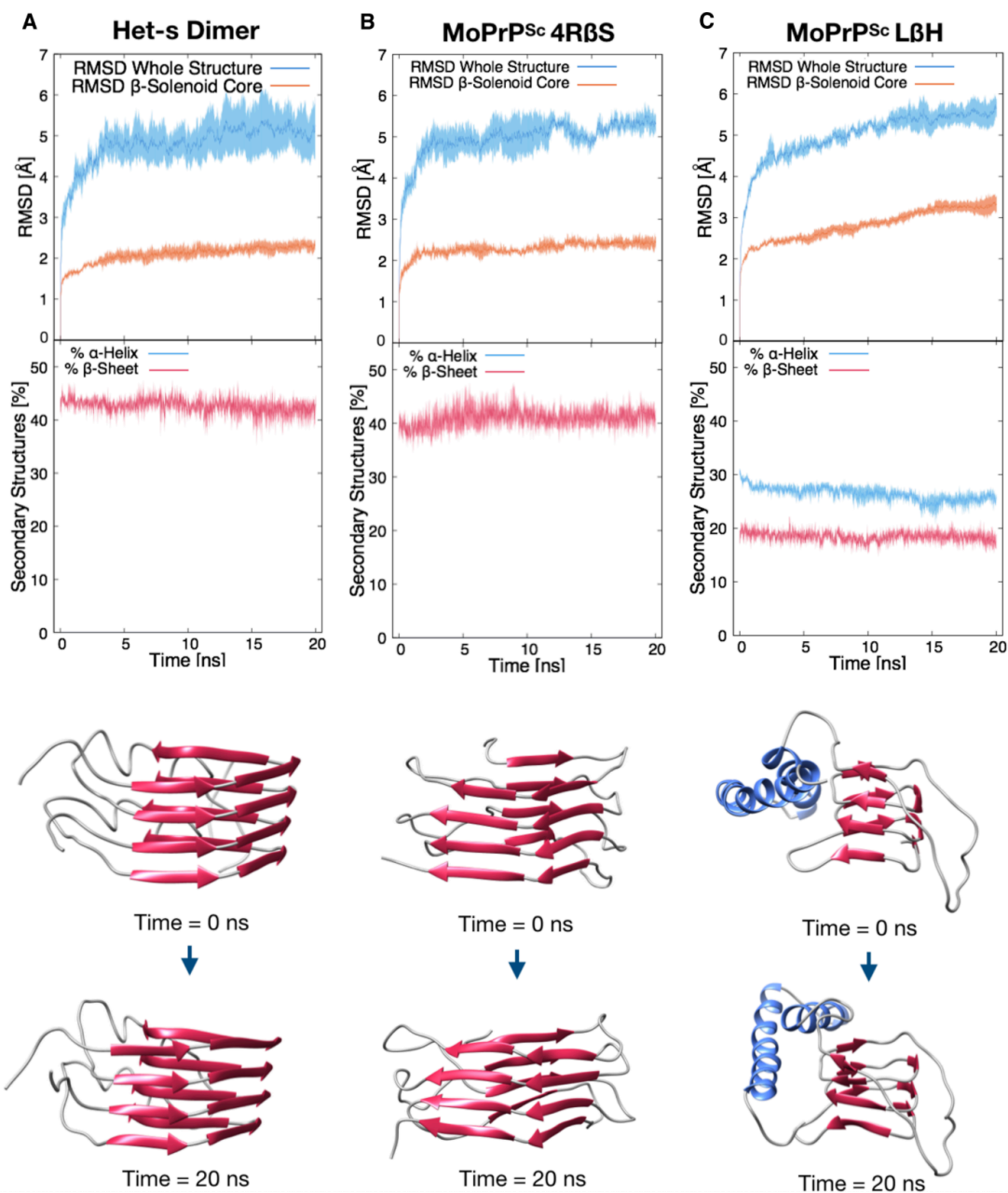
Supplementary Figure 1: Restrained MD simulations of the Het-s dimer as well as the PrP^{Sc} models 4RβS and LβH. Upper plots report the RMSD from initial configurations for the whole structures (blue lines) or the β-solenoid core (orange lines) of the different proteins during the 20 ns of restrained MD simulations. Filled curves represent the standard error of the mean. The graphs indicate a minor rearrangement of the β-solenoid core that is almost identical for the Het-s dimer and the 4RβS model, characterized by a RMSD of 2.3 ± 0.2 Å and 2.4 ± 0.2 Å respectively (calculated as the average of the three trajectories over the last 5 ns, ± standard deviation). In contrast, the β-helical core of the LβH model displays a higher RMSD (3.3 ± 0.3 Å). Lower graphs indicate the α-helical (blue lines) or β-sheet (red lines) content of each protein. The latter is stable for the three structures, due to the presence of the distance restraints. Figure from Spagnolli et al.[215] ©
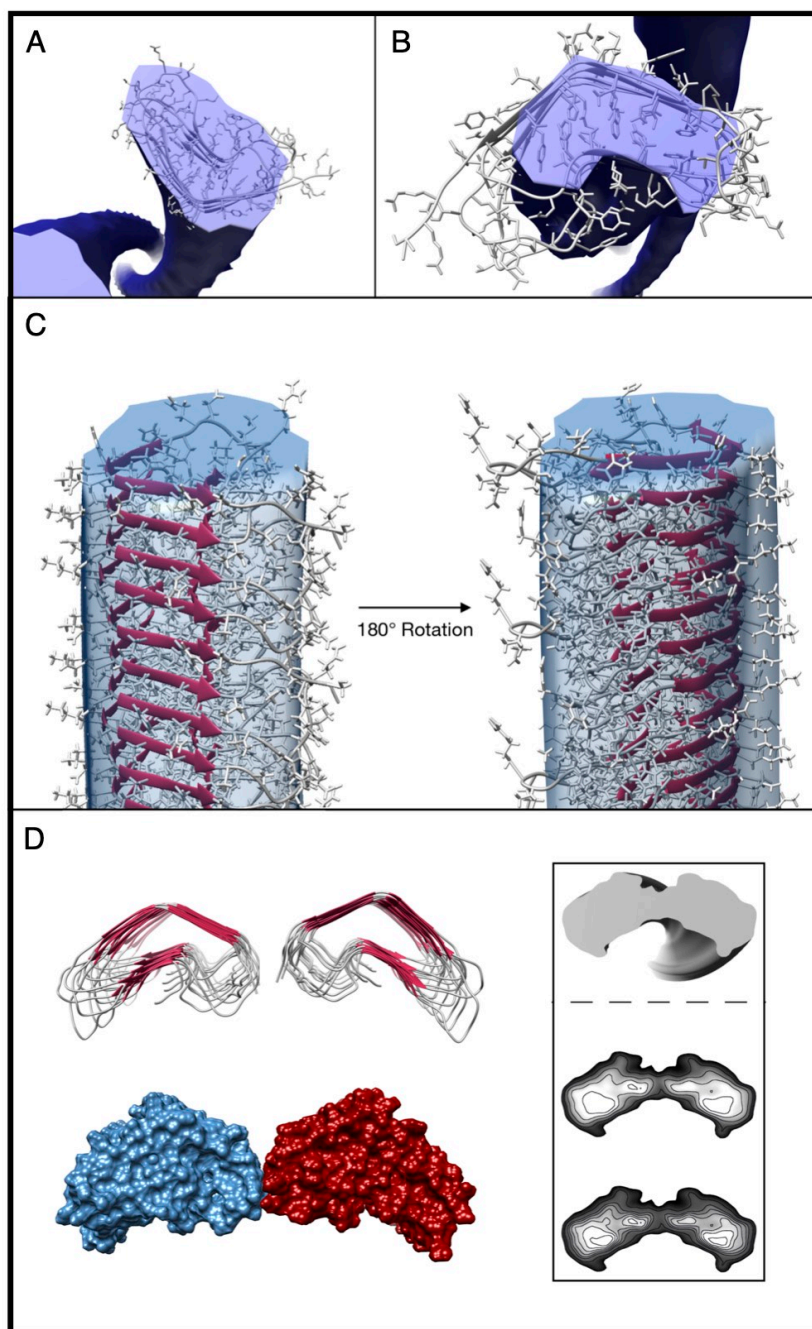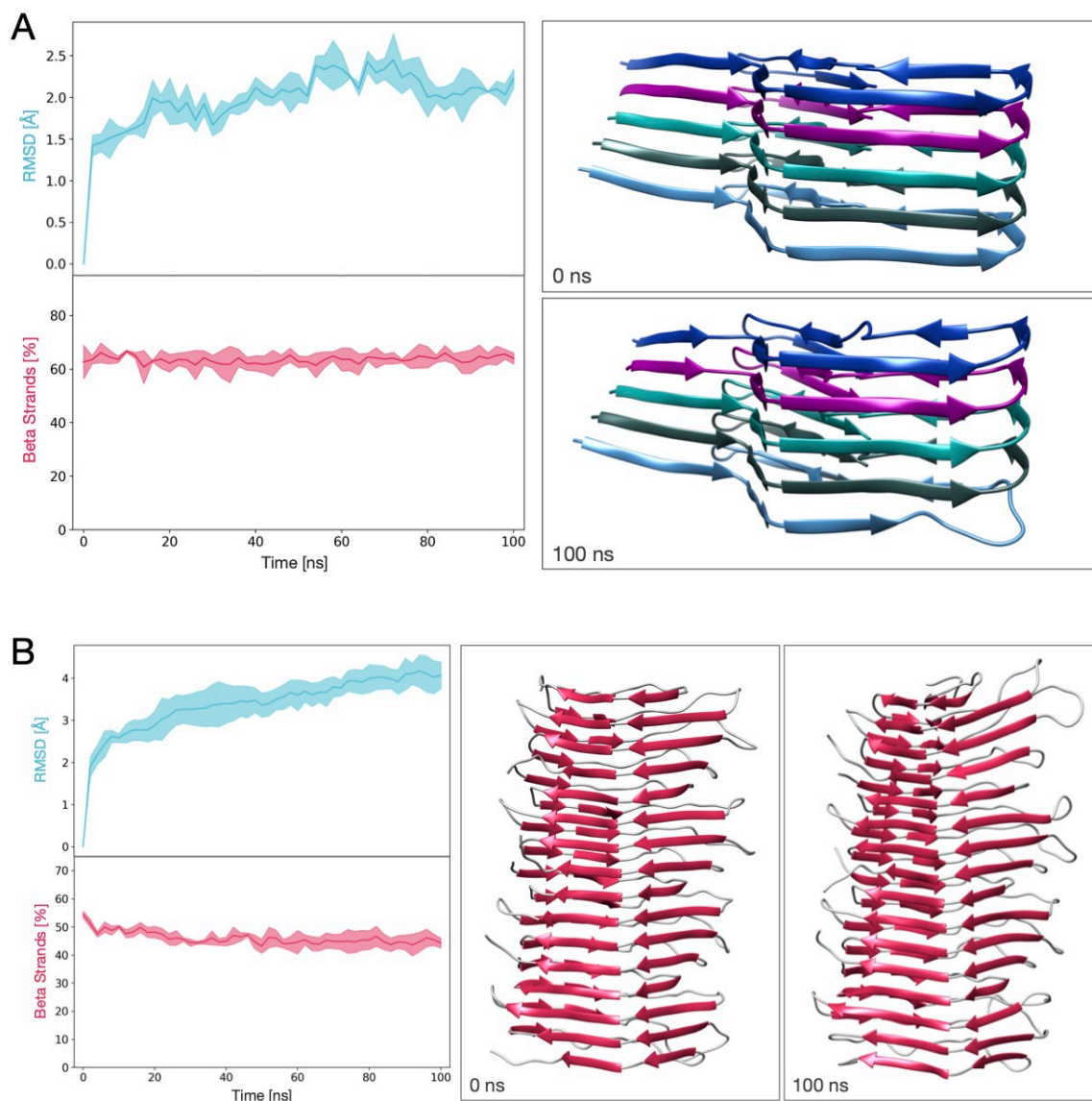
Supplementary Figure 2: 4RβS model of PrP^{Sc} superimposed to the Cryo-EM map of GPI-anchorless mouse PrP^{Sc}. The figure shows that the size of the 4RβS model fits with the protofilament cross-section (50 Å x 30 Å) reconstructed by cryo-EM on mouse GPI-anchorless PrP^{Sc}. (A) The contour level of the cryo-EM volume was set to 3.05 to match the measured protofilament diameter as determined from the raw electron micrograph. (B) Level of contouring was tightened to 3.60 to highlight the superimposition of the hydrophobic core of the 4RβS with the core electron density region of the protofilament. (C) Reconstruction of a protofilament composed of 4RβS monomers (stacked head-to-tail) and superimposed to the cryo-EM volume. (D) View of the cross-section of two PrP^{Sc} protofilaments compared with the orientation observed in the cryo-EM reconstruction. The cryo-EM data are retrieved from Vázquez-Fernández et al.[132]. Figure from Spagnolli et al.[215] (cc)(i)(cc)(i)

Supplementary Figure 3: Illustration of the energy minimized 4RβS tetramer carrying glycans at N180 and N196. (A, B) Two different orientations of the energy minimized tetrameric 4RβS structure with N-linked glycans. (C) Top view of a laterally stacked trimer of glycosylated 4RβS, compatible with the 2D crystals diffraction data[150]. (D) Schematics of the glycans: blue squares indicate N-acetylglucosamine, green circles indicate mannose and the red triangle indicate fucose. Figure from Spagnolli et al.[215]

Supplementary Figure 4: Glycosylated structures of the putative atypical propagative PrP and of the DTC-4RβS model of PrP^{Sc}. (A) Glycosylated structure of a PrP pentamer arranged as a PIRIBS, possibly reflecting the architecture of the atypical propagative PrP species. (B) Glycosylated structure of the DTC-4RβS model of PrP^{Sc}. Both structures are N-linked to GlcNAcMan$_3$Gal$_2$FucNeuNAc$_2$ glycans (two per monomer, at positions N180 and N196, mouse numbering), and displayed after energy minimization. A schematic of the glycan type is represented in (C). UYB and 4YB indicate N-acetylglucosamine, VMB and 2MA mannose, 3LB galactose, 0SA sialic acid and 0FA fucose. Absence of steric clashes was verified using UCSF Chimera. Both structures were subjected to 20 ns of restrained MD (see methods for details) before launching the standard MD simulations. Figure adapted from Spagnolli et al.[217] ©①

Supplementary Figure 5: MD simulations of the unglycosylated recombinant PrP amyloid structure and of the DTC-4RβS model of PrP^Sc. Results of standard MD simulations performed on the structure of recombinant PrP amyloid (PDB 6LNI, A) and on the DTC-4RβS model of PrP^Sc (B), both unglycosylated. The line and the filled curve indicate the mean and the standard error, respectively, computed on 3 performed simulations of 100 ns each. Figure adapted from Spagnolli et al.[217] © ①

Initial Conditions — Propagation from Fibril N-Terminus
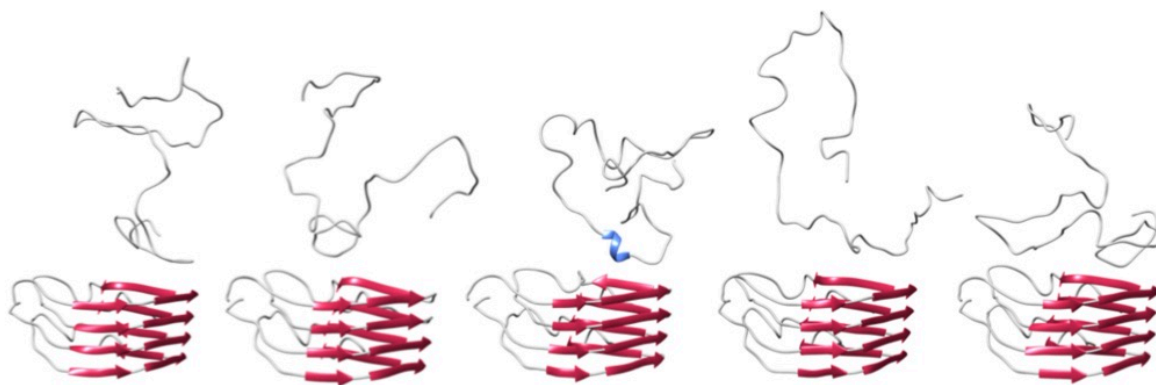
Initial Conditions — Propagation from Fibril C-Terminus
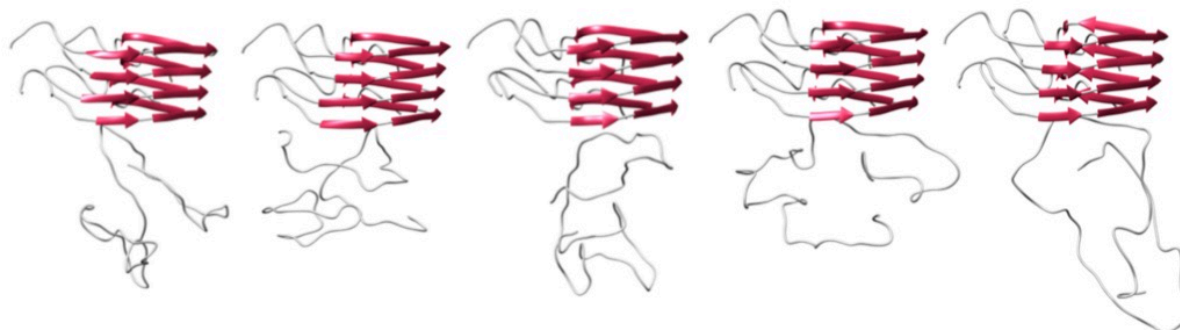
Supplementary Figure 6: Initial denatured conditions of HET-s propagation simulations. The figure illustrates the denatured conditions employed for the SCPS simulations of HET-s. Initial conditions for simulating propagation from the fibril N-terminus were obtained by introducing positional restraints on heavy atoms on the two C-terminal monomers while performing high-temperature MD simulations. The same protocol was employed for generating initial conditions for the C-terminal propagation but introducing the restraints on the N-terminal monomers. Figure from Terruzzi et al.[214]
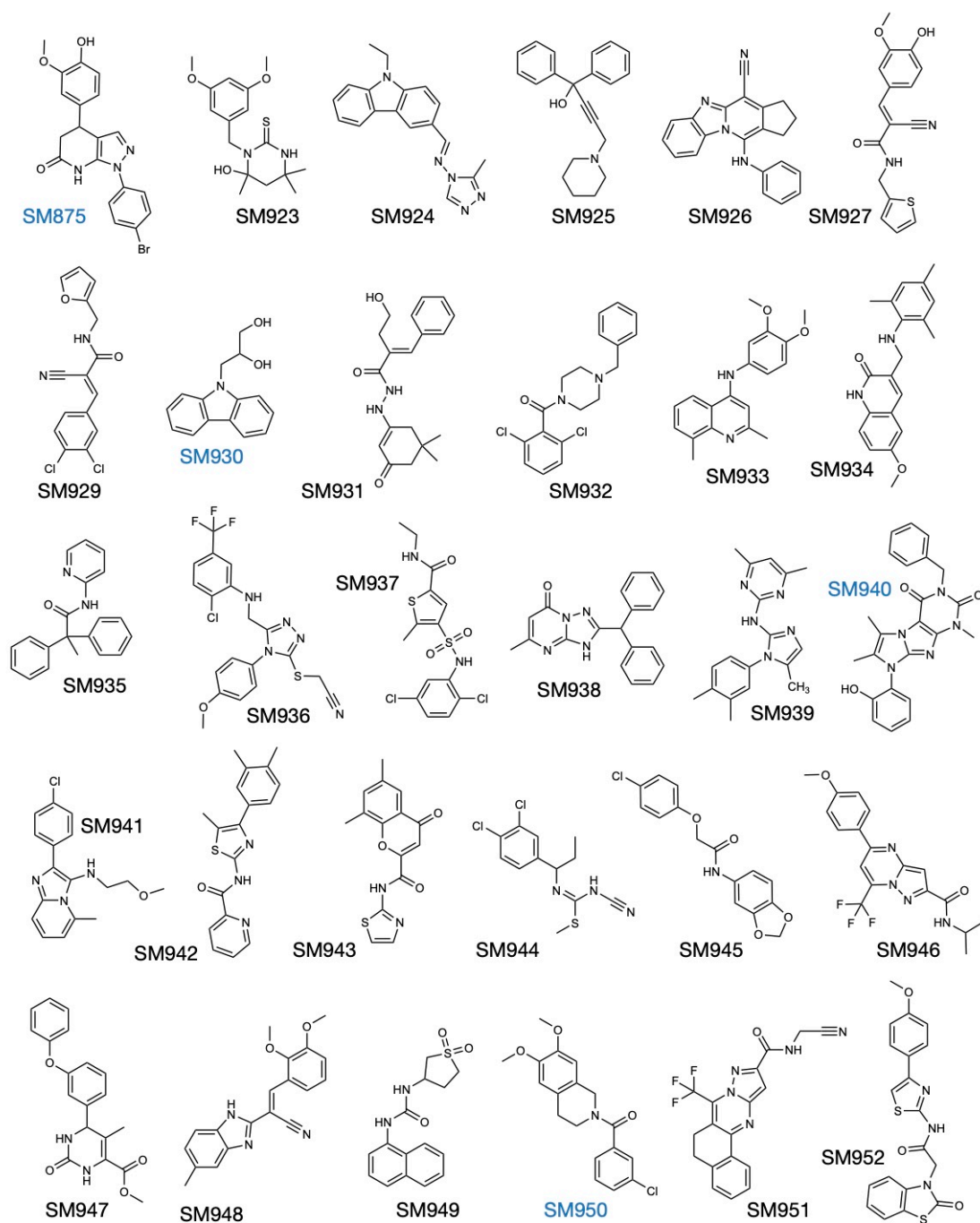
Supplementary Figure 7: Chemical structures of the 30 selected virtual hits. The figure shows the 2D structures of the selected virtual hits. The four compounds resulting positive in the cell-based assays are highlighted in blue. Courtesy of Andrea Astolfi. Figure adapted from Spagnolli et al.[67] ©①
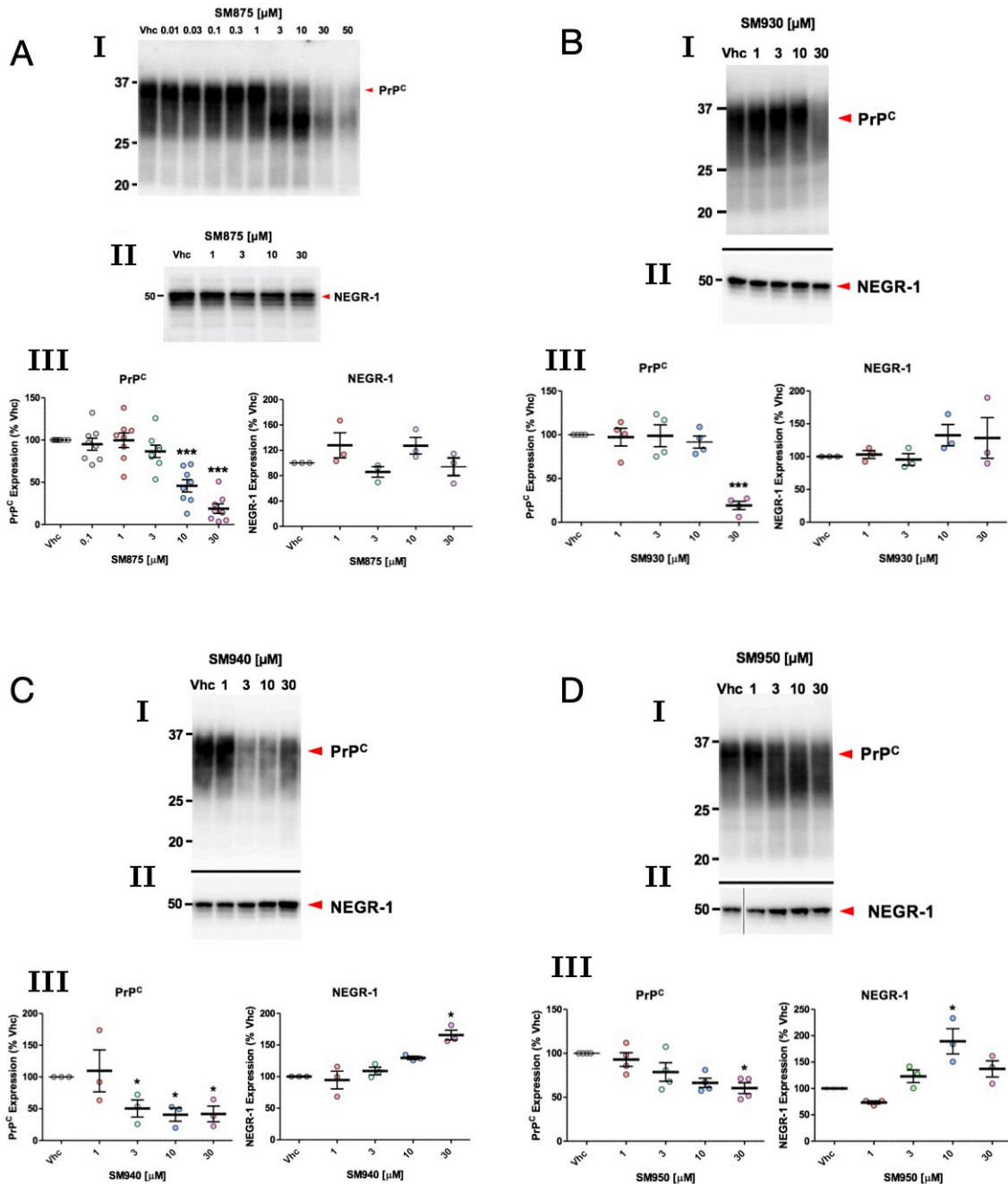
Supplementary Figure 8: Cell-based validation of selected virtual hits. HEK293 cells expressing mouse PrP or NEGR-1 were exposed to different concentrations of SM875 (A), SM930 (B), SM940 (C), or SM950 (D) or vehicle (0.1% DMSO, volume equivalent) for 48 h, lysed in detergent buffer, diluted in Laemmli sample buffer and analyzed by western blotting using anti-PrP (D18) or anti-NEGR-1 antibodies. Red arrowheads indicate the expected sizes of mature, fully glycosylated forms of PrP and NEGR-1. The compounds induce a dose-dependent suppression of PrP (I) but not control protein NEGR-1 (II). The graphs (III) show the densitometric quantification of the levels of full-length PrP or NEGR-1 from different biologically independent replicates. Each signal was normalized on the corresponding total protein lane (detected by UV of stain-free gels) and expressed as the percentage of the level in vehicle (Vhc)-treated controls (*p < 0.05, **p < 0.01, ***p < 0.005, by one-way ANOVA test). Panel A(I) and A(III) are also depicted in figure 4.5. Courtesy of Tania Massignan. Figure adapted from Spagnolli et al.[67] ©①
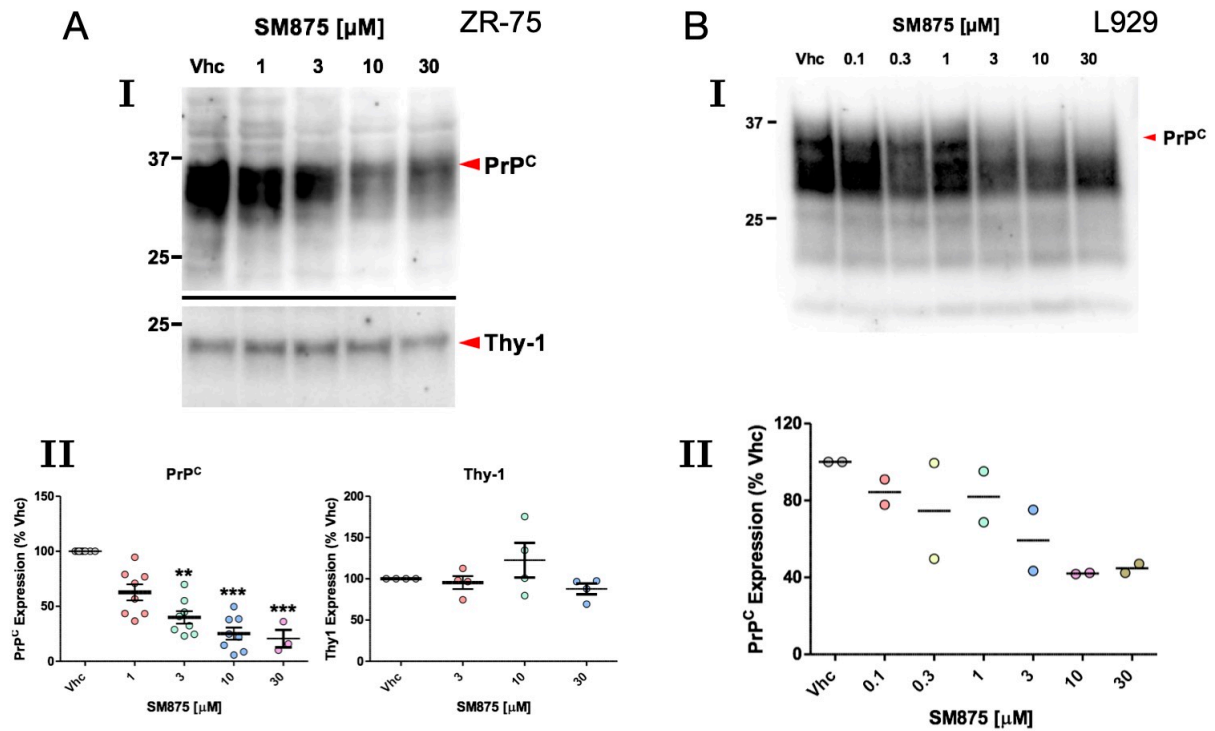
Supplementary Figure 9: SM875 lowers the PrP levels in different cell lines. Cells were treated with different concentrations of SM875 or vehicle for 48 h, lysed, and analyzed by western blotting. (A) SM875 suppresses PrP levels in ZR-75, but not Thy-1, in a concentration-dependent fashion. (B) Similar effects were observed in L929 fibroblasts. The panels show the western blotting analysis (I) and plots reporting the densitometric quantification of signals (II). Signals were normalized on the corresponding total protein lane and expressed as the percentage of vehicle-treated controls (*p < 0.05, **p < 0.01, ***p < 0.005, by one-way ANOVA test). Courtesy of Tania Massignan. Figure adapted from Spagnolli et al.[67] ⓒⓘ
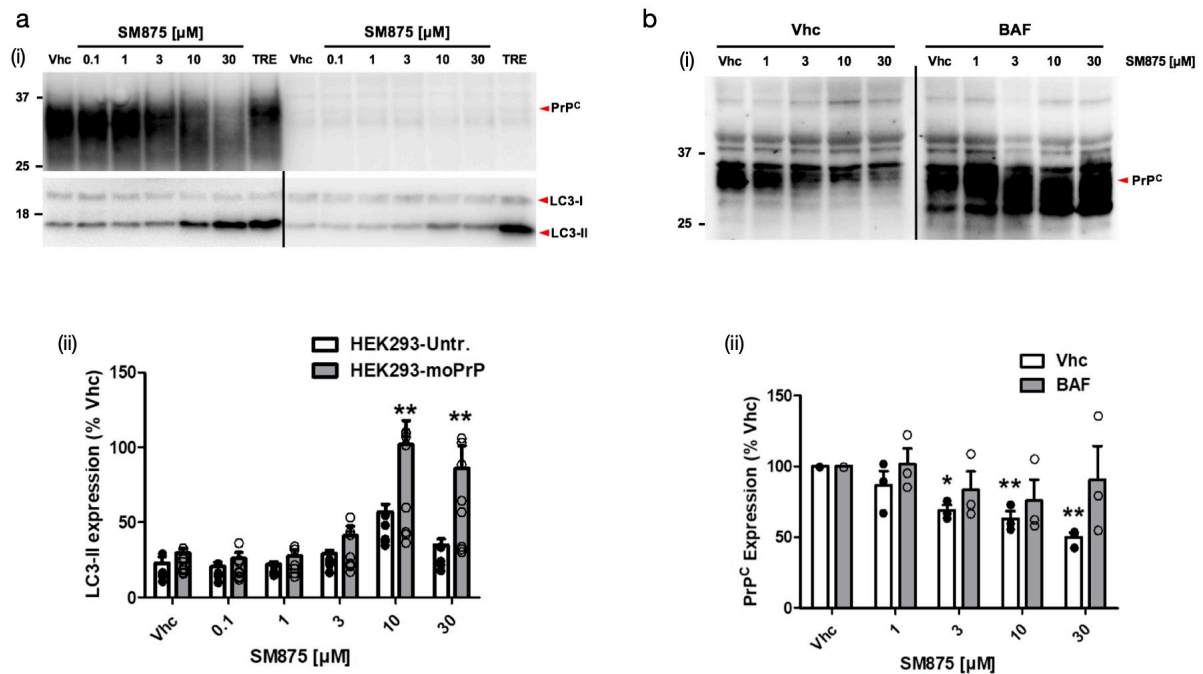
Supplementary Figure 10: SM875 induces the degradation of PrP by the lysosomes. We tested whether SM875 decreases PrP loads by inducing its lysosomal degradation by measuring the levels of the autophagosome-specific marker microtubule-associated protein 1A/1B-light chain 3-II (LC3-II). (A) PrP-transfected or untransfected HEK293 cells were treated with different concentrations of SM875 or vehicle and the levels of PrP, LC3-I, and LC3-II were evaluated by western blotting. Graphs show the densitometric quantification of LC3-II from independent replicates. SM875 (10–30 μM) increases LC3-II levels in a PrP-dependent manner. (B) ZR-75 cells endogenously expressing PrP were treated with different concentrations of SM875 in the presence or absence of autophagy–lysosomal inhibitor bafilomycin A1 (BAF, 10 μM) and PrP levels were evaluated by western blotting. Graphs show the densitometric quantification of full-length PrP from independent replicates. The autophagy inhibitor Bafilomycin A1 largely rescues SM875-induced PrP decrease in these cells (**p < 0.01, by one-way ANOVA test). Courtesy of Tania Massignan. Figure adapted from Spagnolli et al.[67] ©①
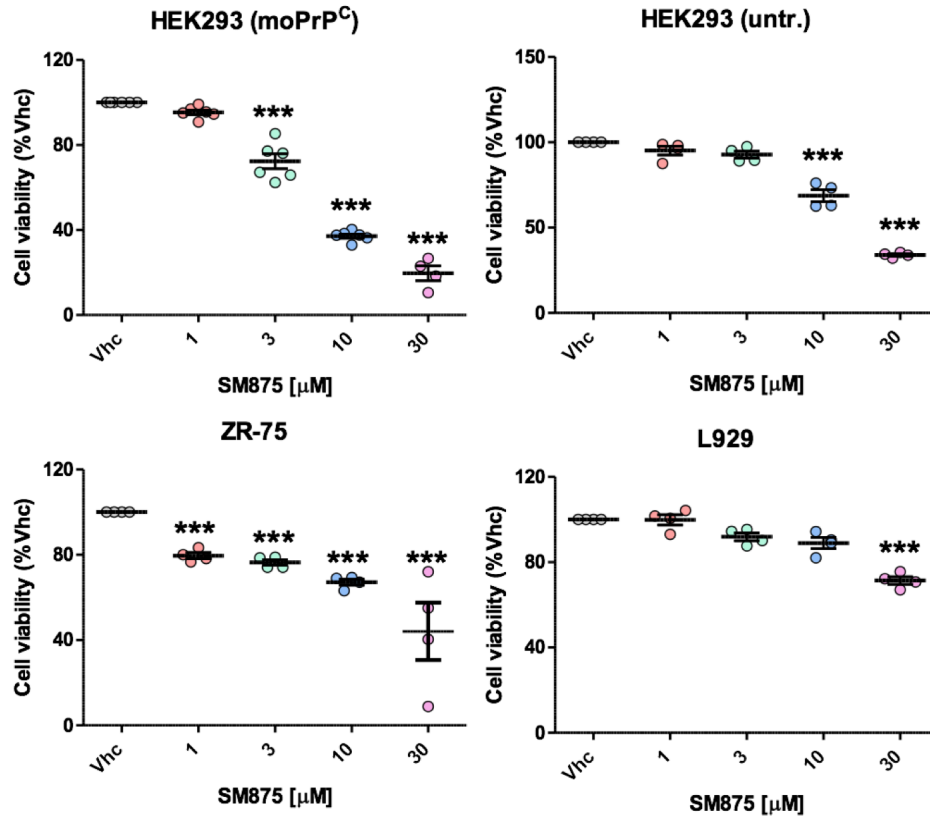
Supplementary Figure 11: Cell-dependent cytotoxic effect of SM875. We assessed the toxicity of SM875 in different cell lines by using the MTT assay (same incubation time and concentration used to study PrP suppression). Results show that SM875 exerts different effects on cell viability on the tested cell lines. In particular, $\sim$28% reduction of cell viability at 3 µM was observed in transfected HEK293; 32% reduction at 10 µM in untransfected HEK293, $\sim$24-33% reduction between 1 and 10 µM in ZR-75 cells and 29% reduction at 30 µM L929 fibroblasts. These results indicate that SM875 requires to be optimized to increase its potency and decrease its toxicity, before becoming suitable for preclinical test (*** p < 0.005). Courtesy of Tania Massignan. Figure adapted from Spagnolli et al.[67] ©①

Supplementary Tables

Descriptor	Threshold	Pocket
SiteScore[†]	≥ 0.8	0.95
DScore[†]	≥ 0.9	0.99
Exposure[†]	≤ 0.5	0.6
Enclosure[†]	≥ 0.7	0.66
Balance[†]	≥ 1.0	0.65
Volume[‡]	≥ 300 Å^3	468.6 Å^3
Depth[‡]	≥ 10 Å	10.4 Å
SimpleScore[‡]	≥ 0.5	0.38
DrugScore[‡]	≥ 0.5	0.23

Supplementary Table 1: Druggability descriptors of the pocket in the PrP folding intermediate. The table shows the computed SiteMap (†) and DogSiteScorer (‡) descriptors for the pocket identified on the centroid of cluster 3, sampled with the BF approach. The exposure, enclosure and depth properties provide different measures of the pocket shape. For the exposure property, the lower the score, the better the site. Conversely, tight binding pockets are characterized by a high enclosure. The balance property expresses the ratio between the relative hydrophobic and hydrophilic character of a pocket. SiteScore and DScore in Sitemap, as well as SimpleScore and DrugScore in DogSiteScorer are druggability estimators obtained by the different software as a linear combination of different descriptors. Thresholds values are slightly less stringent than the standard references for classical pockets, accounting for the innovative character of the target. Table adapted from Spagnolli et al.[67] ©①

Descriptor	Threshold	Representative Pocket Conformations									
		1	2	3	4	5	6	7	8	9	10
SiteScore[†]	≥ 0.8	n/a	0.75	0.79	0.74	0.73	0.62	0.84	0.94	0.95	1.00
DScore[†]	≥ 0.9	n/a	0.73	0.75	0.71	0.74	0.56	0.85	0.94	1.00	1.06
Exposure[†]	≤ 0.5	n/a	0.75	0.71	0.61	0.72	0.66	0.57	0.47	0.59	0.68
Enclosure[†]	≥ 0.7	n/a	0.65	0.74	0.65	0.56	0.59	0.65	0.75	0.64	0.63
Balance[†]	≥ 1.0	n/a	0.58	1.69	1.43	0.90	0.14	1.76	1.58	1.89	0.82
Volume[‡]	≥ 300 Å^3	169.8	154.4	219.5	262.5	210.1	62.0	283.5	313.5	390.4	284.2
Depth[‡]	≥ 10 Å	9.76	10.96	11.13	13.54	11.15	9.00	14.44	13.59	15.56	12.66
SimpleScore[‡]	≥ 0.5	0.18	0.34	0.32	0.41	0.39	0.37	0.36	0.52	0.50	0.42
DrugScore[‡]	≥ 0.5	0.07	0.25	0.25	0.34	0.29	0.31	0.36	0.53	0.48	0.35

Supplementary Table 2: Druggability descriptors of the refined pocket by restrianed MD. The table shows the computed SiteMap (†) and DogSiteScorer (‡) descriptors for the pocket conformations of the cluster centroids sampled with fixed-backbone MD simulations, starting from the intermediate state predicted with the BF approach. The conformation showing the best values of descriptors, that was subsequently employed for virtual screening, is highlighted in cyan. Table adapted from Spagnolli et al.[67] ©①

| Compound	MW	LogP	LogS pH 7.4	TPSA [Å^2]	HB-Donors	HB-Acceptors	Rot-Bonds
SM875	414.2	2.99	1.41	88.03	2	4	3
SM930	399.1	3.18	1.73	44.80	3	3	3
SM940	429.5	3.51	1.40	87.15	1	4	3
SM950	331.8	3.18	2.35	43.056	0	3	4

Supplementary Table 3: Predicted chemicophysical properties of the 4 validated compounds. The table shows predicted physicochemical properties of the compounds that revealed to be capable of suppressing PrP levels in cell-based assays. MW is the molecular weight, LogP is the predicted partition coefficient of octanol/water, LogS7.4 is the intrinsic aqueous solubility at pH of 7.4, TPSA is the topological polar surface area. HB = number of hydrogen bonds, Rot-Bonds = number of rotatable bonds.

Protein	Iteration	T [K]	N_C	k_R [kJ·mol^{-1}]	k_s [kJ·mol^{-1}]	k_ω [kJ·mol^{-1}]	N_{FC}	$<N_F>$
Trp-cage	rMD	290	16	$2 \cdot 10^{-3}$	-	-	13	7 ± 4
	SCPS 1	290	10	-	$2 \cdot 10^{-4}$	$6 \cdot 10^{-4}$	10	12 ± 5
	SCPS 2	290	10	-	$2 \cdot 10^{-4}$	$6 \cdot 10^{-4}$	10	14 ± 4
	SCPS 3	290	10	-	$2 \cdot 10^{-4}$	$6 \cdot 10^{-4}$	10	13 ± 4
Villin Headpiece	rMD	360	10	$5 \cdot 10^{-4}$	-	-	10	15 ± 5
	SCPS 1	360	10	-	$1.6 \cdot 10^{-4}$	$3.3 \cdot 10^{-4}$	10	16 ± 5
	SCPS 2	360	10	-	$1.6 \cdot 10^{-4}$	$3.3 \cdot 10^{-4}$	10	18 ± 2
	SCPS 3	360	10	-	$1.6 \cdot 10^{-4}$	$3.3 \cdot 10^{-4}$	10	16 ± 5
WW Domain	rMD	360	12	$5 \cdot 10^{-4}$	-	-	12	10 ± 4
	SCPS 1	360	12	-	$6 \cdot 10^{-5}$	$8 \cdot 10^{-5}$	11	7 ± 2
	SCPS 2	360	11	-	$6 \cdot 10^{-5}$	$8 \cdot 10^{-5}$	11	8 ± 3
	SCPS 3	360	11	-	$6 \cdot 10^{-5}$	$8 \cdot 10^{-5}$	11	8 ± 3
NTL 9	rMD	355	10	$5 \cdot 10^{-4}$	-	-	9	8 ± 6
	SCPS 1	355	9	-	$1.7 \cdot 10^{-4}$	$3.3 \cdot 10^{-4}$	8	13 ± 4
	SCPS 2	355	8	-	$1.7 \cdot 10^{-4}$	$3.3 \cdot 10^{-4}$	8	13 ± 4
	SCPS 3	355	8	-	$1.7 \cdot 10^{-4}$	$3.3 \cdot 10^{-4}$	8	13 ± 4
Homeo-domain	rMD	360	10	$5 \cdot 10^{-4}$	-	-	10	13 ± 6
	SCPS 1	360	10	-	$1.6 \cdot 10^{-4}$	$3.3 \cdot 10^{-4}$	10	9 ± 5
	SCPS 2	360	8	-	$1.6 \cdot 10^{-4}$	$3.3 \cdot 10^{-4}$	8	11 ± 6
	SCPS 3	360	5	-	$1.6 \cdot 10^{-4}$	$3.3 \cdot 10^{-4}$	5	12 ± 4

Supplementary Table 4: Simulations parameters for the SCPS validation. The table shows additional information regarding the folding simulations for SCPS validation. N_C is the number of initial conditions, T is the simulations temperature, k_R is the ratchet force constant, k_s and k_w are the SCPS force constants, N_{FC} is the number of sets (each set start from a different initial condition) for which at least one folding event is observed and $< N_F >$ is the average number of folding trajectories for each set.

Structural Data of SM875 Analogues
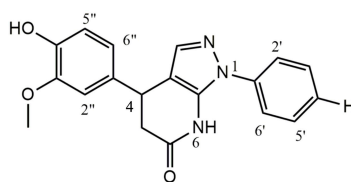
A₁: *1-(4-phenyl)-1,4,5,7-tetrahydro-4-(4-hydroxy-3)-6H-Pyrazolo[3,4-b]pyridin-6-one*

HPLC (RP-18 column, acetonitrile/water 1:1, UV detection at 254 nm, flow 5 mL · min^{-1}, retention time 4.5 min).

^{1}H NMR (400 MHz, CDCl$_3$):
δ_H 7.50 (m, phenyl), 7.30 (s, H-3), 6.89 (d, J=8.84, Hz H-5"), 6.79 (m, H-2" H-6"), 4.23 (dd, J= 9.8, 6.4 Hz, H-4), 3.87 (s, OCH$_3$), 2.95 (dd, J=16.2, 6.4 Hz, H-3) and 2.82(dd, J=16.2, 9.8 Hz, H-3).

^{13}C NMR (100 MHz, CDCl$_3$):
δ_C 171.1 (CONH), 147.3, 145.1, 137.6, 137.3, 133.5, 129.8, 128.3, 123.4, 119.2, 110.7, 105.8, 58.0 (OCH$_3$), 41.0 (C-4), 36.1 (C-3).

HR-ESI-MS:
HR-ESI-MS (+): experimental m/z 358.11603 (calculated for C$_{19}$H$_{17}$N$_3$NaO$_3$, 358.11627); experimental m/z 336.13414 (calculated for C$_{19}$H$_{18}$N$_3$O$_3$, 336.13427); HR-ESI-MS (-): experimental m/z 334.12054 (calculated for C$_{19}$H$_{16}$N$_3$O$_3$, 334.11971).

A₂: *1-(4-fluorophenyl)-4-(4-hydroxy-3-methoxyphenyl)-1,4,5,7-tetrahydro-6H-pyrazolo[3,4-b] pyridin-6-one*

HPLC (RP-18 column, acetonitrile/water 1:1, UV detection at 254 nm, flow 5 mL · min^{-1}, retention time 4 min).

^{1}H NMR (400 MHz, CDCl$_3$):
δ_H 8.06(br s, OH), 7.48(dd, J$_{HH}$ 8.8 Hz, ^{4}J$_{HF}$ 4.6 Hz, H-2' and H'), 7.28(s, H-3), 7.20(pseudo t, J$_{HH}$ 8.8 Hz, ^{3}J$_{HF}$ 8.1 Hz, H-3' and H-5'), 6.89(d, J 8.8 Hz, H-5"), 6.77(br s, H-2" and H-6"), 5.60(br s, NH), 4.22(dd, J 9.8, 6.3 Hz, H-4), 3.87(s,OCH$_3$), 2.94(dd, J 16.0, 6.3 Hz, Ha-5), 2.80(dd, J 16.0, 10.3 Hz, Hb-5).

^{13}C NMR (100 MHz, CDCl$_3$):
δ_C 170.5(C-6), 160.8(d, J$_{C-F}$ 253 Hz, C-F), 146.9(C-3", C-7a), 144.9(C-4"), 137.3(C-3), 133.7(C-1"), 133.0(C-1'), 125.0(d, J$_{C-C-C-F}$ 9 Hz, C-2', C-6'), 120.8(C-6'), 117.8(C-5"), 117.0(d, J$_{C-C-F}$ 21 Hz, C-3', C-5'), 114.0(C-2"), 105.5(C-3a), 55.2 OCH$_3$, 40.5(C-4), 36.2(C-5).

HR-ESI-MS:
HR-ESI-MS (+): experimental m/z 354.12448 ± 0.00500 [M+H]$^{+}$ (calculated for C$_{19}$H$_{17}$FN$_3$O$_3$, 354.12485), experimental m/z 376.10649 ± 0.00500 [M+Na]$^{+}$ (calculated for C$_{19}$H$_{16}$FN$_3$NaO$_3$, 376.10679). HR-ESI-MS (-): experimental m/z 352.11076 ± 0.00500 [M-H]$^{-}$ (calculated for C$_{19}$H$_{15}$FN$_3$O$_3$, 352.11030).

A₃: *1-(4-chlorophenyl)-1,4,5,7-tetrahydro-4-(4-hydroxy-3)-6H-pyrazolo[3,4-b]pyridin-6-one*

HPLC (RP-18 column, acetonitrile/water 1:1, UV detection at 254 nm, flow 5 mL · min⁻¹, retention time 4.5 min).
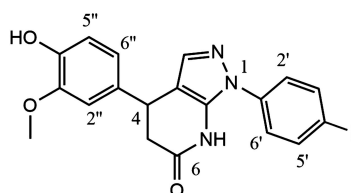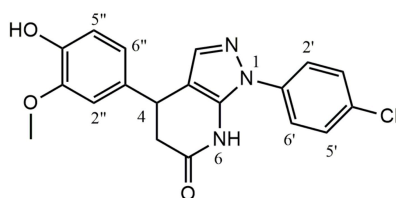
^{1}H NMR (400 MHz, CDCl$_3$):
δ$_H$ 7.78(br s, NH), 7.50(d, J=8.8 Hz, H-2'and H-6'), 7.45 (d, J=8.8 Hz, H-3'and H-5'), 7.3(s, H-3), 6.89 (d, J=8.5 Hz, H-5"), 6.77 (m, H-2", H-6"), 5.58 (bs, OH), 4.22(dd, J=6.4,9.9 Hz, H-4), 3.88(s, OCH$_3$), 2.95 (dd, J=16.2, 6.4 Hz, H-3) and 2.82(dd, J=16.2, 9.9 Hz, H-3).

^{13}C NMR (100 MHz, CDCl$_3$):
δ$_C$ 170.3 (CONH), 147.1, 145.0, 138.3, 136.0, 133.5, 130.0, 124.4, 120.7, 115.4, 114.2, 106.3, 60.4(OCH$_3$), 41.0 (C-4), 36.2 (C-3).

HR-ESI-MS:
HR-ESI-MS (+): experimental m/z 392.07713 (calculated for C$_{19}$H$_{16}$^{35}ClN$_3$NaO$_3$, 392.07724); experimental m/z 370.09590 (calculated for C$_{19}$H$_{17}$^{35}ClN$_3$O$_3$, 370.09530).

A₄: *4-(4-hydroxy-3-methoxyphenyl)-1-(4-iodophenyl)-4,5-dihydro-1H-pyrazolo[3,4-b]pyridin-6(7H)-one*

HPLC (RP-18 column, acetonitrile/water 1:1, UV detection at 254 nm, flow 5 mL · min⁻¹, retention time 4.5 min).
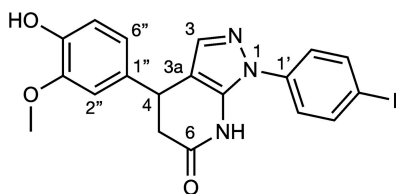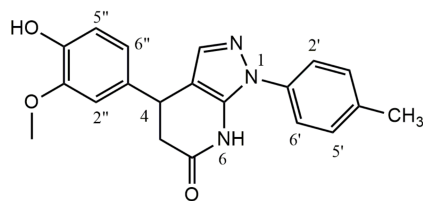
^{1}H NMR (400 MHz, CDCl$_3$):
δ$_H$ 7.24(s, 1H, H-3), 4.21(dd, J=9.8,6.3Hz, 1H, H-4), 2.93(dd, J=16.0,6.4Hz, 1H, H5-a), 2.79(dd, J=16.0,9.8Hz, 1H, H5-b), 8.55(broad s, 1H, NH), 7.28(d, J=8.6Hz, 2H, H-2' and H-6'), 7.80(d, J=8.6Hz, 2H, H-3' and H-5'), 6.76(s, 1H, H-2"), 6.88(d, J=8.8Hz, 1H, H-5"), 6.75(m, 1H, H-6"), 3.86(s, 3H, OCH$_3$).

^{13}C NMR (100 MHz, CDCl$_3$ + drops of CD$_3$OD):
δ$_C$ 138.0(C-3), 106.20(C-3a), 35.2(C-4), 40.7(C-5), 171.2(C-6), 147.5 or 147.4 or 145.0(C-7a, C-3" and C-4"), 138.3(C-1'), 124.8(C-2'), 138.5(C-3'), 92.7(C-4'),138.5(C-5'), 124.8(C-6'), 133.1(C-1"), 114.2(C-2"), 115.0(C-5"), 124.8(C-6"), 60.4(CH$_3$).

HR-ESI-MS:
HR-ESI-MS (+): experimental m/z 462.03050 ± 0.00042 [M+H]$^+$ (calculated for C$_{19}$H$_{17}$IN$_3$O$_3$, 462.03092), 484.01246 ± 0.00040 [M+Na]$^+$ (calculated for C$_{19}$H$_{16}$IN$_3$O$_3$Na, 484.01286); HR-ESI-MS (-): experimental m/z 460.01327 ± 0.00010 [M-H]$^-$ (calculated for C$_{19}$H$_{15}$IN$_3$O$_3$, 460.01637).

A₅: *1-(4-methylphenyl)-1,4,5,7-tetrahydro-4-(4-hydroxy-3)-6H-pyrazolo[3,4-b]pyridin-6-one*

HPLC (RP-18 column, acetonitrile/water 1:1, UV detection at 254 nm, flow $5 \text{ mL} \cdot \text{min}^{-1}$, retention time 4.5 min).
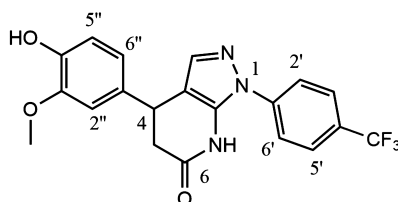
^{1}H NMR (400 MHz, CDCl$_3$):
δ_H 7.50-7.30(series of m, H-3, H-2'/H-6' and H-3'/H-5'), 4.22(m, H-3), 3.87(s, OCH$_3$), 2.96 and 2.82(two broad d, J=16 Hz, H-3), 2.42(s, CH$_3$ H-4').

^{13}C NMR deduced by HMBC experiment:
δ_C: 169.8 (CONH),146.5,146.1, 138.4, 137.0, 133.3, 130.4,120.1, 109.7,105.1, 60.9 (OCH$_3$), 35.5, 21.0 (CH$_3$-4').

HR-ESI-MS:
HR-ESI-MS (+): experimental m/z 372.13159 (calcuted for C$_{20}$H$_{19}$N$_3$NaO$_3$, 372.13186); experimental m/z 350.14964 (calculated for C$_{20}$H$_{20}$N$_3$O$_3$, 350.1499); HR-ESI-MS (-): experimental m/z 348.13591 (calculated for C$_{20}$H$_{18}$N$_3$O$_3$, 348.13537).

A₆:*4-(4-hydroxy-3-methoxyphenyl)-1-(4-(trifluoromethyl)phenyl)-1,4,5,7-tetrahydro-6H-pyrazolo [3,4-b]pyridin-6-one*

HPLC (RP-18 column, acetonitrile/water 1:1, UV detection at 254 nm, flow $5 \text{ mL} \cdot \text{min}^{-1}$, retention time 7 min).
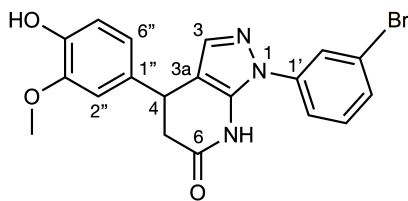
^{1}H NMR (400 MHz, CDCl$_3$):
δ_H 7.73-7.67(series of multiplets, H-2', H-6' and H-3', H-5'), 7.30(s, H-3), 6.89-6.77(series of multiplets, H-2'', H-5'' and H-6''), 4.20(m, H-4), 3.88(s, OCH$_3$), 2.97(br d, J 16.4 Hz, Ha-5), 2.80(br d, 16.4 Hz, Hb-5).

^{13}C NMR (100 MHz, CDCl$_3$ + 30μL CD$_3$OD):
δ_C 171.1(C-6), 147.3(C-3''), 146.5(C-7a), 145.1(C-3''), 140.4(C-1'), 137.9(C-3), 133.3(C-1''), 129.8(q, J$_{C-C-F}$ 35 Hz, C-3', C-5'), 125.5(C-2', C-6'), 123.4(q, J$_{C-F}$ 300 Hz, CF$_3$), 121.8(C-3', C-5'), 119.8(C-6''), 115.5(C-5''), 114.4(C-2''), 106(C-3a), 56.6(OCH$_3$), 40.9(C-4), 36.0(C-5).

HR-ESI-MS:
HR-ESI-MS(+): experimental m/z 404.12151 ± 0.00500 [M+H]$^+$ (calculated for C$_{20}$H$_{17}$F$_3$N$_3$O$_3$, 404.12165), 426.10351 ± 0.00500 [M+Na]$^+$ (calculated for C$_{20}$H$_{16}$F$_3$N$_3$NaO$_3$, 426.10360). HR-ESI-MS(-): experimental m/z 402.10769 ± 0.00500 [M-H]$^-$ (calculated for C$_{20}$H$_{15}$F$_3$N$_3$O, 402.10710).

A₇: *1-(3-bromophenyl)-4-(4-hydroxy-3-methoxyphenyl)-4,5-dihydro-1H-pyrazolo[3,4-b]pyridin-6(7H)-one*(**5**)

HPLC (RP-18 column, acetonitrile/water 1:1, UV detection at 254 nm, flow $5 \text{ mL} \cdot \text{min}^{-1}$, retention time 4.5 min).

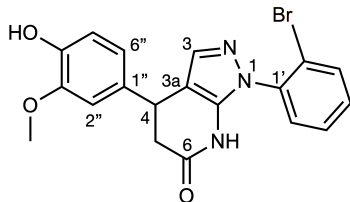^{1}H NMR (400 MHz, CDCl$_3$ + drops of CD$_3$OD):
δ_H 7.26(s, 1H, H-3), 4.18(dd, J=9.9,6.5Hz, 1H, H-4), 2.90(dd, J=16.0,6.5Hz, 1H, H5-a), 2.78(dd, J=16.0,9.9Hz, 1H, H5-b), 7.50-7.30(series of m, 4H, H-2', H-4', H-5' and H-6'), 6.67-6.86(series of m, 3H, H-2", H-5" and H-6"), 3.84(s,3H,OCH$_3$).

^{13}C NMR (100 MHz, CDCl$_3$ + drops of CD$_3$OD):
δ_C 138.4(C-3), 106.0(C-3a), 35.4(C-4), 40.9(C-5), 170.6(C-6), 144.9 or 138.6 or 146.9(C-7a, C-3" and C-4") 133.5, 131.1, 131.0, 126.1, 123.3, 121.4, 120.0, 114.8, 109.6(aromatic), 55.9(CH$_3$).

HR-ESI-MS:
HR-ESI-MS (+): experimental m/z 414.04423 $\pm$ 0.00055 [M+H]$^+$ (calculated for C$_{19}$H$_{17}$^{79}BrN$_3$O$_3$, 414.04478), 436.02623 $\pm$ 0.00050 [M+Na]$^+$ (calculated for C$_{19}$H$_{16}$^{79}BrN$_3$O$_3$Na, 436.02673); HR-ESI-MS (-): experimental m/z 412.02769 $\pm$ 0.00254 [M-H]$^-$ (calculated for C$_{19}$H$_{15}$^{79}BrN$_3$O$_3$, 412.03023).

A₈: *1-(2-bromophenyl)-4-(4-hydroxy-3-methoxyphenyl)-4,5-dihydro-1H-pyrazolo[3,4-b]pyridin-6(7H)-one*

HPLC (RP-18 column, acetonitrile/water 1:1, UV detection at 254 nm, flow $5 \text{ mL} \cdot \text{min}^{-1}$, retention time 4.5 min).

^{1}H NMR (400 MHz, CDCl$_3$ + drops of CD$_3$OD):
δ_H 7.31(s, 1H, H-3), 4.22(dd, J=9.0,6.5Hz, 1H, H-4), 2.92(dd, J=16.3,6.5Hz, 1H, H5-a), 2.75(dd, J=16.3,9.0Hz, 1H, H5-b), 7.50-7.34(series of m, 3H, H-4', H-5' and H-6'), 7.70(d, J=8.0Hz, 1H, H-3'), 6.74(broad s, 1H, H-2"), 6.85(d, J=8.5Hz, 1H, H-5"), 6.75(dd, J=8.0,2.0Hz, 1H, H-6"), 3.84(s, 3H, OCH$_3$).

^{13}C NMR (100 MHz, CDCl$_3$ + drops of CD$_3$OD):
δ_C 138.0(C-3), 104.2(C-3a), 35.3(C-4), 41.1(C-5), 170.4(C-6), 139.0(C-7a), 133.7(C-3'), 131.4 or 129.9 or 128.7 or 119.9(C-4', C-5', C-6' and C-6"), 133.8(C-1"), 114.8 or 119.9(C-2" and C-5"), 146.9 or 144.9(C-3" and C-4"), 55.9(CH$_3$).

HR-ESI-MS:
HR-ESI-MS (+): experimental m/z 414.04427 $\pm$ 0.00051 [M+H]$^+$ (calculated for C$_{19}$H$_{17}$^{79}BrN$_3$O$_3$, 414.04478), 436.02619 $\pm$ 0.00054 [M+Na]$^+$ (calculated for C$_{19}$H$_{16}$^{79}BrN$_3$O$_3$Na, 436.02673); HR-ESI-MS(-): experimental m/z 412.02781 $\pm$ 0.00242 [M-H]$^-$ (calculated for C$_{19}$H$_{15}$^{79}BrN$_3$O$_3$, 412.03023).
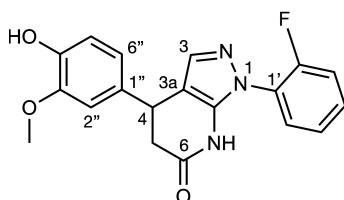
A₉: *1-(2-fluorophenyl)-4-(4-hydroxy-3-methoxyphenyl)-4,5-dihydro-1H-pyrazolo[3,4-b]pyridin-6(7H)-one*

HPLC (RP-18 column, acetonitrile/water 1:1, UV detection at 254 nm, flow 5 mL · min⁻¹, retention time 4.5 min).
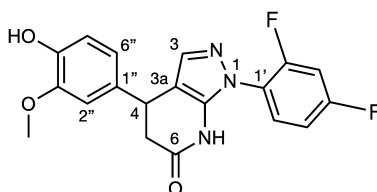
^{1}H NMR (400 MHz, CDCl₃):

δ_H 7.34(s, 1H, H-3), 4.23(dd, J=9.4,6.6Hz, 1H, H-4), 2.92(dd, J=16.2,6.6Hz, 1H, H5-a), 2.76(dd, J=16.2,9.4Hz, 1H, H5-b), 8.23(broad s, 1H, NH), 7.24(m, 2H, H-3' and H-6'), 7.58(ddd, J=8.0,7.8,1.6Hz, 1H, H-4'), 7.43(m, 1H, H-5'), 6.77(s, 1H, H-2"), 5.75(broad s, 1H, OH), 6.89(d, J=7.9Hz, 1H, H-5"), 6.78(d, J=7.9Hz, 1H, H-6"), 3.87(s, 3H, OCH₃).

^{13}C NMR (100 MHz, CDCl₃):

δ_C 128.0 or 133.0(C-3 and C-1"), 105.0(C-3a), 35.4(C-4), 41.0(C-5), 170.3(C-6), 138.8(d, J$_{C-C-C-C-F}$ 3Hz, C-7a), 125.2(d, J$_{C-C-F}$ 12Hz, C-1'), 155.4(d, J$_{C-F}$ 250Hz, C-2'), 116.9(d, J$_{C-C-F}$ 20Hz, C-3'), 130.4(d, J$_{C-C-C-F}$ 8Hz, C-4'), 125.4(d, J$_{C-C-C-F}$ 3.8Hz, C-5'), 128.0(d, J$_{C-C-C-F}$ 17Hz, C-6'), 114.7 or 109.6(C-2" and C-5"), 144.9 or 146.9(C-3" and C-4"), 120.0(C-6"), 56.0(CH₃).

HR-ESI-MS:

HR-ESI-MS(+) : experimental m/z 354.12427 ± 0.00058 [M+H]⁺ (calculated for C₁₉H₁₇FN₃O₃, 354.12485), 376.10614 ± 0.00065 [M+Na]⁺ (calculated for C₁₉H₁₆FN₃O₃Na, 376.10679).

A₁₀: *1-(2,4-difluorophenyl)-4-(4-hydroxy-3-methoxyphenyl)-4,5-dihydro-1H-pyrazolo[3,4-b] pyridin-6(7H)-one*

HPLC (RP-18 column, acetonitrile/water 1:1, UV detection at 254 nm, flow 5 mL · min⁻¹, retention time 4.5 min).
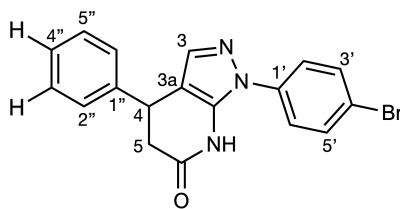
^{1}H NMR (400 MHz, CDCl₃):

δ_H 7.33(s, 1H, H-3), 4.22(dd, J=9.3,6.5Hz, 1H, H-4), 2.90(dd, J=16.1,6.5Hz, 1H, H5-a), 2.75(dd, J=16.1,9.3Hz, 1H, H5-b), 8.49(broad s, 1H, NH), 6.76(s, 1H, H-3'), 7.01 or 7.00(series of m, 2H, H-5' and H-2"), 7.55(m, 1H, H-6'), 4.99(broad s, 1H, OH), 6.90(d, J=8.1, 1H, H-5"), 6.77(d, J=8.2, 1H, H-6"), 3.87(s, 3H, OCH₃).

^{13}C NMR (100 MHz, CDCl₃): δ_C 138.7(C-3), 104.8(C-3a), 35.2(C-4), 40.9(C-5), 170.9(C-6), 147.2(C-7a), 121.5(dd, J$_{C-C-F}$ 12Hz, J$_{C-C-C-F}$ 4Hz, C-1'), 156.6(dd, J$_{C-F}$ 254Hz, J$_{C-C-C-F}$ 13Hz, C-2'), 105.0(dd, J$_{C-C-F}$ 26,23Hz, C-3'), 162.7(dd, J$_{C-F}$ 253Hz, J$_{C-C-C-F}$ 11Hz, C-4'), 112.4(dd, J$_{C-C-F}$ 22.4Hz, J$_{C-C-C-C-F}$ 3.3Hz, C-5'), 129.4(d, J$_{C-C-C-F}$ 10Hz, C-6'), 133.5(C-1"), 109.8(C-2"), 145.0 or 147.11(C-3" and C-4"), 114.9(C-5"), 119.8(C-6"), 55.8(CH₃).

HR-ESI-MS:

HR-ESI-MS (+): experimental m/z 372.11481 ± 0.00061 [M+H]⁺ (calculated for C₁₉H₁₆F₂N₃O₃, 372.11542), 394.09662 ± 0.00075 [M+Na]⁺ (calculated for C₁₉H₁₅F₂N₃O₃Na, 394.09737); HR-ESI-MS (-): experimental m/z 370.09824 ± 0.00263 [M-H]⁻ (calculated for C₁₉H₁₄F₂N₃O₃, 370.10087).

A₁₁: *1-(4-bromophenyl)-4-phenyl-1,4,5,7-tetrahydro-6H-pyrazolo[3,4-b]pyridin-6-one*

HPLC (RP-18 column, acetonitrile/water 1:1, UV detection at 254 nm, flow 5 mL · min⁻¹, retention time 11 min).

¹H NMR (400 MHz, CDCl₃):
δ_H 8.35(br s, 1H, NH), 7.60(br d, J=7.6 Hz, 2H, H-3' and H-5'), 7.38(d, J=7.6 Hz, 2H, H-2' and H-6'), 7.37-7.24(series of multiplets, 6H, -Phenyl and H-3), 4.27(dd, J=8.9, 6.7, 1H, H-4), 2.96(dd, J=16.1, 6.7 Hz, 1H, H$_a$-5), 2.82(dd, J=16.1, 8.9 Hz, 1H, H$_b$-5).
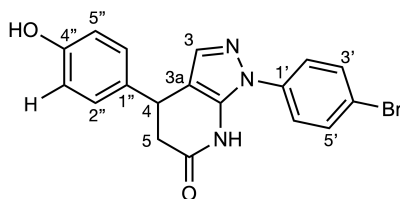
¹³C NMR (100 MHz, CDCl₃):
δ_C 170.3(C-6), 141.8(C-1"), 138.3(C-1'), 137.3(C-3), 132.9(C-3' and C-5'), 129.0(C-3" and C-5"), 127.4, 127.2(C-2" and C-6"), 124.5(C-2' and C-6'), 121.7(C-4'), 105.7(C-3$_a$), 40.6(C-5), 35.1(C-4).

HR-ESI-MS:
HR-ESI-MS (+): experimental m/z 390.02090 ± 0.00051 [M+Na]⁺ (calculated for C₁₈H₁₄⁷⁹BrN₃NaO, 390.02125).
HR-ESI-MS (-): experimental m/z 366.02537 ± 0.00125 [M-H]⁻ (calculated for C₁₈H₁₃⁷⁹BrN₃O, 366.02475).

A₁₂: *1-(4-bromophenyl)-4-(4-hydroxyphenyl)-1,4,5,7-tetrahydro-6H-pyrazolo[3,4-b]pyridin-6-one*

HPLC (RP-18 column, acetonitrile/water 1:1, UV detection at 254 nm, flow 5 mL · min⁻¹, retention time 6 min).

¹H NMR (400 MHz, CDCl₃ + drops of CD₃OD):
δ_H 7.62(d, J=8.6 Hz, 2H, H-3' and H-5'), 7.59(s, 1H, H-3), 7.42(d, J=8.6 Hz, 2H, H-2' and H-6'), 7.10(d, J=8.7 Hz, 2H, H-2" and H-6"), 6.80(d, J=8.7 Hz, 2H, H-3" and H-5"), 4.15(m, 1H, H-4), 2.89(br d, J=16.0 Hz, 1H, H$_a$-5), 2.78(br d, J=16.0 Hz, 1H, H$_b$-5).

HR-ESI-MS:
HR-ESI-MS(+): experimental m/z 384.03402 ± 0.00050 [M+H]⁺ (calculated for C₁₈H₁₅⁷⁹BrN₃O₂ 384.03422); 406.01590 ± 0.0070 [M+Na]⁺ (calculated for C₁₈H₁₄⁷⁹BrN₃O₂Na 406.01616).

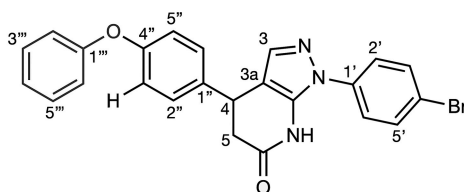**A₁₃**: *1-(4-bromophenyl)-4-(4-phenoxyphenyl)-1,4,5,7-tetrahydro-6H-pyrazolo[3,4-b]pyridin-6-one*

HPLC (RP-18 column, acetonitrile/water 1:1, UV detection at 254 nm, flow 5 mL · min⁻¹, retention time 8 min).
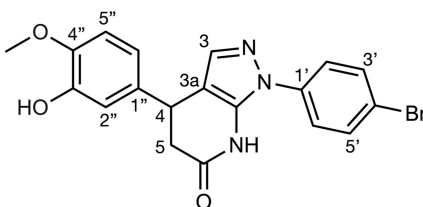
^{1}H NMR (400 MHz, CDCl₃):
δ_H 8.20(br s, 1H, NH), 7.60(d, J=8.2 Hz, 2H, H-3' and H-5'), 7.46(d, J=8.2 Hz, 2H, H-2' and H-6'), 7.32-7.00(series of multiplets, 9H, aromatic protons), 7.30(s, 1H, H-3), 4.27(dd, J=8.9, 6.5 Hz, 1H, H-4), 2.97(dd, J=16.1, 6.5 Hz, 1H, H$_a$-5), 2.82(dd, J=16.1, 8.9 Hz, 1H, H$_b$-5).

^{13}C NMR (100 MHz, CDCl₃):
δ_C 170.3(C-6), 156.9, 156.7, 141.8, 138.3, 137.4, 133.1, 129.9, 129.5(x2), 128.6, 125.2, 124.5, 119.5(x2), 118.7(x2), 105.7(C-3a), 40.7(C-5), 34.5(C-4).

HR-ESI-MS:
HR-ESI-MS (+): experimental m/z 460.06547 ± 0.00080, [M+H]⁺ (calculated for C₂₄H₁₉^{79}BrN₃O₂ 460.06552); m/z 482.04745 ± 0.0050, [M+Na]⁺ (calculated for C₂₄H₁₈^{79}BrN₃Na₁O₂ 482.04746). HR-ESI-MS (-): experimental m/z 458.05182 ± 0.00278, [M-H]⁻ (calculated for C₂₄H₁₇^{79}BrN₃O₂ 458.05096).

A₁₄: *1-(4-bromophenyl)-4-(3-hydroxy-4-methoxyphenyl)-1,4,5,7-tetrahydro-6H-pyrazolo[3,4-b]pyridin-6-one*

HPLC (RP-18 column, acetonitrile/water 1:1, UV detection at 254 nm, flow 5 mL · min⁻¹, retention time 6 min).

^{1}H NMR (400 MHz, CDCl₃):
δ_H 7.82(br s, 1H, NH), 7.61(d, J=8.5 Hz, 2H, H-3' and H-5'), 7.38(d, J=8.5 Hz, 2H, H-2' and H-6'), 7.29(s, 1H, H-3), 6.82(m, 2H, H-2" and H-6"), 6.74(br d, J=8.6 Hz, 1H, H-5"), 4.19(dd, J=9.0, 6.4 Hz, 1H, H-4), 3.88(s, 3H, -OCH₃), 2.93(dd, J=16.1, 6.4 Hz, 1H, H$_a$-5), 2.80(dd, J=16.1, 9.0 Hz, 1H, H$_b$-5).

^{13}C NMR (100 MHz, CDCl₃):
δ_C 169.9(C-6), 146.5, 145.6, 138.0, 137.0, 136.5, 134.9(C-1"), 133.1(C-3' and C-5'), 130.2, 121.6, 119.5, 118.3, 105.6(C-3$_a$), 55.6(-OCH₃), 40.2(C-5), 34.8(C-4).

HR-ESI-MS:
HR-ESI-MS (+): experimental m/z 414.04454 ± 0.0050, [M+H]⁺ (calculated for C₁₉H₁₇^{79}Br₁N₃O₃ 414.04478); experimental m/z 436.02647 ± 0.0050, [M+Na]⁺ (calculated for C₁₉H₁₆^{79}BrN₃O₃Na 436.02673).

A₁₅: *1-(4-bromophenyl)-4-(3-ethoxy-4-methoxyphenyl)-4,5-dihydro-1H-pyrazolo[3,4-b]pyridin-6(7H)-one*

HPLC (RP-18 column, acetonitrile/water 1:1, UV detection at 254 nm, flow 5 mL · min⁻¹, retention time 7 min).

^{1}H NMR (400 MHz, CDCl₃):
δ_H 7.81 (br s, NH), 7.63 (d, J 8.6 Hz, H-3' and H-5'), 7.39 (d, J 8.6 Hz, H-2' and H-6'), 7.29 (s, H-3), 6.87,6.86,6.76 (series of multiplets, H-2", H-5" and H-6"), 4.21 (dd, J 6.3, 9.9 Hz, H-4), 4.07 (q, J 6.8 Hz, ethoxy-CH₂) 3.86 (OCH₃), 2.94 (dd, J 6.3, 16.0 Hz, Ha-5), 2.81 (dd, J 9.9, 16.0 Hz, Hb-5), 1.44 (t, J 6.8 Hz, ethoxy-CH₃).

^{13}C NMR (100 MHz, CDCl₃ with a small amount of CD₃OD):
δ_C 170.0 (C-6), 148.7 (C-7a), 138.7 (C-3" and C-4"), 138.3 (C-1' and C-3), 134.1 (C-1"), 133.0 (C-3' and C-5'), 124.3 (C-2' and C-6'), 119.3 (C-6"), 111.9 (C-2"), 111.8 (C-5"), 105.9 (C-3a), 64.5 (ethoxy-CH₂), 56.0 (OCH₃), 40.9 (C-4), 35.5 (C-5), 14.8 (ethoxy-CH₃).

HR-ESI-MS:
HR-ESI-MS (+): experimental m/z 442.07547 ± 0.00061 [M+H]⁺ (calculated for C₂₁H₁₉⁷⁹BrN₃O₃, 442.07608), 464.05762 ± 0.00041 [M+Na]⁺ (calculated for C₂₁H₂₀BrN₃O₃Na, 464.05803); HR-ESI-MS (-): experimental m/z 440.05937 ± 0.000106 [M-H]⁻ (calculated for C₂₁H₁₉⁷⁹BrN₃O₃, 440.06043).

A₁₆: *1-(4-bromophenyl)-4-(2,3-dihydrobenzo[b][1,4]dioxin-6-yl)-4,5-dihydro-1H-pyrazolo[3,4-b]pyridin-6(7H)-one*

HPLC (RP-18 column, acetonitrile/water 1:1, UV detection at 254 nm, flow 5 mL · min⁻¹, retention time 7 min).

^{1}H NMR (400 MHz, CDCl₃):
δ_H 8.20 (br s, NH), 7.60 (d, J 8.0 Hz, H-3' and H-5'), 7.37 (d, J 8.0 Hz, H-2' and H-6'), 7.29 (s, H-3), 7.23 (m, H-2" and H-6"), 6.84 (d, J 8.3 Hz, H-5"), 4.23 (s,OCH₂-OCH₂), 4.16 (dd, J 6.6, 8.5 Hz, H-4), 2.92 (dd, J 6.6, 16 Hz, Ha-5), 2.76 (dd, J 8.5, 16 Hz, Hb-5).

^{13}C NMR(100 MHz, CDCl₃ + drops of CD₃OD):
δ_C 170.3 (C-6), 143.8, 142.8 (C-3" and C-4"), 138.3 (C-3), 137.3 (C-1'), 135.5-136.65 (series of multiplets, C-1" and C-7a), 132.9 (C-3' and C-5'), 124.4 (C-2' and C-6'), 120.0 (C-4'), 117.7 (C-6"), 115.9 (C-2"), 105.7 (C-3a), 64.4, 64.3 (OCH₂ – CH₂O), 40.7 (C-4), 34.9 (C-5).

HR-ESI-MS:
HR-ESI-MS (+): experimental m/z 426.04411 ± 0.00067 [M+H]⁺ (calculated for C₂₀H₁₇⁷⁹BrN₃O₃, 426.04478), 448.02604 ± 0.00069 [M+Na]⁺ (calculated for C₂₀H₁₆⁷⁹BrN₃O₃Na, 448.02673). HR-ESI-MS (-): experimental m/z 424.02746 ± 0.00277 [M-H]⁻ (calculated for C₂₀H₁₅⁷⁹BrN₃O₃, 424.03023).

A₁₇: *4-(4-(benzyloxy)-3-methoxyphenyl)-1-(4-bromophenyl)-1,4,5,7-tetrahydro-6H-pyrazolo[3,4-b]pyridin-6-one*

HPLC (RP-18 column, acetonitrile/water 1:1, UV detection at 254 nm, flow 5 mL · min⁻¹, retention time 6 min).
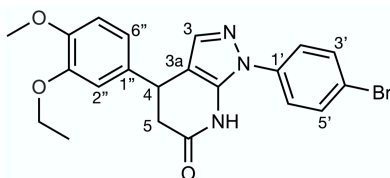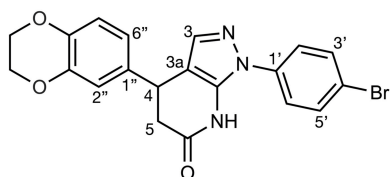
¹H NMR (400 MHz, CDCl₃):
δ_H 8.02(br s, 1H, NH), 7.61(s, 1H, H-3), 7.59-7.17(series of multiplets, 9H, aromatic protons), 6.81(m, 3H, H-2", H-3" and H-6"), 5.14(s, 2H, H-1‴), 3.87(s, 3H, -OCH₃), 4.21(m, 1H, H-4), 2.94(br d, J=15.6 Hz, 1H, Hₐ-5), 2.82(br d, J=15.6 Hz, 1H, H_b-5).

¹³C NMR (100 MHz, CDCl₃):
δ_C 170.6(C-6), 150.1, 147.6, 138.2 and 137.2(C-3 and C1'), 137.1(C-2‴), 136.5, 134.7, 133.0, 128.6(C-4‴ and C-6‴), 128.5(C-3‴ and C-7‴), 127.9(C-5‴), 124.4(C-2' and C-6'), 121.7, 114.3, 105.9(C-3ₐ), 71.3(C-1‴), 55.8(-OCH₃), 40.9 and 34.8(C-5 and C-4).

HR-ESI-MS:
HR-ESI-MS (+): experimental m/z 526.07369 ± 0.00081, [M+Na]⁺ (calculated for $C_{26}H_{22}{}^{79}BrN_3Na_1O_3$ 526.07368); m/z 504.09174 ± 0.00050, [M+H]⁺ (calculated for $C_{26}H_{23}{}^{79}BrN_3O_3$ 504.09173). HR-ESI-MS (-): experimental m/z 502.07798 ± 0.00310, [M-H]⁻ (calculated for $C_{26}H_{21}{}^{79}BrN_3Na_1O_3$ 502.07718).

A₁₈: *1-(4-bromophenyl)-4-(3,4,5-trimethoxyphenyl)-4,5-dihydro-1H-pyrazolo[3,4-b]pyridin-6(7H)-one*

HPLC (RP-18 column, acetonitrile/water 1:1, UV detection at 254 nm, flow 5 mL · min⁻¹, retention time 7 min).
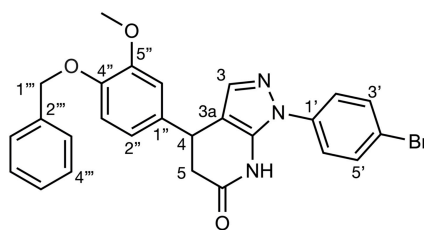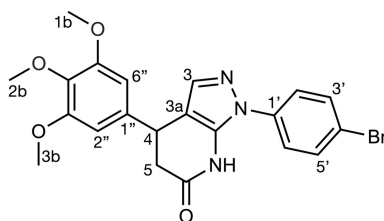
¹H NMR (400 MHz, CDCl₃):
δ_H 8.41 (s, NH), 7.58 (d, J 8.8 Hz, H-3' and H-5'), 7.38 (d, J 8.8 Hz, H-2' and H-6'), 7.30 (s, H-3), 6.48 (s, H-2" and H-6"), 4.19 (dd, J 6.3, 10.10 Hz, H-4), 3.83 (six H) and 3.82 (three H) (2s, OCH₃), 2.92 (dd, J 6.3, 16.1 Hz, Ha-5), 2.79 (dd, J 10.10, 16.1 Hz, Hb-5).

¹³C NMR(100 MHz, CDCl₃ + drops of CD₃OD):
δ_C 170.3 (C-6), 153.5 (C-3" and C-5"), 138.2 (C-1'), 137.4 (C-3), 132.8 (C-3' and C-5'), 124.4 (C-2' and C-6'), 121.6 (C-4'), 105.5 (C-3a), 104.2 (C-2" and C-6"), 60.8 (OCH₃ – 2b), 56.2 (OCH₃ – 1b and OCH₃ – 3b), 40.9 (C-4), 36.2 (C-5).

HR-ESI-MS:
HR-ESI-MS (+): experimental m/z 458.07025 ± 0.00075 [M+H]⁺ (calculated for $C_{21}H_{21}{}^{79}BrN_3O_4$ 458.07100), 480.05236 ± 0.00058 [M+Na]⁺ (calculated for $C_{21}H_{20}{}^{79}BrN_3O_4Na$, 480.05294). HR-ESI-MS (-): experimental m/z 456.05377 ± 0.00267 [M-H]⁻ (calculated for $C_{21}H_{19}{}^{79}BrN_3O_4$, 456.05644).

A₁₉:*1-(3-bromophenyl)-4-(3-hydroxy-4-methoxyphenyl)-4,5-dihydro-1H-pyrazolo[3,4-b]pyridin-6(7H)-one*

HPLC (RP-18 column, acetonitrile/water 1:1, UV detection at 254 nm, flow 5 mL · min^{-1}, retention time 4.5 min).

^{1}H NMR (400 MHz, CDCl$_3$ + drops of CD$_3$OD):
δ_H 7.68(s, 1H, H-3), 4.15(dd, J=9.0, 6.6Hz, 1H, H-4), 2.90(dd, J=15.9, 6.6Hz, 1H, H5-a), 2.76(dd, J=15.9, 9.0Hz, 1H, H5-b), 7.52-7.30(series of m, 4H, H-2', H-4', H-5' and H-6'), 6.83-6.66(series of m, 3H, H-2", H-5" and H-6"), 3.85(s, 3H, OCH$_3$).

^{13}C NMR (100 MHz, CDCl$_3$ + drops of CD$_3$OD):
δ_C 138.3(C-3), 105.87(C-3a), 35.2(C-4), 40.7(C-5), 170.8(C-6), 145.9(C-7a), 140.2(C-1'), 118.4(C-2'), 123.1(C-3'), 126.2(C-4'), 131.0(C-5'), 119.3 (C-6'), 133.5(C-1"), 113.5(C-2"), 146.0(C-3"), 146.0(C-4"), 111.2(C-5"), 121.6(C-6"), 56.0(CH$_3$).

HR-ESI-MS:
HR-ESI-MS (+): experimental m/z 414.04416 ± 0.00062 [M+H]$^+$ (calculated for C$_{19}$H$_{17}$^{79}BrN$_3$O$_3$, 414.04478), 436.02615 ± 0.00058 [M+Na]$^+$ (calculated for C$_{19}$H$_{16}$^{79}BrN$_3$O$_3$Na, 436.02673); HR-ESI-MS (-): experimental m/z 412.02833 ± 0.00190 [M-H]$^-$ (calculated for C$_{19}$H$_{15}$^{79}BrN$_3$O$_3$, 412.03023).

A₂₀: *1-(2-fluorophenyl)-4-(3-hydroxy-4-methoxyphenyl)-4,5-dihydro-1H-pyrazolo[3,4-b]pyridin-6(7H)-one*

HPLC (RP-18 column, acetonitrile/water 1:1, UV detection at 254 nm, flow 5 mL · min^{-1}, retention time 4.5 min).

^{1}H NMR (400 MHz, CDCl$_3$):
δ_H 7.35(s, 1H, H-3), 4.21(dd, J=9.2,6.6Hz, 1H, H-4), 2.92(dd, J=16.1,6.6Hz, 1H, H5-a), 2.78(dd, J=16.1,9.2Hz, 1H, H5-b), 8.21(broad s, 1H, NH), 7.60-7.22(series of m, 4H, H-3', H-4', H-5' and H-6'), 6.88-6.73(series of m, 3H, H-2", H-5" and H-6"), 5.79(broad s, 1H, OH), 3.89(s, 3H, OCH$_3$).

^{13}C NMR (100 MHz, CDCl$_3$):
δ_C 138.8(C-3), 104.9(C-3a), 35.0(C-4), 40.7(C-5), 170.5(C-6), 146.2(C-7a), 125.2(d, J$_{C-C-F}$ 12Hz, C-1'), 155.5(d, J$_{C-F}$ 250Hz, C-2'), 116.9(d, J$_{C-C-F}$ 19.5Hz, C-3'), 130.4(d, J$_{C-C-C-F}$ 7Hz, C-4'), 125.3(d, J$_{C-C-C-C-F}$ 3.9Hz, C-5'), 135.0(C-1"), 113.4(C-2"), 146.0 or 145.9(C-3" and C-4"), 111.0(C-5"), 118.5(C-6"), 56.0(CH$_3$).

HR-ESI-MS:
HR-ESI-MS (+): experimental m/z 354.12419 ± 0.00066 [M+H]$^+$ (calculated for C$_{19}$H$_{17}$FN$_3$O$_3$, 354.12485), 376.10604 ± 0.00075 [M+Na]$^+$ (calculated for C$_{19}$H$_{16}$FN$_3$O$_3$Na, 376.10679); HR-ESI-MS (-): experimental m/z 352.10810 ± 0.00219 [M-H]$^-$ (calculated for C$_{19}$H$_{15}$FN$_3$O$_3$, 352.11029).
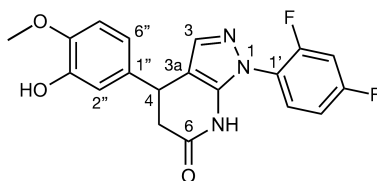
A₂₁: *1-(2,4-difluorophenyl)-4-(3-hydroxy-4-methoxyphenyl)-4,5-dihydro-1H-pyrazolo[3,4-b] pyridin-6(7H)-one*

HPLC (RP-18 column, acetonitrile/water 1:1, UV detection at 254 nm, flow 5 mL · min⁻¹, retention time 4.5 min).
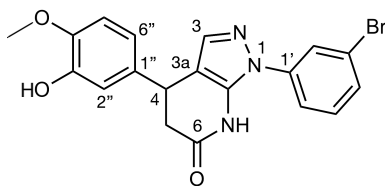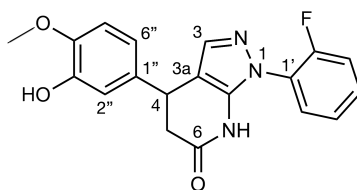
¹H NMR (400 MHz, CDCl₃):

δ$_H$ 7.29(s, 1H, H-3), 4.16(dd, J=8.9,6.7Hz, 1H, H-4), 2.85(dd, J=16.1,6.7Hz, 1H, H5-a), 2.69(dd, J=16.1,8.9Hz, 1H, H5-b), 8.16(broad s, 1H, NH), 6.82(d, J=8Hz, 1H, H-3'), 7.04-6.90(series of m, 3H, H-5', H-2" and H-5"), 7.50(m, 1H, H-6'), 6.0(broad s, 1H, OH), 6.73(dd, J=8.0,2.0Hz, 1H, H-6"), 3.86(s, 1H, OCH₃).

¹³C NMR (100 MHz, CDCl₃):

δ$_C$ 138.8(C-3), 104.7(C-3a), 35.0(C-4), 40.6(C-5), 170.9(C-6), 141.6(d, J$_{C-C-C-C-F}$ 6Hz, C-7a), 121.3(dd, J$_{C-C-F}$ 12Hz, J$_{C-C-C-C-F}$ 3Hz, C-1'), 156.3(dd, J$_{C-F}$ 254Hz, J$_{C-C-C-F}$ 11Hz, C-2'), 105.2(pt, J$_{C-C-F}$ 24Hz, C-3'), 162.8(dd, J$_{C-F}$ 250Hz, J$_{C-C-C-F}$ 11Hz, C-4'), 112.5(dd, J$_{C-C-F}$ 22Hz, J$_{C-C-C-C-F}$ 2.6Hz, C-5'), 129.4(d, J$_{C-C-C-F}$ 10Hz, C-6'), 139.3(C-1"), 111.0 or 113.3(C-2" and C-5"), 146.0 or 145.9(C-3" and C-4"), 118.5(C-6"), 56.0(CH₃).

HR-ESI-MS

HR-ESI-MS (-): experimental m/z 370.09870 ± 0.00217 [M-H]⁻ (calculated for C₁₉H₁₄F₂N₃O₃, 370.10087).

A₂₂: *1-(3-chloro-4-fluorophenyl)-4-(3-hydroxy-4-methoxyphenyl)-4,5-dihydro-1H-pyrazolo[3,4-b]pyridin-6(7H)-one*

HPLC (RP-18 column, acetonitrile/water 1:1, UV detection at 254 nm, flow 5 mL · min⁻¹, retention time 4.5 min).

¹H NMR (400 MHz, CDCl₃ + drops of CD₃OD):
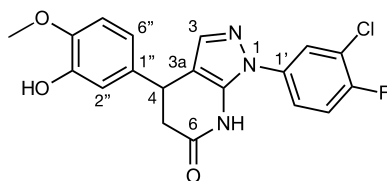
δ$_H$ 7.76-7.16(series of m, 4H, H-3, H-2', H-5' and H-6'), 4.13(dd, J=9.0,7.0Hz, 1H, H-4), 2.88(dd, J=16.2,7.0Hz, 1H, H5-a), 2.73(dd, J=16.2,9.0Hz, 1H, H5-b), 6.85-6.65(series of m, 3H, H-2", H-5" and H-6"), 3.84(s, 3H, OCH₃).

¹³C NMR (100 MHz, CDCl₃ + drops of CD₃OD):

δ$_C$ 138.3(C-3), 105.9(C-3a), 34.8(C-4), 40.5(C-5), 171.3(C-6), 142.7(C-7a), 133.9(d, J$_{C-C-C-C-F}$ 3Hz, C-1'), 123.3(d, J$_{C-C-C-F}$ 8Hz, C-2'), 122.0(d, J$_{C-C-F}$ 18Hz, C-3'), 157.3(d, J$_{C-F}$ 251Hz, C-4'), 117.3(d, J$_{C-C-F}$ 22Hz, C-5'), 113.6(C-6'), 134.0(C-1"), 118.3 or 111.4(C-2" and C-5"), 146.1 or 146.2(C-3" and C-4"), 125.0(C-6"), 55.9(CH₃).

HR-ESI-MS:

HR-ESI-MS (+): experimental m/z 388.08545 ± 0.00042 [M+H]⁺ (calculated for C₁₉H₁₆³⁵ClFN₃O₃, 388.08587);
HR-ESI-MS (-): experimental m/z 386.06891 ± 0.00241 [M-H]⁻ (calculated for C₁₉H₁₄³⁵ClFN₃O₃, 386.07132).
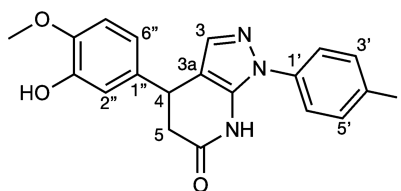
A₂₃:*4-(3-hydroxy-4-methoxyphenyl)-1-(4-iodophenyl)-4,5-dihydro-1H-pyrazolo[3,4-b]pyridin-6(7H)-one*

HPLC (RP-18 column, acetonitrile/water 1:1, UV detection at 254 nm, flow 5 mL · min^{-1}, retention time 4.5 min).

^{1}H NMR (400 MHz, CDCl$_3$ + drops of CD$_3$OD):
δ$_H$ 7.26(s, 1H, H-3), 4.10(dd, J=9.0H,6.2z, 1H, H-4), 2.89(dd, J=16.0,6.2Hz, 1H, H5-a), 2.75(dd, J=16.0,9.0Hz, 1H, H5-b), 7.24(d, J=8.0Hz, 2H, H-2' and H-6'), 7.80(d, J=8.0Hz, 2H, H-3' and H-5'), 6.87-6.63(series of m, 3H, H-2", H-5" and H-6"), 3.84(s, 3H, OCH$_3$).

^{13}C NMR (100 MHz, CDCl$_3$ + drops of CD$_3$OD):
δ$_C$ 138.3(C-3), 105.8(C-3a), 35.0(C-4), 40.6(C-5), 170.7(C-6), 118.4-146.0(C-7a, C-1', C-1" and C-6"), 124.7(C-2' and C-6'), 92.8(C-4'), 138.8(C-3' and C-5'), 111.2 or 113.4(C-2" and C-5"), 146.0 or 138.3(C-3" and C-4"), 56.0(CH$_3$).

HR-ESI-MS:
HR-ESI-MS (+): experimental m/z 462.03036 ± 0.00056 [M+H]$^+$ (calculated for C$_{19}$H$_{17}$IN$_3$O$_3$, 462.03092), 484.01228 ± 0.00058 [M+Na]$^+$ (calculated for C$_{19}$H$_{16}$IN$_3$O$_3$Na, 484.01286); HR-ESI-MS (-): experimental m/z 460.01330 ± 0.000307 [M-H]$^-$ (calculated for C$_{19}$H$_{15}$IN$_3$O$_3$, 460.01637).
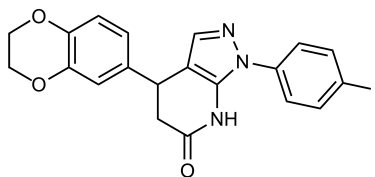
A₂₄: *4-(2,3-dihydrobenzo[b][1,4]dioxin-6-yl)-1-(4-iodophenyl)-1,4,5,7-tetrahydro-6H-pyrazolo[3,4-b]pyridin-6-one*

HPLC (RP-18 column, acetonitrile/water 7:3, UV detection at 254 nm, flow 5 mL · min^{-1}, retention time 7 min).

^{1}H NMR (400 MHz, CDCl$_3$):
δ$_H$ 7.83 (d, J= 8.8 Hz, 2H), 7.80 (br s, NH, 1H), 7.24 (d, J=8.8 Hz, 2H), 7.30 (s, 1H), 6.83 (d, J=8.27Hz, 1H), 6.78 (m, 2H), 4.25 (b s, 4H, OCH$_2$CH$_2$O), 4.18 (dd, J=9.0, 6.5 Hz, 1H), 2.95 (dd, J=16.1, 6.5 Hz, 1H), 2.79 (dd, J =16.1, 9.60Hz, 1H).

^{13}C NMR (100 MHz, CDCl$_3$):
δ$_C$ 169.8, 143.8, 142.8, 139.0, 138.5, 138.4, 139.0 (2C),135.0, 124.5 (2C), 119.9, 117.7, 115.9, 105.7, 92.9, 64.4, 64.3, 40.7, 34.9.

ESI-MS:
ESI-MS(-): experimental m/z 471.9 [M-H]$^-$.
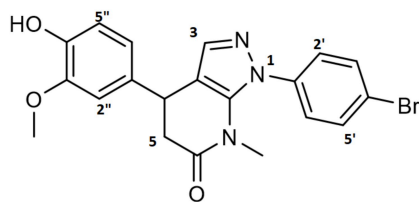
A$_{25}$: *1-(4-bromophenyl)-4-(4-hydroxy-3methoxyphenyl)-7-methyl-1,4,5,7-tetrahydro-6H-pyrazolo[3,4-b]pyridin-6-one*

HPLC (RP-18 column, acetonitrile/water 7:3, UV detection at 254 nm, flow 5 mL $\cdot$ min^{-1}, retention time 4.5 min).

^{1}H NMR (400 MHz, CDCl$_3$):
δ_H 7.62(D, J=8.6Hz H-3' and H-5'), 7.32(d, J=8.6Hz H-2' and H-6'), 7.3(s, H=3), 6.88 (d, J=8.7Hz H-5"), 6.75 (m, H-2", H-6"), 4.14(dd, J=9.8, 5.4Hz H-4), 3.86(s, 3"OCH$_3$), 2.98 (dd, J=15.3, 9.8Hz H-5), 2.95 (s, 7-NCH$_3$).

^{13}C NMR (400 MHz, CDCl$_3$) deduced from HMBC experiment:
δ_C 171(C-6), 147.4 (C-3"), 141.5 (C-7a), 136.8 (C-1'), 133.7 (C-3), 133.5 (C-1"), 122.3 (C-2', C-5'), 119.4 (C-6"), 55.0 (C-3" OCH$_3$), 42.0 (C-4), 34.8 (C-5), 31.5 (7-NCH$_3$).

HR-ESI-MS:
HR-ESI-MS (+): experimental m/z 450.04210 $\pm$ 0.00500 [M + Na]$^+$ (calculated for C$_{20}$H$_{18}$^{79}BrN$_3$O$_4$Na, 450.04238),
HR-ESI-MS (-): experimental m/z 462.04678 $\pm$ 0.00500 [M - H]$^-$ (calculated for C$_{20}$H$_{17}$^{79}BrN$_3$O$_4$, 426.04588).
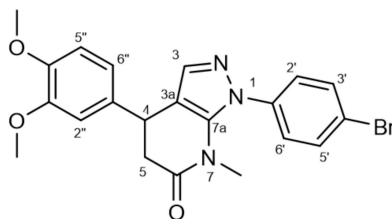
A$_{26}$: *1-(4-bromophenyl)-4-(3,4-dimethoxyphenyl)-7-methyl-1,4,5,7-tetrahydro-6H-pyrazolo[3,4-b]pyridin-6-one*

HPLC (RP-18 column, acetonitrile/water 7:3, UV detection at 254 nm, flow 5 mL $\cdot$ min^{-1}, retention time 7 min).

^{1}H NMR (400 MHz, CDCl$_3$):
δ_H 7.72(ddd, J=8.7,2.8Hz, 1,9Hz, H-3' and H-5'), 7.37(ddd, J=8.7,2.8Hz,1.9Hz H-2' and H-6'), 7.3(s, H=3), 6.38(d, J=8.7Hz, H-5"), 6.77(m, H-2" and H-6"), 4.15(dd, J=9.7,5.8Hz, H-4) 3.86(s, 3"-OCH$_3$), 2.9 (dd, J=5.8,2.3Hz, H-5), 2.95(s, 7-NCH$_3$), 2.91(dd, J=15.3,3.5Hz, H-5).

^{13}C NMR (400 MHz, CDCl$_3$) deduced from HMBC experiment:
δ_C 170.8(C-6), 149-3 (C-4"), 148.3 (C-3"), 138.4 (C-3),138.2 (C-1'), 133.5 (C-1"), 132.6(C-3', C-5'), 121.8(C-4'), 121(C-2', C-5'), 114(C-5"), 109.3(C-2"), 109(C-3), 56.3 and 55.9(C-3" OCH$_3$ and C-4"OCH$_3$), 42.3 (C-4), 34.7(7-NCH$_3$), 32.2(C-5).

HR-ESI-MS:
HR-ESI-MS (+): experimental m/z 442.07588 $\pm$ 0.00500 [M + Na]$^+$ (calculated for C$_{21}$H$_{22}$^{79}BrN$_3$O$_4$Na, 442.07608),
HR-ESI-MS (-): experimental m/z 462.05784 $\pm$ 0.00500 [M - H]$^-$ (calculated for C$_{21}$H$_{21}$^{79}BrN$_3$O$_3$, 464.05803).
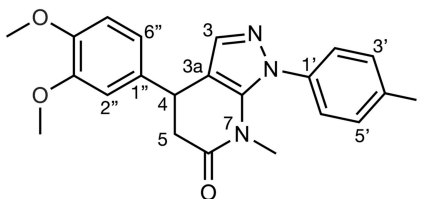
A₂₇: *4-(3,4-dimethoxyphenyl)-1-(4-iodophenyl)-7-methyl-4,5-dihydro-1H-pyrazolo[3,4-b]pyridin-6(7H)-one*:

HPLC (RP-18 column, acetonitrile/water7:3, UV detection at 254 nm, flow 5 mL · min⁻¹, retention time 7 min).

¹H NMR (400 MHz, CDCl₃):

δ_H 7.82 (br d, J 8.6 Hz, H-3' and H-5'), 7.29 (s, H-3), 7.24 (dd, J 8.6 Hz, H-2' and H-6'), 6.86-6.73 (series of multiplets, H-2", H-5", H-6"), 4.15 (dd, J 5.8,9.3 Hz, H-4), 3.85-3.86 (2s, OCH₃-1b and OCH₃-2b), 2.97 (dd, J 5.8,15.8 Hz, Ha-5), 2.96 (s, NCH₃), 2.91 (dd, J 9.3,15.8 Hz, Hb-5).

¹³C NMR (100 MHz, CDCl₃ + drops of CD₃OD):

δ_C 170.7 (C-6), 137.9,139.0,148.3,149.3 (series of multiplets, C-7a, C-1', C-3" and C-4"), 138.5 (C-3 plus C-3' and C-6'), 133.5 (C-1"), 126.6 (C-2' and C-6'), 119.3 (C-6"), 111.5,110.3,109.6 (series of multiplets, C-2", C-3a and C-5"), 93.6 (C-4'), 56.0 OCH₃-1b and OCH₃-2b), 42.3 (C-4), 35.0 (C-5), 32.4 (NCH₃).

HR-ESI-MS:

HR-ESI-MS (+): experimental m/z 490.06168 ± 0.00054 [M+H]⁺ (calculated for C₂₁H₂₁IN₃O₃, 490.06222), 512.04348 ± 0.00068 [M+Na]⁺ (calculated for C₂₁H₂₀IN₃O₃Na, 512.04416). HR-ESI-MS (-): experimental m/z 488.04410 ± 0.00357 [M-H]⁻ (calculated for C₂₁H₁₉IN₃O₃, 488.04767).

A₂₈:*1-(4-bromophenyl)-4-(3-ethoxy-4-methoxyphenyl)-7-methyl-1,4,5,7-tetrahydro-6H-pyrazolo[3,4-b]pyridin-6-one*

HPLC (RP-18 column, acetonitrile/water 1:1, UV detection at 254 nm, flow 5 mL · min⁻¹, retention time 5.5 min).

¹H NMR (400 MHz, CDCl₃):
δ_H 7.62(d, J=8.6Hz, 2H), 7.37(d, J=8.8Hz, 2H), 7.30(s, 1H), 6.83 (d, J = 8.7Hz, 1H), 6.78 (m, 2H),4.14 (dd, J = 9.6, 5.7 Hz, 1H), 4.06 (q, J= 6.8 Hz, 2H, OCH₂), 3.85 (s, 3H, OCH₃), 2.98 (dd, J 15.2, 5.7 Hz, 1H), 2.95 (s, NCH₃, 3H), 2.90 (dd, J = 15.2, 9.6 Hz, 1H), 1.44 (t, J =6.8 Hz, OCH₂CH₃, 3H).

¹³C NMR (100 MHz, CDCl₃):
δ_C 170.7, 148.7, 148.6, 141.5, 138.4, 137.8, 133.8, 132.5 (2C), 126.5 (2C), 119.3, 111.9, 111.8, 110.8, 109.6, 64.5, 56.0, 42.2, 34.9, 32.3, 14.8.

ESI-MS:
ESI-MS(-): experimental m/z 442.2 [M-H]⁻.
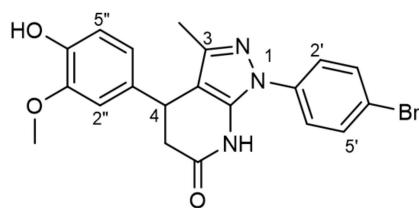
A$_{29}$: *1-(4-bromophenyl)-4-(4-hydroxy-3methoxyphenyl)-3-methyl-1,4,5,7-tetrahydro-6H-pyrazolo[3,4-b]pyridin-6-one*

HPLC (RP-18 column, acetonitrile/water 7:3, UV detection at 254 nm, flow 5 mL · min^{-1}, retention time 7 min).
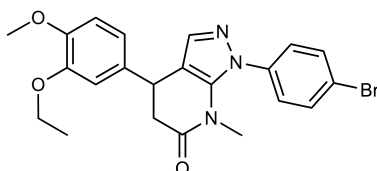
^{1}H NMR (400 MHz, CDCl$_3$):
δ_H 7.64(d, J=8.8Hz, H-3' and H=5') 7.4 (d, J=8.8Hz, H-2' and H-6'), 7.22(s, H=3), 6.83(m, H-5", H-2", H-6"), 4.53(s, H-4), 4.12(dd, CH$_2$), 3.85(s, 3"-OCH$_3$), 2.91 (dd, J=15.3,3.5Hz, H-5).

^{13}C NMR (400 MHz, CDCl$_3$) deduced from HMBC experiment:
δ_C 170.8(C-6), 149.3 (C-4"), 148.3 (C-3"), 141.5 (C-7a), 138.4(C-1'), 138.2 (C-1'), 133.5(C-1"), 132.6(C-3', C-5'), 121.8(C-4'), 121(C-2', C-5'), 119.5(C-6"), 114.0(C-5"), 109.3(C-2"), 56.3 and 55.9(C-3" OCH$_3$ and C-4"OCH$_3$), 42.3 (C-4), 34.7(7-NCH$_3$), 32.2(C-5).

HR-ESI-MS:
HR-ESI-MS (+): experimental m/z 428.06053 ± 0.00500 [M + Na]$^+$ (calculated for C$_{20}$H$_{19}$^{79}BrN$_3$O$_4$, 428.06043).

Bibliography

[1] Balch WE, Morimoto RI, Dillin A, Kelly JW. Adapting proteostasis for disease intervention. Science. 2008 Feb 15;319(5865):916-9. doi: 10.1126/science.1141448. PMID: 18276881.

[2] Dobson CM. Protein folding and misfolding. Nature. 2003 Dec 18;426(6968):884-90. doi: 10.1038/nature02261. PMID: 14685248.

[3] Chen B, Retzlaff M, Roos T, Frydman J. Cellular strategies of protein quality control. Cold Spring Harb Perspect Biol. 2011 Aug 1;3(8):a004374. doi: 10.1101/cshperspect.a004374. PMID: 21746797; PMCID: PMC3140689.

[4] Frydman J. Folding of newly translated proteins in vivo: the role of molecular chaperones. Annu Rev Biochem. 2001;70:603-47. doi: 10.1146/annurev.biochem.70.1.603. PMID: 11395418.

[5] Pohl C, Dikic I. Cellular quality control by the ubiquitin-proteasome system and autophagy. Science. 2019 Nov 15;366(6467):818-822. doi: 10.1126/science.aax3769. Epub 2019 Nov 14. PMID: 31727826.

[6] Meusser B, Hirsch C, Jarosch E, Sommer T. ERAD: the long road to destruction. Nat Cell Biol. 2005 Aug;7(8):766-72. doi: 10.1038/ncb0805-766. PMID: 16056268.

[7] Sikorska N, Lemus L, Aguilera-Romero A, Manzano-Lopez J, Riezman H, Muñiz M, Goder V. Limited ER quality control for GPI-anchored proteins. J Cell Biol. 2016 Jun 20;213(6):693-704. doi: 10.1083/jcb.201602010. PMID: 27325793; PMCID: PMC4915193.

[8] Fregno I, Molinari M. Proteasomal and lysosomal clearance of faulty secretory proteins: ER-associated degradation (ERAD) and ER-to-lysosome-associated degradation (ERLAD) pathways. Crit Rev Biochem Mol Biol. 2019 Apr;54(2):153-163. doi: 10.1080/10409238.2019.1610351. Epub 2019 May 14. PMID: 31084437.

[9] Kaganovich D, Kopito R, Frydman J. Misfolded proteins partition between two distinct quality control compartments. Nature. 2008 Aug 28;454(7208):1088-95. doi: 10.1038/nature07195. PMID: 18756251; PMCID: PMC2746971.

[10] Fink AL. Protein aggregation: folding aggregates, inclusion bodies and amyloid. Fold Des. 1998;3(1):R9-23. doi: 10.1016/S1359-0278(98)00002-9. PMID: 9502314.

[11] Zapadka KL, Becher FJ, Gomes Dos Santos AL, Jackson SE. Factors affecting the physical stability (aggregation) of peptide therapeutics. Interface Focus. 2017 Dec 6;7(6):20170030. doi: 10.1098/rsfs.2017.0030. Epub 2017 Oct 20. PMID: 29147559; PMCID: PMC5665799.

[12] Yoshimura Y, Lin Y, Yagi H, Lee YH, Kitayama H, Sakurai K, So M, Ogi H, Naiki H, Goto Y. Distinguishing crystal-like amyloid fibrils and glass-like amorphous aggregates from their kinetics of formation. Proc Natl Acad Sci U S A. 2012 Sep 4;109(36):14446-51. doi: 10.1073/pnas.1208228109. Epub 2012 Aug 20. PMID: 22908252; PMCID: PMC3437889.

[13] Rambaran RN, Serpell LC. Amyloid fibrils: abnormal protein assembly. Prion. 2008 Jul-Sep;2(3):112-7. doi: 10.4161/pri.2.3.7488. Epub 2008 Jul 20. PMID: 19158505; PMCID: PMC2634529.

[14] Sipe JD, Cohen AS. Review: history of the amyloid fibril. J Struct Biol. 2000 Jun;130(2-3):88-98. doi: 10.1006/jsbi.2000.4221. PMID: 10940217.

[15] Knowles, T. P., Vendruscolo, M. & Dobson, C. M. The amyloid state and its association with protein misfolding diseases. Nat. Rev. Mol. Cell. Biol. 15, 384–396 (2014).

[16] Glabe CG. Common mechanisms of amyloid oligomer pathogenesis in degenerative disease. Neurobiol Aging. 2006 Apr;27(4):570-5. doi: 10.1016/j.neurobiolaging.2005.04.017. Epub 2006 Feb 14. PMID: 16481071.

[17] Meisl G, Kirkegaard JB, Arosio P, Michaels TC, Vendruscolo M, Dobson CM, Linse S, Knowles TP. Molecular mechanisms of protein aggregation from global fitting of kinetic models. Nat Protoc. 2016 Feb;11(2):252-72. doi: 10.1038/nprot.2016.010. Epub 2016 Jan 7. PMID: 26741409.

[18] Iadanza MG, Jackson MP, Hewitt EW, Ranson NA, Radford SE. A new era for understanding amyloid structures and disease. Nat Rev Mol Cell Biol. 2018 Dec;19(12):755-773. doi: 10.1038/s41580-018-0060-8. PMID: 30237470.

[19] Kraus A, Hoyt F, Schwartz CL, Hanses B, Hughson AG, Artikis E, Race B, Caughey B. Structure of an infectious mammalian prion. BioRxiv. 2021 Feb 15, doi: 10.1101/2021.02.14.431014

[20] Sunde M, Serpell LC, Bartlam M, Fraser PE, Pepys MB, Blake CC. Common core structure of amyloid fibrils by synchrotron X-ray diffraction. J Mol Biol. 1997 Oct 31;273(3):729-39. doi: 10.1006/jmbi.1997.1348. PMID: 9356260.

[21] Sawaya MR, Sambashivan S, Nelson R, Ivanova MI, Sievers SA, Apostol MI, Thompson MJ, Balbirnie M, Wiltzius JJ, McFarlane HT, Madsen AØ, Riekel C, Eisenberg D. Atomic structures of amyloid cross-beta spines reveal varied steric zippers. Nature. 2007 May 24;447(7143):453-7. doi: 10.1038/nature05695. Epub 2007 Apr 29. PMID: 17468747.

[22] Wiegand T, Malär AA, Cadalbert R, Ernst M, Böckmann A, Meier BH. Asparagine and Glutamine Side-Chains and Ladders in HET-s(218-289) Amyloid Fibrils Studied by Fast Magic-Angle Spinning NMR. Front Mol Biosci. 2020 Sep 30;7:582033. doi: 10.3389/fmolb.2020.582033. PMID: 33195425; PMCID: PMC7556116.

[23] Smith JF, Knowles TP, Dobson CM, Macphee CE, Welland ME. Characterization of the nanoscale properties of individual amyloid fibrils. Proc Natl Acad Sci U S A. 2006 Oct 24;103(43):15806-11. doi: 10.1073/pnas.0604035103. Epub 2006 Oct 12. PMID: 17038504; PMCID: PMC1635084.

[24] Tuttle MD, Comellas G, Nieuwkoop AJ, Covell DJ, Berthold DA, Kloepper KD, Courtney JM, Kim JK, Barclay AM, Kendall A, Wan W, Stubbs G, Schwieters CD, Lee VM, George JM, Rienstra CM. Solid-state NMR structure of a pathogenic fibril of full-length human α-synuclein. Nat Struct Mol Biol. 2016 May;23(5):409-15. doi: 10.1038/nsmb.3194. Epub 2016 Mar 28. PMID: 27018801; PMCID: PMC5034296.

[25] Qiang W, Yau WM, Luo Y, Mattson MP, Tycko R. Antiparallel β-sheet architecture in Iowa-mutant β-amyloid fibrils. Proc Natl Acad Sci U S A. 2012 Mar 20;109(12):4443-8. doi: 10.1073/pnas.1111305109. Epub 2012 Mar 8. PMID: 22403062; PMCID: PMC3311365.

[26] Kajava AV, Steven AC. Beta-rolls, beta-helices, and other beta-solenoid proteins. Adv Protein Chem. 2006;73:55-96. doi: 10.1016/S0065-3233(06)73003-0. PMID: 17190611.

[27] Hennetin J, Jullian B, Steven AC, Kajava AV. Standard conformations of beta-arches in beta-solenoid proteins. J Mol Biol. 2006 May 12;358(4):1094-105. doi: 10.1016/j.jmb.2006.02.039. Epub 2006 Mar 2. Erratum in: J Mol Biol. 2006 Jul 7;360(2):520-1. PMID: 16580019.

[28] Richardson JS, Richardson DC. Natural beta-sheet proteins use negative design to avoid edge-to-edge aggregation. Proc Natl Acad Sci U S A. 2002 Mar 5;99(5):2754-9. doi: 10.1073/pnas.052706099. PMID: 11880627; PMCID: PMC122420.

[29] Wasmer C, Lange A, Van Melckebeke H, Siemer AB, Riek R, Meier BH. Amyloid fibrils of the HET-s(218-289) prion form a beta solenoid with a triangular hydrophobic core. Science. 2008 Mar 14;319(5869):1523-6. doi: 10.1126/science.1151839. Erratum in: Science. 2008 Apr 4;320(5872):50. PMID: 18339938.

[30] Daskalov A, Martinez D, Coustou V, Mammeri NE, Berbon M, Andreas LB, Bardiaux B, Stanek J, Noubhani A, Kauffmann B, Wall JS, Pintacuda G, Saupe SJ, Habenstein B, Loquet A. Structural and molecular basis of cross-seeding barriers in amyloids. Proc Natl Acad Sci U S A. 2021 Jan 5;118 (1) e201408511. doi: 10.1073/pnas.2014085118

[31] Chien P, Weissman JS, DePace AH. Emerging principles of conformation-based prion inheritance. Annu Rev Biochem. 2004;73:617-56. doi: 10.1146/annurev.biochem.72.121801.161837. PMID: 15189155.

[32] Walker LC, LeVine H 3rd. The cerebral proteopathies. Neurobiol Aging. 2000 Jul-Aug;21(4):559-61. doi: 10.1016/s0197-4580(00)00160-3. PMID: 10924770.

[33] Chiti F, Dobson CM. Protein Misfolding, Amyloid Formation, and Human Disease: A Summary of Progress Over the Last Decade. Annu Rev Biochem. 2017 Jun 20;86:27-68. doi: 10.1146/annurev-biochem-061516-045115. Epub 2017 May 12. PMID: 28498720.

[34] Johnson RT. Prion diseases. Lancet Neurol. 2005 Oct;4(10):635-42. doi: 10.1016/S1474-4422(05)70192-7. PMID: 16168932.

[35] Prusiner SB. Novel proteinaceous infectious particles cause scrapie. Science. 1982 Apr 9;216(4542):136-44. doi: 10.1126/science.6801762. PMID: 6801762.

[36] Chen C, Dong XP. Epidemiological characteristics of human prion diseases. Infect Dis Poverty. 2016 Jun 2;5(1):47. doi: 10.1186/s40249-016-0143-8. PMID: 27251305; PMCID: PMC4890484.

[37] Kovács GG, Puopolo M, Ladogana A, Pocchiari M, Budka H, van Duijn C, Collins SJ, Boyd A, Giulivi A, Coulthart M, Delasnerie-Laupretre N, Brandel JP, Zerr I, Kretzschmar HA, de Pedro-Cuesta J, Calero-Lara M, Glatzel M, Aguzzi A, Bishop M, Knight R, Belay G, Will R, Mitrova E; EUROCJD. Genetic prion disease: the EUROCJD experience. Hum Genet. 2005 Nov;118(2):166-74. doi: 10.1007/s00439-005-0020-1. Epub 2005 Nov 15. PMID: 16187142.

[38] Yegya-Raman N, Aziz R, Schneider D, Tobia A, Leitch M, Nwobi O. A Case of Sporadic Creutzfeldt-Jakob Disease Presenting as Conversion Disorder. Case Rep Psychiatry. 2017;2017:2735329. doi: 10.1155/2017/2735329. Epub 2017 May 3. Erratum in: Case Rep Psychiatry. 2018 Feb 21;2018:3826863. PMID: 28553554; PMCID: PMC5434310.

[39] Knight R. Infectious and Sporadic Prion Diseases. Prog Mol Biol Transl Sci. 2017;150:293-318. doi: 10.1016/bs.pmbts.2017.06.010. Epub 2017 Aug 14. PMID: 28838665.

[40] Smith PG, Bradley R. Bovine spongiform encephalopathy (BSE) and its epidemiology. Br Med Bull. 2003;66:185-98. doi: 10.1093/bmb/66.1.185. PMID: 14522859.

[41] BSE in North America BSE (Bovine Spongiform Encephalopathy) Prion Diseases. CDC. 2 October 2018.

[42] Brown P, Cathala F, Castaigne P, Gajdusek DC. Creutzfeldt-Jakob disease: clinical analysis of a consecutive series of 230 neuropathologically verified cases. Ann Neurol. 1986 Nov;20(5):597-602. doi: 10.1002/ana.410200507. PMID: 3539001.

[43] Belay ED, Schonberger LB. Variant Creutzfeldt-Jakob disease and bovine spongiform encephalopathy. Clin Lab Med. 2002 Dec;22(4):849-62, v-vi. doi: 10.1016/s0272-2712(02)00024-0. PMID: 12489284.

[44] Bird SM. Recipients of blood or blood products "at vCJD risk". BMJ. 2004 Jan 17;328(7432):118-9. doi: 10.1136/bmj.328.7432.118. PMID: 14726314; PMCID: PMC314493.

[45] Whitfield JT, Pako WH, Collinge J, Alpers MP. Mortuary rites of the South Fore and kuru. Philos Trans R Soc Lond B Biol Sci. 2008 Nov 27;363(1510):3721-4. doi: 10.1098/rstb.2008.0074. PMID: 18849288; PMCID: PMC2581657.

[46] Wadsworth JD, Joiner S, Linehan JM, Asante EA, Brandner S, Collinge J. Review. The origin of the prion agent of kuru: molecular and biological strain typing. Philos Trans R Soc Lond B Biol Sci. 2008 Nov 27;363(1510):3747-53. doi: 10.1098/rstb.2008.0069. PMID: 18849291; PMCID: PMC2581656.

[47] Alpers MP. A history of kuru. P N G Med J. 2007 Mar-Jun;50(1-2):10-9. PMID: 19354007.

[48] Collins S, McLean CA, Masters CL. Gerstmann-Sträussler-Scheinker syndrome,fatal familial insomnia, and kuru: a review of these less common human transmissible spongiform encephalopathies. J Clin Neurosci. 2001 Sep;8(5):387-97. doi: 10.1054/jocn.2001.0919. PMID: 11535002.

[49] Moody KM, Schonberger LB, Maddox RA, Zou WQ, Cracco L, Cali I. Sporadic fatal insomnia in a young woman: a diagnostic challenge: case report. BMC Neurol. 2011 Oct 31;11:136. doi: 10.1186/1471-2377-11-136. PMID: 22040318; PMCID: PMC3214133.

[50] Nonno R, Notari S, Di Bari MA, Cali I, Pirisinu L, d'Agostino C, Cracco L, Kofskey D, Vanni I, Lavrich J, Parchi P, Agrimi U, Gambetti P. Variable Protease-Sensitive Prionopathy Transmission to Bank Voles. Emerg Infect Dis. 2019 Jan;25(1):73-81. doi: 10.3201/eid2501.180807. PMID: 30561322; PMCID: PMC6302590.

[51] Mastrianni JA. The genetics of prion diseases. Genet Med. 2010 Apr;12(4):187-95. doi: 10.1097/GIM.0b013e3181cd7374. PMID: 20216075.

[52] Zanusso G, Bongianni M, Caughey B. A test for Creutzfeldt-Jakob disease using nasal brushings. N Engl J Med. 2014 Nov 6;371(19):1842-3. doi: 10.1056/NEJMc1410732. PMID: 25372096.

[53] Maddox RA, Person MK, Blevins JE, Abrams JY, Appleby BS, Schonberger LB, Belay ED. Prion disease incidence in the United States: 2003-2015. Neurology. 2020 Jan 14;94(2):e153-e157. doi: 10.1212/WNL.0000000000008680. Epub 2019 Nov 22. PMID: 31757870.

[54] Hartl FU. Protein Misfolding Diseases. Annu Rev Biochem. 2017 Jun 20;86:21-26. doi: 10.1146/annurev-biochem-061516-044518. Epub 2017 Apr 24. PMID: 28441058.

[55] Carlson GA, Kingsbury DT, Goodman PA, Coleman S, Marshall ST, DeArmond S, Westaway D, Prusiner SB. Linkage of prion protein and scrapie incubation time genes. Cell. 1986 Aug 15;46(4):503-11. doi: 10.1016/0092-8674(86)90875-5. PMID: 3015416.

[56] Büeler H, Aguzzi A, Sailer A, Greiner RA, Autenried P, Aguet M, Weissmann C. Mice devoid of PrP are resistant to scrapie. Cell. 1993 Jul 2;73(7):1339-47. doi: 10.1016/0092-8674(93)90360-3. PMID: 8100741.

[57] Legname G, Baskakov IV, Nguyen HO, Riesner D, Cohen FE, DeArmond SJ, Prusiner SB. Synthetic mammalian prions. Science. 2004 Jul 30;305(5684):673-6. doi: 10.1126/science.1100195. PMID: 15286374.

[58] Major Prion Protein Precursor, Uniprot entry: P04156 (PRIO_HUMAN)

[59] Orlean P, Menon AK. Thematic review series: lipid posttranslational modifications. GPI anchoring of protein in yeast and mammalian cells, or: how we learned to stop worrying and love glycophospholipids. J Lipid Res. 2007 May;48

[60] Riesner D. Biochemistry and structure of PrP(C) and PrP(Sc). Br Med Bull. 2003;66:21-33. doi: 10.1093/bmb/66.1.21. PMID: 14522846.

[61] Shiraishi N, Ohta Y, Nishikimi M. The octapeptide repeat region of prion protein binds Cu(II) in the redox-inactive state. Biochem Biophys Res Commun. 2000 Jan 7;267(1):398-402. doi: 10.1006/bbrc.1999.1944. PMID: 10623631.

[62] Harrison CF, Lawson VA, Coleman BM, Kim YS, Masters CL, Cappai R, Barnham KJ, Hill AF. Conservation of a glycine-rich region in the prion protein is required for uptake of prion infectivity. J Biol Chem. 2010 Jun 25;285(26):20213-23. doi: 10.1074/jbc.M109.093310. Epub 2010 Mar 31. PMID: 20356832; PMCID: PMC2888434.

[63] Wang F, Yin S, Wang X, Zha L, Sy MS, Ma J. Role of the highly conserved middle region of prion protein (PrP) in PrP-lipid interaction. Biochemistry. 2010 Sep 21;49(37):8169-76. doi: 10.1021/bi101146v. PMID: 20718504; PMCID: PMC2950782.

[64] Norstrom EM, Mastrianni JA. The AGAAAAGA palindrome in PrP is required to generate a productive PrPSc-PrPC complex that leads to prion propagation. J Biol Chem. 2005 Jul 22;280(29):27236-43. doi: 10.1074/jbc.M413441200. Epub 2005 May 25. PMID: 15917252.

[65] Welker E, Raymond LD, Scheraga HA, Caughey B. Intramolecular versus intermolecular disulfide bonds in prion proteins. J Biol Chem. 2002 Sep 6;277(36):33477-81. doi: 10.1074/jbc.M204273200. Epub 2002 Jun 24. PMID: 12082114.

[66] Baskakov IV, Katorcha E. Multifaceted Role of Sialylation in Prion Diseases. Front Neurosci. 2016 Aug 8;10:358. doi: 10.3389/fnins.2016.00358. PMID: 27551257; PMCID: PMC4976111.

[67] Spagnolli G, Massignan T, Astolfi A, Biggi S, Rigoli M, Brunelli P, Libergoli M, Ianeselli A, Orioli S, Boldrini A, Terruzzi L, Bonaldo V, Maietta G, Lorenzo NL, Fernandez LC, Codeseira YB, Tosatto L, Linsenmeier L, Vignoli B, Petris G, Gasparotto D, Pennuto M, Guella G, Canossa M, Altmeppen HC, Lolli G, Biressi S, Pastor MM, Requena JR, Mancini I, Barreca ML, Faccioli P, Biasini E. Pharmacological inactivation of the prion protein by targeting a folding intermediate. Commun Biol. 2021 Jan 12;4(1):62. doi: 10.1038/s42003-020-01585-x. PMID: 33437023; PMCID: PMC7804251.

[68] Zahn R, Liu A, Lührs T, Riek R, von Schroetter C, López García F, Billeter M, Calzolai L, Wider G, Wüthrich K. NMR solution structure of the human prion protein. Proc Natl Acad Sci U S A. 2000 Jan 4;97(1):145-50. doi: 10.1073/pnas.97.1.145. PMID: 10618385; PMCID: PMC26630.

[69] Antonyuk SV, Trevitt CR, Strange RW, Jackson GS, Sangar D, Batchelor M, Cooper S, Fraser C, Jones S, Georgiou T, Khalili-Shirazi A, Clarke AR, Hasnain SS, Collinge J. Crystal structure of human prion protein bound to a therapeutic antibody. Proc Natl Acad Sci U S A. 2009 Feb 24;106(8):2554-8. doi: 10.1073/pnas.0809170106. Epub 2009 Feb 9. PMID: 19204296; PMCID: PMC2637903.

[70] Legname G. Elucidating the function of the prion protein. PLoS Pathog. 2017 Aug 31;13(8):e1006458. doi: 10.1371/journal.ppat.1006458. PMID: 28859171; PMCID: PMC5578479.

[71] Criado JR, Sánchez-Alavez M, Conti B, Giacchino JL, Wills DN, Henriksen SJ, Race R, Manson JC, Chesebro B, Oldstone MB. Mice devoid of prion protein have cognitive deficits that

are rescued by reconstitution of PrP in neurons. Neurobiol Dis. 2005 Jun-Jul;19(1-2):255-65. doi: 10.1016/j.nbd.2005.01.001. PMID: 15837581.

[72] Tobler I, Gaus SE, Deboer T, Achermann P, Fischer M, Rülicke T, Moser M, Oesch B, McBride PA, Manson JC. Altered circadian activity rhythms and sleep in mice devoid of prion protein. Nature. 1996 Apr 18;380(6575):639-42. doi: 10.1038/380639a0. PMID: 8602267.

[73] Bremer J, Baumann F, Tiberi C, Wessig C, Fischer H, Schwarz P, Steele AD, Toyka KV, Nave KA, Weis J, Aguzzi A. Axonal prion protein is required for peripheral myelin maintenance. Nat Neurosci. 2010 Mar;13(3):310-8. doi: 10.1038/nn.2483. Epub 2010 Jan 24. PMID: 20098419

[74] Nuvolone M, Hermann M, Sorce S, Russo G, Tiberi C, Schwarz P, Minikel E, Sanoudou D, Pelczar P, Aguzzi A. Strictly co-isogenic C57BL/6J-Prnp-/- mice: A rigorous resource for prion science. J Exp Med. 2016 Mar 7;213(3):313-27. doi: 10.1084/jem.20151610. Epub 2016 Feb 29. PMID: 26926995; PMCID: PMC4813672.

[75] Küffer A, Lakkaraju AK, Mogha A, Petersen SC, Airich K, Doucerain C, Marpakwar R, Bakirci P, Senatore A, Monnard A, Schiavi C, Nuvolone M, Grosshans B, Hornemann S, Bassilana F, Monk KR, Aguzzi A. The prion protein is an agonistic ligand of the G protein-coupled receptor Adgrg6. Nature. 2016 Aug 25;536(7617):464-8. doi: 10.1038/nature19312. Epub 2016 Aug 8. PMID: 27501152; PMCID: PMC5499706.

[76] Slapšak U, Salzano G, Amin L, Abskharon RN, Ilc G, Zupančič B, Biljan I, Plavec J, Giachin G, Legname G. The N Terminus of the Prion Protein Mediates Functional Interactions with the Neuronal Cell Adhesion Molecule (NCAM) Fibronectin Domain. J Biol Chem. 2016 Oct 14;291(42):21857-21868. doi: 10.1074/jbc.M116.743435. Epub 2016 Aug 17. PMID: 27535221; PMCID: PMC5063971.

[77] You H, Tsutsui S, Hameed S, Kannanayakal TJ, Chen L, Xia P, Engbers JD, Lipton SA, Stys PK, Zamponi GW. Aβ neurotoxicity depends on interactions between copper ions, prion protein, and N-methyl-D-aspartate receptors. Proc Natl Acad Sci U S A. 2012 Jan 31;109(5):1737-42. doi: 10.1073/pnas.1110789109. Epub 2012 Jan 17. PMID: 22307640; PMCID: PMC3277185.

[78] Kanaani J, Prusiner SB, Diacovo J, Baekkeskov S, Legname G. Recombinant prion protein induces rapid polarization and development of synapses in embryonic rat hippocampal neurons in vitro. J Neurochem. 2005 Dec;95(5):1373-86. doi: 10.1111/j.1471-4159.2005.03469.x. PMID: 16313516.

[79] Slapšak U, Salzano G, Amin L, Abskharon RN, Ilc G, Zupančič B, Biljan I, Plavec J, Giachin G, Legname G. The N Terminus of the Prion Protein Mediates Functional Interactions with the Neuronal Cell Adhesion Molecule (NCAM) Fibronectin Domain. J Biol Chem. 2016 Oct 14;291(42):21857-21868. doi: 10.1074/jbc.M116.743435. Epub 2016 Aug 17. PMID: 27535221; PMCID: PMC5063971.

[80] You H, Tsutsui S, Hameed S, Kannanayakal TJ, Chen L, Xia P, Engbers JD, Lipton SA, Stys PK, Zamponi GW. Aβ neurotoxicity depends on interactions between copper ions, prion protein, and N-methyl-D-aspartate receptors. Proc Natl Acad Sci U S A. 2012 Jan 31;109(5):1737-42. doi: 10.1073/pnas.1110789109. Epub 2012 Jan 17. PMID: 22307640; PMCID: PMC3277185.

[81] Gasperini L, Meneghetti E, Pastore B, Benetti F, Legname G. Prion protein and copper cooperatively protect neurons by modulating NMDA receptor through S-nitrosylation. Antioxid Redox Signal. 2015 Mar 20;22(9):772-84. doi: 10.1089/ars.2014.6032. Epub 2015 Feb 4. PMID: 25490055; PMCID: PMC4361008.

[82] Kristián T, Siesjö BK. Calcium in ischemic cell death. Stroke. 1998 Mar;29(3):705-18. doi: 10.1161/01.str.29.3.705. PMID: 9506616.

[83] Wu QJ, Tymianski M. Targeting NMDA receptors in stroke: new hope in neuroprotection. Mol Brain. 2018 Mar 13;11(1):15. doi: 10.1186/s13041-018-0357-8. PMID: 29534733; PMCID: PMC5851248.

[84] Minikel EV, Vallabh SM, Lek M, Estrada K, Samocha KE, Sathirapongsasuti JF, McLean CY, Tung JY, Yu LP, Gambetti P, Blevins J, Zhang S, Cohen Y, Chen W, Yamada M, Hamaguchi T, Sanjo N, Mizusawa H, Nakamura Y, Kitamoto T, Collins SJ, Boyd A, Will RG, Knight R, Ponto C, Zerr I, Kraus TF, Eigenbrod S, Giese A, Calero M, de Pedro-Cuesta J, Haïk S, Laplanche JL, Bouaziz-Amar E, Brandel JP, Capellari S, Parchi P, Poleggi A, Ladogana A, O'Donnell-Luria AH, Karczewski KJ, Marshall JL, Boehnke M, Laakso M, Mohlke KL, Kähler A, Chambert K, McCarroll S, Sullivan PF, Hultman CM, Purcell SM, Sklar P, van der Lee SJ, Rozemuller A, Jansen C, Hofman A, Kraaij R, van Rooij JG, Ikram MA, Uitterlinden AG, van Duijn CM; Exome Aggregation Consortium (ExAC), Daly MJ, MacArthur DG. Quantifying prion disease penetrance using large population control cohorts. Sci Transl Med. 2016 Jan 20;8(322):322ra9. doi: 10.1126/scitranslmed.aad5169. PMID: 26791950; PMCID: PMC4774245.

[85] Mead S, Whitfield J, Poulter M, Shah P, Uphill J, Campbell T, Al-Dujaily H, Hummerich H, Beck J, Mein CA, Verzilli C, Whittaker J, Alpers MP, Collinge J. A novel protective prion protein variant that colocalizes with kuru exposure. N Engl J Med. 2009 Nov 19;361(21):2056-65. doi: 10.1056/NEJMoa0809716. PMID: 19923577.

[86] Nozaki I, Hamaguchi T, Sanjo N, Noguchi-Shinohara M, Sakai K, Nakamura Y, Sato T, Kitamoto T, Mizusawa H, Moriwaka F, Shiga Y, Kuroiwa Y, Nishizawa M, Kuzuhara S, Inuzuka T, Takeda M, Kuroda S, Abe K, Murai H, Murayama S, Tateishi J, Takumi I, Shirabe S, Harada M, Sadakane A, Yamada M. Prospective 10-year surveillance of human prion diseases in Japan. Brain. 2010 Oct;133(10):3043-57. doi: 10.1093/brain/awq216. Epub 2010 Sep 20. PMID: 20855418.

[87] Pocchiari M, Puopolo M, Croes EA, Budka H, Gelpi E, Collins S, Lewis V, Sutcliffe T, Guilivi A, Delasnerie-Laupretre N, Brandel JP, Alperovitch A, Zerr I, Poser S, Kretzschmar HA, Ladogana A, Rietvald I, Mitrova E, Martinez-Martin P, de Pedro-Cuesta J, Glatzel M, Aguzzi A, Cooper S, Mackenzie J, van Duijn CM, Will RG. Predictors of survival in sporadic Creutzfeldt-Jakob disease and other human transmissible spongiform encephalopathies. Brain. 2004 Oct;127(Pt 10):2348-59. doi: 10.1093/brain/awh249. Epub 2004 Sep 10. PMID: 15361416.

[88] Mead S, Uphill J, Beck J, Poulter M, Campbell T, Lowe J, Adamson G, Hummerich H, Klopp N, Rückert IM, Wichmann HE, Azazi D, Plagnol V, Pako WH, Whitfield J, Alpers MP, Whittaker J, Balding DJ, Zerr I, Kretzschmar H, Collinge J. Genome-wide association study in multiple

human prion diseases suggests genetic risk factors additional to PRNP. Hum Mol Genet. 2012 Apr 15;21(8):1897-906. doi: 10.1093/hmg/ddr607. Epub 2011 Dec 30. PMID: 22210626; PMCID: PMC3313791.

[89] Khan Z, Bollu PC. Fatal Familial Insomnia. 2020 May 27. In: StatPearls [Internet]. Treasure Island (FL): StatPearls Publishing; 2020 Jan–. PMID: 29489284.

[90] Mead S, Webb TE, Campbell TA, Beck J, Linehan JM, Rutherfoord S, Joiner S, Wadsworth JD, Heckmann J, Wroe S, Doey L, King A, Collinge J. Inherited prion disease with 5-OPRI: phenotype modification by repeat length and codon 129. Neurology. 2007 Aug 21;69(8):730-8. doi: 10.1212/01.wnl.0000267642.41594.9d. PMID: 17709704.

[91] Paladino S, Lebreton S, Zurzolo C. Trafficking and Membrane Organization of GPI-Anchored Proteins in Health and Diseases. Curr Top Membr. 2015;75:269-303. doi: 10.1016/bs.ctm.2015.03.006. Epub 2015 Apr 15. PMID: 26015286.

[92] Jung S, Tatzelt J. Impaired transport of intrinsically disordered proteins through the Sec61 and SecY translocon; implications for prion diseases. Prion. 2018 Mar 4;12(2):88-92. doi: 10.1080/19336896.2018.1435936. Epub 2018 Mar 29. PMID: 29388511; PMCID: PMC6016518.

[93] Walmsley AR, Watt NT, Taylor DR, Perera WS, Hooper NM. alpha-cleavage of the prion protein occurs in a late compartment of the secretory pathway and is independent of lipid rafts. Mol Cell Neurosci. 2009 Feb;40(2):242-8. doi: 10.1016/j.mcn.2008.10.012. Epub 2008 Nov 12. PMID: 19056496.

[94] Linsenmeier L, Altmeppen HC, Wetzel S, Mohammadi B, Saftig P, Glatzel M. Diverse functions of the prion protein - Does proteolytic processing hold the key? Biochim Biophys Acta Mol Cell Res. 2017 Nov;1864(11 Pt B):2128-2137. doi: 10.1016/j.bbamcr.2017.06.022. Epub 2017 Jul 8. PMID: 28693923.

[95] Guillot-Sestier MV, Sunyach C, Druon C, Scarzello S, Checler F. The alpha-secretase-derived N-terminal product of cellular prion, N1, displays neuroprotective function in vitro and in vivo. J Biol Chem. 2009 Dec 18;284(51):35973-86. doi: 10.1074/jbc.M109.051086. PMID: 19850936; PMCID: PMC2791025.

[96] Guillot-Sestier MV, Sunyach C, Ferreira ST, Marzolo MP, Bauer C, Thevenet A, Checler F. α-Secretase-derived fragment of cellular prion, N1, protects against monomeric and oligomeric amyloid β (Aβ)-associated cell death. J Biol Chem. 2012 Feb 10;287(7):5021-32. doi: 10.1074/jbc.M111.323626. Epub 2011 Dec 19. Erratum in: J Biol Chem. 2013 Jul 19;288(29):21210. PMID: 22184125; PMCID: PMC3281657.

[97] Johanssen VA, Johanssen T, Masters CL, Hill AF, Barnham KJ, Collins SJ. C-terminal peptides modelling constitutive PrPC processing demonstrate ameliorated toxicity predisposition consequent to α-cleavage. Biochem J. 2014 Apr 1;459(1):103-15. doi: 10.1042/BJ20131378. PMID: 24438129.

[98] Stahl N, Baldwin MA, Burlingame AL, Prusiner SB. Identification of glycoinositol phospholipid linked and truncated forms of the scrapie prion protein. Biochemistry. 1990 Sep 25;29(38):8879-84. doi: 10.1021/bi00490a001. PMID: 1980209.

[99] Shyng SL, Heuser JE, Harris DA. A glycolipid-anchored prion protein is endocytosed via clathrin-coated pits. J Cell Biol. 1994 Jun;125(6):1239-50. doi: 10.1083/jcb.125.6.1239. PMID: 7911471; PMCID: PMC2290925.

[100] Kang YS, Zhao X, Lovaas J, Eisenberg E, Greene LE. Clathrin-independent internalization of normal cellular prion protein in neuroblastoma cells is associated with the Arf6 pathway. J Cell Sci. 2009 Nov 15;122(Pt 22):4062-9. doi: 10.1242/jcs.046292. Epub 2009 Oct 20. PMID: 19843586; PMCID: PMC2798124.

[101] Grant BD, Donaldson JG. Pathways and mechanisms of endocytic recycling. Nat Rev Mol Cell Biol. 2009 Sep;10(9):597-608. doi: 10.1038/nrm2755. PMID: 19696797; PMCID: PMC3038567.

[102] Cortes CJ, Qin K, Norstrom EM, Green WN, Bindokas VP, Mastrianni JA. Early Delivery of Misfolded PrP from ER to Lysosomes by Autophagy. Int J Cell Biol. 2013;2013:560421. doi: 10.1155/2013/560421. Epub 2013 Dec 17. PMID: 24454378; PMCID: PMC3877647.

[103] Drisaldi B, Stewart RS, Adles C, Stewart LR, Quaglio E, Biasini E, Fioriti L, Chiesa R, Harris DA. Mutant PrP is delayed in its exit from the endoplasmic reticulum, but neither wild-type nor mutant PrP undergoes retrotranslocation prior to proteasomal degradation. J Biol Chem. 2003 Jun 13;278(24):21732-43. doi: 10.1074/jbc.M213247200. Epub 2003 Mar 26. PMID: 12663673.

[104] Yedidia Y, Horonchik L, Tzaban S, Yanai A, Taraboulos A. Proteasomes and ubiquitin are involved in the turnover of the wild-type prion protein. EMBO J. 2001 Oct 1;20(19):5383-91. doi: 10.1093/emboj/20.19.5383. PMID: 11574470; PMCID: PMC125653.

[105] Kang SC, Brown DR, Whiteman M, Li R, Pan T, Perry G, Wisniewski T, Sy MS, Wong BS. Prion protein is ubiquitinated after developing protease resistance in the brains of scrapie-infected mice. J Pathol. 2004 May;203(1):603-8. doi: 10.1002/path.1555. PMID: 15095484.

[106] Alves RN, Iglesia RP, Prado MB, Melo Escobar MI, Boccacino JM, Fernandes CFL, Coelho BP, Fortes AC, Lopes MH. A New Take on Prion Protein Dynamics in Cellular Trafficking. Int J Mol Sci. 2020 Oct 20;21(20):7763. doi: 10.3390/ijms21207763. PMID: 33092231; PMCID: PMC7589859.

[107] Fevrier B, Vilette D, Archer F, Loew D, Faigle W, Vidal M, Laude H, Raposo G. Cells release prions in association with exosomes. Proc Natl Acad Sci U S A. 2004 Jun 29;101(26):9683-8. doi: 10.1073/pnas.0308413101. Epub 2004 Jun 21. PMID: 15210972; PMCID: PMC470735.

[108] Kanu N, Imokawa Y, Drechsel DN, Williamson RA, Birkett CR, Bostock CJ, Brockes JP. Transfer of scrapie prion infectivity by cell contact in culture. Curr Biol. 2002 Apr 2;12(7):523-30. doi: 10.1016/s0960-9822(02)00722-4. PMID: 11937020.

[109] Gousset K, Schiff E, Langevin C, Marijanovic Z, Caputo A, Browman DT, Chenouard N, de Chaumont F, Martino A, Enninga J, Olivo-Marin JC, Männel D, Zurzolo C. Prions hijack tunnelling

nanotubes for intercellular spread. Nat Cell Biol. 2009 Mar;11(3):328-36. doi: 10.1038/ncb1841. Epub 2009 Feb 8. PMID: 19198598.

[110] Jiménez-Huete A, Lievens PM, Vidal R, Piccardo P, Ghetti B, Tagliavini F, Frangione B, Prelli F. Endogenous proteolytic cleavage of normal and disease-associated isoforms of the human prion protein in neural and non-neural tissues. Am J Pathol. 1998 Nov;153(5):1561-72. doi: 10.1016/S0002-9440(10)65744-6. PMID: 9811348; PMCID: PMC1853409.

[111] Owen JP, Rees HC, Maddison BC, Terry LA, Thorne L, Jackman R, Whitelam GC, Gough KC. Molecular profiling of ovine prion diseases by using thermolysin-resistant PrPSc and endogenous C2 PrP fragments. J Virol. 2007 Oct;81(19):10532-9. doi: 10.1128/JVI.00640-07. Epub 2007 Jul 25. PMID: 17652380; PMCID: PMC2045483.

[112] Caughey B, Raymond GJ, Ernst D, Race RE. N-terminal truncation of the scrapie-associated form of PrP by lysosomal protease(s): implications regarding the site of conversion of PrP to the protease-resistant state. J Virol. 1991 Dec;65(12):6597-603. doi: 10.1128/JVI.65.12.6597-6603.1991. PMID: 1682507; PMCID: PMC250721.

[113] Mangé A, Béranger F, Peoc'h K, Onodera T, Frobert Y, Lehmann S. Alpha- and beta- cleavages of the amino-terminus of the cellular prion protein. Biol Cell. 2004 Mar;96(2):125-32. doi: 10.1016/j.biolcel.2003.11.007. PMID: 15050367.

[114] Yadavalli R, Guttmann RP, Seward T, Centers AP, Williamson RA, Telling GC. Calpain-dependent endoproteolytic cleavage of PrPSc modulates scrapie prion propagation. J Biol Chem. 2004 May 21;279(21):21948-56. doi: 10.1074/jbc.M400793200. Epub 2004 Mar 16. PMID: 15026410.

[115] Watt NT, Taylor DR, Gillott A, Thomas DA, Perera WS, Hooper NM. Reactive oxygen species-mediated beta-cleavage of the prion protein in the cellular response to oxidative stress. J Biol Chem. 2005 Oct 28;280(43):35914-21. doi: 10.1074/jbc.M507327200. Epub 2005 Aug 24. PMID: 16120605.

[116] Rogers M, Yehiely F, Scott M, Prusiner SB. Conversion of truncated and elongated prion proteins into the scrapie isoform in cultured cells. Proc Natl Acad Sci U S A. 1993 Apr 15;90(8):3182-6. doi: 10.1073/pnas.90.8.3182. PMID: 8475059; PMCID: PMC46263.

[117] Hughes D, Halliday M. What Is Our Current Understanding of PrPSc-Associated Neurotoxicity and Its Molecular Underpinnings? Pathogens. 2017 Dec 1;6(4):63. doi: 10.3390/pathogens6040063. PMID: 29194372; PMCID: PMC5750587.

[118] Mallucci G, Dickinson A, Linehan J, Klöhn PC, Brandner S, Collinge J. Depleting neuronal PrP in prion infection prevents disease and reverses spongiosis. Science. 2003 Oct 31;302(5646):871-4. doi: 10.1126/science.1090187. PMID: 14593181.

[119] Chesebro B, Trifilo M, Race R, Meade-White K, Teng C, LaCasse R, Raymond L, Favara C, Baron G, Priola S, Caughey B, Masliah E, Oldstone M. Anchorless prion protein results in infectious amyloid disease without clinical scrapie. Science. 2005 Jun 3;308(5727):1435-9. doi: 10.1126/science.1110837. PMID: 15933194.

[120] Torres M, Matamala JM, Duran-Aniotz C, Cornejo VH, Foley A, Hetz C. ER stress signaling and neurodegeneration: At the intersection between Alzheimer's disease and Prion-related disorders. Virus Res. 2015 Sep 2;207:69-75. doi: 10.1016/j.virusres.2014.12.018. Epub 2014 Dec 31. PMID: 25556124.

[121] Moreno JA, Radford H, Peretti D, Steinert JR, Verity N, Martin MG, Halliday M, Morgan J, Dinsdale D, Ortori CA, Barrett DA, Tsaytler P, Bertolotti A, Willis AE, Bushell M, Mallucci GR. Sustained translational repression by eIF2α-P mediates prion neurodegeneration. Nature. 2012 May 6;485(7399):507-11. doi: 10.1038/nature11058. Erratum in: Nature.2014 Jul 17;511(7509):370. PMID: 22622579; PMCID: PMC3378208.

[122] McKinnon C, Goold R, Andre R, Devoy A, Ortega Z, Moonga J, Linehan JM, Brandner S, Lucas JJ, Collinge J, Tabrizi SJ. Prion-mediated neurodegeneration is associated with early impairment of the ubiquitin-proteasome system. Acta Neuropathol. 2016 Mar;131(3):411-25. doi: 10.1007/s00401-015-1508-y. Epub 2015 Dec 8. PMID: 26646779; PMCID: PMC4752964.

[123] Xu Y, Tian C, Wang SB, Xie WL, Guo Y, Zhang J, Shi Q, Chen C, Dong XP. Activation of the macroautophagic system in scrapie-infected experimental animals and human genetic prion diseases. Autophagy. 2012 Nov;8(11):1604-20. doi: 10.4161/auto.21482. Epub 2012 Aug 9. PMID: 22874564; PMCID: PMC3494590.

[124] Ratté S, Prescott SA, Collinge J, Jefferys JG. Hippocampal bursts caused by changes in NMDA receptor-dependent excitation in a mouse model of variant CJD. Neurobiol Dis. 2008 Oct;32(1):96-104. doi: 10.1016/j.nbd.2008.06.007. Epub 2008 Jun 26. PMID: 18638557.

[125] Biasini E, Medrano AZ, Thellung S, Chiesa R, Harris DA. Multiple biochemical similarities between infectious and non-infectious aggregates of a prion protein carrying an octapeptide insertion. J Neurochem. 2008 Mar;104(5):1293-308. doi: 10.1111/j.1471-4159.2007.05082.x. Epub 2007 Nov 21. PMID: 18034781.

[126] Chiesa R, Piccardo P, Quaglio E, Drisaldi B, Si-Hoe SL, Takao M, Ghetti B, Harris DA. Molecular distinction between pathogenic and infectious properties of the prion protein. J Virol. 2003 Jul;77(13):7611-22. doi: 10.1128/jvi.77.13.7611-7622.2003. PMID: 12805461; PMCID: PMC164780.

[127] Requena JR, Wille H. The Structure of the Infectious Prion Protein and Its Propagation. Prog Mol Biol Transl Sci. 2017;150:341-359. doi: 10.1016/bs.pmbts.2017.06.009. Epub 2017 Jul 31. PMID: 28838667

[128] Makarava N, Baskakov IV. Genesis of tramsmissible protein states via deformed templating. Prion. 2012 Jul 1;6(3):252-5. doi: 10.4161/pri.19930. Epub 2012 Jul 1. PMID: 22561163; PMCID: PMC3399541.

[129] Makarava N, Kovacs GG, Savtchenko R, Alexeeva I, Ostapchenko VG, Budka H, Rohwer RG, Baskakov IV. A new mechanism for transmissible prion diseases. J Neurosci. 2012 May 23;32(21):7345-55. doi: 10.1523/JNEUROSCI.6351-11.2012. PMID: 22623680; PMCID: PMC3368278.

[130] Tycko R, Savtchenko R, Ostapchenko VG, Makarava N, Baskakov IV. The α-helical C-terminal domain of full-length recombinant PrP converts to an in-register parallel β-sheet structure in PrP fibrils: evidence from solid state nuclear magnetic resonance. Biochemistry. 2010 Nov 9;49(44):9488-97. doi: 10.1021/bi1013134. PMID: 20925423; PMCID: PMC3025268.

[131] Requena JR, Wille H. The structure of the infectious prion protein: experimental data and molecular models. Prion. 2014 Jan-Feb;8(1):60-6. doi: 10.4161/pri.28368. PMID: 24583975; PMCID: PMC7030906.

[132] Vázquez-Fernández E, Vos MR, Afanasyev P, Cebey L, Sevillano AM, Vidal E, Rosa I, Renault L, Ramos A, Peters PJ, Fernández JJ, van Heel M, Young HS, Requena JR, Wille H. The Structural Architecture of an Infectious Mammalian Prion Using Electron Cryomicroscopy. PLoS Pathog. 2016 Sep 8;12(9):e1005835. doi: 10.1371/journal.ppat.1005835. PMID: 27606840; PMCID: PMC5015997.

[133] Muchmore DC, McIntosh LP, Russell CB, Anderson DE, Dahlquist FW. Expression and nitrogen-15 labeling of proteins for proton and nitrogen-15 nuclear magnetic resonance. Methods Enzymol. 1989;177:44-73. doi: 10.1016/0076-6879(89)77005-1. PMID: 2691846.

[134] Caughey B, Baron GS, Chesebro B, Jeffrey M. Getting a grip on prions: oligomers, amyloids, and pathological membrane interactions. Annu Rev Biochem. 2009;78:177-204. doi: 10.1146/annurev.biochem.78.082907.145410. PMID: 19231987; PMCID: PMC2794486.

[135] Wang F, Wang X, Yuan CG, Ma J. Generating a prion with bacterially expressed recombinant prion protein. Science. 2010 Feb 26;327(5969):1132-5. doi: 10.1126/science.1183748. Epub 2010 Jan 28. PMID: 20110469; PMCID: PMC2893558.

[136] Caughey B, Raymond GJ, Bessen RA. Strain-dependent differences in beta-sheet conformations of abnormal prion protein. J Biol Chem. 1998 Nov 27;273(48):32230-5. doi: 10.1074/jbc.273.48.32230. PMID: 9822701.

[137] Wemheuer WM, Wrede A, Schulz-Schaeffer WJ. Types and Strains: Their Essential Role in Understanding Protein Aggregation in Neurodegenerative Diseases. Front Aging Neurosci. 2017 Jun 16;9:187. doi: 10.3389/fnagi.2017.00187. PMID: 28670273; PMCID: PMC5472693.

[138] Choi JK, Cali I, Surewicz K, Kong Q, Gambetti P, Surewicz WK. Amyloid fibrils from the N-terminal prion protein fragment are infectious. Proc Natl Acad Sci U S A. 2016 Nov 29;113(48):13851-13856. doi: 10.1073/pnas.1610716113. Epub 2016 Nov 14. PMID: 27849581; PMCID: PMC5137684.

[139] Theint T, Xia Y, Nadaud PS, Mukhopadhyay D, Schwieters CD, Surewicz K, Surewicz WK, Jaroniec CP. Structural Studies of Amyloid Fibrils by Paramagnetic Solid-State Nuclear Magnetic Resonance Spectroscopy. J Am Chem Soc. 2018 Oct 17;140(41):13161-13166. doi: 10.1021/jacs.8b06758. Epub 2018 Oct 9. PMID: 30295029; PMCID: PMC6193843.

[140] Caughey BW, Dong A, Bhat KS, Ernst D, Hayes SF, Caughey WS. Secondary structure analysis of the scrapie-associated protein PrP 27-30 in water by infrared spectroscopy. Biochem-

istry. 1991 Aug 6;30(31):7672-80. doi: 10.1021/bi00245a003. Erratum in: Biochemistry 1991 Oct 29;30(43):10600. PMID: 1678278.

[141] Pan KM, Baldwin M, Nguyen J, Gasset M, Serban A, Groth D, Mehlhorn I, Huang Z, Fletterick RJ, Cohen FE, et al. Conversion of alpha-helices into beta-sheets features in the formation of the scrapie prion proteins. Proc Natl Acad Sci U S A. 1993 Dec 1;90(23):10962-6. doi: 10.1073/pnas.90.23.10962. PMID: 7902575; PMCID: PMC47901.

[142] Smirnovas V, Baron GS, Offerdahl DK, Raymond GJ, Caughey B, Surewicz WK. Structural organization of brain-derived mammalian prions examined by hydrogen- deuterium exchange. Nat Struct Mol Biol. 2011;18(4):504–506.

[143] Vázquez-Fernández E, Alonso J, Pastrana MA, Ramos A, Stitz L, Vidal E, Dynin I, Petsch B, Silva CJ, Requena JR. Structural organization of mammalian prions as probed by limited proteolysis. PLoS One. 2012;7(11):e50111. doi: 10.1371/journal.pone.0050111. Epub 2012 Nov 20. PMID: 23185550; PMCID: PMC3502352.

[144] Sevillano AM, Fernández-Borges N, Younas N, Wang F, R Elezgarai S, Bravo S, Vázquez-Fernández E, Rosa I, Eraña H, Gil D, Veiga S, Vidal E, Erickson-Beltran ML, Guitián E, Silva CJ, Nonno R, Ma J, Castilla J, R Requena J. Recombinant PrPSc shares structural features with brain-derived PrPSc: Insights from limited proteolysis. PLoS Pathog. 2018 Jan 31;14(1):e1006797. doi: 10.1371/journal.ppat.1006797. PMID: 29385212; PMCID: PMC5809102.

[145] Anderson M, Bocharova OV, Makarava N, Breydo L, Salnikov VV, Baskakov IV. Polymorphism and ultrastructural organization of prion protein amyloid fibrils: an insight from high resolution atomic force microscopy. J Mol Biol. 2006 Apr 28;358(2):580-96. doi: 10.1016/j.jmb.2006.02.007. Epub 2006 Feb 20. PMID: 16519898.

[146] Piro JR, Wang F, Walsh DJ, Rees JR, Ma J, Supattapone S. Seeding specificity and ultrastructural characteristics of infectious recombinant prions. Biochemistry. 2011 Aug 23;50(33):7111-6. doi: 10.1021/bi200786p. Epub 2011 Jul 21. PMID: 21776987; PMCID: PMC3319715.

[147] Prusiner SB, McKinley MP, Bowman KA, Bolton DC, Bendheim PE, Groth DF, Glenner GG. Scrapie prions aggregate to form amyloid-like birefringent rods. Cell. 1983 Dec;35(2 Pt 1):349-58. doi: 10.1016/0092-8674(83)90168-x. PMID: 6418385.

[148] Wille H, Michelitsch MD, Guenebaut V, Supattapone S, Serban A, Cohen FE, Agard DA, Prusiner SB. Structural studies of the scrapie prion protein by electron crystallography. Proc Natl Acad Sci U S A. 2002 Mar 19;99(6):3563-8. doi: 10.1073/pnas.052703499. Epub 2002 Mar 12. PMID: 11891310; PMCID: PMC122563.

[149] Govaerts C, Wille H, Prusiner SB, Cohen FE. Evidence for assembly of prions with left-handed beta-helices into trimers. Proc Natl Acad Sci U S A. 2004 Jun 1;101(22):8342-7. doi: 10.1073/pnas.0402254101. Epub 2004 May 21. PMID: 15155909; PMCID: PMC420396.

[150] Wille H, Bian W, McDonald M, Kendall A, Colby DW, Bloch L, Ollesch J, Borovinskiy AL, Cohen FE, Prusiner SB, Stubbs G. Natural and synthetic prion structure from X-ray fiber diffraction. Proc

Natl Acad Sci U S A. 2009 Oct 6;106(40):16990-5. doi: 10.1073/pnas.0909006106. Epub 2009 Sep 28. PMID: 19805070; PMCID: PMC2761340.

[151] Amenitsch H, Benetti F, Ramos A, Legname G, Requena JR. SAXS structural study of PrP(Sc) reveals ~11 nm diameter of basic double intertwined fibers. Prion. 2013 Nov-Dec;7(6):496-500. doi: 10.4161/pri.27190. Epub 2013 Nov 18. PMID: 24247356; PMCID: PMC4201618.

[152] Müller H, Brener O, Andreoletti O, Piechatzek T, Willbold D, Legname G, Heise H. Progress towards structural understanding of infectious sheep PrP-amyloid. Prion. 2014;8(5):344-58. doi: 10.4161/19336896.2014.983754. PMID: 25482596; PMCID: PMC4601355.

[153] Groveman BR, Dolan MA, Taubner LM, Kraus A, Wickner RB, Caughey B. Parallel in-register intermolecular β-sheet architectures for prion-seeded prion protein (PrP) amyloids. J Biol Chem. 2014 Aug 29;289(35):24129-42. doi: 10.1074/jbc.M114.578344. Epub 2014 Jul 15. PMID: 25028516; PMCID: PMC4148845.

[154] Terry C, Harniman RL, Sells J, Wenborn A, Joiner S, Saibil HR, Miles MJ, Collinge J, Wadsworth JDF. Structural features distinguishing infectious ex vivo mammalian prions from non-infectious fibrillar assemblies generated in vitro. Sci Rep. 2019 Jan 23;9(1):376. doi: 10.1038/s41598-018-36700-w. PMID: 30675000; PMCID: PMC6344479.

[155] Aguzzi A, Lakkaraju AKK, Frontzek K. Toward Therapy of Human Prion Diseases. Annu Rev Pharmacol Toxicol. 2018 Jan 6;58:331-351. doi: 10.1146/annurev-pharmtox-010617-052745. Epub 2017 Sep 27. PMID: 28961066.

[156] Ma Y, Ma J. Immunotherapy against Prion Disease. Pathogens. 2020 Mar 14;9(3):216. doi: 10.3390/pathogens9030216. PMID: 32183309; PMCID: PMC7157205.

[157] Biasini E, Seegulam ME, Patti BN, Solforosi L, Medrano AZ, Christensen HM, Senatore A, Chiesa R, Williamson RA, Harris DA. Non-infectious aggregates of the prion protein react with several PrPSc-directed antibodies. J Neurochem. 2008 Jun 1;105(6):2190-204. doi: 10.1111/j.1471-4159.2008.05306.x. PMID: 18298665.

[158] Petsch B, Müller-Schiffmann A, Lehle A, Zirdum E, Prikulis I, Kuhn F, Raeber AJ, Ironside JW, Korth C, Stitz L. Biological effects and use of PrPSc- and PrP-specific antibodies generated by immunization with purified full-length native mouse prions. J Virol. 2011 May;85(9):4538-46. doi: 10.1128/JVI.02467-10. Epub 2011 Feb 23. PMID: 21345946; PMCID: PMC3126253.

[159] White AR, Enever P, Tayebi M, Mushens R, Linehan J, Brandner S, Anstee D, Collinge J, Hawke S. Monoclonal antibodies inhibit prion replication and delay the development of prion disease. Nature. 2003 Mar 6;422(6927):80-3. doi: 10.1038/nature01457. PMID: 12621436.

[160] Silveira JR, Raymond GJ, Hughson AG, Race RE, Sim VL, Hayes SF, Caughey B. The most infectious prion protein particles. Nature. 2005 Sep 8;437(7056):257-61. doi: 10.1038/nature03989. PMID: 16148934; PMCID: PMC1513539.

[161] Knowles TP, Waudby CA, Devlin GL, Cohen SI, Aguzzi A, Vendruscolo M, Terentjev EM, Welland ME, Dobson CM. An analytical solution to the kinetics of breakable filament assembly. Science. 2009 Dec 11;326(5959):1533-7. doi: 10.1126/science.1178250. PMID: 20007899.

[162] Herrmann US, Schütz AK, Shirani H, Huang D, Saban D, Nuvolone M, Li B, Ballmer B, Åslund AK, Mason JJ, Rushing E, Budka H, Nyström S, Hammarström P, Böckmann A, Caflisch A, Meier BH, Nilsson KP, Hornemann S, Aguzzi A. Structure-based drug design identifies polythiophenes as antiprion compounds. Sci Transl Med. 2015 Aug 5;7(299):299ra123. doi: 10.1126/scitranslmed.aab1923. PMID: 26246168.

[163] Giles K, Olson SH, Prusiner SB. Developing Therapeutics for PrP Prion Diseases. Cold Spring Harb Perspect Med. 2017 Apr 3;7(4):a023747. doi: 10.1101/cshperspect.a023747. PMID: 28096242; PMCID: PMC5378016.

[164] Giles K, Berry DB, Condello C, Hawley RC, Gallardo-Godoy A, Bryant C, Oehler A, Elepano M, Bhardwaj S, Patel S, Silber BM, Guan S, DeArmond SJ, Renslo AR, Prusiner SB. Different 2-Aminothiazole Therapeutics Produce Distinct Patterns of Scrapie Prion Neuropathology in Mouse Brains. J Pharmacol Exp Ther. 2015 Oct;355(1):2-12. doi: 10.1124/jpet.115.224659. Epub 2015 Jul 29. PMID: 26224882; PMCID: PMC4576665.

[165] Moreno JA, Halliday M, Molloy C, Radford H, Verity N, Axten JM, Ortori CA, Willis AE, Fischer PM, Barrett DA, Mallucci GR. Oral treatment targeting the unfolded protein response prevents neurodegeneration and clinical disease in prion-infected mice. Sci Transl Med. 2013 Oct 9;5(206):206ra138. doi: 10.1126/scitranslmed.3006767. PMID: 24107777.

[166] Béranger F, Crozet C, Goldsborough A, Lehmann S. Trehalose impairs aggregation of PrPSc molecules and protects prion-infected cells against oxidative damage. Biochem Biophys Res Commun. 2008 Sep 12;374(1):44-8. doi: 10.1016/j.bbrc.2008.06.094. Epub 2008 Jul 3. PMID: 18602368.

[167] Turturici G, Sconzo G, Geraci F. Hsp70 and its molecular role in nervous system diseases. Biochem Res Int. 2011;2011:618127. doi: 10.1155/2011/618127. Epub 2011 Feb 24. PMID: 21403864; PMCID: PMC3049350.

[168] Sim VL. Prion disease: chemotherapeutic strategies. Infect Disord Drug Targets. 2012 Apr;12(2):144-60. doi: 10.2174/187152612800100161. PMID: 22420513.

[169] Taubner LM, Bienkiewicz EA, Copié V, Caughey B. Structure of the flexible amino-terminal domain of prion protein bound to a sulfated glycan. J Mol Biol. 2010 Jan 22;395(3):475-90. doi: 10.1016/j.jmb.2009.10.075. Epub 2009 Nov 10. PMID: 19913031; PMCID: PMC2830820.

[170] Shyng SL, Lehmann S, Moulder KL, Harris DA. Sulfated glycans stimulate endocytosis of the cellular isoform of the prion protein, PrPC, in cultured cells. J Biol Chem. 1995 Dec 15;270(50):30221-9. doi: 10.1074/jbc.270.50.30221. PMID: 8530433.

[171] Caughey B, Brown K, Raymond GJ, Katzenstein GE, Thresher W. Binding of the protease-sensitive form of PrP (prion protein) to sulfated glycosaminoglycan and congo red [corrected]. J

Virol. 1994 Apr;68(4):2135-41. doi: 10.1128/JVI.68.4.2135-2141.1994. Erratum in: J Virol 1994 Jun;68(6):4107. PMID: 7511169; PMCID: PMC236688.

[172] Doh-ura K, Ishikawa K, Murakami-Kubo I, Sasaki K, Mohri S, Race R, Iwaki T. Treatment of transmissible spongiform encephalopathy by intraventricular drug infusion in animal models. J Virol. 2004 May;78(10):4999-5006. doi: 10.1128/jvi.78.10.4999-5006.2004. PMID: 15113880; PMCID: PMC400350.

[173] Honda H, Sasaki K, Minaki H, Masui K, Suzuki SO, Doh-Ura K, Iwaki T. Protease-resistant PrP and PrP oligomers in the brain in human prion diseases after intraventricular pentosan polysulfate infusion. Neuropathology. 2012 Apr;32(2):124-32. doi: 10.1111/j.1440-1789.2011.01245.x. Epub 2011 Aug 1. PMID: 21801238.

[174] Kocisko DA, Vaillant A, Lee KS, Arnold KM, Bertholet N, Race RE, Olsen EA, Juteau JM, Caughey B. Potent antiscrapie activities of degenerate phosphorothioate oligonucleotides. Antimicrob Agents Chemother. 2006 Mar;50(3):1034-44. doi: 10.1128/AAC.50.3.1034-1044.2006. PMID: 16495266; PMCID: PMC1426446.

[175] Doh-Ura K, Iwaki T, Caughey B. Lysosomotropic agents and cysteine protease inhibitors inhibit scrapie-associated prion protein accumulation. J Virol. 2000 May;74(10):4894-7. doi: 10.1128/jvi.74.10.4894-4897.2000. PMID: 10775631; PMCID: PMC112015.

[176] Korth C, May BC, Cohen FE, Prusiner SB. Acridine and phenothiazine derivatives as pharmacotherapeutics for prion disease. Proc Natl Acad Sci U S A. 2001 Aug 14;98(17):9836-41. doi: 10.1073/pnas.161274798. PMID: 11504948; PMCID: PMC55539.

[177] Barreca ML, Iraci N, Biggi S, Cecchetti V, Biasini E. Pharmacological Agents Targeting the Cellular Prion Protein. Pathogens. 2018 Mar 7;7(1):27. doi: 10.3390/pathogens7010027. PMID: 29518975; PMCID: PMC5874753.

[178] Stincardini C, Massignan T, Biggi S, Elezgarai SR, Sangiovanni V, Vanni I, Pancher M, Adami V, Moreno J, Stravalaci M, Maietta G, Gobbi M, Negro A, Requena JR, Castilla J, Nonno R, Biasini E. An antipsychotic drug exerts anti-prion effects by altering the localization of the cellular prion protein. PLoS One. 2017 Aug 7;12(8):e0182589. doi: 10.1371/journal.pone.0182589. PMID: 28787011; PMCID: PMC5546605.

[179] Collinge J, Gorham M, Hudson F, Kennedy A, Keogh G, Pal S, Rossor M, Rudge P, Siddique D, Spyer M, Thomas D, Walker S, Webb T, Wroe S, Darbyshire J. Safety and efficacy of quinacrine in human prion disease (PRION-1 study): a patient-preference trial. Lancet Neurol. 2009 Apr;8(4):334-44. doi: 10.1016/S1474-4422(09)70049-3. Epub 2009 Mar 9. PMID: 19278902; PMCID: PMC2660392.

[180] Ghaemmaghami S, Ahn M, Lessard P, Giles K, Legname G, DeArmond SJ, Prusiner SB. Continuous quinacrine treatment results in the formation of drug-resistant prions. PLoS Pathog. 2009 Nov;5(11):e1000673. doi: 10.1371/journal.ppat.1000673. Epub 2009 Nov 26. PMID: 19956709; PMCID: PMC2777304.

[181] Caughey WS, Raymond LD, Horiuchi M, Caughey B. Inhibition of protease-resistant prion protein formation by porphyrins and phthalocyanines. Proc Natl Acad Sci U S A. 1998 Oct 13;95(21):12117-22. doi: 10.1073/pnas.95.21.12117. PMID: 9770449; PMCID: PMC22794.

[182] Nicoll AJ, Trevitt CR, Tattum MH, Risse E, Quarterman E, Ibarra AA, Wright C, Jackson GS, Sessions RB, Farrow M, Waltho JP, Clarke AR, Collinge J. Pharmacological chaperone for the structured domain of human prion protein. Proc Natl Acad Sci U S A. 2010 Oct 12;107(41):17610-5. doi: 10.1073/pnas.1009062107. Epub 2010 Sep 27. PMID: 20876144; PMCID: PMC2955083.

[183] Rajora MA, Lou JWH, Zheng G. Advancing porphyrin's biomedical utility via supramolecular chemistry. Chem Soc Rev. 2017 Oct 30;46(21):6433-6469. doi: 10.1039/c7cs00525c. PMID: 29048439.

[184] Yamaguchi K, Kamatari YO, Ono F, Shibata H, Fuse T, Elhelaly AE, Fukuoka M, Kimura T, Hosokawa-Muto J, Ishikawa T, Tobiume M, Takeuchi Y, Matsuyama Y, Ishibashi D, Nishida N, Kuwata K. A designer molecular chaperone against transmissible spongiform encephalopathy slows disease progression in mice and macaques. Nat Biomed Eng. 2019 Mar;3(3):206-219. doi: 10.1038/s41551-019-0349-8. Epub 2019 Feb 11. PMID: 30948810.

[185] Biasini E. A designer chaperone against prion diseases. Nat Biomed Eng. 2019 Mar;3(3):167-168. doi: 10.1038/s41551-019-0367-6. PMID: 30948815.

[186] Raymond GJ, Zhao HT, Race B, Raymond LD, Williams K, Swayze EE, Graffam S, Le J, Caron T, Stathopoulos J, O'Keefe R, Lubke LL, Reidenbach AG, Kraus A, Schreiber SL, Mazur C, Cabin DE, Carroll JB, Minikel EV, Kordasiewicz H, Caughey B, Vallabh SM. Antisense oligonucleotides extend survival of prion-infected mice. JCI Insight. 2019 Jul 30;5(16):e131175. doi: 10.1172/jci.insight.131175. PMID: 31361599; PMCID: PMC6777807.

[187] Source: Ionis Pharmaceutical Website (Pipeline)

[188] Finkel RS, Chiriboga CA, Vajsar J, Day JW, Montes J, De Vivo DC, Yamashita M, Rigo F, Hung G, Schneider E, Norris DA, Xia S, Bennett CF, Bishop KM. Treatment of infantile-onset spinal muscular atrophy with nusinersen: a phase 2, open-label, dose-escalation study. Lancet. 2016 Dec 17;388(10063):3017-3026. doi: 10.1016/S0140-6736(16)31408-8. Epub 2016 Dec 7. PMID: 27939059.

[189] Astolfi A, Spagnolli G, Biasini E, Barreca ML. The Compelling Demand for an Effective PrPC-Directed Therapy against Prion Diseases. ACS Med Chem Lett. 2020 Nov 2;11(11):2063-2067. doi: 10.1021/acsmedchemlett.0c00528. PMID: 33209189; PMCID: PMC7667650.

[190] Englander SW, Mayne L. The nature of protein folding pathways. Proc Natl Acad Sci U S A. 2014 Nov 11;111(45):15873-80. doi: 10.1073/pnas.1411798111. Epub 2014 Oct 17. PMID: 25326421; PMCID: PMC4234557.

[191] Gershenson A, Gosavi S, Faccioli P, Wintrode PL. Successes and challenges in simulating the folding of large proteins. J Biol Chem. 2020 Jan 3;295(1):15-33. doi: 10.1074/jbc.REV119.006794. Epub 2019 Nov 11. PMID: 31712314; PMCID: PMC6952611.

[192] Chan CK, Hu Y, Takahashi S, Rousseau DL, Eaton WA, Hofrichter J. Submillisecond protein folding kinetics studied by ultrarapid mixing. Proc Natl Acad Sci U S A. 1997 Mar 4;94(5):1779-84. doi: 10.1073/pnas.94.5.1779. PMID: 9050855; PMCID: PMC19993.

[193] Schuler B, Eaton WA. Protein folding studied by single-molecule FRET. Curr Opin Struct Biol. 2008 Feb;18(1):16-26. doi: 10.1016/j.sbi.2007.12.003. Epub 2008 Jan 24. PMID: 18221865; PMCID: PMC2323684.

[194] Li R, Woodward C. The hydrogen exchange core and protein folding. Protein Sci. 1999 Aug;8(8):1571-90. doi: 10.1110/ps.8.8.1571. PMID: 10452602; PMCID: PMC2144413.

[195] Cornwell O, Radford SE, Ashcroft AE, Ault JR. Comparing Hydrogen Deuterium Exchange and Fast Photochemical Oxidation of Proteins: a Structural Characterisation of Wild-Type and ΔN6 β2-Microglobulin. J Am Soc Mass Spectrom. 2018 Dec;29(12):2413-2426. doi: 10.1007/s13361-018-2067-y. Epub 2018 Sep 28. PMID: 30267362; PMCID: PMC6276068.

[196] Bolder SG, Sagis LM, Venema P, van der Linden E. Thioflavin T and birefringence assays to determine the conversion of proteins into fibrils. Langmuir. 2007 Apr 10;23(8):4144-7. doi: 10.1021/la063048k. Epub 2007 Mar 7. PMID: 17341102.

[197] Lindorff-Larsen K, Piana S, Dror RO, Shaw DE. How fast-folding proteins fold. Science. 2011 Oct 28;334(6055):517-20. doi: 10.1126/science.1208351. PMID: 22034434.

[198] Apetri AC, Maki K, Roder H, Surewicz WK. Early intermediate in human prion protein folding as evidenced by ultrarapid mixing experiments. J Am Chem Soc. 2006 Sep 6;128(35):11673-8. doi: 10.1021/ja063880b. PMID: 16939293; PMCID: PMC2856597.

[199] Yang YI, Shao Q, Zhang J, Yang L, Gao YQ. Enhanced sampling in molecular dynamics. J Chem Phys. 2019 Aug 21;151(7):070902. doi: 10.1063/1.5109531. PMID: 31438687.

[200] Torrie GM and Vallea JP, Nonphysical sampling distributions in Monte Carlo free-energy estimation: Umbrella sampling. J. Comput. Phys. 23, 187 (1977). doi: 10.1016/0021-9991(77)90121-8

[201] Laio A, Parrinello M. Escaping free-energy minima. Proc Natl Acad Sci U S A. 2002 Oct 1;99(20):12562-6. doi: 10.1073/pnas.202427399. Epub 2002 Sep 23. PMID: 12271136; PMCID: PMC130499.

[202] Sugita Y and Okamoto Y, Replica-exchange molecular dynamics method for protein folding, Chem. Phys. Lett. 314, 141 (1999). doi: 10.1016/s0009-2614(99)01123-9

[203] Voelz VA, Jäger M, Yao S, Chen Y, Zhu L, Waldauer SA, Bowman GR, Friedrichs M, Bakajin O, Lapidus LJ, Weiss S, Pande VS. Slow unfolded-state structuring in Acyl-CoA binding protein folding revealed by simulation and experiment. J Am Chem Soc. 2012 Aug 1;134(30):12565-77. doi: 10.1021/ja302528z. Epub 2012 Jul 19. PMID: 22747188; PMCID: PMC3462454.

[204] Bitran A, Jacobs WM, Shakhnovich E. Validation of DBFOLD: An efficient algorithm for computing folding pathways of complex proteins. PLoS Comput Biol. 2020 Nov 16;16(11):e1008323. doi: 10.1371/journal.pcbi.1008323. PMID: 33196646; PMCID: PMC7704049.

[205] Rojas A, Liwo A, Browne D, Scheraga HA. Mechanism of fiber assembly: treatment of Aβ peptide aggregation with a coarse-grained united-residue force field. J Mol Biol. 2010 Dec 3;404(3):537-52. doi: 10.1016/j.jmb.2010.09.057. Epub 2010 Oct 1. PMID: 20888834; PMCID: PMC2981693.

[206] Baiesi M, Seno F, Trovato A. Fibril elongation mechanisms of HET-s prion-forming domain: topological evidence for growth polarity. Proteins. 2011 Nov;79(11):3067-81. doi: 10.1002/prot.23133. Epub 2011 Aug 30. PMID: 21989930.

[207] Ingólfsson HI, Lopez CA, Uusitalo JJ, de Jong DH, Gopal SM, Periole X, Marrink SJ. The power of coarse graining in biomolecular simulations. Wiley Interdiscip Rev Comput Mol Sci. 2014 May;4(3):225-248. doi: 10.1002/wcms.1169. PMID: 25309628; PMCID: PMC4171755.

[208] Okumura H, Itoh SG. Structural and fluctuational difference between two ends of Aβ amyloid fibril: MD simulations predict only one end has open conformations. Sci Rep. 2016 Dec 9;6:38422. doi: 10.1038/srep38422. PMID: 27934893; PMCID: PMC5146922.

[209] Hashemi M, Zhang Y, Lvac Z, and Lyubchenko YL. Spontaneous self-assembly of amyloid β (1–40) into dimers. Nanoscale Adv., 2019,1, 3892-3899. doi: 10.1039/C9NA00380K.

[210] A Beccara S, Fant L, Faccioli P. Variational scheme to compute protein reaction pathways using atomistic force fields with explicit solvent. Phys Rev Lett. 2015 Mar 6;114(9):098103. doi: 10.1103/PhysRevLett.114.098103. Epub 2015 Mar 4. PMID: 25793854.

[211] Orioli S, A Beccara S, Faccioli P. Self-consistent calculation of protein folding pathways. J Chem Phys. 2017 Aug 14;147(6):064108. doi: 10.1063/1.4997197. PMID: 28810783.

[212] Ianeselli A, Orioli S, Spagnolli G, Faccioli P, Cupellini L, Jurinovich S, Mennucci B. Atomic Detail of Protein Folding Revealed by an Ab Initio Reappraisal of Circular Dichroism. J Am Chem Soc. 2018 Mar 14;140(10):3674-3682. doi: 10.1021/jacs.7b12399. Epub 2018 Mar 6. PMID: 29473417.

[213] Best RB, Hummer G, Eaton WA. Native contacts determine protein folding mechanisms in atomistic simulations. Proc Natl Acad Sci U S A. 2013 Oct 29;110(44):17874-9. doi: 10.1073/pnas.1311599110. Epub 2013 Oct 15. PMID: 24128758; PMCID: PMC3816414.

[214] Terruzzi L, Spagnolli G, Boldrini A, Requena JR, Biasini E, Faccioli P. All-atom simulation of the HET-s prion replication. PLoS Comput Biol. 2020 Sep 18;16(9):e1007922. doi: 10.1371/journal.pcbi.1007922. PMID: 32946455; PMCID: PMC7526898.

[215] Spagnolli G, Rigoli M, Orioli S, Sevillano AM, Faccioli P, Wille H, Biasini E, Requena JR. Full atomistic model of prion structure and conversion. PLoS Pathog. 2019 Jul 11;15(7):e1007864. doi: 10.1371/journal.ppat.1007864. PMID: 31295325; PMCID: PMC6622554.

[216] Mizuno N, Baxa U, Steven AC. Structural dependence of HET-s amyloid fibril infectivity assessed by cryoelectron microscopy. Proc Natl Acad Sci U S A. 2011 Feb 22;108(8):3252-7. doi: 10.1073/pnas.1011342108. Epub 2011 Feb 7. PMID: 21300906; PMCID: PMC3044374.

[217] Spagnolli G, Rigoli M, Novi Inverardi G, Codeseira YB, Biasini E, Requena JR. Modeling PrP^{Sc} Generation Through Deformed Templating. Front Bioeng Biotechnol. 2020 Oct 6;8:590501. doi: 10.3389/fbioe.2020.590501. PMID: 33123520; PMCID: PMC7573312.

[218] Wang LQ, Zhao K, Yuan HY, Wang Q, Guan Z, Tao J, Li XN, Sun Y, Yi CW, Chen J, Li D, Zhang D, Yin P, Liu C, Liang Y. Cryo-EM structure of an amyloid fibril formed by full-length human prion protein. Nat Struct Mol Biol. 2020 Jun;27(6):598-602. doi: 10.1038/s41594-020-0441-5. Epub 2020 Jun 8. PMID: 32514176.

[219] Artikis E, Roy A, Verli H, Cordeiro Y, Caughey B. Accommodation of In-Register N-Linked Glycans on Prion Protein Amyloid Cores. ACS Chem Neurosci. 2020 Dec 16;11(24):4092-4097. doi: 10.1021/acschemneuro.0c00635. Epub 2020 Nov 12. PMID: 33180459.

[220] Rudd PM, Wormald MR, Wing DR, Prusiner SB, Dwek RA. Prion glycoprotein: structure, dynamics, and roles for the sugars. Biochemistry. 2001 Apr 3;40(13):3759-66. doi: 10.1021/bi002625f. PMID: 11300755.

[221] Bartolucci G, Orioli S, Faccioli P. Transition path theory from biased simulations. J Chem Phys. 2018 Aug 21;149(7):072336. doi: 10.1063/1.5027253. PMID: 30134709.

[222] Zhao YL, Wu YD. A theoretical study of beta-sheet models: is the formation of hydrogen-bond networks cooperative? J Am Chem Soc. 2002 Feb 27;124(8):1570-1. doi: 10.1021/ja016230a. PMID: 11853419.

[223] Kung VM, Cornilescu G, Gellman SH. Impact of Strand Number on Parallel β-Sheet Stability. Angew Chem Int Ed Engl. 2015 Nov 23;54(48):14336-9. doi: 10.1002/anie.201506448. Epub 2015 Oct 12. PMID: 26457984; PMCID: PMC4715541.

[224] Moroncini G, Kanu N, Solforosi L, Abalos G, Telling GC, Head M, Ironside J, Brockes JP, Burton DR, Williamson RA. Motif-grafted antibodies containing the replicative interface of cellular PrP are specific for PrPSc. Proc Natl Acad Sci U S A. 2004 Jul 13;101(28):10404-9. doi: 10.1073/pnas.0403522101. Epub 2004 Jul 6. PMID: 15240877; PMCID: PMC478584.

[225] Nicholson EM, Mo H, Prusiner SB, Cohen FE, Marqusee S. Differences between the prion protein and its homolog Doppel: a partially structured state with implications for scrapie formation. J Mol Biol. 2002 Feb 22;316(3):807-15. doi: 10.1006/jmbi.2001.5347. PMID: 11866533.

[226] Safety, Tolerability, Pharmacokinetics, and Pharmacodynamics of ISIS 443139 in Participants With Early Manifest Huntington's Disease. ClinicalTrials.gov Identifier: NCT02519036

[227] Wang Y, Jiang X, Feng F, Liu W, Sun H. Degradation of proteins by PROTACs and other strategies. Acta Pharm Sin B. 2020 Feb;10(2):207-238. doi: 10.1016/j.apsb.2019.08.001. Epub 2019 Aug 13. PMID: 32082969; PMCID: PMC7016280.

[228] Petrosyan R, Patra S, Rezajooei N, Garen CR, Woodside MT. Unfolded and intermediate states of PrP play a key role in the mechanism of action of an antiprion chaperone. PNAS Mar 2021, 118 (9) e2010213118; doi: 10.1073/pnas.2010213118

[229] Halgren TA. Identifying and characterizing binding sites and assessing druggability. J Chem Inf Model. 2009 Feb;49(2):377-89. doi: 10.1021/ci800324m. PMID: 19434839.

[230] Volkamer A, Kuhn D, Grombacher T, Rippmann F, Rarey M. Combining global and local measures for structure-based druggability predictions. J Chem Inf Model. 2012 Feb 27;52(2):360-72. doi: 10.1021/ci200454v. Epub 2012 Jan 5. PMID: 22148551.

[231] Gastreich M, Lilienthal M, Briem H, Claussen H. Ultrafast de novo docking combining pharmacophores and combinatorics. J Comput Aided Mol Des. 2006 Dec;20(12):717-34. doi: 10.1007/s10822-006-9091-x. Epub 2007 Jan 30. PMID: 17265098.

[232] Schneider N, Lange G, Hindle S, Klein R, Rarey M. A consistent description of HYdrogen bond and DEhydration energies in protein-ligand complexes: methods behind the HYDE scoring function. J Comput Aided Mol Des. 2013 Jan;27(1):15-29. doi: 10.1007/s10822-012-9626-2. Epub 2012 Dec 27. PMID: 23269578.

[233] Arellano-Anaya ZE, Huor A, Leblanc P, Andréoletti O, Vilette D. Expression of Heterologous PrP and Prion Propagation in RK13 Cells. Methods Mol Biol. 2017;1658:95-104. doi: 10.1007/978-1-4939-7244-9_8. PMID: 28861785.

[234] Taraboulos A, Raeber AJ, Borchelt DR, Serban D, Prusiner SB. Synthesis and trafficking of prion proteins in cultured cells. Mol Biol Cell. 1992 Aug;3(8):851-63. doi: 10.1091/mbc.3.8.851. PMID: 1356522; PMCID: PMC275644.

[235] Vorberg I, Raines A, Story B, Priola SA. Susceptibility of common fibroblast cell lines to transmissible spongiform encephalopathy agents. J Infect Dis. 2004 Feb 1;189(3):431-9. doi: 10.1086/381166. Epub 2004 Jan 21. PMID: 14745700.

[236] Bradford H. Hirth, Andrew Janjigian, Fred Vinick. Preparation of pyrazole derivatives as antibacterial agents. Patent: US6410533B1

[237] Selvaraju S, Niradha Sachinthani KA, Hopson RA, McFarland FM, Guo S, Rheingold AL, Nelson TL. Eumelanin-inspired core derived from vanillin: a new building block for organic semiconductors. Chem Commun (Camb). 2015 Feb 18;51(14):2957-9. doi: 10.1039/c4cc09011j. PMID: 25594078.

[238] Massignan T, Boldrini A, Terruzzi L, Spagnolli G, Astolfi A, Bonaldo V, Pischedda F, Pizzato M, Lolli G, Barreca ML, Biasini E, Faccioli P, Pieri L. Antimalarial Artefenomel Inhibits Human SARS-CoV-2 Replication in Cells while Suppressing the Receptor ACE2. arXiv 2021 Jan. doi: arXiv:2004.13493v4

[239] Ge B, Jiang X, Chen Y, Sun T, Yang Q, Huang F. Kinetic and thermodynamic studies reveal chemokine homologues CC11 and CC24 with an almost identical tertiary structure have different folding pathways. BMC Biophys. 2017 Sep 12;10:7. doi: 10.1186/s13628-017-0039-4. PMID: 28919974; PMCID: PMC5596964.

[240] Wang F, Cazzolli G, Wintrode P, Faccioli P. Folding Mechanism of Proteins Im7 and Im9: Insight from All-Atom Simulations in Implicit and Explicit Solvent. J Phys Chem B. 2016 Sep 8;120(35):9297-307. doi: 10.1021/acs.jpcb.6b05819. Epub 2016 Aug 29. PMID: 27532482.

[241] Jiménez JL, Hegemann B, Hutchins JR, Peters JM, Durbin R. A systematic comparative and structural analysis of protein phosphorylation sites based on the mtcPTM database. Genome Biol. 2007;8(5):R90. doi: 10.1186/gb-2007-8-5-r90. PMID: 17521420; PMCID: PMC1929158.

[242] Pettersen EF, Goddard TD, Huang CC, Couch GS, Greenblatt DM, Meng EC, Ferrin TE. UCSF Chimera–a visualization system for exploratory research and analysis. J Comput Chem. 2004 Oct;25(13):1605-12. doi: 10.1002/jcc.20084. PMID: 15264254.

[243] Sali A, Blundell TL. Comparative protein modelling by satisfaction of spatial restraints. J Mol Biol. 1993 Dec 5;234(3):779-815. doi: 10.1006/jmbi.1993.1626. PMID: 8254673.

[244] Van Der Spoel D, Lindahl E, Hess B, Groenhof G, Mark AE, Berendsen HJ. GROMACS: fast, flexible, and free. J Comput Chem. 2005 Dec;26(16):1701-18. doi: 10.1002/jcc.20291. PMID: 16211538.

[245] Lindorff-Larsen K, Piana S, Palmo K, Maragakis P, Klepeis JL, Dror RO, Shaw DE. Improved side-chain torsion potentials for the Amber ff99SB protein force field. Proteins. 2010 Jun;78(8):1950-8. doi: 10.1002/prot.22711. PMID: 20408171; PMCID: PMC2970904.

[246] Emsley P, Lohkamp B, Scott WG, Cowtan K. Features and development of Coot. Acta Crystallogr D Biol Crystallogr. 2010 Apr;66(Pt 4):486-501. doi: 10.1107/S0907444910007493. Epub 2010 Mar 24. PMID: 20383002; PMCID: PMC2852313.

[247] Danne R, Poojari C, Martinez-Seara H, Rissanen S, Lolicato F, Róg T, Vattulainen I. doGlycans-Tools for Preparing Carbohydrate Structures for Atomistic Simulations of Glycoproteins, Glycolipids, and Carbohydrate Polymers for GROMACS. J Chem Inf Model. 2017 Oct 23;57(10):2401-2406. doi: 10.1021/acs.jcim.7b00237. Epub 2017 Oct 12. PMID: 28906114; PMCID: PMC5662928.

[248] Kirschner KN, Yongye AB, Tschampel SM, González-Outeiriño J, Daniels CR, Foley BL, Woods RJ. GLYCAM06: a generalizable biomolecular force field. Carbohydrates. J Comput Chem. 2008 Mar;29(4):622-55. doi: 10.1002/jcc.20820. PMID: 17849372; PMCID: PMC4423547.

[249] Bussi G, Donadio D, Parrinello M. Canonical sampling through velocity rescaling. J Chem Phys. 2007 Jan 7;126(1):014101. doi: 10.1063/1.2408420. PMID: 17212484.

[250] Parrinello M, and Rahman A. Polymorphic transitions in single crystals: a new molecular dynamics method. J. Appl. Phys. 52:7182. (1981) doi: 10.1063/1.328693

[251] Humphrey W, Dalke A, Schulten K. VMD: visual molecular dynamics. J Mol Graph. 1996 Feb;14(1):33-8, 27-8. doi: 10.1016/0263-7855(96)00018-5. PMID: 8744570.

[252] Bonomi M, Branduardi D, Bussi G, Camilloni C, Provasi D, Raiteri D, Donadio D, Marinelli F, Pietrucci F, Broglia RA and Parrinello M. PLUMED: a portable plugin for free energy calculations with molecular dynamics, Comp. Phys. Comm. 180, 1961 (2009). doi: 10.1016/j.cpc.2009.05.011

[253] Huang J, Rauscher S, Nawrocki G, Ran T, Feig M, de Groot BL, Grubmüller H, MacKerell AD Jr. CHARMM36m: an improved force field for folded and intrinsically disordered proteins. Nat Methods. 2017 Jan;14(1):71-73. doi: 10.1038/nmeth.4067. Epub 2016 Nov 7. PMID: 27819658; PMCID: PMC5199616.

254 R. Team, RStudio: Integrated Development for R. RStudio, Inc., Boston, MA (Computer Softwarev0.98.1074). http://www.rstudio.com/ (2015).

255 Gaussian 16, Frisch MJ, Trucks GW, Schlegel HB, Scuseria GE, Robb MA, Cheeseman JR, Scalmani G, Barone V, Petersson GA, Nakatsuji H, Li X, Caricato M, Marenich A. V, Bloino J, Janesko BG, Gomperts R, Mennucci B, Hratchian HP, Ortiz JV, Izmaylov AF, Sonnenberg JL, Williams-Young D, Ding F, Lipparini F, Egidi F, Goings J, Peng B, Petrone A, Henderson T, Ranasinghe D, Zakrzewski VG, Gao J, Rega N, Zheng G, Liang W, Hada M, Ehara M, Toyota K, Fukuda R, Hasegawa J, Ishida M, Nakajima T, Honda Y, Kitao O, Nakai H, Vreven T, Throssell K, Montgomery JA, Peralta JE, Ogliaro F, Bearpark MJ, Heyd JJ, Brothers EN, Kudin KN, Staroverov VN, Keith TA, Kobayashi R, Normand J, Raghavachari K, Rendell AP, Burant JC, Iyengar SS, Tomasi J, Cossi M, Millam, JM, Klene M, Adamo C, Cammi R, Ochterski JW, Martin RL, Morokuma K, Farkas O, Foresman JB, Fox DJ. Gaussian, Inc., Wallingford CT, 2016.

256 Zeng LY, Liu T, Yang J, Yang Y, Cai C, Liu S. "On-Water" Facile Synthesis of Novel Pyrazolo[3,4-b]pyridinones Possessing Anti-influenza Virus Activity. ACS Comb Sci. 2017 Jul 10;19(7):437-446. doi: 10.1021/acscombsci.7b00016. Epub 2017 Jun 23. PMID: 28581706.

257 Onuchic JN, Luthey-Schulten Z, Wolynes PG. Theory of protein folding: the energy landscape perspective. Annu Rev Phys Chem. 1997;48:545-600. doi: 10.1146/annurev.physchem.48.1.545. PMID: 9348663.

Author Contributions

In this section I report my specific contributions as well as that of other collaborators in the described research projects.

The Study of Prion Structure and Conversion

General project supervisors: Emiliano Biasini (associate professor at CIBIO, University of Trento), Pietro Faccioli (associate professor at the department of Physics, University of Trento) and Jesús Requena (associate professor at CIMUS, University of Santiago de Compostela).

The threading schemes of the first 4RβS and the DTC-4RβS models of PrP^{Sc} were designed by me and Jesús Requena. I constructed the 3D models and carried out the MD simulations. Modelling of the glycosylated structures and data analysis were performed by me and Marta Rigoli (former master's student at CIBIO, University of Trento). Emiliano Biasini, Pietro Faccioli and I conceived the idea underlying the simulations of prion propagation. The statistical model describing the conversion of PrP^C into a 4RβS-PrP^{Sc} was developed and implemented by me and Pietro Faccioli. The validation of the SCPS scheme and the simulations of the HET-s prion propagation were carried out and analyzed by me and Luca Terruzzi (former master's student at CIBIO, University of Trento). The implementation of the CVs to perform SCPS on Gromacs was done by Alberto Boldrini (former master's student at CIBIO, University of Trento).

Identification of Pharmacological Degraders for PrP

General project supervisors: Emiliano Biasini, Pietro Faccioli and Maria Letizia Barreca (associate professor at the department of Pharmaceutical Sciences, University of Perugia). I carried out and analyzed the folding simulation of PrP, and identified the target folding intermediate. Virtual screening was carried out in collaboration with the D^2 medicinal chemistry group led by Maria Letizia Barreca, and Andrea Astolfi (department of pharmaceutical sciences, University of Perugia) selected the 30 virtual hits. Most of the cell-based assays were performed by Tania Massignan (former post-doc at CIBIO, University of Trento), Silvia Biggi (former PhD student at CIBIO, University of Trento) and Valerio Bonaldo (PhD student at CIBIO, University of Trento). Purification of mouse recombinant PrP 111-230 was performed by me under the supervision of Jesús Requena, while purification of human recombinant PrP 23-231 was carried out by the laboratory of Jesús Requena. Silvia Biggi performed the DMR assays. Extended MD simulations of native PrP were carried out by me and Marta Rigoli and I analyzed the trajectories. I carried out the crystallization attempt under the supervision of Graziano Lolli (CIBIO, University of Trento). The temperature-dependent detergent

insolubility assays were designed by me and Emiliano Biasini and performed by Paolo Brunelli (former bachelor's student at CIBIO, University of Trento). The samples for FESEM analysis were prepared by me and Yaiza Bugallo (PhD student at CIMUS, University of Santiago de Compostela), micrographs were acquired by the electron microscopy facility at CIMUS. I designed and performed the synthesis of SM875 under the supervision of Ines Mancini (associate professor at the Department of Physics, University of Trento). I carried out the structural characterization of the compound and of its enantiomers. CD spectra of SM875 were simulated by Petri Tähtinen (University of Turku, Finland). The synthesis of the SM875 analogs was performed by me and a group of bachelor's students I was supervising.

Marco Sessa created the illustrations shown in figures 1.1, 1.2, 1.8, 1.13